UNCLASSIFIED

AD NUMBER

AD913977

NEW LIMITATION CHANGE

TO

Approved for public release, distribution unlimited

FROM

Distribution authorized to U.S. Gov't. agencies only; Test and Evaluation; MAR 1978. Other requests shall be referred to Air Force Avionics Lab., Wright-Patterson AFB, OH 45433.

AUTHORITY

SAMSO, USAF ltr, 11 Apr 1978

THIS PAGE IS UNCLASSIFIED

AD 913977

AFAL-TR-73-154

ATMOSPHERIC TRANSMISSION MEASUREMENT 1

H. V. Hance

Lockheed Missiles & Space Company, Inc.

and

B. Grabois

ITT-Gilfillan, Inc.

DDC
RECEIVED
OCT 23 1973
E

TECHNICAL REPORT AFAL-TR-73-154
August 1973



Distribution is limited to U.S. Government agencies only; test and evaluation, March 1973. Other requests for this document must be referred to AFAL/TEL/405B, Wright-Patterson AFB, Ohio 45433.

Air Force Avionics Laboratory
Air Force Systems Command
Wright-Patterson Air Force Base Ohio

NOTICE

When Government drawings, specifications, or other data are used for any purpose other than in connection with a definitely related Government procurement operation, the United States Government thereby incurs no responsibility nor any obligation whatsoever; and the fact that the government may have formulated, furnished, or in any way supplied the said drawings, specifications, or other data, is not to be regarded by implication or otherwise as in any manner licensing the holder or any other person or corporation, or conveying any rights or permission to manufacture, use, or sell any patented invention that may in any way be related thereto.

Copies of this report should not be returned unless return is required by security considerations, contractual obligations, or notice on a specific document.

ATMOSPHERIC TRANSMISSION MEASUREMENT 1

H. V. Hance
B. Grabois

Distribution is limited to U.S. Government agencies only; test and evaluation, March 1973. Other requests for this document must be referred to AFAL/TEL/405B, Wright-Patterson AFB, Ohio 45433.

FOREWORD

This report covers work performed from 22 May 1972 to 8 March 1973 under Contract F33615-72-C-1938, for the Air Force Avionics Laboratory of the Air Force Systems Command. This contract was initiated by and administered under the direction of the 405B Program of the Air Force Avionics Laboratory.

This report was prepared by H. V. Hance of the Lockheed Palo Alto Research Laboratory of Lockheed Missiles & Space Company, Inc., (LMSC), Palo Alto, California, and B. Grabois of ITT-Gilfillan, Inc., Van Nuys, California. Assistance in designing and assembling the optical and electronic equipment used in the experiments was provided by D. S. Oppenheimer and S. E. Patterson of LMSC. L. Cardone, R. A. Deters, and R. O. Waddoups of ITT-Gilfillan assisted in the design of the star image sensor, and R. D. Merrill of LMSC was responsible for design of the data recording and preliminary processing system. Analytical support in all phases of the project was provided by D. L. Fried of Optical Science Consultants, Inc., Yorba Linda, California. R. C. Ohlmann of LMSC had overall responsibility for the program and provided substantial technical guidance.

The report was submitted by the authors in March 1973. The LMSC report number is D315126.

This technical report has been reviewed and is approved.

Paul Freedman

PAUL M. FREEDMAN, MAJ USAF
Program Manager
405B Advanced Development Program

ABSTRACT

A novel method for improving the performance of laser communication links through a turbulent atmosphere, called "fast tracking," has been demonstrated experimentally in the laboratory to be both theoretically sound and practicable. Also, a design has been prepared for an atmospheric transmission measurement (ATM) system suitable for use at field sites for evaluation of atmospheric turbulence effects on ground-to-space laser communication links. The ATM system makes use of a fast-response (1 msec) star tracker and image intensity sensor; it is relatively simple and economical to use because neither flight hardware nor flight operations is involved, and it is capable of day or night operation. A field measurement plan is presented that is designed to aid in the selection of laser transmitter sites and to indicate the performance of ground-to-space links using those sites.

Because the concept of optical antenna gain reciprocity is central to both the fast-tracking technique and to the ATM system, an initial experimental objective of the program was to test this theory. The key test was conducted over a 450-ft outdoor path using two laser-transmitter/pinhole-receiver units directed toward one another. In each unit, the transmitter and receiver were in a conjugate relationship to one another and shared a common aperture, as required by the theory. For a series of measurements with beam diameters from 1.25 to 5 cm, the normalized cross correlation of the two received signals was found to be 0.964 ± 0.023 (1σ), a value in satisfactory agreement with the theoretical value of unity. As beam breakup ranged from negligible to severe for the range of aperture sizes used, the validity of reciprocity theory is considered to be well substantiated for all beam-perturbation conditions of practical interest.

To provide quantitative criteria for the design of the experiments, the reciprocity theory was reviewed in detail and was extended to cover the quasicoherent pinhole-detector receiver using a pinhole of finite size. Boresight requirements also were derived for a fast-tracking transmitter.

In the fast-tracking experiment, an optical tracker associated with the transmitting laser sensed angle deflections of the beam from a beacon laser co-located with the receiver and applied an equal correction to the transmitter by means of beam steering optics. When using artificial turbulence that produced tracking errors similar to those expected with real atmospheric turbulence, it was found that activation of the beam steerers reduced signal strength fluctuations at the receiver by 18 dB or more. The magnitude of this improvement is regarded as adequate to demonstrate the soundness of the fast-tracking concept.

CONTENTS

Section		Page
I	INTRODUCTION	1
	1. General	1
	a. Background	1
	b. Major Program Objectives	2
	c. Program Organization	3
	2. Report Organization	3
II	FADE CORRELATION EXPERIMENT	5
	1. General	5
	2. Optical Antenna Gain Reciprocity Theory	5
	a. Reciprocity Concept and Summary of Theory Developed	5
	b. Extension to Incoherent Reception	7
	3. Experiment Concept	10
	a. Brief Description of Experiment	10
	b. Statistical Quantities to be Measured	12
	4. Experimental Equipment and Alignment Methods	17
	a. Overall System Description	17
	b. Optics Configuration	21
	c. Signal Conditioning and Monitoring Electronics	24
	d. Fourier Analyzer Operation	29
	e. Optics Alignment and Adjustment	33
	5. Fade Correlation Measurements	36
	a. Short-Path Laboratory Test	36
	b. Medium- and Long-Path Laboratory Test	36
	c. Outdoor Measurement	42
	6. Significance of Reciprocity Verifications	45

PRECEDING PAGE BLANK-NOT FILMED

Section		Page
III	BEACON FAST-TRACKING, TRANSMITTER FAST-STEERING EXPERIMENT	47
	1. General Considerations	47
	2. Theoretical Background	49
	3. Description of Experimental System	50
	4. Measurement Program	56
	a. Objectives of Measurement Program	56
	b. Preparation of Turbulence Generator, Optics, and Tracker	56
	c. Turbulence Effect – Fast Beam Steerers Off	61
	d. Reduction of Turbulence Effect by Fast Beam Steering	61
	e. Turbulence Effect on Frequency Response of Fast-Tracking Loop	69
	f. Effect of Aperture Size on Fading Reduction by Fast Tracking	69
	g. Boresight Tolerance	71
IV	ATMOSPHERIC TRANSMISSION MEASUREMENT SYSTEM DESIGN	75
	1. General Considerations	75
	a. Summary Discussion of Atmospheric Turbulence Effects on Ground to-Space Link Design	75
	b. Need for Atmospheric Transmission Measurements for Ground-to-Space Link Design	76
	c. Advantages of Approach Based on Star Image Sensing	77
	d. Overall System Description and Operational Concept	79
	e. Summary of Measurement System Performance Characteristics	83
	f. Measurement System Design Study Approach	84
	2. Optical Sensor Design	34
	a. Measurement System Overview	81
	b. Telescope	87
	c. Telescope Mount and Astrodome	92
	d. Star Image Sensor	99
	e. Operational Considerations	123
	3. Data Analysis and Recording Subsystem	127
	a. General Considerations	127
	b. Data Processing System Concept	127
	c. Overall Description of the Data Processing System	132
	d. Performance Characteristics	137
	e. Summary	143

Section		Page
	4. Experimental Program Definition	143
	a. Measurement Procedure	143
	b. Measurement Schedule	144
	c. Test Plan Review	146
	5. Major Component Specifications	147
	a. General Considerations	147
	b. Specification for Star Image Sensor	147
	c. Specification for Telescope	152
V	CONCLUSIONS AND RECOMMENDATIONS	155
	1. Conclusions	155
	2. Recommendations	155

Appendixes

I	FORMAL PROOF OF OPTICAL ANTENNA GAIN RECIPROCITY FOR PROPAGATION THROUGH A TURBULENT MEDIUM	159
II	EQUIVALENCE OF RECEIVERS	175
III	BORESIGHT REQUIREMENTS FOR APPLICABILITY OF ANTENNA GAIN RECIPROCITY	185
IV	PRELIMINARY PARAMETER CONSIDERATIONS FOR A WAVEFRONT DISTORTION SENSITIVE STAR TRACKER	215
V	NOTES ON THE DESIGN OF A WAVEFRONT DISTORTION SENSITIVE STAR TRACKER TELESCOPE	233
VI	METHOD OF COMPUTING STAR DESIGNATION DATA AS USED AT VANDENBERG AIR FORCE BASE	255
VII	DERIVATION OF COORDINATE TRANSFORMATION OF SIDEREAL MOUNT	259
VIII	NOVA TIMING FOR CONVERSION, PROCESSING, AND RECORDING	267
IX	MEASUREMENT RESULTS – FADE CORRELATION EXPERIMENT	273
	REFERENCES	287
	DD-1473	291

ILLUSTRATIONS

Figure		Page
1	Transmitter/Receiver System Using (a) Heterodyne Receiver and (b) Photon-Counting Detector With Pinhole Aperture — Schematic	8
2	Error Due to Finite Pinhole Aperture Size in a Photon-Counting Receiver	10
3	Optical Schematic Showing Essential Features of Experimental Arrangement for Testing Optical Antenna Gain Reciprocity	11
4	Experimental System — General View	18
5	Arrangement of Optics	19
6	Transmitter/Receiver Unit — Overall View	20
7	Signal-Conditioning Electronics and Signal Processing System — Functional Block Diagram	25
8	A-Channel and B-Channel Electronics Units	27
9	Frequency Response of Anti-Aliasing Filters at 1-kHz Bandwidth Setting	28
10	Oscillogram of Simultaneously Recorded A-Channel and B-Channel Signals	30
11	Real Part of Complex Fourier Spectrum of a Portion of Waveform From Figure 10	30
12	Averaged Power Spectrum — Linear Scale of Frequency for Abscissa; Logarithmic Scale (5 dB/Div) for Ordinate	32
13	$\rho^2(\tau)$ Displayed by the Fourier Analyzer With $\rho(\tau)$ as the Normal Cross-Correlation Function	32
14	Partially Disassembled Beam Magnifier (In Use, the Two Microscope Objectives are Positioned Nose-to-Nose With Coincident Axes and Focal Planes.)	33
15	Square of Normalized Cross-Correlation Function of Signal Transmitted Over 50-ft Indoor Path, With Secondary Maxima Indicating Presence of Periodic Components in the Signal	37

Figure		Page
16	Power Spectrum of One of the Signals From Which Figure 15 Was Derived — Frequencies of Periodic Components Indicated by Peaks at 50 and 110 Hz; Frequency Resolution (Spacing Between Points) = 10 Hz	38
17	Received Beam Images at Camera Focal Plane and Photodetector Pinhole Plane for Three Primary Aperture Sizes	39
18	Transmitter/Receiver Unit With Air Shields in Place	41
19	View Along Test Path Used in Outdoor Fade Correlation Measurements — Transmitter/Receiver Units Located on Concrete Walkway in Immediate Foreground and Path-Folding Mirror Place Just to Right of Single Tree in Background at Center Left	43
20	Beacon Fast-Tracking Experiment — Simplified Schematic	48
21	Beacon Fast-Tracking Experiment — Optical Components and Beam Paths	51
22	Acquisition and Tracking Evaluation Subsystem Used for Beacon Fast-Tracking Experiment	52
23	Beacon Transmitter and Intensity Detector Used to Simulate Communication Link Transmitting Terminal	53
24	Laser, Tracker, and Fine-Beam Steerers Used to Simulate Communication Link Receiving Terminal	54
25	Longitudinal Cross Section of Turbulence Generator	57
26	Oscilloscope Traces of Tracker Horizontal Channel Output Showing Effect of Simulated Turbulence — (a) Low-Strength Air Turbulence, (b) Higher-Strength Air Turbulence	58
27	Received Signal Intensity Fluctuations Due to Simulated Turbulence — Beam Steerers Off	60
28	Power Spectral Density of Indicated Beacon Direction Fluctuations Caused by Simulated Atmospheric Turbulence (Beam Steerers Off) — (a) Heat Input to Turbulence Generator, (b) Heat Plus Air Input	62
29	Pointing and Tracking Detector Outputs With Simulated Atmospheric Turbulence — (a) Beam Steerers Off, (b) Beam Steerers On	64
30	Comparison of Power Spectra of Tracker Vertical-Channel Error Signals With Beam Steerers Off (Upper Trace) and On (Lower Trace)	65

Figure		Page
31	Comparison of Power Spectra of Pointing Detector Vertical-Channel Angle Error Signals With Beam Steerers Off (Upper Trace) and On (Lower Trace)	65
32	Output Fluctuations of Intensity Detector Communication Receiver Due to Simulated Atmospheric Turbulence – (a) Beam Steerers Off, (b) Beam Steerers On	67
33	Intensity Detector Output Signal Power Spectra – Beam Steerers Off (Upper Trace), Beam Steerers On (Lower Trace); 25-μm Pinhole	68
34	Intensity Detector Output Signal Power Spectra – Beam Steerers Off (Upper Trace), Beam Steerers On (Lower Trace); 10-μm Pinhole	68
35	Component Relationships in Tracking and Beam Steering System–tem – With Only Portion of System Within Dashed Line Active in Fast-Tracking Experiment	70
36	Antenna Gain Correlation $C_T\theta$ for a Tracking/Pointing System Employing Fast Beam Steering – Aperture Diameter: $D = 1.5\ r_d$	73
37	System Configuration	80
38	Cassegrain Reflector Telescope – 16 in.	81
39	Major Elements of Measurement System – Functional Block Diagram	85
40	Optical System – Schematic	89
41	Cassegrain Reflector Telescope Mount – Supplier Specifications	94
42	Selected Astrodome Chart (Parabam, Inc.)	100
43	Typical Star Tracker	102
44	Star Image Sensor – Block Diagram	104
45	Search-Scan Waveforms	105
46	SIS Spatial Relationship	107
47	Signal Current as a Function of Lens Diameter	111
48	Tracking Nea Vs. Tracking Loop BW	114
49	Spatial Relationship	115
50	Amplitude S/N Ratio Vs. Sample BW	117
51	Spatial Relationsip to Provide a Sampling Period With Zero Scan Deflection	118
52	Amplitude S/N Ratio Vs. Sample BW – Modified Scanning Pattern of Figure 51	119

Figure		Page
53	Tracking NEA Vs. Tracking Loop BW for Modified Scanning Pattern of Figure 51	120
54	Minimum Lens Diameter Vs. Tracking Loop Bandwidths for Different G-0 Star Magnitudes	121
55	Data Processor System Hardware	133
56	Typical Processor Hardware Configuration	134
57	Program Schedule	145
58	Site Operation Schedule for Initial Operation	146
59	Site Operation Schedule for Normal Operation	147

TABLES

Table		Page
1	Focusing Objective Lenses Used for Various Primary Aperture Diameters	23
2	Summary of Fade Correlation Measurements, Using 450-ft Outdoor Path	44
3	Summary of Measurement Results	63
4	Intensity Detector Output Fluctuation Magnitude and Variance Reduction With Beam Steering	66
5	Astronomical Refractions	124
6	SIS and Voice Signal Characteristics	130
7	NOVA (Data General) Configuration and Costs	139
8	PDP 11 and Varian 73 Equipment Description and Costs	141
9	Clock Description and Cost	142
10	Strip-Chart Recorder Description and Cost	143
11	Cost/Performance Tradeoff	143

SECTION I

INTRODUCTION

1. GENERAL

a. Background

A program previously conducted by Lockheed Missiles & Space Company, Inc., (LMSC) for the U. S. Air Force, entitled "Design Study for a Space Data Relay Subsystem," involved, among other matters, the design of a laser link capable of transmitting extremely high-rate data from a ground terminal to a relay satellite in synchronous orbit. In the final report on that project (Reference 1) it was emphasized that optical inhomogeneity of the atmosphere, associated with turbulence and convection processes, could severely degrade error rate of such an up-link unless special measures were employed. The deleterious effects were of two types – reduction of average gain of the transmitting optics (beam spreading), and signal fading induced by time-varying beam distortions (wander and breakup). The study also showed that the problem caused by time-varying inhomogeneity of the atmosphere (referred to hereafter as "atmospheric turbulence"), could not be dealt with adequately in a practical sense by such obvious expedients as increasing transmitter power or the size of the transmitting optics.

In arriving at a practical solution to the up-link problem, LMSC carried out under the Space Data Relay Subsystem Study an extensive analysis of the effects of atmospheric turbulence on ground-to-space propagation of a laser beam. It was found, for a given strength of turbulence, that the deleterious effects of the atmosphere could be minimized by choosing the proper size transmitting aperture. More important, by employing special "fast-tracking" optics designed to steer the transmitting beam, instant-by-instant, in a way to counteract beam deflections that would subsequently be caused by the atmosphere, the optimum size of the antenna is about three times larger than that of an optimum conventional (slow-tracking) transmitter. Associated with this increase in antenna size is an improvement of about 10 dB in effective transmitter power.

The required beam steering action is obtained by using an optical tracker that shares the transmitter optics, including the beam steerer, and senses changes in the apparent location of the intended receiver by tracking a beacon laser co-located with the receiver. The error signals generated by the tracker drive the fast-tracking optics through a servo-amplifier in a way to reduce the tracking error and, in the process, also deflect the transmitted beam by exactly the desired amount. A transmitter whose beam direction is controlled in this way can equally well be described by the term "fast-steering," (if the emphasis is to be placed on the action of the optics in controlling the transmitted beam direction) or fast-tracking (if it is desired to emphasize the means by which the steering action is mechanized). These two terms will be used interchangeably (or coupled together), depending upon the aspects of the problem requiring emphasis.

The analysis of atmospheric turbulence effects performed in the abovementioned design study (Reference 1) and the concept of a fast-tracking transmitter were both based in large part on a theory of optical antenna gain reciprocity, also presented in the design study. Briefly, this theory states that, given an optical signal link consisting of two optical apertures or antennas, a propagation path between them, and one aperture representing a laser transmitter and the other an optical heterodyne receiver, then the signal generated at the receiver is the same, under certain conditions, regardless of which aperture is used as the receiver. That is, the effect of atmospheric turbulence and of aperture wave function variations (e.g., transmitter primary aperture illumination pattern) is the same, no matter which way the optical signal is flowing.

The reciprocity theory derived in that design study involved the simplifying assumption of coherent (e.g., heterodyne) reception. To improve the applicability of reciprocity theory to laser communication systems employing incoherent (e.g., photon counting) receivers, the theory has been extended to that case. (See Appendix II.)

In order to arrive at a practical design of an up-link, it was necessary in the system design study mentioned above to make quantitative (absolute) performance predictions. In that study, it was shown that, on the basis of reciprocity theory, certain existing data on star image fluctuations could be used as a basis for predicting performance of an up-link under the atmospheric conditions that existed during the measurements. Finally, the study showed that the quantitative experimental data on the optical properties of the atmosphere that was available was inadequate for predicting the performance of a ground-to-space link, particularly during daytime. The best available data are based on measurements of star image fluctuations made only at night, at only a few locations, and over only short periods of time. The need for more intensive measurements was clearly indicated.

b. Major Program Objectives

This program is based in large part on the findings of the Space Data Relay Subsystem Design Study (Reference 1) and had the following main objectives:

(1) Experimentally test optical reciprocity theory for propagation over a turbulent atmospheric path.

(2) Demonstrate the effectiveness of transmitter fast-steering, in combination with beacon fast tracking, in reducing signal fading on a laser link that traverses a turbulent path.

(3) Design a transportable measurement system capable of providing quantitative data, day or night, on the transmission properties of a ground-to-space optical link. The system is to make use of a novel approach, originated by LMSC, and based on reciprocity theory, in which a star tracking sensor that is coupled to an astronomical telescope measures fluctuations in intensity and position of stellar images. The measurements are to be made in such a way that the results will allow interpretation directly in terms of performance of an up-link through the atmosphere. The design is to be sufficiently detailed to serve as a basis for a follow-on development program. Also, a plan for a field measurement program is to be prepared.

The verification of the optical reciprocity theory (first objective) is of central importance in the program because the validity of the fast-steering concept (second objective) and of the approach to atmospheric transmission based on use of a tracking star sensor (third objective) depend in a fundamental way on the validity of the theory. Accordingly, a

major part of the work performed has been related to the verification of the theory. As a result, the theory is now considered by LMSC to have been confirmed in an unambiguous way and with ample accuracy to assure that the concepts underlying the last two objectives are sound. The experimental results obtained in the Beacon Fast Tracking experiment further substantiate the reciprocity theory and, in addition, directly support the approach to atmospheric transmission measurement based on star image sensing.

c. Program Organization

The reciprocity verification test was carried out at the Lockheed Palo Alto Research Laboratories by LMSC personnel with assistance from Dr. David L. Fried, of Optical Science Consultants, on the initial design of the experiment. The Beacon Fast Tracking experiment was also conducted at the Lockheed Palo Alto Research Laboratory by LMSC personnel, with assistance from ITT-Gilfillan personnel. The experiment was performed using an optical acquisition and tracking system developed jointly by LMSC and ITT-Gilfillan for other purposes, but made available for use on this program. A major part of the study effort relating to the design of an Atmospheric Transmission Measurement (ATM) system was conducted by ITT-Gilfillan under subcontract from LMSC. Dr. Fried assisted in formulating the measurement system concept and in performing analyses leading to an initial definition of measurement system parameters. LMSC was responsible for the design of a data recording and preliminary processing subsystem that would be an integral part of the transportable measurement system and also prepared the field measurement program plan.

2. REPORT ORGANIZATION

This report presents, in Sections II, III, and IV, the work accomplished under the ATM 1 program in order to fulfill the previously noted major program objectives. Section IV also includes a recommended schedule and task breakdown for a follow-on effort for development of the ATM system and for the conduct of a field measurement program. Section V summarizes conclusions and recommendations, and supporting data are provided in Appendixes I through IX.

SECTION II

FADE CORRELATION EXPERIMENT

1. GENERAL

This experiment is designed to test the validity of the theory of optical antenna gain reciprocity for propagation through a turbulent atmosphere. In Section I, the need for a critical and unambiguous test to establish the applicability of the theory as a basis for measuring and predicting the performance of optical links employing atmospheric paths has already been indicated. In this section, the experimental testing of reciprocity theory that has been conducted under this contract is described, and the test results are presented and evaluated. Before detailing the tests, a review of the concept of propagation reciprocity, and a summary of the principal consequences of the theory are presented. Also, a review is given of the optical principles involved and of the statistical measurement methods employed that are basic to an understanding of the experiments.

2. OPTICAL ANTENNA GAIN RECIPROCITY THEORY

a. Reciprocity Concept and Summary of Theory Developed

In Appendix I, optical reciprocity theory is developed rigorously for the case of a laser transmitter and a heterodyne (coherent) receiver. Because of its relative simplicity, a photon-counting or "incoherent" receiver is preferable to a heterodyne receiver for this experiment, as well as for many other situations. However, the applicability of reciprocity theory to a link using a photon-counting receiver had not previously been established and therefore required investigation. The necessary extension of reciprocity theory is carried out in Appendix II where it is shown that the theory applies with only minor qualification. The conditions of applicability are presented and discussed in Section II, 2, b.

(1) Reciprocity Concept. The concept of propagation reciprocity in its most commonly used form relates to microwave antenna gain. Put into simplest terms, the concept states that an antenna will perform equally well, i.e., provide the same antenna gain, whether used as part of either a transmitter system or receiver system. In applying the concept of reciprocity to microwave antennas, it is usually the effect of imperfections and misalignments in the antenna that are of interest. In this program, however, the effect of the propagation medium on the performance of an optical link is emphasized. It is not imperfections in the antenna per se (which are assumed to be ideal) that concerns us, but rather the effect of the atmosphere in distorting the wave launched by the antenna if it is acting as part of a transmitter system, or the wave received by the antenna if it is part of a receiver system. The concept of reciprocity as applied to optical propagation asserts that under certain conditions the effects of atmospheric inhomogeneities on the performance of an optical link is quantitatively the same whether the antenna functions as part of a transmitter or a receiver. Although physically, the

PRECEDING PAGE BLANK-NOT F

link degradation of interest here is caused by time-varying beam distortions that occur in the path between the antennas, it is convenient to think of the degradation as due to a reduction of antenna gain caused by perturbations of the actual transmitter (or receiver) beam pattern. Much of the following discussion is couched in these terms.

When reciprocity is claimed for optical system performance in the presence of atmospheric turbulence, it is said, in essence, that if (1) an optical link were established between a laser transmitter and an optical heterodyne receiver (with atmospheric turbulence somewhere in the propagation path), and (2) if the role of the two ends of the link were then interchanged, (leaving the antenna apertures as they were), the signal strength developed over the link would remain the same. It should be noted that this claim of reciprocity is to be understood as applying on an instantaneous, random-sample basis, as well as on a statistical basis.

A consideration that almost never arises in the microwave case, but which must always be kept in mind in dealing with optical systems is the distinction between systems that are sensitive or insensitive, respectively, to wavefront distortion. Because the ultimate interest of this effort points toward improving antenna pointing as a means for improving the transmission characteristics of optical links through the atmosphere, the photon bucket receiver or the searchlight transmitter, are not of concern here since they fall into the wavefront insensitive category. Attention is therefore restricted to the laser transmitter and the optical heterodyne or pinhole detector receiver, in which performance indicates sensitivity to wavefront tilt or other distortions.

(2) Summary of Reciprocity Theory. A theoretical proof of optical antenna gain reciprocity for transmission through random, inhomogeneous media is given in Appendix I. The appendix begins with a detailed presentation of the general proof of reciprocity for the so-called point-to-point case in the form given by Lutomirski and Yura (Reference 2). They show that, if a nondirectional transmitter of unit strength located at a point defined by position vector $\vec{r}_1$ produces a signal $\psi(\vec{r}_1, \vec{r}_2)$ at a point receiver located at $\vec{r}_2$, the same transmitter located at point $\vec{r}_2$ would then produce the same signal at $\vec{r}_1$. This result is expressed by the simple relation

$$\psi(\vec{r}_1, \vec{r}_2) = \psi(\vec{r}_2, \vec{r}_1) \qquad (1)$$

An interesting feature of the proof is its simplicity and freedom from approximations, such as truncations of infinite series, that create so much difficulty and uncertainty in many aspects of the theory of optical propagation through random media. Especially important is the fact that the proof requires no specification of the nature of the path inhomogeneity. That is, the results are independent of the cause or nature of the path perturbations and therefore do not depend upon the validity of any particular model of atmospheric turbulence.[1]

[1]More precisely, the proof requires that the propagation process be governed by a scalar wave equation. This restriction excludes nonlinear and gyromagnetic media, but these cases do not concern us.

Next, the case is taken up of propagation between a laser transmitter with telescope optics and a point receiver, on the one hand and, on the other, the reciprocal situation of propagation between a point transmitter and an optical heterodyne receiver with the same telescope optics. Again, the reciprocity relation Eq. (1) is shown to hold if the quantity ψ is now taken to be the receiver beat-frequency output signal, and the heterodyning is accomplished in an appropriate manner. The receiver configuration required is discussed in the following Section.

Finally, Appendix I treats the case of aperture-to-aperture reciprocity, i.e., transmission between telescopes. In this instance, only a sketch of the proof is presented, but all essential steps are indicated. Again, without approximations or restrictions other than those previously stated, exact reciprocity is demonstrated.

b. Extension to Incoherent Reception

The development of reciprocity theory in Appendix I for the case of finite transmitting apertures involves the concept of a heterodyne receiver with a local oscillator beam that has a wavefront structure identical to the transmitting beam with which the receiver is associated. In Appendix II, the theory is extended to the case of a diffraction-limited, photon-counting receiver that does not employ a local oscillator but, rather, uses a pinhole aperture at the focal plane to obtain sensitivity to wavefront changes in the received signal. These receiver types are illustrated and compared as a basis for presenting the conclusion of the theory for the incoherent receiver.

Figure 1(a) represents an optical heterodyne receiver in which the transmitting beam passes through a beamsplitter located between the laser and the primary optics (the latter not shown). The local oscillator produces a wavefront that is identical in amplitude and phase to the transmitter wave at each point on the beamsplitter, except that the local oscillator wave is offset in frequency. The received signal (from the primary optics) is partially reflected by the beamsplitter and combines with the portion of the local-oscillator wave that is transmitted by the beamsplitter. These two signals produce a beat-frequency component in the photodetector output current. This component is selected by the beat-frequency filter; it is square-law detected; and it is then low-pass filtered to select the signal modulation components of interest as the useful receiver output.

Figure 1 shows focal points of the transmitter and local oscillator beams at O_T and O_R, respectively. When these points are mirror images of one another in the beamsplitter, the receiver and transmitter are said to be conjugated to one another. Under this condition, a received beam with wavefronts identical to the transmitted wavefronts at the beamsplitter, except for having opposite propagation direction, will produce maximum receiver output. Distortion or tilt of the received wavefront will reduce the output. It can be shown that the heterodyne receiver is sensitive to such wavefront changes even though no aperture is used at the focal point O_R.

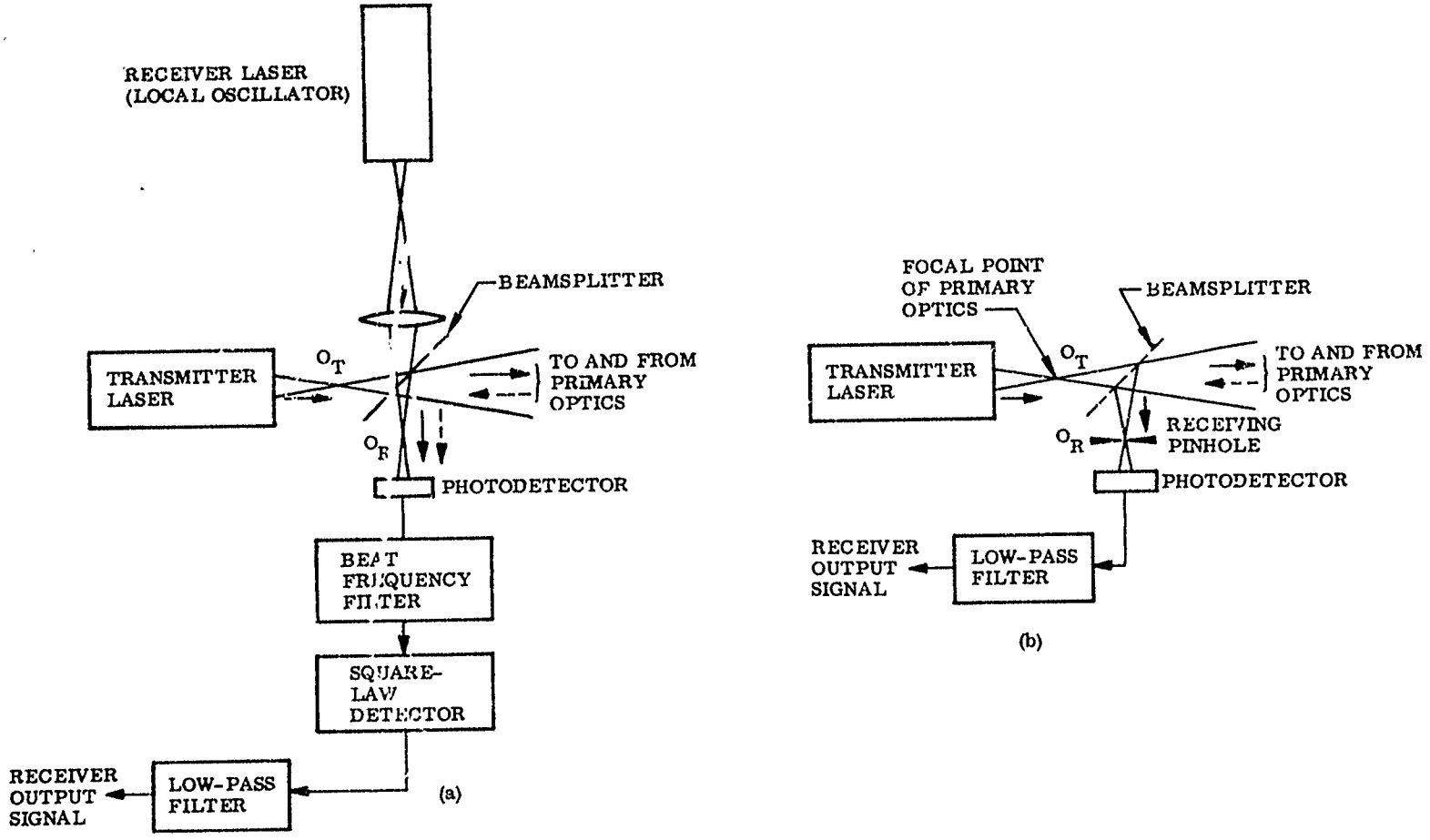


Figure 1 Transmitter/Receiver System Using (a) Heterodyne Receiver and (b) Photon-Counting Detector With Pinhole Aperture – Schematic

Ideally, a heterodyne receiver would be used in an experimental test of optical antenna reciprocity theory because this is the type assumed in the development of the theory. However, choice of such a receiver would lead to a major complication of the experiment because of the need to stabilize the frequency of the receiver local oscillator relative to that of the transmitter at the opposite end of the link. (Without stabilization, the bandwidth of the beat-frequency signal would become excessive.) Also, a heterodyne receiver is not representative of the type that is attractive for most practical applications, namely, a photon-counting receiver. In view of these considerations, the question arises as to whether, or under what conditions, a photon-counting receiver can be used in an experimental test of reciprocity theory. This question is taken up in Appendix II where a receiver of the type represented in Figure 1(b) is analyzed. A local oscillator is not used. Instead, wavefront sensitivity is obtained by placing a pinhole aperture ahead of the photodetector at the focal point of the primary optics, as reflected in the beamsplitter. It is shown in Appendix B that this receiver responds to changes of the received signal wavefront in exactly the same manner as the heterodyne detector, provided that the photodetector pinhole is made sufficiently small. Assuming this latter condition is met, it follows that the photon-counting detector is equivalent to the heterodyne receiver, at least insofar as wavefront distortions are manifested as signal strength changes at the receiver output. (The heterodyne receiver will also sense changes of wavefront phase whereas the photon counter will not.) These consequences of reciprocity theory can be applied to a laser communication subsystem both as a means of maintaining precise pointing of a laser transmitter (and associated beacon receiver) toward an intended receiver (and associated beacon transmitter), and the reverse.

Because of the restriction on pinhole size, the questions of how small is "small enough" and what fraction of the available light is then transmitted must be considered. An upper bound on the error in indicated signal-strength fluctuations is derived in Appendix II. The analysis shows that the error decreases rapidly as the pinhole diameter is reduced relative to the theoretical size of the diffraction spot at the pinhole plane that would be produced by ideal optics imaging a uniform wavefront. Taking $f\lambda$ as a measure of the diffraction spot size, where f is the convergence angle produced by the primary optics (also the effective f/number of the receiving optics as referred to the pinhole plane) and λ is the wavelength, the measurement error η is found to vary with detector pinhole diameter, as shown in Figure 2. The abscissa α is the ratio of pinhole diameter to diffraction spot size $f\lambda$; for example, the error will be less than 10 percent if the pinhole diameter is less than $0.6\ f\lambda$. Under this condition, it can be shown that the pinhole will transmit almost 20 percent of the light that is available when the wave front at the primary aperture is undistorted. This criterion is used in the design of the Atmospheric Transmission Measurement (ATM) system described in Section IV.

In the experimental system used for the test of optical reciprocity theory, a more severe diameter criterion is adopted, namely $\alpha \leq 0.4$. According to Figure 2, this choice assures that measurement errors due to departure from the conditions for exact reciprocity will be less than approximately 5 percent.

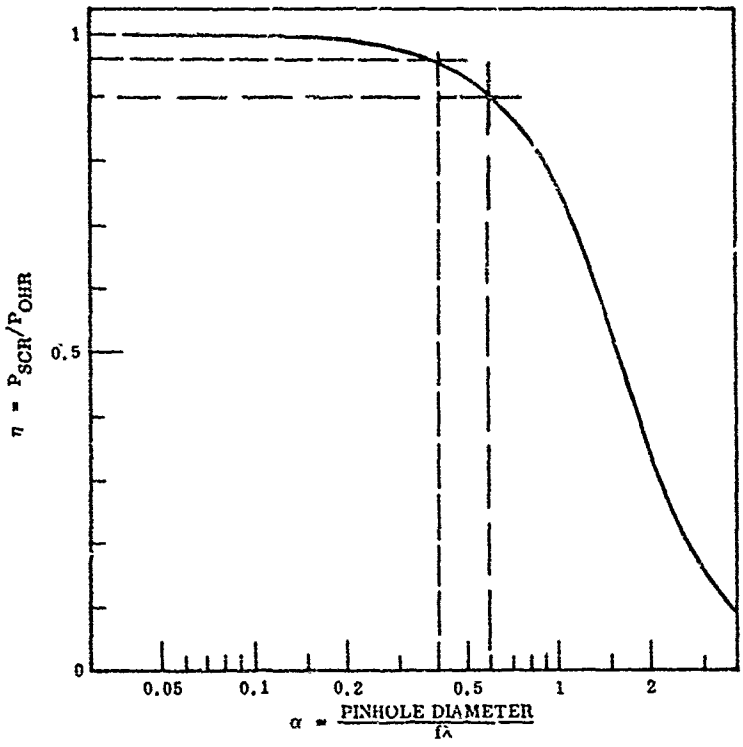


Figure 2 Error Due to Finite Pinhole Aperture Size in a Photon-Counting Receiver

3. EXPERIMENT CONCEPT

a. Brief Description of Experiment

An experimental arrangement that incorporates all of the features needed for a rigorous test of optical antenna gain reciprocity is shown schematically in Figure 3. Two sets of telescope optics are used to project laser beams toward each other via a path-folding mirror. A portion of the energy received by each set of optics is directed, as shown, into a photodetector by means of a beamsplitter. In each transmitter/receiver unit, a pinhole aperture is located at the focal plane of the received beam. In Figure 3, the telescopes at each end of the link, and their respective receiving pinholes, are shown as having identical configurations, but there is no requirement for such symmetry.[2]

[2]In designing and carrying out the experiment, certain variations from the configuration shown were found necessary or desirable. However, as these changes did not involve any fundamental changes in the experiment concept, discussion of these variations will be included in the description of the experimental system actually used. (See Section 4.)

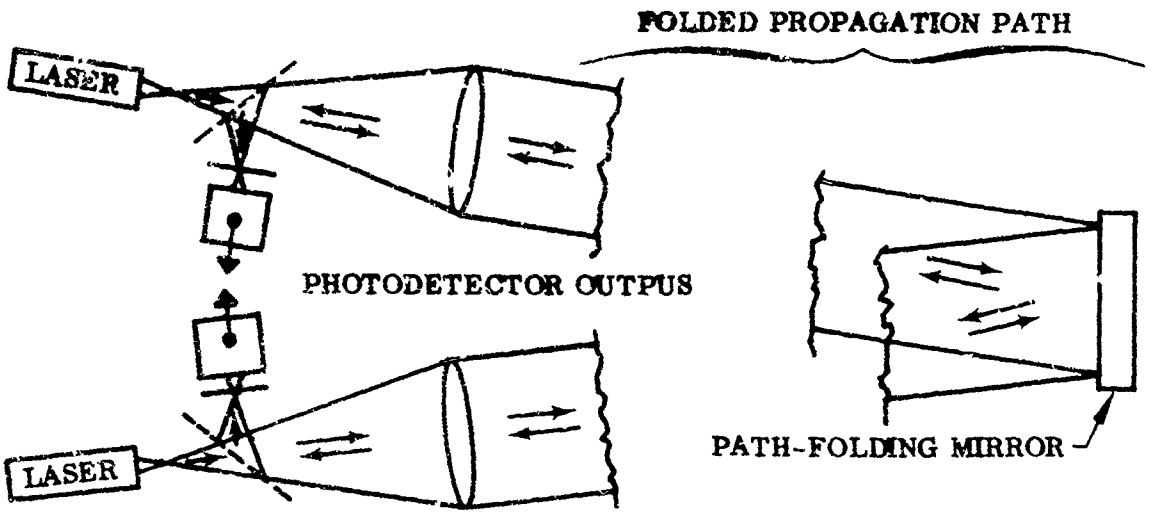


Figure 3 Optical Schematic Showing Essential Feature of Experimental Arrangement for Testing Optical Antenna Gain Reciprocity

According to reciprocity theory, any perturbation of the optical path will cause the two photodetector output signals to fluctuate identically. In order to measure the degree of identity, these signals will be fed to a signal analyzer that will calculate their correlation coefficient. Ideally, the value of this quantity would be unity, and any departure (below unity) would indicate some degree of non-identity. In Section II, 3, b, the sense in which the correlation coefficient is a measure of signal identity is shown.

This experiment has two special requirements. The first of these is that the receiving pinhole and the transmitter beam focus be conjugate to one another (i.e., mirror images), with respect to the beamsplitter. (See Section II, 2, b.) This means that the optical path length from any arbitrary point in the primary aperture of the optics to the pinhole point, including refractive disturbances, is the same as the path length from the aperture point to a corresponding point in the transmitter focal plane. With the pinhole defining a receiver, and with the conjugate transmitter focal point defining a transmitter effective source location, the transmitter and receiver operate over the same propagation path forward of the lens aperture.

The second special requirement of the experiment is that the size of the optics and their arrangement be such that the effects of atmospheric turbulence on propagation will make the signal fluctuate significantly. In particular, the design must permit the detected signal strength to be affected by wavefront distortion at the lens aperture (e.g., wavefront tilt) even if the disturbance is not great enough to cause variation of the total radiation falling on the lens. This sensitivity to wave-front distortion is obtained by using a large-enough primary aperture, and by using photodetector pinholes small enough to satisfy the criterion, previously stated in Section II, 2, b, that assures applicability of reciprocity to the case of a photon-counting receiver.

b. Statistical Quantities to be Measured

In this section, the sense in which the correlation coefficient of two random signals is a measure of their similarity, or alternatively, the degree to which they differ will be shown. Further, the relationship of the correlation coefficient of the two signals to their correlation function as computed by the signal analyzer will be indicated, followed by a brief discussion of the other statistical quantities that must be measured in order to define the strength of signal fading.

(1) Cross-Correlation Coefficient. It will be convenient to represent the two random signals in the following form:

$$A(t) = \overline{A} + a(t)$$
$$B(t) = \overline{B} + b(t)$$

where $\overline{A}$ and $a(t)$ are, respectively, the d-c and a-c components of signal $A(t)$, and $\overline{B}$ and $B(t)$ are similar components for $B(t)$. The instantaneous difference between the two signals, denoted by $\delta(t)$, is

$$\delta(t) = A(t) - B(t) = (\overline{A} - \overline{B}) - [a(t) - b(t)] \qquad (2)$$

Because $A(t)$ and $B(t)$ are random variables and not necessarily identical to one another, $\delta(t)$ is, in general, a nonzero random variable.

In the experiment, the relative amplitudes of the two signals are adjusted (by adjustment of the optical attenuator of one of the transmitters) so that the two signals have the same mean level. Under this condition, the term, $(\overline{A} - \overline{B})$ vanishes in the expression for $\delta(t)$, Eq. (2), and the instantaneous signal difference becomes

$$\delta(t) = a(t) - b(t) \qquad (3)$$

As a statistical measure of the signal difference, the time average of the quantity $\delta^2(t)$ is next calculated – working with the square of $\delta(t)$ because the simple average would vanish since, by definition, both $a(t)$ and $b(t)$ are pure a-c quantities – squaring Eq. (3) then gives

$$\delta^2(t) = a^2(t) + b^2(t) - 2\,a(t)\,b(t). \qquad (4)$$

Denoting time averages by an overbar gives

$$\overline{\delta^2(t)} = \overline{a^2(t)} + \overline{b^2(t)} - 2\,\overline{a(t)\,b(t)} \qquad (5)$$

This equation states that the average power of the difference variable $\delta(t)$ is equal to the sum of the a-c powers of the two input signals reduced by twice the average of the product of the two signals. In statistics, the average of a product of two random

variables a (t) and b (t) is termed cross correlation. Therefore, an equivalent statement in statistical terms is that the variance of the difference is equal to the sum of the variances of the given or "input" variables reduced by twice their cross correlation.

It has already been postulated that the two input variables have been adjusted so that their d-c or mean values are equal. The assumption is now made that, under this condition, they will also have the same a-c power or variance.[3] Under this assumption, Eq. (5) can be rewritten in the form:

$$\overline{\delta^2(t)} = 2\left[\sigma^2 - \overline{a(t)\,b(t)}\right] \tag{6}$$

Dividing both sides by σ^2 gives

$$\frac{\overline{\delta^2(t)}}{\sigma^2} = 2\left[1 - \frac{\overline{a(t)\,b(t)}}{\sigma^2}\right] \tag{7}$$

The left-hand quantity is the normalized difference variance. It is the difference variance that would be measured if the input variance were adjusted to a value of unity. The quantity $\overline{a(t)\,b(t)}/\sigma^2$ on the right-hand side is the normalized cross-correlation coefficient and will be designated by ρ. Using this notation, Eq. (6) can be rewritten as

$$\frac{\overline{\delta^2(t)}}{\sigma^2} = 2(1 - \rho) \tag{8}$$

It is obvious that as $\rho \to 1.0$, $\delta^2(t) \to 0$; that is, a correlation coefficient close to unity implies a small (mean square) value of the difference signal and, therefore, near identity of the two input signals.

Further interpretation of ρ as a measure of signal difference can be obtained by solving Eq. (8) for ρ and squaring. This gives

$$(\rho)^2 = 1 - \frac{\overline{\delta^2(t)}}{\sigma^2} + \frac{1}{4}\left(\frac{\overline{\delta^2(t)}}{\sigma^2}\right)^2$$

Attention is now restricted to the case of high correlation; i.e., $\rho \simeq 1$. As just indicated, under this condition $\delta^2(t)/\sigma^2 << 1$. Therefore, the third term on the right is much smaller than the second and can be neglected. Solving the resulting expression for $\delta^2(t)/\sigma^2$ gives the approximate result

$$\frac{\overline{\delta^2(t)}}{\sigma^2} \simeq 1 - \rho^2 \tag{9}$$

[3] At first thought, it may appear that this assumption prejudices the results of this development by artificially imposing a degree of equality of the signals. In actuality, this is not the case since the assumption does not preclude the possibility that the signals can fluctuate relative to one another by arbitrarily large amounts. It requires only that the squared values of these two sets of fluctuations have the same long-term average value.

That is, for high correlation values, the normalized difference power is just the difference between unity and the square of the correlation coefficient. It is the latter quantity, rather than the unsquared correlation coefficient, that actually is calculated and displayed by the signal analyzer. However, the true correlation coefficient is given wherever values are quoted in the text or listed in summary tables, since this is the more generally accepted statistical measure of signal identity.

(2) Normalized Cross-Correlation Function. The cross-correlation function of two random variables, $a(t)$ and $b(t)$, is an extension of the concept of cross-correlation coefficient in that a time-shift parameter τ is now involved. Instead of calculating the time average of the product $a(t) \cdot b(t)$, as in the previous section, the average of the product with one of the signals shifted by an amount τ is calculated. This average (ideally) is then calculated for all values of τ, negative as well as positive. In general, a different cross-correlation value is obtained for each value of the time shift τ; that is, the cross correlation is now a function of τ. This shift-and-average process is represented by $\overline{a(t)\, b(t-\tau)}$, where $b(t-\tau)$ represents the b signal after it has been delayed in time by τ sec (e.g., by passing it through a delay line of "length" τ). When this product average is suitably normalized, it is denoted by $\rho(\tau)$.

For the purposes of this analysis, it is advantageous to use a slightly different approach to normalization than that used in the previous discussion, namely, one that yields unity correlation when the two signals are identical except for a possible difference in amplitude scale for the two. (This change is made because, experimentally, it is difficult to assure equality of mean values of two randomly, fluctuating signals.) The definition of normalized cross-correlation function adopted is

$$\rho(\tau) = \frac{\overline{a(t)\, b(t-\tau)}}{\left[\sigma_a^2 \quad \sigma_b^2\right]^{1/2}} \tag{10}$$

where σ_a^2 and σ_b^2 are, respectively, the variances of the a- and b- signals. With $\tau = 0$, this expression reduces to the correlation coefficient discussed in the previous section, except for the change in normalization. It agrees exactly if the two signals become identical, even as to amplitude scale.

In actuality, the signal analyzer does not calculate the correlation function by directly averaging the product of the two signals in the way suggested by Eq. (10). Instead, use is made of the fact proved in statistical signal theory that the cross-correlation function of two signals and the cross-power spectrum of the two signals are Fourier transforms of one another (Reference 3). The cross power spectrum of two signals $a(t)$ and $b(t)$ is denoted by $G_{ab}(\omega)$ and is defined by the relation

$$G_{ab}(\omega) = G_a(\omega)\, G_b^*(\omega) \tag{11}$$

where $G_a(\omega)$ and $G_b(\omega)$ are the ordinary Fourier transforms (complex spectra) of $a(t)$ and $b(t)$, and the asterisk denotes complex conjugation.

The signal analyzer first calculates $G_a(\omega)$ and $G_b(\omega)$ by means of the Fast Fourier Transform (FFT) algorithm. (See Reference 4.) Next the cross power spectrum $G_a(\omega)$ $G_b^*(\omega)$ is calculated. Because the input signals A (t) and B (t) each contain a random component (in addition to their d-c components), the Fourier spectra, $G_a(\omega)$, and $G_b(\omega)$, and the cross power spectrum, $G_a(\omega)$ $G_b^*(\omega)$, are also random in nature. These spectra, as computed from any one short sequence of input data points, therefore will not be representative of the cross power spectrum. Further, a cross-correlation function obtained by transforming the cross spectrum also would not be representative. To overcome this difficulty, a sequence of data blocks is processed, and the resulting cross power spectra are averaged. The inverse FFT operation is then performed, and the resulting cross-correlation function is normalized in accordance with Eq. (10) to obtain the required normalized cross-correlation function.

At first thought, it may appear as a somewhat roundabout procedure to calculate the cross-power spectrum as an intermediate step in obtaining the cross-correlation function when the latter could be calculated directly from the signal data. Actually, however, the two-step process is much faster because of the speed advantage of the FFT algorithm and because the latter is applied as many times as there are data blocks to be averaged (typically 25 in the present experiments) while the inverse transformation is applied only once at the end of the averaging process.

(3) Signal Variance. Analogous to the cross-correlation of two signals, the autocorrelation function of a signal a (t) is defined as the time product average, $\overline{a(t)\, a(t-\tau)}$; it is denoted by $\mu_a(\tau)$. This function (of τ) is the Fourier inverse transform of the power spectrum of signal A (t), and similarly for signal B (t). The autocorrelation functions, $\mu_a(t) = \overline{a(t)\, a(t-\tau)}$, $\mu_b(\tau) = \overline{b(t)\, b(t-\tau)}$, can be calculated by a process similar to that used to calculate the cross-correlation function. However, the process actually used differs in that the self power spectra of the A and B signals, $G_a(\omega) \times G_a^*(\omega)$ and $G_b(\omega)\, G_b^*(\omega)$, respectively, are calculated for each data block and averaged. These average spectra are then inversely transformed to obtain the averaged autocorrelation functions of the A and B signals. It is known from statistical theory (Reference 3) that for a signal with zero mean, the value of the autocorrelation function for $\tau = 0$ is precisely the variance of the random variable; that is

$$\sigma_a^2 = \mu_a(0) \tag{12}$$

and

$$\sigma_a^2 = \mu_b(0) \tag{13}$$

Thus, the variance of the A and B signals is obtained by first obtaining their autocorrelation functions. The values of these functions at zero time shift ($\tau = 0$) are then the values of variances required in Eq. (10) to obtain the normalized covariance.

(4) Signal Mean Value. The mean value of input signal A (or B) is represented in its Fourier spectrum by the zero-frequency term. As with the power spectra, this term fluctuates randomly from one data block to the next (but is always of the same polarity); so again, averaging is used to obtain an estimate of the true mean. This is the quantity called $\bar{A}$ (or $\bar{B}$) as discussed in Section II, 2, b, (1).

In the preceding sections, it has been tacitly assumed, in describing the methods used to evaluate normalized cross-correlation and variance, that the d-c component of the signal was already removed from the signal and that the a-c component was available for processing. Actually the d-c component must be suppressed intentionally, and it can now be seen how this is done. It has already been noted that the d-c component of either signal is represented by the zero-frequency term of its complex Fourier spectrum $G_a(\omega)$. All that is required, therefore, is to set the value of this term equal to zero in the analyzer before the cross- or self-power spectra are calculated. It is this d-c suppressed spectrum that has been denoted previously by $G_a(\omega)$ or $G_b(\omega)$. The d-c suppression is accomplished by clearing the appropriate element in the analyzer memory. However, the zero-frequency term is not discarded; it is accumulated in another memory location for averaging as required in order to determine the signal d-c value.

(5) Strength of Signal Fading. A suitable measure of strength of signal fading is the ratio of signal-intensity variance to mean intensity squared, denoted here by γ_A (or γ_B). Since the photodetector output signal is proportional to instantaneous signal intensity, an equivalent measure of fading strength is

$$\gamma_A = \frac{\alpha_a^2}{(\bar{A})^2} \tag{14}$$

$$\gamma_B = \frac{\alpha_b^2}{(\bar{B})^2} \tag{15}$$

If the intensity I (or signal current) has a log-normal distribution, as is frequently the case (i.e., the "log amplitude" defined by $\ell = \log_e I^{0.5}$ has a normal probability density), it can be shown that the log-normal variance C_ℓ, the variance of ℓ, is related to γ by the equation

$$C_\ell = \frac{1}{4}\left[\exp(\gamma) - 1\right] \tag{16}$$

For $\gamma << 1$, this can be simplified to

$$C_\ell \simeq \frac{\gamma}{4}. \tag{17}$$

In the present experiment, the probability distribution of signal strength fluctuations is not measured. Therefore, it cannot be asserted that the signal has log-normal statistics and, consequently, the calculation of C_ℓ by use of Eq. (15) cannot be rigorously justified. Instead, this equation is used to calculate an effective value of C_ℓ and it is asserted only that this is the value that would be measured if the signal had log-normal statistics and an intensity variance equal to the value actually measured.

4. EXPERIMENTAL EQUIPMENT AND ALIGNMENT METHODS

a. Overall System Description

Figure 4 is a general view of the measurement system. The two specially constructed transmitter/receiver units are shown at right and left sides of the photograph with the associated signal-conditioning electronics units. The signal analyzer, located in the rack at center rear, is a Hewlett-Packard Model 5452A Digital Fourier Analyzer. Output data from the analyzer are displayed on the oscilloscope unit in the rack and can be printed out by the teletype unit. The oscilloscope unit to the left of the rack, and the meter unit above it, are used for equipment alignment and for signal monitoring.

The arrangement of the optics of the two transmitter/receiver units used in the experiment is shown schematically in Figure 5, and the equipment itself is illustrated in Fig- Figure 6. Starting with the laser at the right, the numbers 1 through 10 indicate the transmitting sequence. The focusing lens is positioned so that the focal point of the laser beam is at the plane of the pinhole aperture, and the two are moved together to place the beam focus in the focal plane of the primary mirror so that the output beam is collimated. Figures 5 and 6 are similarly oriented so that the components shown in Figure 6 can be easily identified.

Under the condition of adjustment just described, an incoming collimated (plane-wave) beam is brought to a focus by the primary mirror and then recollimated by the focusing lens. Approximately one-half of the received signal power is reflected by the transmit/receive beamsplitter (4) into the receiver optics chain. This reflected energy, after being deflected by a folding mirror (11), passes through a beam magnifier (12) and a focusing lens (13). Finally, a portion is reflected into the photodetector by a second beamsplitter (Figure 5). The remaining portion of the received beam passes through the beamsplitter and falls on the ground glass viewing screen in the camera. The receiver focusing lens is mounted in the forward end of the focusing bellows (Figure 6) and is positioned to bring a collimated beam to focus at the photodetector. Immediately in front of the photodetector is a pinhole aperture (250 μm diam.) which serves as the field-defining aperture of the receiver. As discussed more fully in Section II, 4, e, this pinhole is equivalent to a pinhole at the prime focus that is smaller than the photodetector pinhole by the magnification factor of the receiving optics. The magnification ratios used in the measurements ranged from 12× to 100×. Correspondingly, the receiving pinhole size as referred to the prime focus ranged from 21 to 2.5 μm.

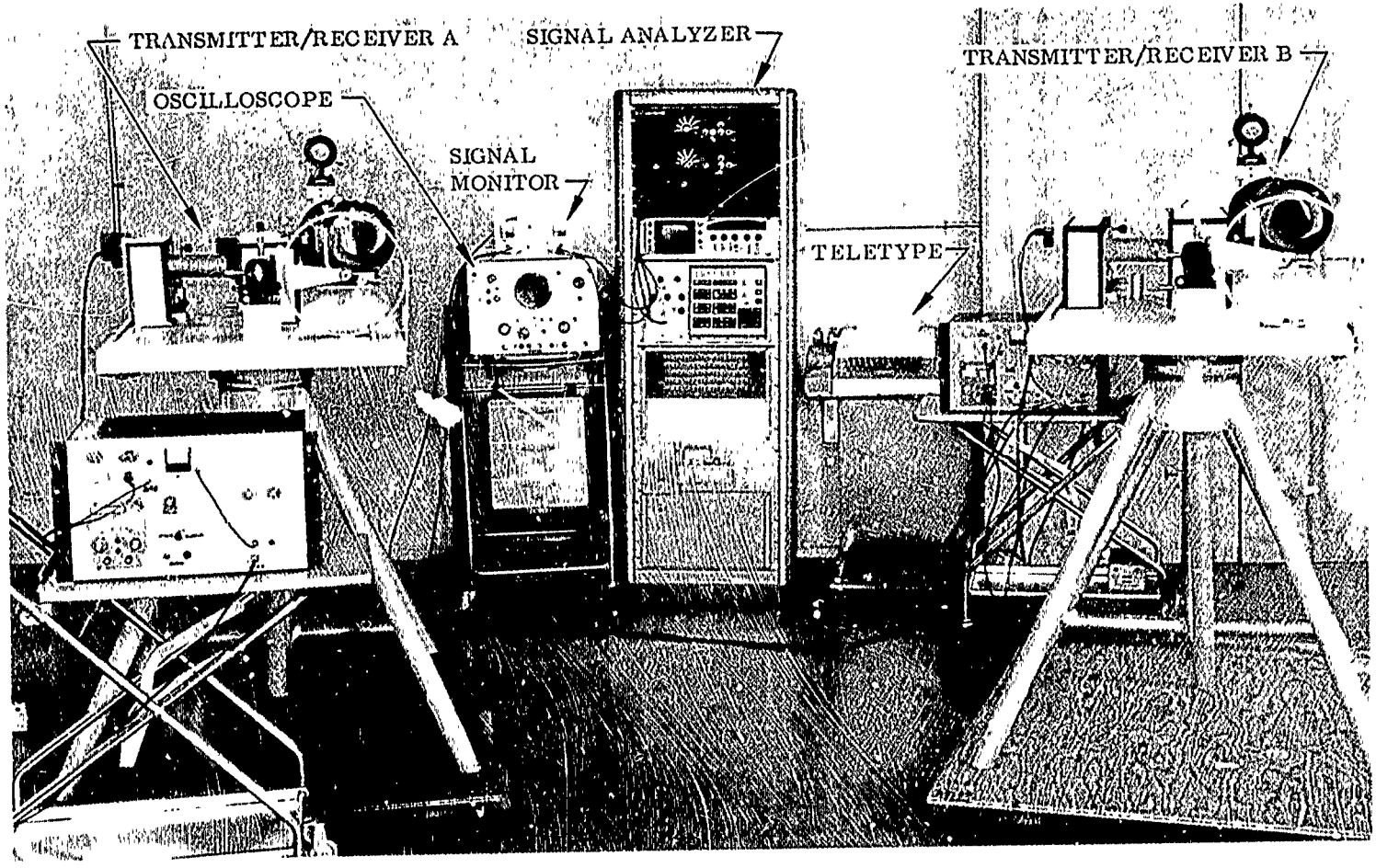


Figure 4 Experimental System – General View

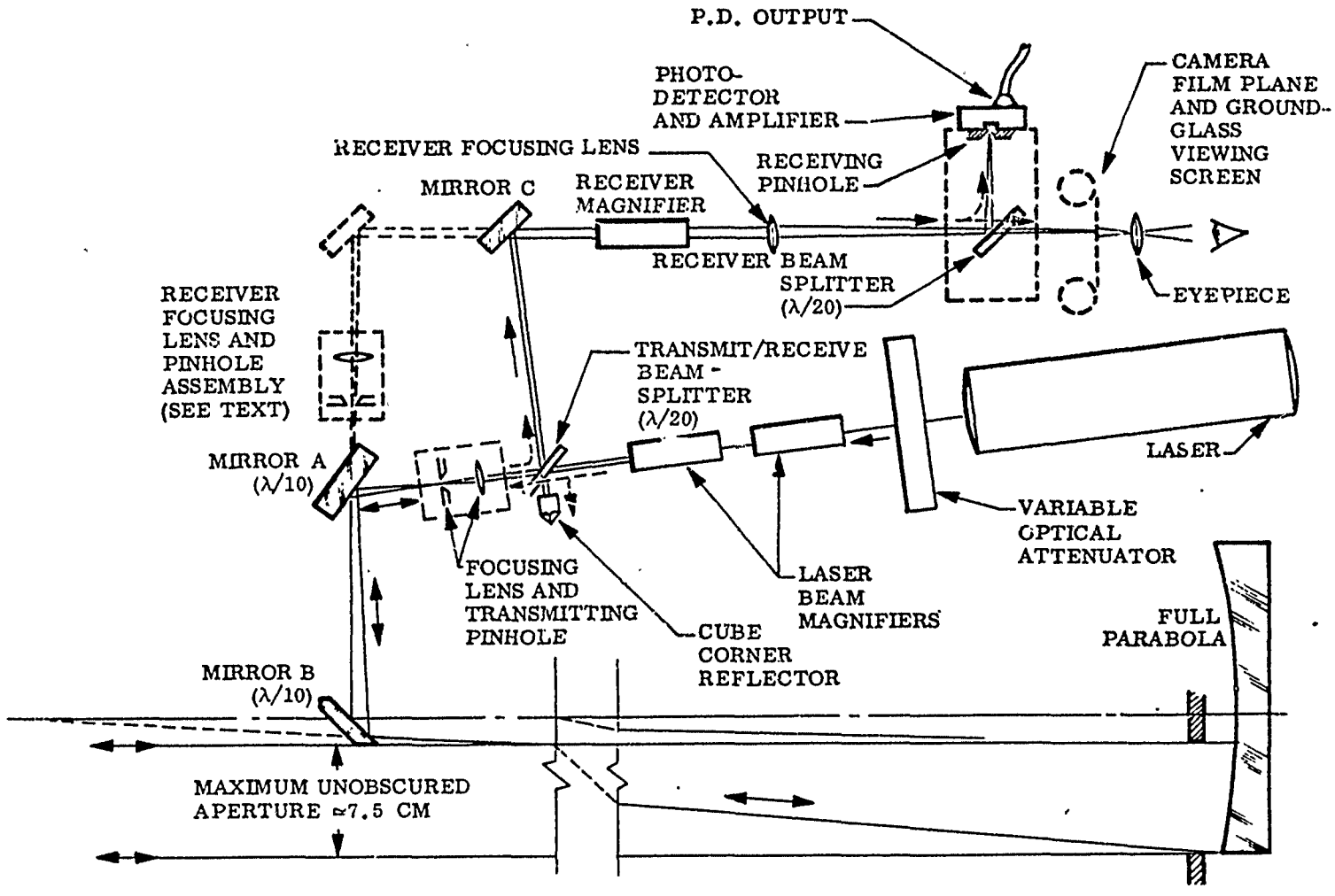


Figure 5 Arrangement of Optics

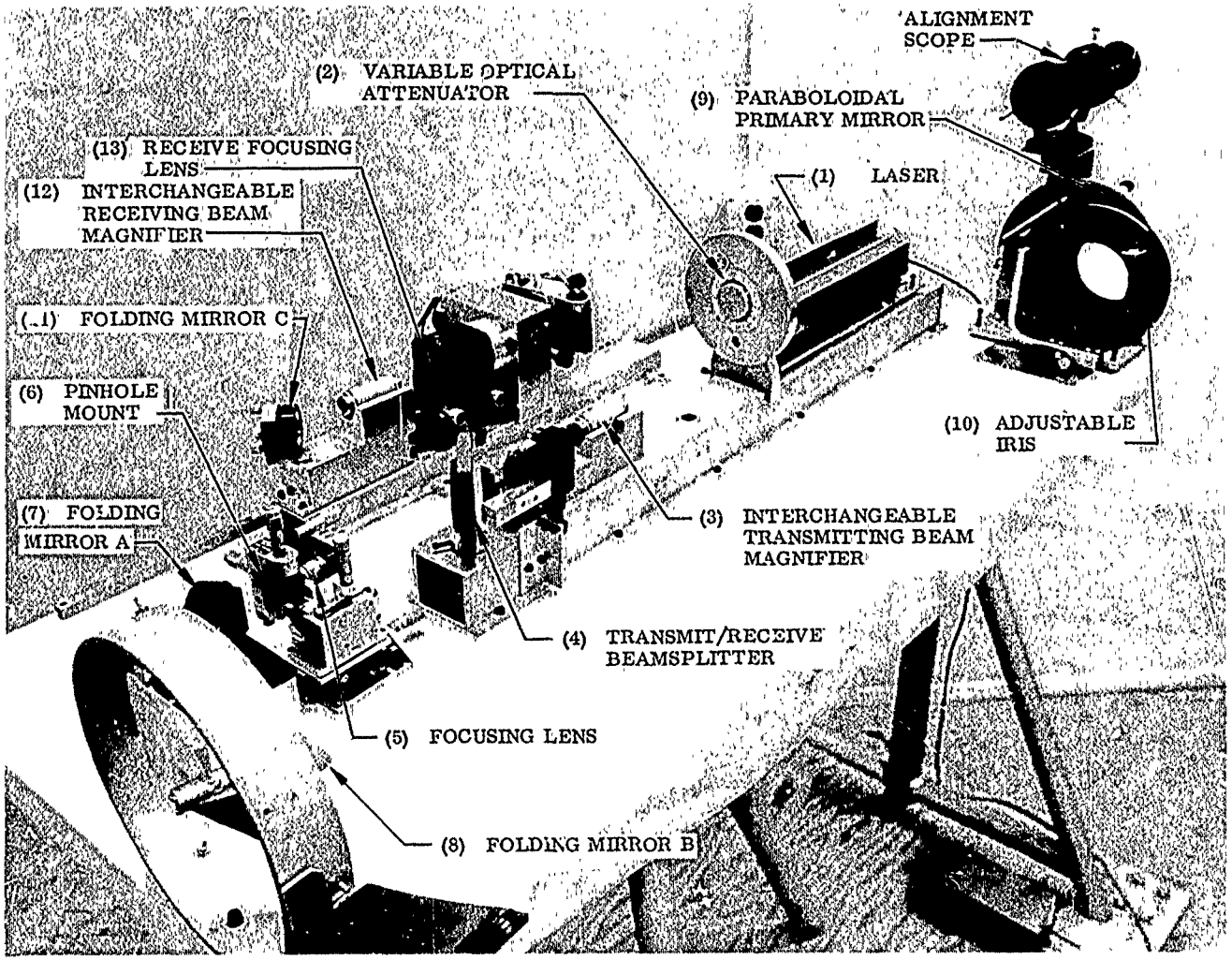


Figure 6 Transmitter/Receiver Unit – Overall View

The cube-corner reflector shown above the transmit/receive beamsplitter, (Figure 5) although not included initially in the experiment concept, proved to be of major importance in simplifying internal alignment of the optical units. This use of the corner reflector was made possible by a change of the beamsplitter arrangement from that originally planned. (The latter is indicated by the dotted lines at the upper left of Figure 5. The reasons for this change are discussed later in this section.) The function of the corner reflector is to return directly back on itself the portion of the transmitted beam that is split off by the beamsplitter. A part of this retroreflected beam passes through the beamsplitter and into the receiving optics, and is focused by the latter at the photodetector pinhole plane and at the ground-glass viewing screen. If the corner reflector is an exact cube corner, then the retroreflected beam will be collimated, just as the laser beam, more important, its direction will be exactly the same as that of a received beam that is antiparallel to the transmitted beam.

The corner-reflector beam therefore, can be used to align the receiving optics so that the focal spot of such a received beam will be centered on the photodetector pinhole. This alignment is accomplished by adjusting the orientation of the transmit/receiver beamsplitter, the receiver folding mirror, and the beamsplitter associated with the camera and photodetector, so as to maximize photodetector output signal. After this alignment is completed, the corner reflector beam is blocked to prevent interference with the received signal. The adjustment procedure is detailed further in Section II, 4, e.

b. Optics Configuration

(1) Reflective Vs. Refractive Optics. The choice between reflective and refractive primary optics is largely dictated by the requirement that the same element be simultaneously usable for transmission and reception. This requires, in turn, that backscatter or reflection of the transmitted beam be kept small enough to avoid interference with the received beam. To satisfy this requirement, it was decided early in the program that a minimum condition for the primary optics was that there should be no optical elements in the region common to the transmitted-and-received beams with surfaces that were normal to any incident ray of the laser beam. This requirement dictated off-axis operation of optics, but still left open the choice between reflective and refractive optics, provided the latter were properly designed. For example, multi-element lenses could not have any internal surfaces that would be normal to a ray of the laser illumination.

An additional factor was cost, especially since off-axis operation, if standard circular optics were used, would require the overall diameter to be somewhat in excess of twice the diameter of the largest aperture desired. As a maximum aperture diameter of 10 cm was desired, the overall diameter could not be less than about 10 in. and preferably would be nearer 16 in. On the basis of available catalog information on standard astronomical quality lenses and paraboloidal mirrors, it was decided that reflective optics would be the most economical choice. This choice was reinforced when it was learned that ITT/Gilfillan Corp., who were participating on another portion of this contract, could make available on loan two 8-in.-diam. paraboloids for use until the desired mirrors could be procured. Because of late delivery of the special off-axis mirrors ordered for this experiment, however, the 8-in. mirrors were used throughout the experiment. Therefore, some aperture blockage occurred for beam diameters larger than approximately 5 cm, although usable beams as large as 10 cm could be obtained.

(2) Beamsplitter Arrangement. Initially, it was planned that the transmit/receive beamsplitter would be at the position occupied by mirror A, in Figure 5, and that a separate focusing lens and associated receiving pinhole would be used, as shown by the dotted lines at the upper-left portion of Figure 5. This arrangement had the advantage that there would not be a lens element common to the transmitting and receiving paths that could reflect laser energy back into the receiver. However, because the beamsplitter would then be at a position where the received beam would be converging, aberration would occur if a beamsplitter of appreciable thickness were used. For example, a standard beamsplitter substrate of 8-mm thickness would produce astigmatism which, expressed in terms of spread in axial focus position, exceeds, by a factor of 32, the limit set by the Rayleigh criterion of $\lambda/4$ phase error over the beam cross section. (See Reference 5.)

To avoid astigmatism and other forms of aberration of possible importance, such as coma and spherical aberration, it was decided initially to use a pellicle beamsplitter. This type consists of an extremely thin plastic membrane stretched over a supporting ring and coated with dielectric or metallic films to obtain the desired reflectance. Pellicle beamsplitters were procured and tested but were found to be unsatisfactory for two reasons. First, the specified (and required) flatness was not achieved; second, the reflectance of the multilayer coating used was excessively sensitive to incidence angle of the laser beam, and varied significantly over the diverging cone of the primary mirror illumination. Further discussions with pellicle suppliers gave little assurance that a satisfactory component could be produced.

Because of the serious deficiencies of the pellicle beamsplitter, two alternate arrangements were considered. First, a considerable effort was made to find ways of compensating for the abovementioned aberrations that would be caused by an optical substrate or plate if either was used as a base for a beamsplitter film. Second, the arrangement diagrammed in Figure 5 was tried experimentally, even though it involved use of a lens in the region common to the transmitting and receiving beams.

It was determined that workable solutions were possible with either approach. The first involved inserting an antireflection-coated compensator plate in the receiving leg and orienting it to produce an astigmatism that would cancel the astigmatism caused by the beamsplitter. This left a residual coma distortion that was observable at the largest aperture but probably tolerable. With the second approach, it was found that laser-beam reflection from the lens back into the receiver could be reduced to an acceptably low level by offsetting the lens laterally to avoid normal incidence. Moreover, this offset could be used to produce the beam deflection needed for off-axis illumination of the primary mirror. The latter approach was adopted because it allowed the beamsplitter to be placed in the collimated beam region. This arrangement permitted, in turn, the addition of the cube-corner reflector as an aid to initial internal alignment of the receiving and transmitting optics, as already discussed.

(3) Transmitter Beam Size Adjustment Method. The overall diameter of the transmitting beam is determined by the setting of the adjustable iris immediately in front of the primary mirror. (See Figures 5 and 6.) However, the uniformity of the beam across this aperture is determined by the nominal divergence angle of the expanding gaussian beam

produced by the focusing lens and the preceding laser beam magnifier, both acting on the laser beam. (Placement of a pinhole at the focal plane of the focusing lens would further modify the divergence angle. In this experiment, however, (as previously noted) a transmitting pinhole was not needed, and the receiving pinhole was located at the photodetector.)

In order that the beam intensity distribution would stay essentially constant as the beam diameter changed, it was thought advisable to maintain the intensity nearly constant over the aperture (rather, for example, than attempting to maintain a constant percentage of truncation of the Gaussian laser beam) even though a considerable fraction of the available laser power would have to be wasted. As a compromise between uniformity and utilization of available power, it was decided that a power variation up to 1 dB could be tolerated. Focal lengths of focusing objectives that met this requirement were then determined experimentally. It was found convenient to use a 1.5× laser beam magnifier. With that choice, the focusing objective lenses used for the various primary aperture diameters are shown in Table 1 as follows:

Table 1. Focusing Objective Lenses Used for Various Primary Aperture Diameters

Aperture Diameter (cm)	Focusing (Objective) Lens	
	Focal Length (mm)	Rated Magnification
1.25	46.0	4×
2.50	18.6	10×
5.0	18.6	10×
7.5	9.3	20×

As the focusing lenses actually are microscope objectives and are specified in terms of their magnifying power, the latter value is given in each case. These values are of importance in the discussion under II, 4, b, (4).

(4) Receiver Magnification Choice. The basic requirement of the receiving optics is that the focal spot formed at the prime focus of the primary mirror be relayed to the photodetector pinhole plane with sufficient magnification so that the diameter of the focal spot exceeds the pinhole diameter by a ratio of approximately 2.5 to 1. (This is the ratio of sizes needed to satisfy the condition $\alpha \leq 0.4$, relating to equivalence of photon-counting and heterodyne receivers, as developed in Section II, 2, b.). As an example, consider the case of a 5-cm primary aperture for which the diffraction-limited focal-spot diameter at the prime focus of a 60-in. focal length primary mirror is

$$d_p \simeq \frac{F}{D}\lambda = \frac{60 \times 2.54}{(5\ \text{cm})}\ (0.6328\ \mu\text{m}) \simeq 20\ \mu\text{m}$$

Letting d_d be the photodetector pinhole diameter, it is then required that the receiver magnification factor M_R be such that

$$d_d \leq \alpha M_R \, d_p \tag{18}$$

or, solving for M_R, requires

$$M_R \geq \frac{1}{\alpha} \cdot \frac{d_d}{d_p} \tag{19}$$

As the pinhole diameter is 10 mils ($\simeq$250 μm), Eq. (12) requires that $M_R \geq 33$ be chosen. The total receiver magnification is the product of the focusing objective power and the power of the interchangeable beam magnifier. The objective power has already been determined by transmitter considerations to be 10 for a 5-cm aperture (from Table 1), and the receiver magnifier power therefore must be ≥ 3.3. As the nearest available magnifier power is 3× this value is chosen and the possibility of a slight penalty in accuracy is accepted. (Magnifiers of higher power were available, but their use excessively reduces the received signal power transmitted by the pinhole.)

When this calculation is repeated for the other beam diameters and their associated objective (focusing) lenses, as shown in Table 1, the 3× receiver magnifier is still the appropriate choice; that is, the receiver magnifier need not be changed when aperture diameter is changed, but only the focusing lens power (or focal length). This is a fortunate circumstance because it is then unnecessary to realign the receiver optics to the transmitter when changing beam diameter, as would be the case if it were necessary to change receiver magnifiers. This considerably simplifies the experimental procedure.

c. Signal Conditioning and Monitoring Electronics

(1) Signal Conditioning. The following kinds of signal conditioning are provided:

- Low-noise amplification
- Anti-aliasing filtering
- Signal differencing

Figure 7 represents these functions and shows that the first two are performed for each of the two signal channels, A and B, before the signals are fed to the Fourier Analyzer. Unless otherwise noted, the following discussion applies to each of these channels.

The signals originate in the photodetectors located behind the receiving pinholes (Figure 5) and are amplified first within the photodetector itself. The photodetector units (Texas Instruments, Type TLXL 79) consist of an avalanche photodiode packaged integrally with a special solid-state amplifier. The package has a rated frequency response of d-c to 50 MHz and has built-in temperature compensation. The photodiode sensitive area is a circle of approximately 30 mil (0.76 mm) diameter.

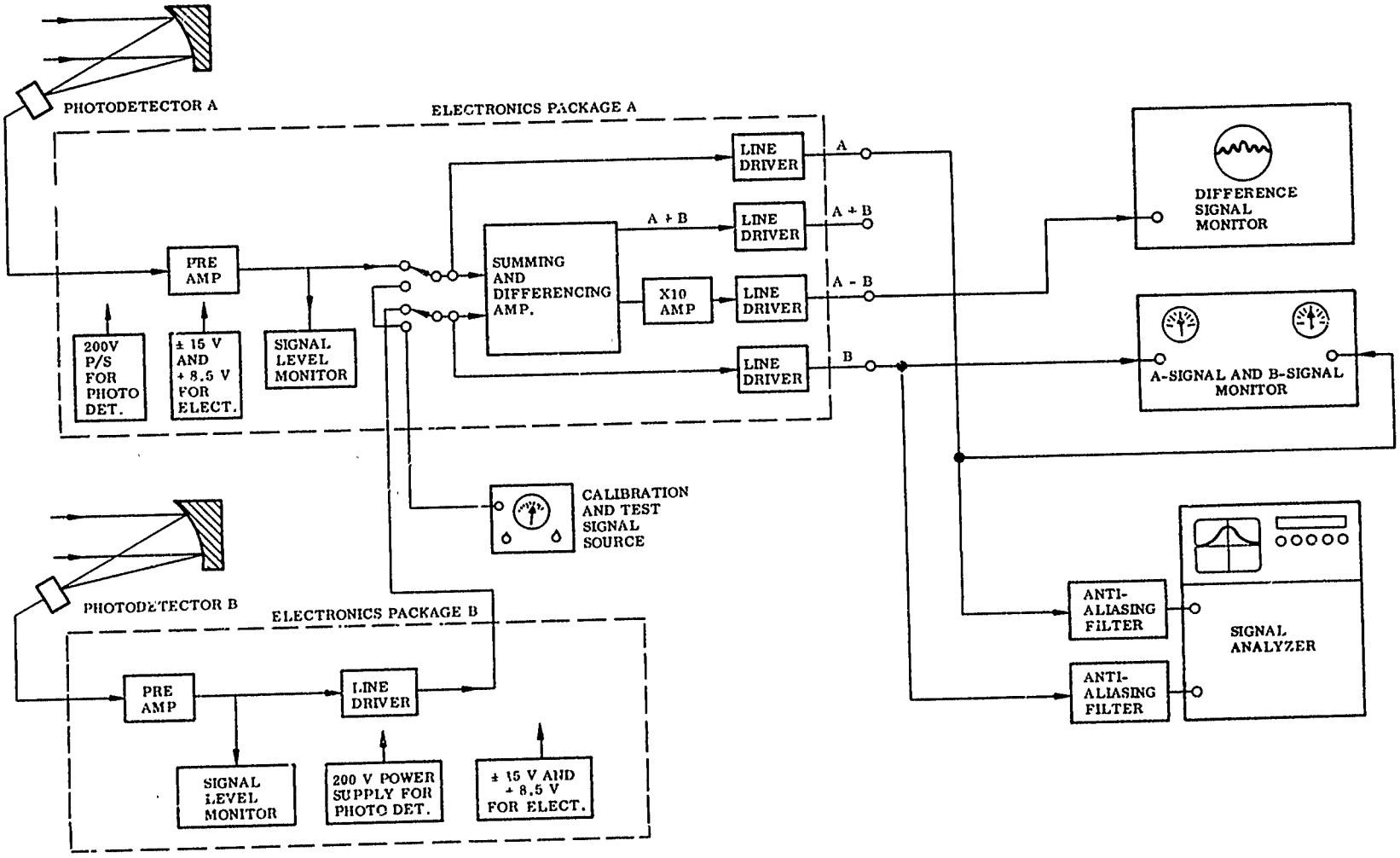


Figure 7 Signal-Conditioning Electronics and Signal Processing Systems – Functional Block Diagram

The amplified photocurrent is next fed to an integrated-circuit, low-noise preamplifier, shown at the left in Figure 7. This stage has a voltage gain of 10×. The signal then goes to a line driver with adjustable gain (3× max.) and also is fed to summing and differencing amplifiers. The output of the latter, after additional 30× amplification (including 3× amplification in the line driver) feeds the Difference Signal Monitor oscilloscope. (The role of the latter in the experiment procedure is described in Section II, 4, e following. The amplitude-versus-frequency characteristics of each signal-conditioning channel is flat from d-c to above 10 kHz.

Figure 8 shows the A-channel and B-channel electronics units. The summing and differencing amplifiers are contained in the A-channel unit, as are the four adjustable-gain line drivers. Separate adjustments for controlling photodetector gain are provided at the upper left of the panel on each unit as are the vernier adjustments to set "zero level", i.e., the d-c output with zero light input to the photodetector. The zero-center meters at the upper-middle position on the panels are used for zero setting and have a sensitivity (0.1 V full scale) compatible with the resolution of the 10-turn, level-setting helical potentiometers (lower middle). A toggle switch (below the meter) allows a 10× reduction in sensitivity so that the meters can be used to monitor high-level. The patch cord permits the meter to be connected to any of the output terminals of the unit.

Each of the line drivers is capable of a maximum output in excess of ±10 V (saturation occurs at ±15 V) but is normally operated in the ±1-V range. With zero light input to the photodetectors, extraneous signals at the A and B outputs consisted predominantly of a 120-Hz saw-tooth component (power supply ripple) of less than 3 mV peak-to-peak. With laser light into the photodetector of intensity sufficient to produce a 0.1 Vdc output, the ripple level remains unchanged; however, photocurrent noise is added in an amount not exceeding 0.5 mV rms in a 1-kHz band. When referenced to a 0.1 Vdc level, the power supply component thus is at least 10^3 to 1 (-30 dB) down in power, and the noise component is over 4×10^4 to 1 (-46 dB) down. As 0.1 Vdc is representative of the mean signal level used in most of the correlation measurements, it is seen that extraneous signal power is less than 0.1 percent of the d-c power of the laser signal.

(2) The A-Signal and B-Signal Monitor. This unit (mounted on top of oscilloscope in Figure 4) consists of two independent channels of unity-gain amplification followed by zero-center d-c meters. Within their response speed limitations, these meters indicate the instantaneous optical signal in their respective channels. The use of this monitor in the adjustment procedure is described in Section II, 4, e.

(3) Anti-Aliasing Filters. These filters are located in the upper portion of the signal analyzer rack. (See Figure 4.) Their function is to suppress noise and, if present, signal components at frequencies above the maximum frequency that is compatible with the sampling rate selected in the Fourier Analyzer. Switches on the panels allow selection of filter cutoff frequencies in the 10-Hz to 10-kHz range in a 1 to 3 to 10 sequence. For the 1-kHz setting used in most of the tests in this experiment series, the amplitude-versus-frequency response was as shown in Figure 9. The amplitude response is seen to start "rolling off" at about 500 Hz and is 6 dB (2 to 1) down at 1 kHz. Above 1 kHz, the response drops approximately 24 dB/octave for over two octaves. For other bandwidth settings, the response curve is similar, except that it is shifted to higher or lower frequencies by the multiples mentioned above.

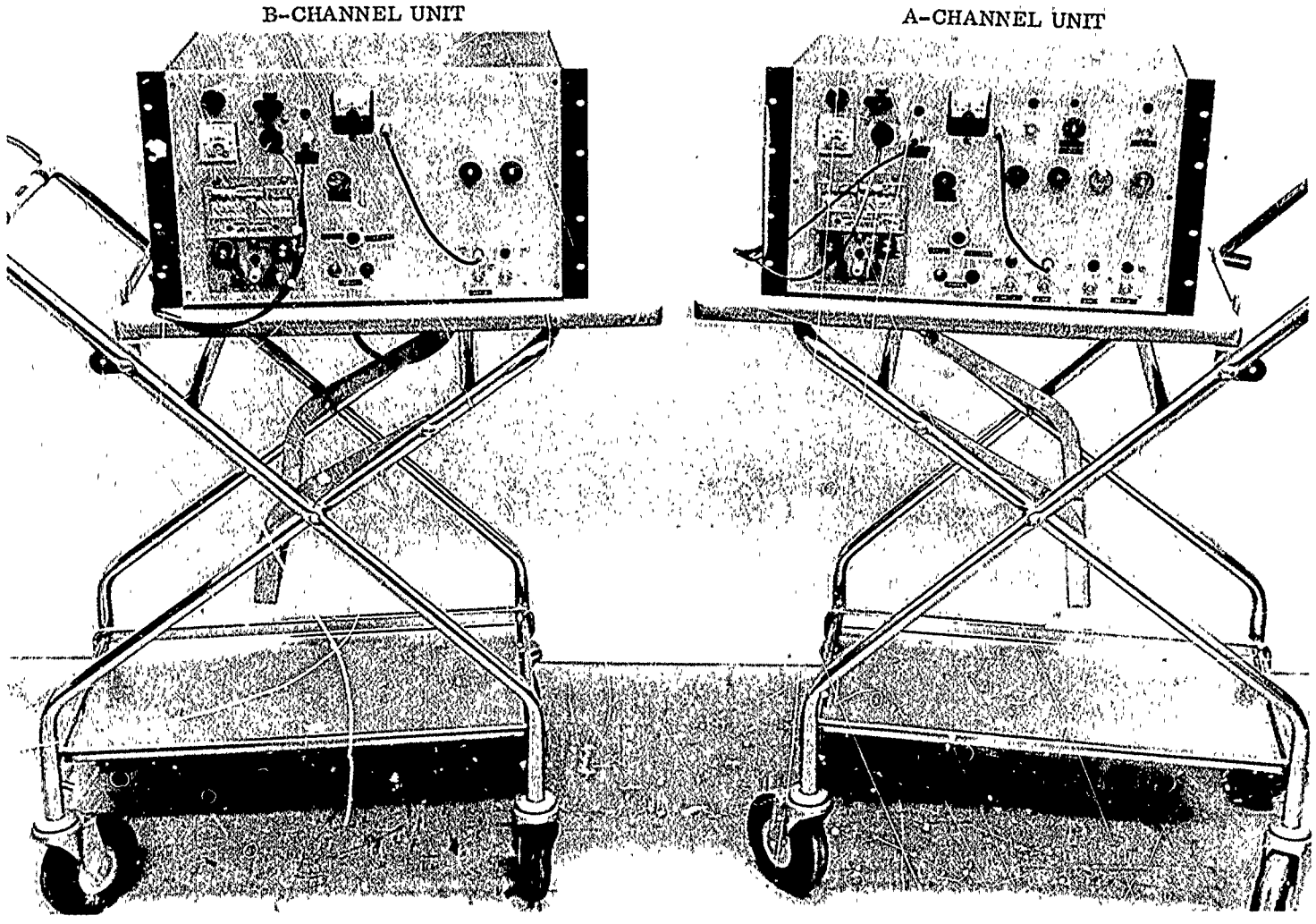


Figure 8 A-Channel and B-Channel Electronics Units

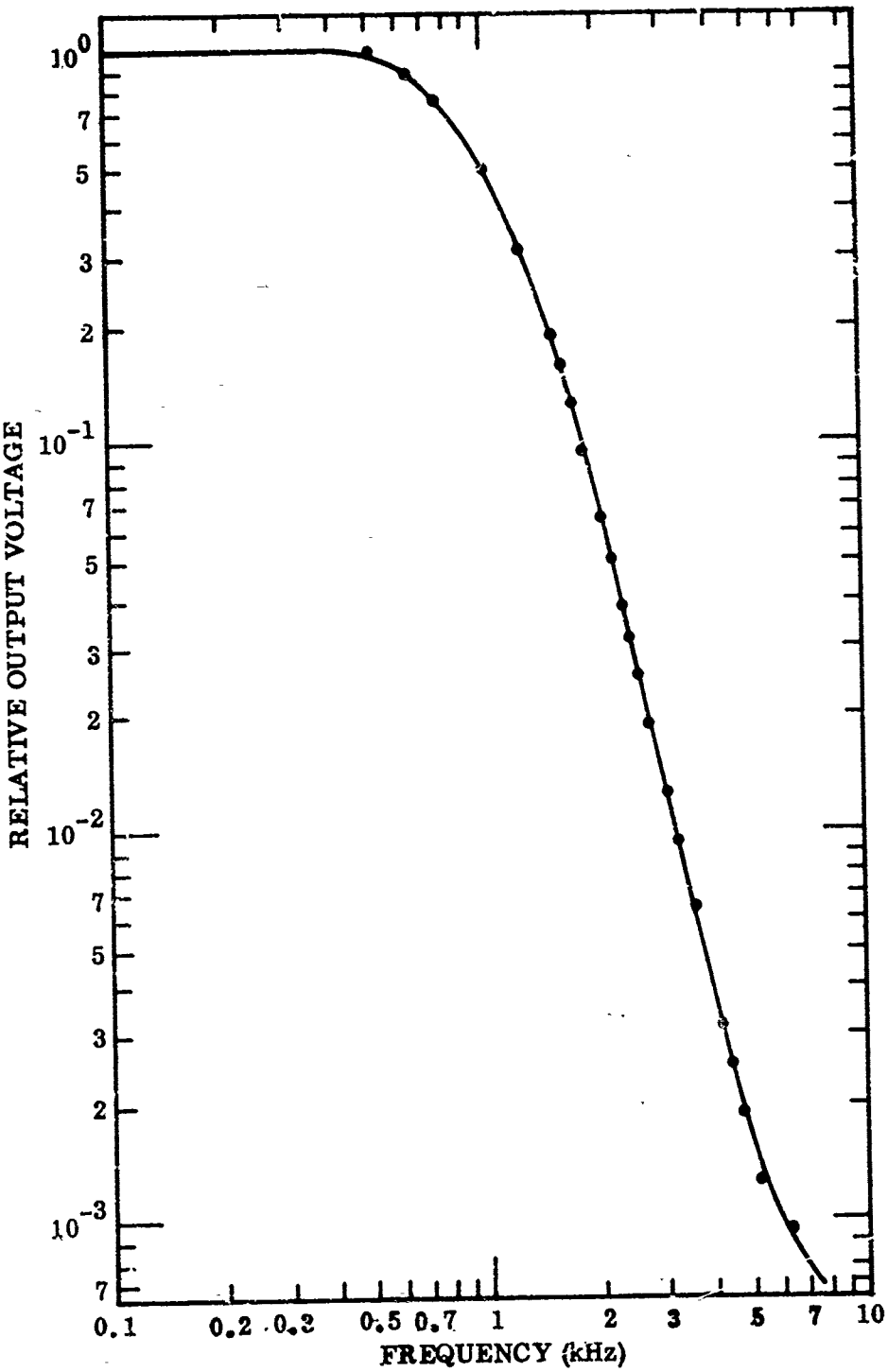


Figure 9 Frequency Response of Anti-Aliasing Filters at 1-kHz Bandwidth Setting

Ideally, the bandwidth of the anti-aliasing filter would be chosen so that its response would be nil at a frequency equal to one-half the Fourier Analyzer sampling frequency. However, it was not always possible to select such a setting without, at the same time, modifying the signal spectrum. In those cases, a filter cutoff frequency was chosen that did not appreciably alter the signal spectrum (although still attenuating higher frequency noise), and the analyzer sampling rate chosen was high enough to accommodate the actual signal bandwidth.

d. Fourier Analyzer Operation

In Section II, 3, b, the statistical quantities that must be derived from the signal data for each experiment have already been defined. Also, the theoretical basis for the process by which these quantities are calculated in the Fourier Analyzer has been outlined. In this section, the action of the analyzer will be illustrated by means of samples of correlation functions and spectra produced by it during experiment runs.

(1) Input Data Sampling. The first step in the signal analysis process is sampling and analog-to-digital (A/D) conversion of each of the two input signals. To assure validity of the data sample, a sampling rate that is at least twice the highest frequency component present in the signal is used. The sampling is continued until blocks of memory assigned to the two signal channels are filled. Typically, in these experiments, the block size used was 256 data points for each channel, and the points were spaced over a total time interval of 200 msec; the corresponding sampling rate was 1,280 samples/sec. The nature of the signal fluctuations to be analyzed is indicated by the oscillograms in Figure 10. The two traces represent simultaneously recorded 1-sec samples of A-channel and B-channel signals received over a 450-ft outdoor path using 1.25-cm-diam. transmitting and receiving apertures. In spite of the severe fading, it is evident that the two signals are highly correlated.

(2) Complex Fourier Spectrum. When a random signal such as that of Figure 10 is Fourier-transformed, the resulting complex Fourier spectrum is also highly random. This is illustrated in Figure 11, which shows the real part of the Fourier spectrum. Frequency is represented by the horizontal scale and amplitude by the vertical scale. The prominence of the zero-frequency or d-c component (the large upward spike at the left) should be noted. (In fact, the full amplitude of the zero-frequency component is double that indicated in Figure 11, the upper half being "off-screen.") The imaginary part of the complex Fourier spectrum (not shown) is equally random but it does not have a d-c component. When successive data blocks are transformed and then averaged together (frequency-by-frequency), only the d-c component survives; all other frequency components tend toward zero because each one randomly takes on positive and negative values. The d-c values of the A and B signals are measured in this way, as already discussed in Section II, 3, (4).

(3) Power Spectrum of Data Block. The power spectrum of the signal segment represented by a given data block is obtained by multiplying the complex spectrum value at each frequency by its complex conjugate. (This process is termed "conjugate multiplication.") Thus, if $G_a(\omega_n)$ is the complex spectrum value at the nth frequency point,

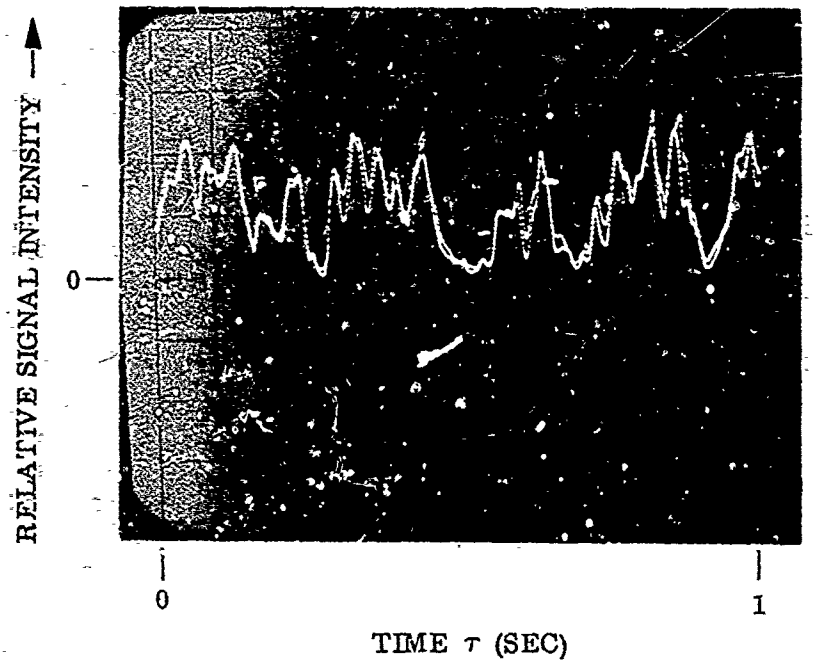


Figure 10 Oscillogram of Simultaneously Recorded A-Channel and B-Channel Signals

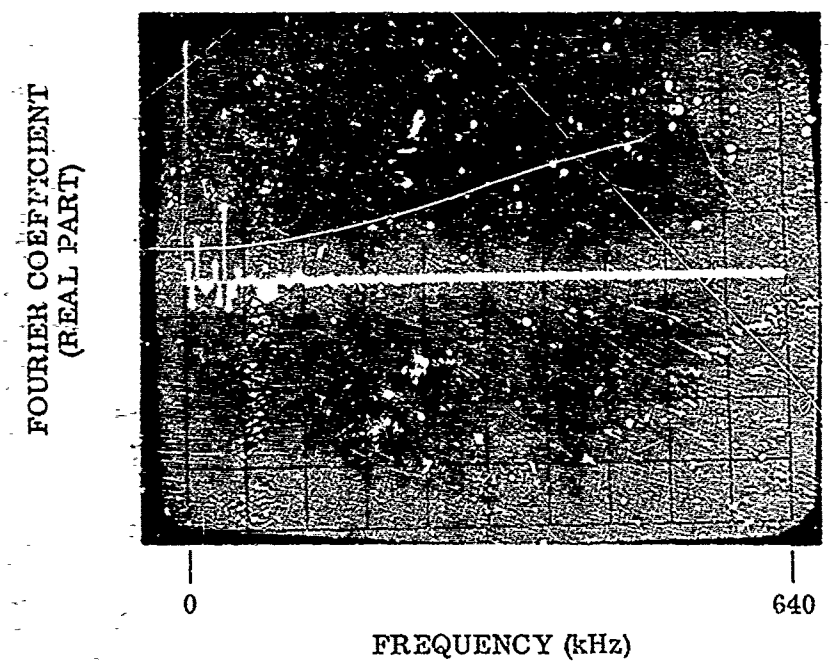


Figure 11 Real Part of Complex Fourier Spectrum of a Portion of Waveform From Figure 10

the corresponding spectral power at this point is $G_a(\omega_n)\, G_a^*(\omega_n)$. This function of (ω_n) is called the "self power spectrum" (or, simply, power spectrum) and has a purely real and positive value at every frequency.[4] Because $G_a(\omega_n)$ is a random variable from frequency-to-frequency, as just discussed, the power spectrum value at each ω_n is also a random variable. Since only positive values occur in the power spectrum, however, the average of a number of such random spectra does not tend to zero, as in the case of the Fourier spectrum. Rather, the average tends to a definite value for each ω_n. Figure 12 is a representative averaged power spectrum. In this case, the vertical scale was converted to dB units in order to obtain a better display of the "tail" of the spectrum. (However, the spectrum averaging is performed on the original power spectra, i.e., before logarithmic conversion.) It is seen that the spectral density was down 30 dB from its low-frequency value at a frequency of about 180 Hz. As this frequency is well below one-half the analyzer sampling frequency used (1280 Hz), the latter was more than adequate for handling this particular signal.

(4) Averaged Cross-Power Spectrum. This spectrum is obtained in exactly the same way as the self-power spectrum except that spectra of the A and B signals are conjugate-multiplied, instead of multiplying one of the spectra by its own conjugate. When the two signals are highly correlated, the result is a function of almost exactly the same form as the self-power spectrum; it is therefore not necessary to illustrate the cross-power spectrum.

(5) Normalized Cross-Correlation Function. As already discussed in Section II, 3, b (2), the inverse Fourier transform of the averaged cross-power spectrum is the cross-correlation function of the two inputs. Normalization and squaring of this function yields the function $\rho^2(\tau)$ that provides the required measure of identity of the two signal waveforms. Figure 13 is a sample of the function $\rho^2(\tau)$ as produced and displayed by the Fourier Analyzer. The abscissa is the time-shift (delay) parameter τ, with $\tau = 0$ at the center of the scale; full-scale values are ±100 msec. The vertical scale is $\rho^2(\tau)$, and the scale factor is such that unity correlation corresponds to two divisions.

---

[4] Before performing this multiplication, the d-c term of the complex spectrum is cleared from the analyzer memory, as already mentioned in Section II, 3, b (4). If this is not done, the large amplitude of the d-c component in the product, relative to the other spectral components (see Figure 11), would cause a serious loss of accuracy in subsequent calculations. This would occur because the analyzer adjusts scale factors according to the largest value in a given memory block, and the smaller values are "pushed off" the lower end of the available dynamic range of the data registers.

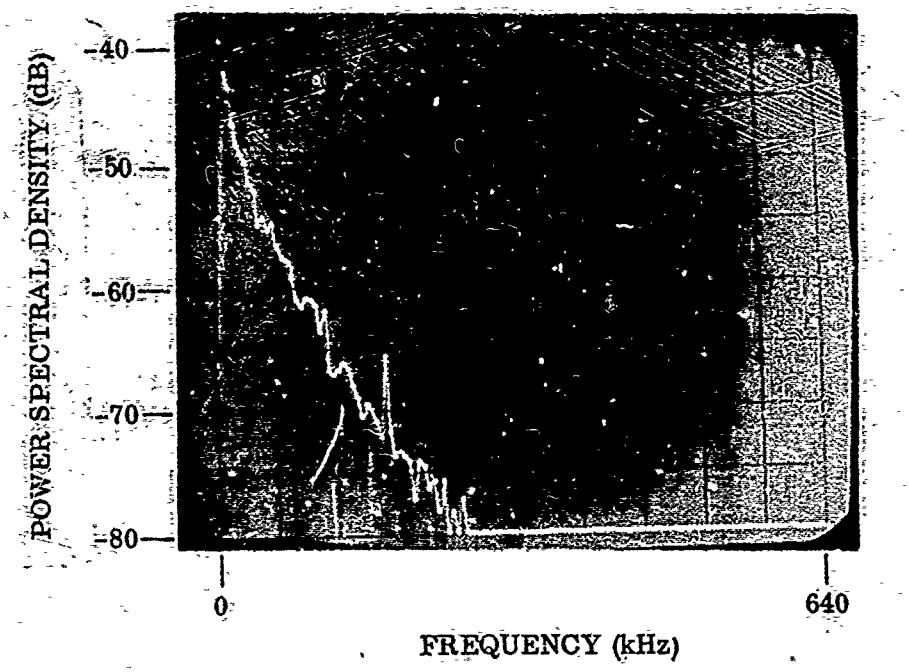


Figure 12 Averaged Power Spectrum – Linear Scale of Frequency for Abscissa; Logarithmic Scale (5 dB/Div) for Ordinate

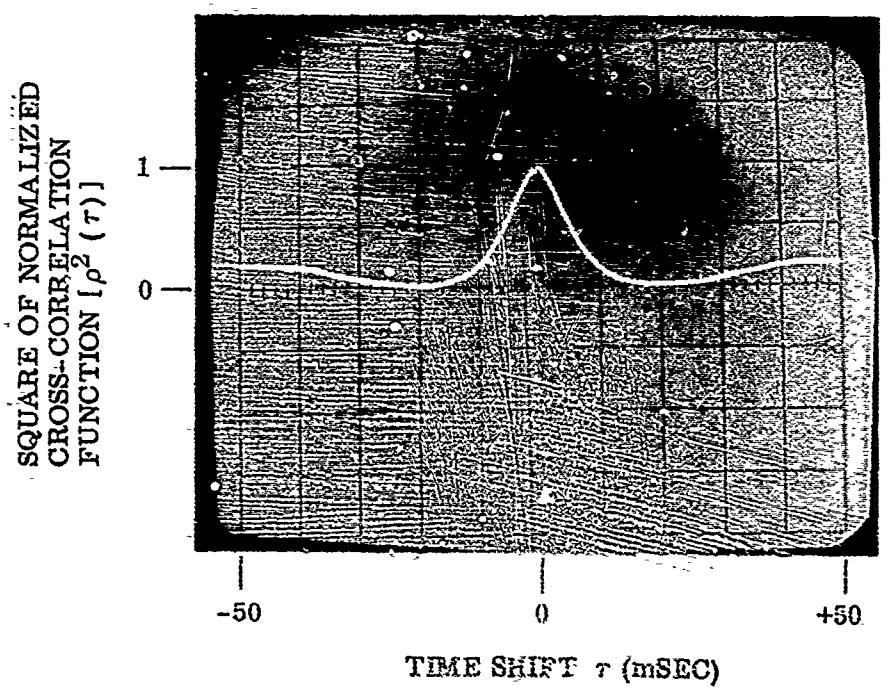


Figure 13 $\rho^2(\tau)$ Displayed by the Fourier Analyzer

The point of particular interest in the correlation plot of Figure 13 is that at $\tau = 0$, corresponding to which, $\rho^2(\tau) \simeq 0.96$, or $\rho(\tau) = 0.98$. (For maximum accuracy, the value of $\rho^2(\tau)$ given is that of the computer printout.) The actual shape of the correlation curve is not of particular interest in connection with this test of optical reciprocity. But knowledge of this function, together with its counterpart, the power spectrum, is of considerable theoretical interest in connection with the problem of understanding the underlying turbulence mechanisms.

e. Optics Alignment and Adjustment

(1) Transmitter Beam Magnifiers. With reference to the schematic diagram of the optics (Figure 5), folding mirror A is removed temporarily, and an autocollimating alignment telescope is aligned to the laser beam with no transmitter beam magnifiers in place. The telescope is then focused at infinity by means of its autocollimation feature; thereafter, no change is made in its focus adjustment. Next, the first beam magnifier (nearest to the laser) is put in place and its lenses are positioned relative to one another so that the emerging laser beam is parallel to that entering and is accurately collimated. (A partially disassembled magnifier unit is shown in Figure 14.) The first condition will be indicated by lack of movement of the focal spot, as seen in the telescope, when the magnifier is rotated in the V-groove. The second is indicated by the sharpness of the focal spot. Additional magnifiers could be brought into adjustment by the same procedure, but a more convenient method that is applicable, once a beam that is known to be collimated is available, will be described in the next paragraph. (The method just described is inconvenient because the magnifier cannot be reached for adjustment while viewing the telescope.)

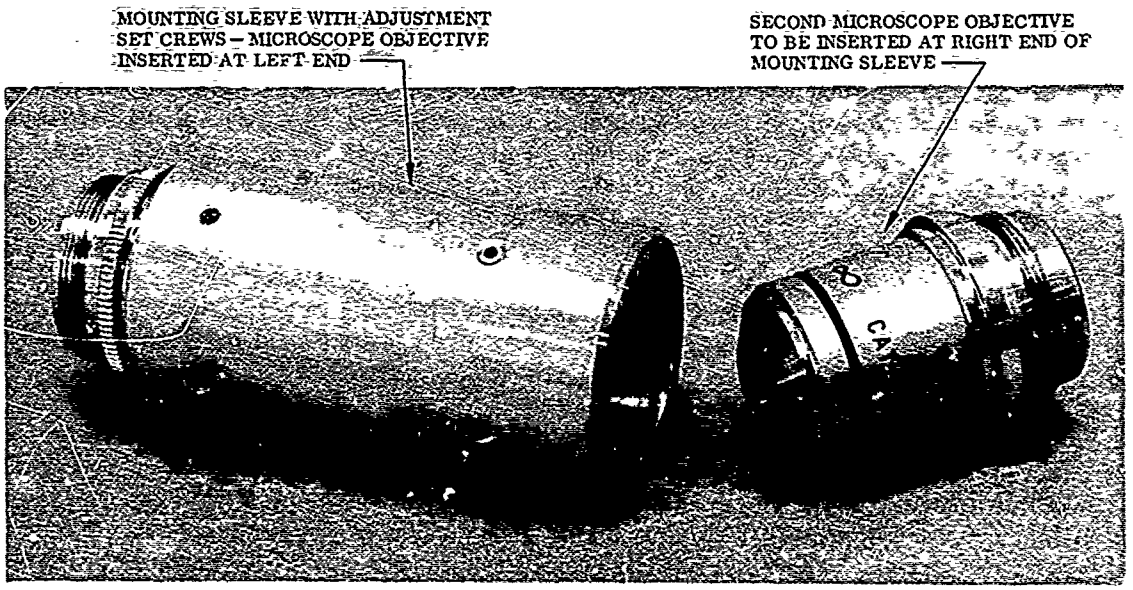


Figure 14 Partially Disassembled Beam Magnifier (In Use, the Two Microscope Objectives are Positioned Nose-to-Nose With Coincident Axes and Focal Planes.)

(2) Receiver Optics Focusing. The cube corner reflector is put in place and the beamsplitter and receiver folding mirror are oriented so that an image of the transmitter beam is obtained at the camera ground glass viewing screen. With the receiver beam magnifier out, the receiver focusing lens (located in the front of the focusing bellows) is positioned so as to obtain a sharp focal spot. The focusing bellows is then locked in place and thereafter remains fixed. Receiver beam magnifiers can now be put in place in the receiver V-groove and adjusted as before for sharp focus and to prevent any movement of the focal spot when the magnifier is rotated. This same method can be used to align additional transmitting beam magnifiers.

(3) Receiver/Transmitter Initial Conjugate Adjustment. The object of this adjustment is to bring the photodetector pinhole into coincidence with the sample of the transmitted beam that is reflected into the receiving optics via the cube-corner reflector. For this purpose, the receiver beamsplitter is oriented to direct the reflected portion of the received beam into the pinhole. Adjustment is made to maximize photo-current as indicated by the signal strength meter on the associated signal monitoring electronics unit.

(4) Transmitter Focusing. To focus the transmitter, the folding mirror A is first put back into place and the focusing lens immediately preceding it (on the laser side) is installed in the focusing mount. The transverse position (vertical and horizontal) of the focusing lens, and the orientation of folding mirror A are next adjusted in combination so that the primary aperture (the opening of the adjustable iris) is symmetrically illuminated. At the same time, the laser beam reflection back into the receiver is minimized. The primary mirror is then oriented so that the transmitted beam is nominally parallel to the table. The alignment telescope is next aligned to the primary beam, and again focused at infinity by means of its autocollimation feature. Finally, the focusing lens is positioned longitudinally for the sharpest focal spot as seen in the alignment telescope. Because the telescope was focused at infinity, the transmitted beam is now collimated.

With this focus adjustment, a plane wave, when received from a direction opposite to the transmitted beam direction, will be brought to a focus by the primary optics and then be recollimated by the focusing lens. Because of the previous adjustment of the receiving optics established with the help of the cube-corner reflection, the recollimated received beam will, in turn, be brought to a focus at the photodetector pinhole. This is the required condition of internal transmitter/receiver adjustment needed for the reciprocity test, subject to one qualification: the procedure for receiver/transmitter conjugate adjustment (detailed in Section II, 4, e, (3) is not sufficiently precise to assure high correlation of the signals from the two receivers. The method used to further refine this adjustment is described in Section II, 4, e, (6).

(5) Alignment of Beams and Folding Mirror. The first step in setting up the complete system for correlation measurements is to point each of the beams so that it is centered on the folding mirror (Figure 3). The mirror must then be oriented so that each beam, after reflection, propagates in a direction opposite to that of the other beam. These alignment steps are accomplished with the help of a screen covered with high reflectivity material, such as 3M-Scotchlite Type 7610 reflective sheeting. First, this screen

is used to "follow" the beam away from the transmitter. (The expanded beam is too dim to be seen on a white card in broad daylight, but it is easily seen by an observer looking along the beam toward the high reflectivity screen.) As the card is "walked" along the beam, the observer corrects the pointing of the transmitter until the beam is centered on the mirror. The second transmitter is aligned in the same way so that its beam is also centered.

A similar procedure is used to orient the folding mirror. With one of the laser transmitters (No. 1) turned off, the other beam from the other transmitter (No. 2) is followed away from the folding mirror toward receiver No. 1, and the mirror is adjusted so that the beam is centered in the No. 1 primary aperture. Next, No. 2 transmitter is turned off and No. 1 is turned on. The centering of the No. 1 beam in the No. 2 aperture is checked and, if necessary, a fine adjustment of pointing of the transmitter/receiver No. 1 unit is made to center its beam in the aperture of the other unit.

Fine pointing adjustments of one of the units is now made so that the received beams are centered – first in the focusing lenses, and then in the viewing optics. Finally, the beams are centered in the receiving pinholes. This latter adjustment is most easily made by means of the vernier angle orientation controls of one (or both) of the folding mirror A mounts.

(6) Fine Conjugate Adjustment. If the initial conjugate adjustment described above in Section II, 4, e, (3) were exact, the fine pointing adjustment just made would result in the focal spots in both receivers being identically positioned relative to their respective photodetectors. Then, as atmospheric turbulence progressively altered the shape and position of one spot, according to reciprocity theory, the other would be altered in exactly the same way. Consequently, the two photodetector output signals will fluctuate identically, and their difference will remain zero regardless of intensity variations, provided, of course, that the two transmitted laser beams have the same strength. On the other hand, if the conjugate adjustment of one unit has been improperly made, the received signals will not track one another.

The latter fact suggests a simple means for improving conjugate adjustment, i.e., observing the difference between the two received signals on an oscilloscope (see Section II, 4, c) while making fine adjustments of the orientation of one receiver beamsplitter to change image position relative to the photodetector pinhole so as to minimize the difference signal. By successively adjusting spot position and the intensity of one of the laser beams, it is found that a near null of the difference signal can be reached. Correlation measurements are made under this null adjustment condition.

In making this null adjustment, it was found useful not only to observe the difference signal. as just described, but also the meter indications of the A- and B-signal monitor (see Section II, 4, c). Under most test conditions, these meters fluctuate widely. However, as the desired conjugate adjustment is approached, the fluctuations of the meters become strongly correlated. Under this condition, their deflections, especially during relatively "quiet" periods, provide an indication of the relative strengths of the two received signals. Using this indication, one of the variable optical attenuators is varied

until approximate equality is reached. However, the final fine adjustment is made by observing the difference signal.

5. FADE CORRELATION MEASUREMENTS

Three different optical paths were used in carrying out the correlation measurement program, as follows:

- Short path in the laboratory (10 ft)
- Medium and long paths in the laboratory (500 ft)
- Outdoor path (450 ft)

This section describes the purpose and principal results for each test phase. The correlation measurements are discussed and interpreted in Section II, 6.

a. Short Path Laboratory Test

Initially, correlation measurements were made with the two transmitter-receiver units as close together as possible, consistent with experimental convenience, in order to conduct verification tests of the entire experimental system with minimum atmospheric turbulence effects. The two units were pointed toward each other but the tables were separated by approximately 3 ft to allow access on all sides. The primary objective of this test was to determine whether inherent laser intensity fluctuations or other noise sources within the equipment would significantly influence the signal correlation obtainable. Under this experimental condition, it was found that, even with the largest beam diameters of interest (5 to 10 cm), very good nulling of the difference signal could be achieved. With care not to cause table vibration while making the fine conjugate adjustment (described in Section II, 4, e, (6)) it was found possible to reduce the peak difference signal to as small as 2 to 3 percent of the individual signals applied to the differences. As previously indicated by Eq. (8), this implies a value $\rho(0) \rightarrow 0.998$. A series of 10 measurements of correlation under this condition produced a value $\rho(0) = 0.997 \pm 0.005\ (1 - \sigma)$. The latter result is consistent with the former, and implies a measurement error of appreciably less than 1 percent in the determination of correlation values. It is evident that there are no internal noise sources which will grossly degrade measurement accuracy.

b. Medium- and Long-Path Laboratory Test

Two series of indoor tests were made — one with an approximate 50-ft path length and the other with an approximate 500-ft path length. Both were primarily intended to provide additional experience in alignment of the telescopes and in signal analyzer operation. In the course of these tests, several factors came to light that were considered of sufficient importance for later outdoor measurement to require further investigation.

In the tests using the 50-ft path, it was observed that the plot of $\rho^2(\tau)$ displayed by the analyzer had a series of secondary peaks at approximately equal spacing from the central (main) peak. Figure 15 is typical of the plots obtained for a range of aperture diameters

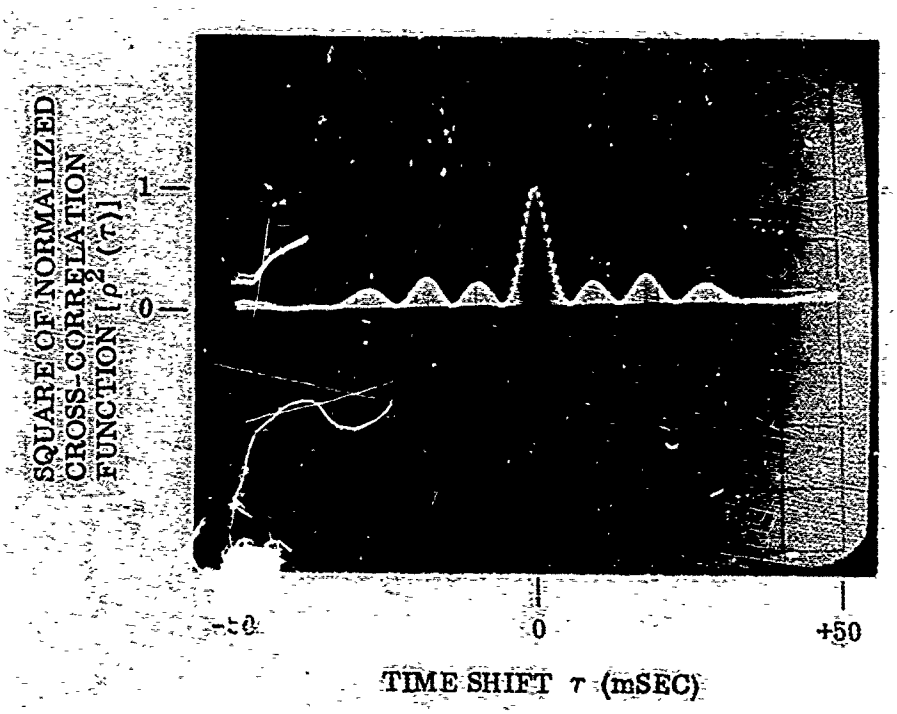


Figure 15 Square of Normalized Cross-Correlation Function of Signal Transmitted Over 50-ft Indoor Path, With Secondary Maxima Indicating Presence of Periodic Components in the Signal

from 2.5 to 10 cm. This periodicity in the cross-correlation function indicates the presence of a periodic component in the photodetector output signal. In order to determine the nature of this extraneous signal, it is useful to determine both its frequency and amplitude relative to the main signal. This was easily done since the power spectrum of each of the input signals is generated by the signal analyzer program. It was merely necessary to display the power spectrum as stored in the analyzer at the end of a processing sequence. Figure 16 is such a spectrum. The frequency resolution (spacing between points) is 10 Hz, the horizontal scale factor is 64 Hz/div. and the vertical scale is 5 dB/division. It is seen that peaks occur at 50 and 110 Hz. The periodic component therefore cannot be attributed primarily to 60- or 120-Hz power supply effects. (However, minor contributions at the latter frequencies could not be ruled out at this point. In fact, some reduction in the secondary peaks was noted when the laser power supplies were removed from the optical table, thus eliminating transformer vibration – at 60 Hz – as a possible disturbance source.)

Probable causes of the 50- and 110-Hz disturbances were mechanical building vibrations due to rotating machinery and/or pulsations of the air in the path due to the building air-conditioning system. Further effort to identify the source of this periodic disturbance was deferred pending the results of correlation measurements over longer paths.

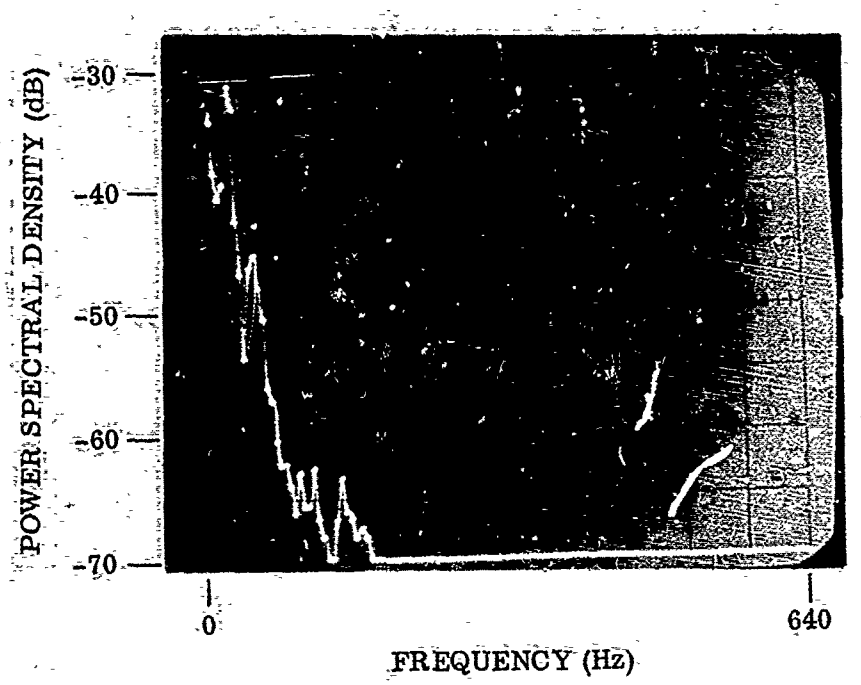


Figure 16 Power Spectrum of One of Signals From Which Figure 15 Derived – Frequencies of Periodic Components Indicated by Peaks at 50 and 110 Hz; Frequency Resolution (Spacing Between Points) = 10 Hz

The first long-path measurements were conducted in the laboratory, rather than outdoors, because of bad weather conditions. In this series, the two transmitter units were set up in the main corridor of the laboratory building, near one end, with the path folding mirror at the other end. The units were separated laterally about 5 ft, and the path length was approximately 500 ft. Tests were conducted after working hours to minimize interruptions due to traffic in the corridors.

Correlation measurements made over a range of aperture sizes from 0.75 to 5.0 cm showed, at most, only a barely discernible periodic component. In view of the fact that the telescope units had been moved only about 10 ft from their location in the short-path test, it was apparent that building (floor) mechanical vibration was not the cause of the periodic signal component in the photodetector output. The absence of any appreciable periodic components due to atmospheric pulsation effects with the longer path is attributable to the lack of air-conditioning outlets in the corridor, which had only return-air inlets. Air pulsations in the corridor path were therefore undoubtedly weaker than for the shorter path which was entirely within a laboratory work area and close to air outlets. It is considered that the periodic disturbances seen in the short-path tests were due to effects of the air-conditioning system which, of course, would be absent in outdoor operation.

The effect of varying primary aperture size on the character of the received beam image at the camera focal plane (or at the photodetector pinhole plane) is illustrated in Figure 17. Three sequences of four exposures each are shown, one for each of three primary

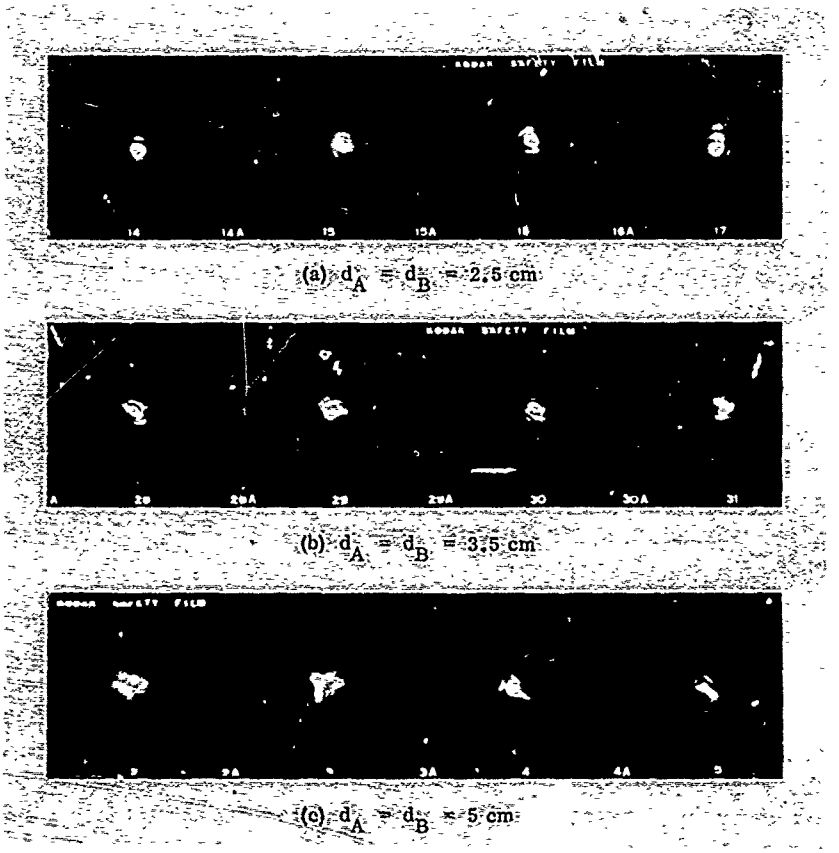


Figure 17 Received Beam Images at Camera Focal Plane and Photodetector Pinhole Plane for Three Primary Aperture Sizes — (a) $d_A = d_B = 2.5$ cm: (b) $d_A = d_B = 3.5$ cm; (c) $d_A = d_B = 5$ cm (Successive Exposures in Each Sequence (Left to Right) Made at Approximate 10-sec Intervals)

aperture sizes. The top sequence at Figure 17 (a) was obtained using 2.5-cm apertures (both transmitter/receiver units). It is seen that the central spot remains almost circular and only the diffraction rings are distorted, or broken up. With a 3.5-cm aperture, there is noticeable blurring and shifting of the central spot, and the structure in the diffraction "sidelobes" is finer, but not otherwise much different than at (a). With 5-cm apertures, central spot is either missing altogether, or badly distorted. The successive exposures in each sequence were taken at approximately 10-sec intervals.

With some study, it can be seen from the photographs that the centroid of the beam image moves appreciably, relative to a mean position. This motion is much more evident when observing the image in the camera ground-glass viewing system, because many of the displacements occur on a time scale of the order of 0.1 to 1 sec, a range to which the eye is quite sensitive.

A second finding of the long-path indoor test was that fine conjugate adjustment (by difference signal nulling) became more difficult than had been the case with the shorter paths. The reason was that deep and persistent signal fades occurred much more frequently. Because a signal fade has the same effect on the difference signal as an adjustment toward a better null, it was found to be difficult to avoid making erroneous

adjustments. It became necessary to watch both the signal-strength monitor and the difference signal display, and only attempt adjustments during strong-signal intervals. The larger the aperture, the more severe the problem, because the duration of deep fades increased. As a consequence, it was found impractical to attempt measurements using the available instrumentation, at aperture sizes greater than 5 cm.[5]

A possible limitation on the extent to which the difference signal could be nulled was the effect of uncorrelated atmospheric turbulence on the optical paths that are not common to the transmitter and receiver elements of a given unit, i.e., the path between the laser and the beamsplitter, on the one hand, and between the beamsplitter and the receiving photodetector on the other. in an effort to eliminate such effects, air shields were added, as shown in Figure 18.[6] The addition of the air shields proved to be quite helpful in increasing the correlation coefficient, although a quantitative estimate of improvement was not made.

Finally the indoor tests showed that the method originally programmed into the analyzer for determining the strength of signal fading was not entirely satisfactory. Fading strength as defined by Eqs. (13) or (14) is the ratio of signal a-c power to d-c power. Unfortunately, under conditions of moderate or weak fading, where the d-c component becomes comparable to or larger than the a-c component, it was found that the d-c component consumed most of the significant digits available in the memory locations used at the point in the program at which the cross-power spectrum was calculated from the Fourier spectrum. As a result, the accuracy of determination of the cross-correlation coefficient was degraded.

Before the outdoor tests were conducted, the program used in the analyzer to determine the signal d-c component was changed and the problem of loss of accuracy due to the d-c component was satisfactorily solved. The method finally adopted and used in the outdoor measurements is described in Section II, 3, b (4), and amplified in Section II, 4, d, (2), so it will not be detailed here.

A total of nine measurements of cross-correlation coefficient $\rho(0)$ were made using the 500-ft indoor path with aperture diameters from 0.75 to 5.0 cm. The results were as follows:

Average value of $\rho(0)$ = 0.971
Standard deviation = 0.017

---

[5] From visual observation of the received beam, as imaged in the viewing system, it was noted that much of the signal fading was due to simple beam wander. It was obvious, therefore, that the depth of fading and the frequency of deep fades would have been greatly reduced by the substitution of a fast-steering transmitter at one end of the link.

[6] The plastic box and the tubular shield along the far side of the unit actually are in front of the beamsplitter; hence they were not needed for correlation measurement. (They were added, originally, during preliminary testing of the optics to minimize beam distortion due to room air turbulence.)

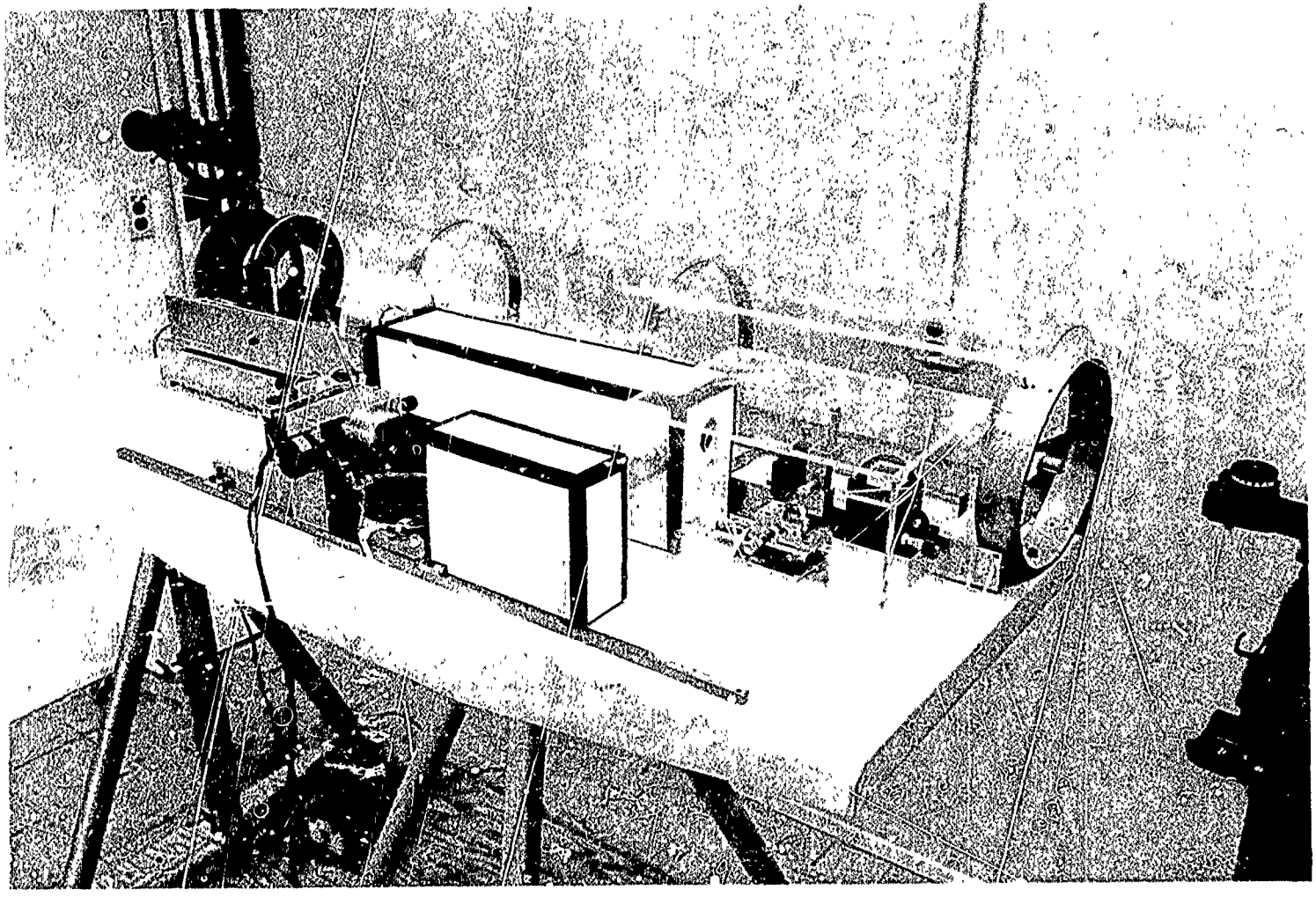


Figure 18 Transmitter/Receiver Unit With Air Shields in Place

c. Outdoor Measurement

Figure 19 is a view along the test path used in the outdoor measurements. The two transmitter/receiver units were located on the concrete walkway in the foreground and were spaced approximately 3 m (10 ft) apart along the walk. The path-folding mirror was mounted on a heavy-duty tripod located just to the right of the tree in the background at center left. The weather was fair, and the wind (when present) was from a direction at about 45 deg to the left of the direction of view. During the measurement sequence the wind speed varied widely up to a maximum estimated speed of 15 mph. (Knowledge of wind speed during any given measurement was not required since theoretically, at least, propagation reciprocity holds even in the presence of turbulent fluctuation of the medium.) The measurement sequence extended over a period from approximately 11:00 a.m. to 5:30 p.m.

During the outdoor measurements, the only difference noted between indoor (long-path) and outdoor operation was that the transmitter units tended to drift out of alignment (with a consequent loss of signal strength) more rapidly during outdoor than indoor operation. This effect was especially noticeable (and troublesome) toward the end of the tests when the air temperature was dropping rapidly. It was concluded, therefore, that alignment drift was due to temperature changes in the telescope components or the supporting structure. However, this drift of beam alignment did not affect the validity of this experiment as a test of optical reciprocity. In fact, if drift had not occurred, it would have been desirable to misalign the two beams purposely as a further test of reciprocity theory since the theory predicts that the two received signals would remain correlated regardless of misalignment. This prediction follows from the fact that a mechanical misalignment of one of the transmitter/receiver units is equivalent in its effect on both transmitted and received waves to that of placing an optical wedge in the path. The latter, in turn, can be regarded simply as a special form of perturbation in the propagation path and, therefore, one to which reciprocity theory applies.

A total of eight measurement runs that yielded valid data were made using aperture sizes of 1.25, 2.5, and 5 cm respectively. At the lower end of the range, the received beam image was a well defined spot with distinct, relatively stable diffraction rings. Nevertheless, spot wander of an amount comparable to the spot size was not uncommon. At the intermediate aperture size (2.5 cm), the central diffraction spot was still moderately well defined, but diffraction rings were almost never present. Instead, a pattern of constantly evolving spots and streaks was seen. In addition, the central spot would occasionally split into two or more segments and frequently show displacements of several spot diameters. At the 5-cm aperture there was virtually no semblance of a central spot, but only a constantly evolving set of spots and/or streaks.

The results of the outdoor measurement series using the 450-ft path are summarized in Table 2.



Figure 19 View Along Test Path Used in Outdoor Fade Correlation Measurements – Transmitter/Receiver Units Located on Concrete Walkway in Immediate Foreground and Path-Folding Mirror Placed Just to Right of Single Tree in Background at Center Left; Round-Trip Path Length Approximately 140 m (450 ft)

Table 2. Summary Of Fade Correlation Measurements, Using 450-ft Outdoor Path

Measurement No.	$d_A = d_B$ = Primary Aperture Diameter (cm)	γ = Normalized Intensity Variance	C_ℓ = Equivalent Log-Amplitude Variance	$\rho(0)$ Normalized Cross-Correlation Coefficient
1	1.25	0.068	0.0165	0.990
2	1.25	0.073	0.0176	0.983
3	2.50	0.372	0.0792	0.978
4	2.50	0.190	0.0435	0.957
5	2.50	0.472	0.0966	0.980
6	2.50	0.110	0.026	0.980
7	5.0	1.09	0.184	0.956
8	5.0	1.82	0.260	0.938
9	5.0	3.60	0.382	0.917
Average				0.964
Standard Deviation				0.023

It is seen from Table 2 that the range of aperture sizes was such as to produce a range of signal fading strengths of more than 50 to 1. At the lower end of the range, the value of equivalent log-amplitude variance, $C_\ell = 0.0165$, implies a communication link fading loss[7] of somewhat less than 3 dB. At the upper end of the range, on the other hand, the value $C_\ell = 0.26$ implies a fading loss of approximately 16 dB.

[7]The concept of fading loss and the relationship between log amplitude variance and fading loss is given in Reference 1, Section 1.4, Atmospheric Turbulence Effects. Briefly, fading loss expressed in dB is defined as the required dB increase in average received signal strength needed to maintain a specified bit error rate, as compared to the signal strength required by an identical link without fading. Fading loss does not account for the reduction in average received signal strength due to transmitter beam spread caused by turbulence.

The most significant feature of these results is that the measured cross-correlation remains high for all signal fading conditions, in accordance with the predictions of reciprocity theory. The slight drop at the largest aperture size is not surprising in view of the increasing difficulty that is experienced under these conditions in making the nulling adjustment, as noted in the discussion of the indoor long-path tests. (See Section II, 5, b.)

The Fourier Analyzer outputs from which the results given in the above table are derived are presented in Appendix IX. Printouts are given for all of the measurement runs, showing on each printout page the square of the normalized cross-correlation function, the autocorrelation function, the d-c value, and the signal power spectrum.

6. SIGNIFICANCE OF RECIPROCITY VERIFICATIONS

The experimental verification of optical reciprocity theory is of immediate importance to the Air Force 405B program in three major ways. First, it establishes the validity of the theoretical concepts that underlie the Fast-Steering technique for improvement of atmospheric links. This conclusion is given further direct support in Section 3 by the results of experiments designed to test this technique. Second, the soundness of the Atmospheric Transmission Measurement Technique based on star image sensing and tracking is provided strong support. Finally, the positive results of this experimental test of reciprocity theory justifies increased confidence in the theoretical design and performance predictions of the up-link portion of the Space Data Relay System as carried out under Contract F04701-71-C-0329. The reason this increased confidence is justified is that the predictions and design were based on data derived from measurements of star image fluctuation, and on theoretical analyses of atmospheric turbulence effects on heterodyne receiver performance. Reciprocity theory was used to apply these results directly to the problem of transmitter design optimization and performance prediction.

SECTION III

BEACON FAST-TRACKING, TRANSMITTER FAST-STEERING EXPERIMENT

1. GENERAL CONSIDERATIONS

As already indicated in Section I, a major problem in the design of a ground-to-space (or aircraft-to-space) laser communication link is that the quality of a beam transmitted upward from the ground is degraded by the fluctuating optical inhomogeneity of the atmosphere.[8] In this section, an experiment designed to test the effectiveness of a technique for alleviating this problem, called beacon fast tracking, will be described. This technique was devised by LMSC in the course of work performed on the Air Force Program entitled Optical Space Data Relay Subsystem Preliminary Design (SDRS). (See Reference 1.)

The experiment was performed by using existing optical beam tracking and pointing equipment that had been developed in a joint effort by LMSC and ITT-Gilfillan for use in a related program to evaluate optical beam tracking and pointing techniques. As shown in Figure 20, this equipment incorporates two laser sources, one representing, in the present application, a satellite-borne beacon transmitter and the other, a ground-based communication transmitter. Signals from the latter are detected by a photoreceptor arranged to simulate a communication receiver that shares the optics of the beacon transmitter. Artificial turbulence is introduced into a region common to the beacon and data-link beams. The fluctuations of wavefront orientation of the beacon beam, after it has passed through the turbulent region, are sensed by an image-dissector tracker. This information is then used to control fast-steering mirrors that point the communication laser beam so as to counteract deflection to which the beam will be subjected in traveling through the turbulent region.

Quantitative measurements of the strength of signal fading caused by the artificial turbulence were made under several conditions of adjustment of the optics and under different turbulence conditions. Under such conditions, producing effects representative of those to be expected in an actual ground-to-space link, the reduction of fading strength, as measured by the variance of the received signal, was found to be of the order of 20 dB.

After presenting the theoretical basis of the fast-steering concept, the experimental equipment arrangement and the sequence of experiments carried out will be detailed. Finally, the question of the required precision of boresight alignment of the transmitting laser with respect to the receiving axis direction will be considered.

---

[8] This fluctuation phenomena, although closely related to atmospheric turbulence per se, also involves other effects such as local heating and convection. However, for convenience, it will be referred to simply as "atmospheric turbulence."

PRECEDING PAGE BLANK-NOT FI

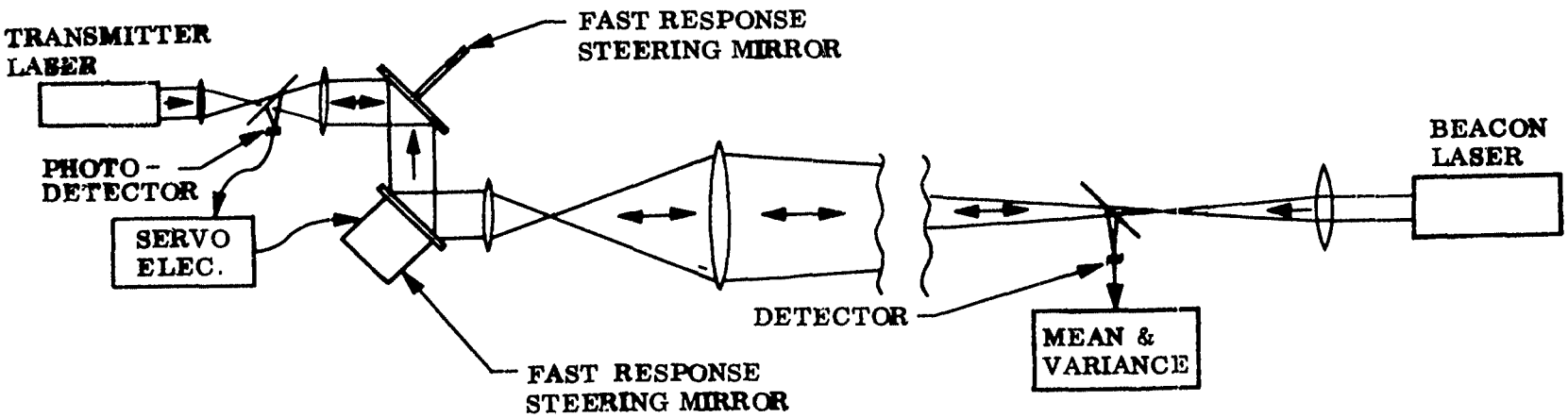


Figure 20 Beacon Fast-Tracking Experiment – Simplified Schematic

2. THEORETICAL BACKGROUND

The basic concept underlying the fast-tracking, fast-steering approach to improving the performance of atmospheric links is that of optical antenna gain reciprocity. This concept has already been developed at considerable length in Section II, 2. However, the present application involves some extension of that concept and, for this reason, it is useful first to consider the action of the tracking-pointing system for a highly simplified model of atmospheric inhomogeneity.

According to this simplified model, the atmosphere, through the mechanism of turbulence, has the effect of randomly introducing and removing weak optical wedges and lenses of various orientations and strengths into a propagation path. This action causes the beam to bend and to start spreading or converging at various points. If the effect of the introduction of a single wedge near an antenna aperture is considered, the required insight can be obtained.

For a laser transmitter, introducing a weak wedge into the beam just after the aperture will bend the transmitted beam so that it will not continue in exactly the same direction that it started. Similarly, a beam approaching the aperture will appear to be coming from somewhere other than its actual direction of origin. If the aperture has associated with it a focal plane detector that looks in the same direction as the laser transmitter, and if the beacon comes from the direction the laser is pointed, then the laser transmitter will not reach its target, nor will the subcoherent receiver detect the beacon.[9] If the system is slewed until the receiver is detecting the beacon with maximum signal output, the amount of slewing will exactly correspond to the bending of the beacon beam induced by the wedge, but will be oppositely oriented to it. The transmitted laser beam will be bent just as much as the beacon beam by the atmospheric wedge, and, therefore, this amount of slewing is exactly that required to make the laser point at its target. That is, the right amount of correction is supplied to take care of the atmospheric effect, for both the beacon receiver and the laser transmitter.

Obviously, atmospheric inhomogeneity effects cannot be fully described simply in terms of wedges because such a model ignores the "lens components" of inhomogeneity. Nevertheless, the random-wedge concept is a useful one because it has been shown that, to a significant extent, atmospheric turbulence-induced wave-front distortion can be considered as simply a matter of random tilting of the wavefront. (See Reference 6.) This means that a large part of the effect of wavefront distortion can be cancelled by alignment of the antenna to follow the random tilt, i.e., by fast tracking. In fact, analysis of the performance of such a fast tracking system, as applied to an optical heterodyne receiver, shows that its performance can be about 10 dB better than that which the atmosphere will allow a static optical heterodyne receiver system to achieve. (See Reference 1, Appendixes L and M.)

---

[9] In the absence of the atmospheric wedge, the laser would be pointed directly at its target, and the beacon would be directly "on" the subcoherent receiver.

For an optical heterodyne receiver, or for a diffraction-limited optical tracker, the approach to fast tracking is straightforward. It is necessary only to collect the wave-front in a way that allows its tilt to be sensed, and then provide servo capabilities to counteract the tilt. On the other hand, for a laser transmitter, there is no obvious or straightforward method that can be implemented within the transmitter to obtain the necessary information for controlling a servo system to compensate for a tilt which the atmosphere will put into the beam after it leaves the transmitter. However, because of reciprocity, it follows that if the receiver at the other end of the link has associated with it a laser beacon, then if the laser transmitter shares its aperture with a beacon tracking receiver (either an optical heterodyne receiver or a diffraction-limited imaging receiver), the appropriate tilt for the aperture can be derived from tracking of the beacon. This tilt measurement can then be used to point the laser transmitter. Because of reciprocity, it is known that the tilt developed from the beacon tracker is exactly the right tilt to use to realize the benefits of fast tracking for a laser transmitter.

3. DESCRIPTION OF EXPERIMENTAL SYSTEM

As already noted, the equipment used for the beacon fast-tracking experiment was assembled in a joint effort by LMSC and ITT-Gilfillan. This equipment was made available for use on this program and, at the same time, was used for Acquisition and Tracking System Performance Evaluation tests conducted under another contract.

Figure 21 shows the principal system components and optical beam paths involved, and Figure 22 is a pictorial view of the acquisition and tracking equipment used in this experiment. As shown in these figures, the system has a tracking detector, servocontrolled beam steering optics, and a pointing laser at one terminal. At the other terminal there is a beacon laser, a pointing detector, and an optical power detector. The term, "pointing laser," refers to the laser that represents the transmitting end of a communication link. However, no data are to be transmitted in this experiment. The pointing detector is a special sensor designed to measure the wave-front tilt of the transmitter beam as received at the beacon end of the link. The optical power detector indicates the instantaneous received signal power and represents the receiver of the communication link. Both terminals are mounted on a single, air-supported slab of concrete to provide high relative stability of the two terminals, to isolate them from ground motions, and to permit precision control of their angular relationship. For this experiment, a turbulence generator is placed in the optical path between the two terminals in a region common to the two laser beams.

The two terminals are diagrammed in greater detail in Figures 23 and 24. The first shows the beacon transmitter terminal. An HeNe laser is attached rigidly to an optical bench and pointed directly at the scanning mirror of the tracking terminal (Figure 22). This beacon beam is transmitted through a beam expander and spatial filter assembly. The spatial filter provides a highly collimated beam and rejects light components that are not exactly parallel to the main energy beam, and which might show up as angular noise in the transmitted signal.

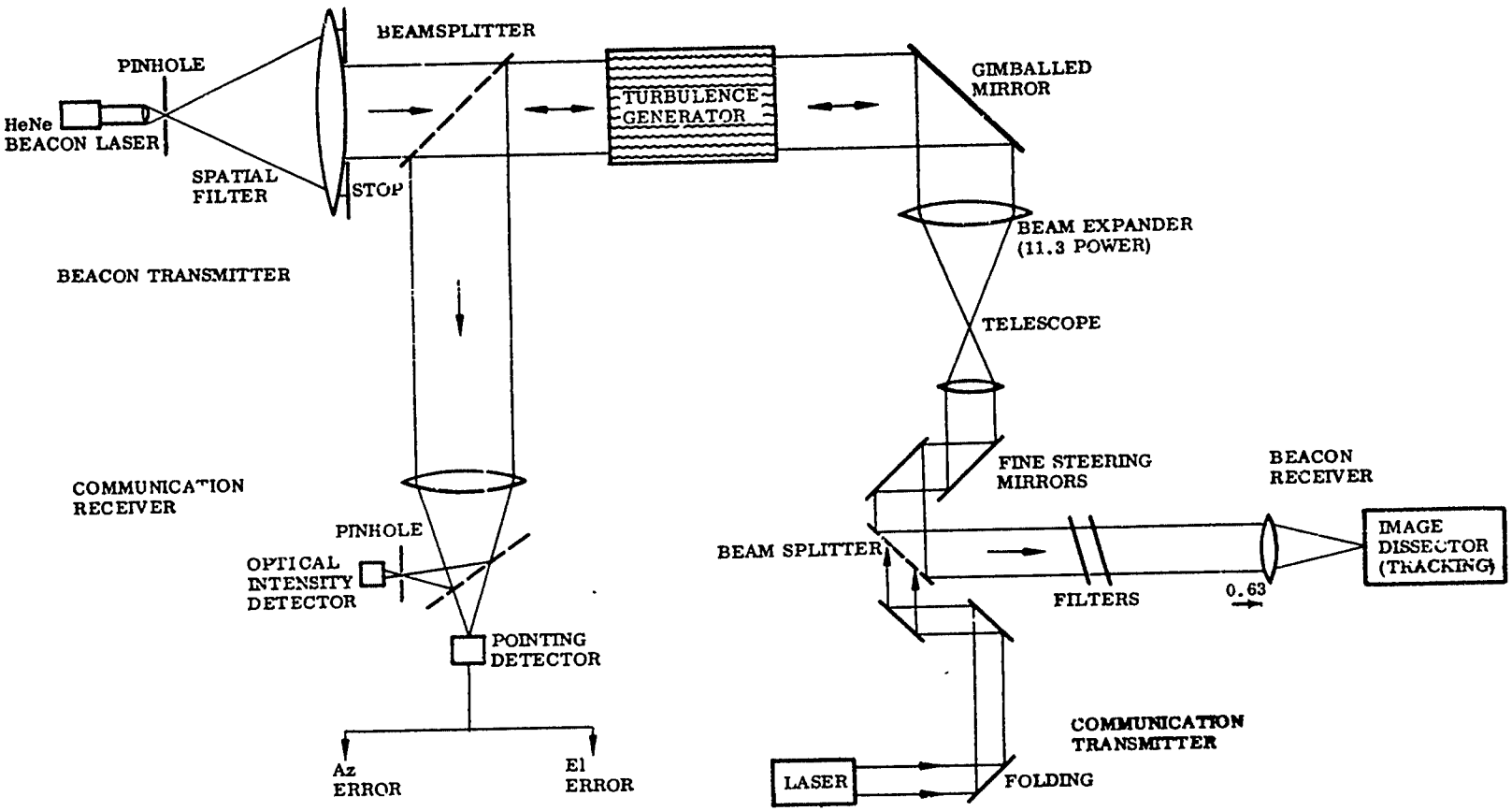


Figure 21 Beacon Fast-Tracking Experiment – Optical Components and Beam Paths

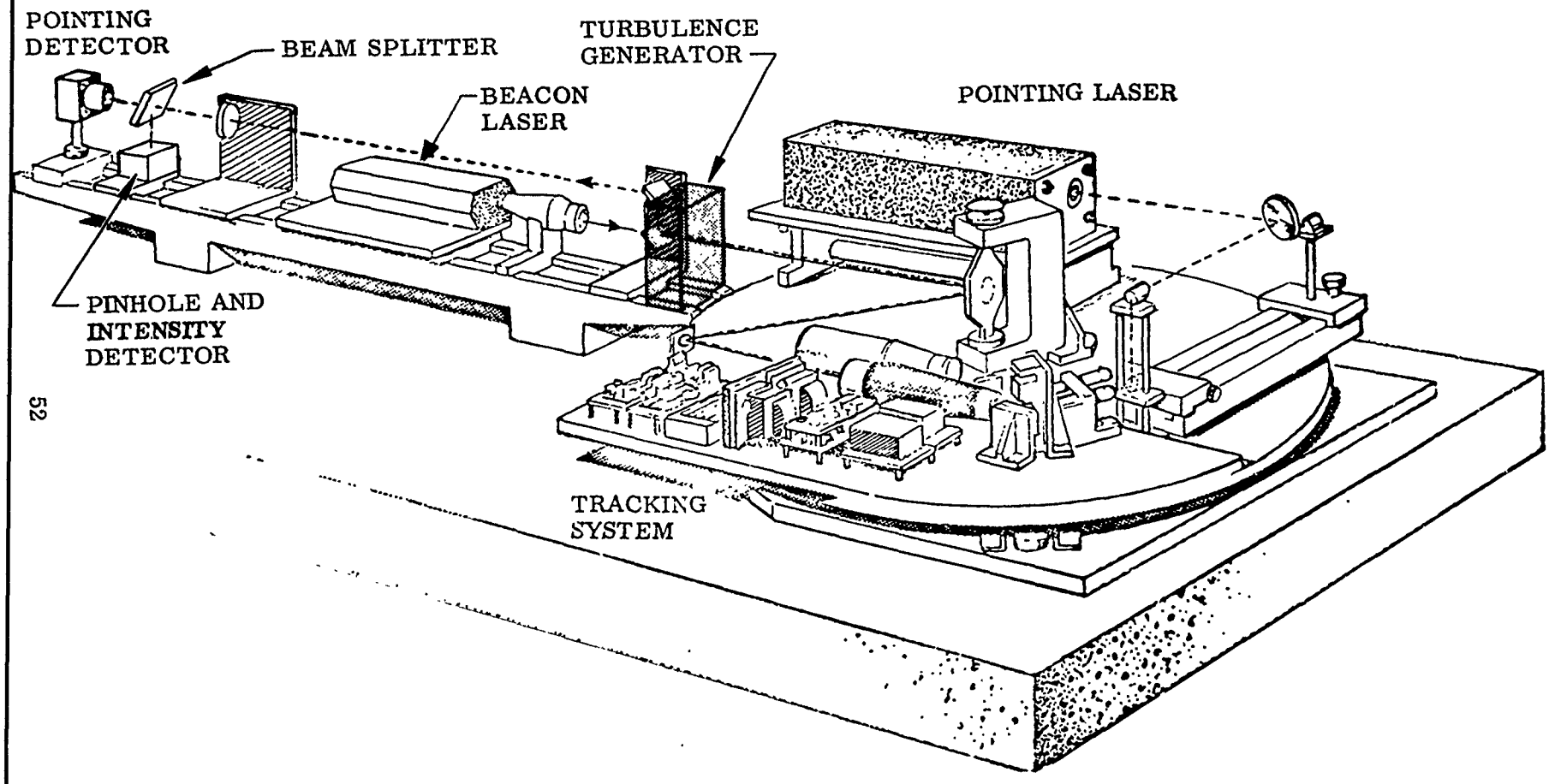


Figure 22 Acquisition and Tracking Evaluation Subsystem Used for Beacon Fast-Tracking Experiment

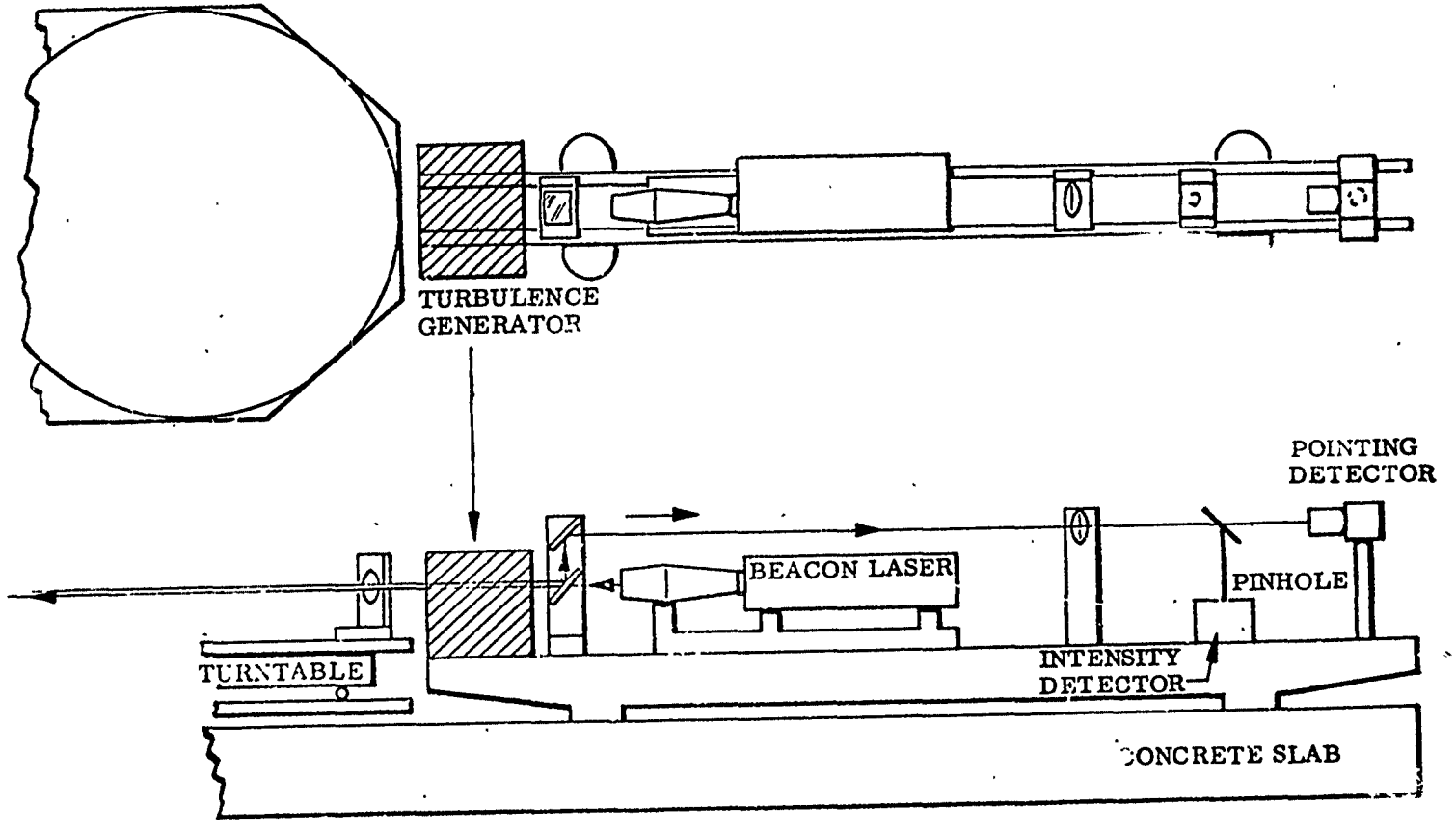


Figure 23 Beacon Transmitter and Intensity Detector Used to Simulate Communication Link Transmitting Terminal

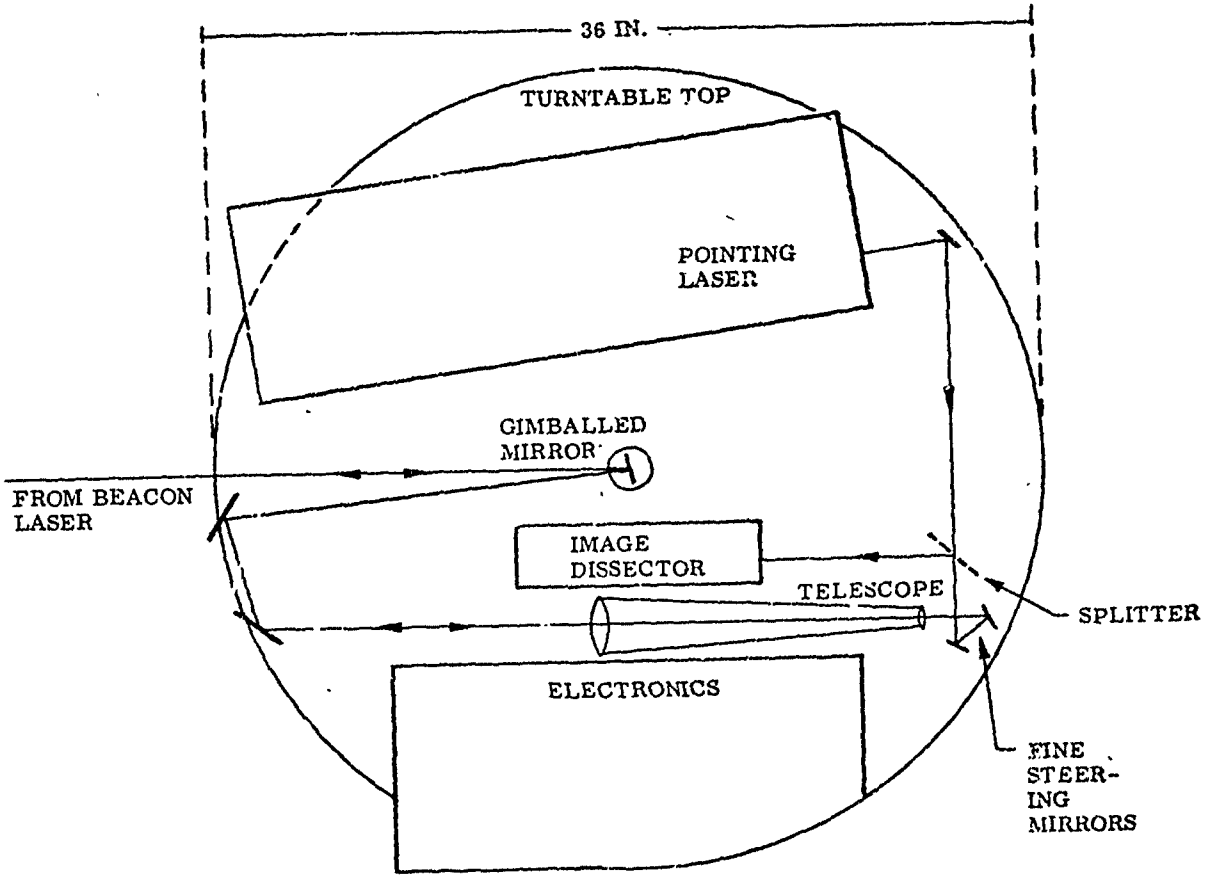


Figure 24 Laser, Tracker, and Fine-Beam Steerers Used to Simulate Communication Link Receiving Terminal

The beam expander at the beacon laser increases the beam diameter to 2 in. This expanded beam is then stopped down to 23 mm (7/8 in.) the diameter of the beamsplitter, or less by means of a variable iris. Use of the central portion of the beam gives nearly uniform illumination, representative of widely separated operational terminals. The beamsplitter also separates the incoming pointing beam from the outgoing HeNe laser beacon beam aimed at the tracker. The former goes to a pointing error detector, a four-quadrant position detector that measures the direction from which the pointing beam is received at the beacon terminal. Measurement of the effect that pointing noise would have on a communication link is made by splitting off a portion of the received pointing signal and focusing it on a pinhole much smaller than the focused spot. Behind the pinhole is a photodetector with an instantaneous output proportional to the light intensity reaching it through the pinhole. As the spot moves around because of pointing error, the amount of light going through the pinhole will vary in accordance with the variation in intensity at the particular portion of the focal plane pattern of the received beam that falls on the pinhole. This arrangement of a pinhole at the focal plane of the received beam corresponds to a receiving aperture in the far field of a transmitting aperture, and motion of the focal plane pattern corresponds to the motion of the far field pattern of a collimated beam.[10] Since both terminals in the test are fixed in position, variations in the direction from which signals are received indicate pointing errors due to tracking error, pointing system error, or turbulence effects.

As shown in the optical schematic diagram (Figure 21), incoming radiation to the tracking terminal is reflected from the first (gimballed) mirror. From there, it travels to a folding mirror (not shown) that directs the light along the axis of the 11.3-power refracting telescope which reduces the beam diameter to 2-mm. Next, the beam is reflected from tandem fine steering mirrors and a dichroic beamsplitter, and finally is focused on the image dissector-tracking detector.

The tracking error voltages generated in the image dissector-tracker are applied to the fine steering mirrors so as to drive the error voltages toward zero. These voltages are a measure of the tracking error. The image dissector error signal is calibrated in angle space, using precision optical wedges. A detailed description of the tracker and of the calibration method can be found in the final report (Reference 7) on the Acquisition and Tracking System Performance Evaluation Program.

The turbulence generator is placed between the two terminals. Its function is to provide controllable air turbulence in the optical path. It consists of a heat source, in the form of an electrical element, an air source, an elongated slit orifice, and a structure for channeling the turbulent air flow across the laser beam. Control of the heat and air flow gives a wide range of air turbulence effects, as described more fully in Section III, 4, c.

---

[10] Since a collimated beam is in reality a beam focused at infinity, the details of the far-field pattern of a collimated beam and of the focal plane pattern of a beam focused at a finite distance are identical except for the dimensional scale.

4. MEASUREMENT PROGRAM

a. Objectives of Measurement Program

The primary objective of the program is to determine the degree to which fast tracking, based on reciprocity theory, can improve pointing accuracy and reduce signal strength fluctuations. Secondary objectives are to measure the effects of air turbulence in the beam path on tracking loop frequency response, and to measure the effects of varying transmitter beam diameter and tracking loop bandwidth on tracking and pointing accuracy, as well as signal strength fluctuation, when using fast steering optics. The primary objective and the first of the secondary objectives were accomplished, but the latter two were not because of problems encountered during the measurement program. Although these problems were solved, the time delay involved and the limited availability of the acquisition and tracking system due to the high priority of the evaluation program, made it impossible to carry out the planned experiments involving variation of transmitter beam diameter and tracking loop bandwidth. The nature of the technical difficulties encountered and their solution will be discussed more fully in Section III,4,b,(2).

After describing the methods used to generate turbulence and to verify proper operation of the tracking and pointing optics under turbulence conditions, the remainder of this section will be devoted to detailing the series of experiments carried out to evaluate the effects of turbulence and the benefits of fast steering.

b. Preparation of Turbulence Generator, Optics, and Tracker

(1) Turbulence Generator. Figures 21 and 22 indicate the position at which the turbulence generator is introduced into the optical path. As already mentioned, the maximum laser-beam diameter available at that point is 23 mm. The turbulence generator is designed to accommodate a beam of that size. Figure 25 is a longitudinal cross section of the turbulence generator in a plane perpendicular to the laser beam axis. Compressed air from a pressure regulator is admitted to the plenum chamber from the left. The ends of the chamber are closed so that the air flows out through the slit orifice at the right. The orifice opening is adjusted by tightening or loosening the through-bolt, as shown in Figure 25. In most tests, an orifice opening of 0.33 mm (as measured by means of a feeler gauge) was used, although openings up to 1.25 mm were used in initial experiments. The length of the orifice is 6.3 cm. Air from the orifice passes over the solenoidal heater coil and then expands to fill the flow expansion chamber before passing across the laser beam.

The optical inhomogeneity at the laser-beam cross section is caused by a combination of the effects of turbulence generated by air flow through the orifice and by convection currents resulting from the heater action. Each of these effects could easily be seen separately by observing tracking error signals with only one or the other of the turbulence sources active. However, as expected, none of these sources by itself produced a satisfactory turbulence effect. With heat alone, the magnitude of beam wander was great enough, but the beam motion was characterized by large and often sudden

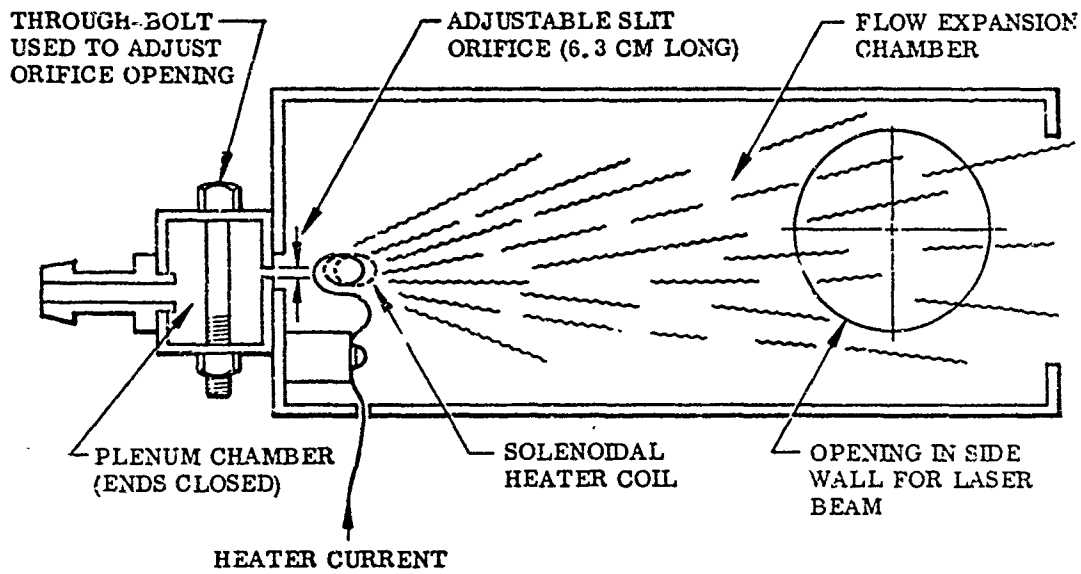
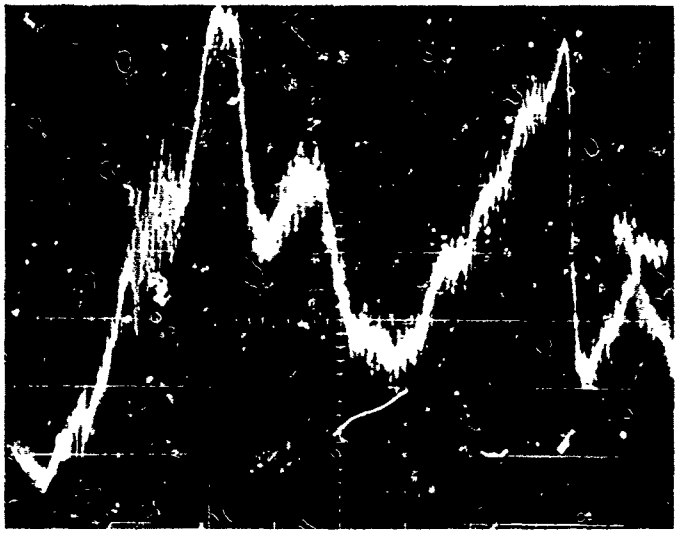


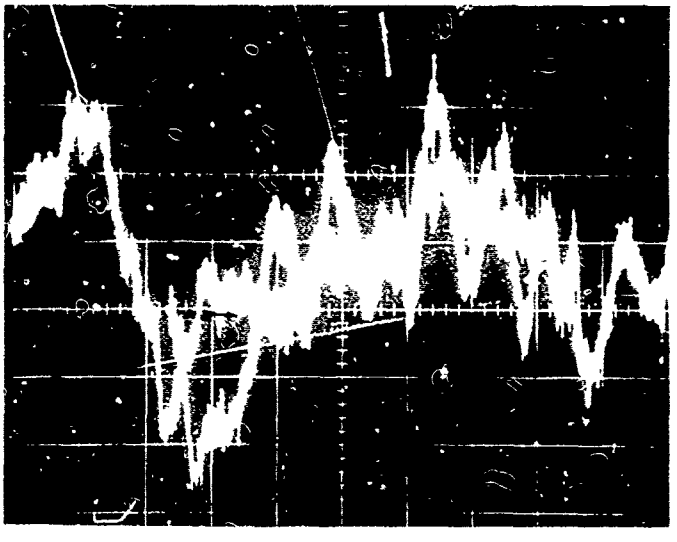
Figure 25 Longitudinal Cross Section of Turbulence Generator

transitions of the type appearing in Figure 26 (a), which is an oscilloscope trace of the tracker horizontal channel output (error) signal. The large transitions are believed to be due primarily to convection currents caused by the heater, although some flow turbulence effect also was present. However, the latter effect was small because the air pressure was low and the orifice gap was at its widest. Figure 26 (b) shows the effect of narrowing the orifice to 0.33 mm and increasing the plenum air pressure to 0.1 lb/in.^{2}. Power input to the heater was 15 W. The latter case, although still exhibiting convection effects, also shows considerable fine structure, which is indicative of high-frequency fluctuations. The latter set of conditions was used throughout the test program, unless otherwise noted, and is referred to as the "standard condition."

Thus far, the turbulence condition has been described only in a qualitative way; in fact, it was not intended that any characterization in terms of fundamental turbulence parameters would be attempted. Rather, the turbulence condition was to be described in terms of its effect in perturbing laser-beam direction and in causing beam-intensity fluctuations. The quantitative measurement made to characterize turbulence in the latter sense are presented in the following sections. Specifically, the rms angle deviation and the power spectral density of the angle fluctuations, as sensed by the image dissector tracker, are measured, as are the intensity variance and power spectral density of the beam transmitted through the turbulence and detected by means of a pinhole detector.



(a)



(b)

Figure 26 Oscilloscope Traces of Tracker Horizontal Channel Output Showing Effect of Simulated Turbulence – (a) Low-Strength Air Turbulence, (b) Higher-Strength Air Turbulence (Convection Effects Due to Heater Element Present in Both Cases)

(2) Optics and Tracker Preparation. Because the purpose of the tests was to determine how well fast tracking can reduce pointing errors due to atmospheric turbulence, and the associated signal fading, it was essential that the contributions from all sources of pointing error other than the turbulence generator be small. These extraneous sources include:

- Ambient light impinging on the detectors
- Air turbulence outside of turbulence generator
- Effects of mechanical or acoustical vibrations
- Boresight shifts between the tracker and the pointing laser
- Noise in the pointing laser or the detector

Fortunately, all of these sources had been brought under close control by the extensive effort applied in the preparation for the acquisition and tracking tests, and further relevant system improvement was not required. With regard to the tracking tests, optimum tracking accuracy was obtained by using as high a laser power as possible while remaining within the linear range of the pointing detector.

Prior to the performance of the tests, preliminary checkout and alignment were accomplished as follows:

- Verification that the beams were collimated and co-linear between the terminals and that the detector lenses were properly focused to insure that angle error signals were indicative solely of angular rather than translational beam motion
- Centering of detectors relative to the received beams
- Verification that the fine steering mirror drives were functioning
- Verification that image dissector acquisition and tracking circuits were operative
- Calibration of angle detectors by inserting a sequence of thin prisms (optical wedges) into beam and observing the error signals produced

Detailed descriptions of the methods used for carrying out the foregoing preparatory alignment and checkout tests are contained in Reference 7 and need not be repeated here.

One special adjustment made in these tests that was not required in the evaluation tests was to use a beacon laser-beam diameter of 6 mm, the same as that used for the pointing beam. This adjustment was necessary in order that the basic condition for reciprocity be satisfied, namely that the tracker, and the transmitter beam pointing controlled

by the tracker (the pointing laser), effectively share a common aperture. Since it was inconvenient to place an aperture in the optics shared by the tracker and the pointing laser, an equivalent effect was obtained by making the beacon transmitter aperture the same diameter as that of the pointing laser. This ensured that the tracker would "see" the effects of turbulence only over the same volume that would affect the pointing laser.[11]

The waveforms shown in Figure 26 represent fluctuations in the wave-front direction of the beacon laser beam at the tracker. According to reciprocity theory, the beam of the simulated communication transmitter (pointing laser) undergoes similar perturbations in passing through the turbulence region. Therefore, when the beam is detected by the communication receiver, fluctuations in instantaneous received signal strength are expected. Figure 27 is a sample of a chart recording of the signal received through a 25-μm pinhole simulating the aperture of a receiver in the far field of the transmitter. Turbulence conditions were the same as those for Figure 26 (a). The transmitter beam was focused at the pinhole plane, and had a diameter of 100 μm, as measured by the diameter of the first Airy dark ring. Qualitatively, the signal fading obviously is severe. Further discussion of the significance of the fading will be deferred until a later section in this report where a quantitative measure of fading strength is presented.

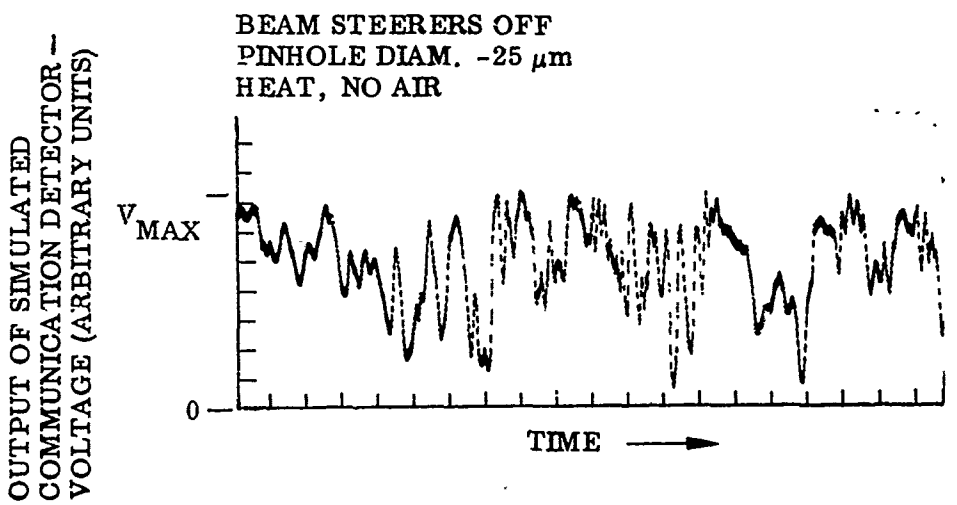


Figure 27 Received Signal Intensity Fluctuations Due to Simulated Turbulence – Beam Steerers Off

[11] In the case of a ground-to-space link, the common aperture would have to be located at the transmitter-tracker end, rather than at the beacon end, in order to satisfy the requirements of reciprocity theory. In the case of this experiment, however, it was permissible to place the common aperture at the opposite end because of the collimated beam condition in the turbulence region.

c. Turbulence Effect – Fast Beam Steerers Off

In this section, the main emphasis is placed on further defining the simulated atmospheric turbulence condition in terms of its effect in causing fluctuations of laser beam direction. In the previous section, the nature of the time-variation of beacon beam direction, as sensed by the tracker, has already been discussed. In order to obtain a more definitive description of this fluctuation process, as illustrated by Figure 26, the related power spectral density was measured by means of a Hewlett Packard Model 5452A Digital Fourier Analyzer. (See Section II, 4, d. for a description of the Fourier Analyzer operation.)

Figure 28 (a) shows the measured power spectral density of the tracker vertical channel output when only heat was used to produce turbulence, i.e., approximately the same conditions as those represented by Figure 26 (a). The abscissa is a logarithmic frequency scale (f_{max} = 1 kHz, 2 divisions/decade) and the vertical scale represents power spectral density in dB units (5 dB/division). The full-scale decibel value (-30 dB) is not of immediate significance but is needed later to allow comparison among related spectrum plots. It is evident that the spectrum peak is at some frequency below ~2 Hz, the lowest frequency represented. Also, it is seen that the power density drops rapidly above a few Hz. The plateau region extending from about 30 to above 300 Hz is due to noise at the tracker output caused primarily by photocurrent shot noise. It should be noted that the noise power density is at least 30 dB (1000 to 1) below the low-frequency peak. The spectrum shown in Figure 28 (b) results from adding turbulent air flow, that is, the same conditions as for Figure 26 (b). Now at this point, the spectrum peak is above 10 Hz, and significant fluctuation components are present at least to 100 Hz.

In addition to measuring the power spectrum of beam angle fluctuation, the rms output of the tracker vertical and horizontal channels was measured by means of an rms voltmeter (Ballantine Laboratories, Inc., Model 320). The rms reading was then converted to equivalent rms beam direction fluctuation by multiplying the voltmeter reading by the sensitivity factor of the tracker, which was 0.055 mrad/mV. The indicated value of beam direction fluctuation was 14 μrad rms. Similar measurements of power spectral density and rms direction fluctuation were made for the tracker horizontal channel output. As the results were virtually identical to those for the vertical channel, they have not been shown.

d. Reduction of Turbulence Effect by Fast-Beam Steering

(1) Tracking and Beam-Pointing Errors. The effectiveness of the fast-beam steerers in reducing turbulence effects will be detailed in this section, first with reference to the beacon beam direction fluctuations, as indicated by the tracker output or "error" signals, and with reference to the angle fluctuations of the transmitter beam as indicated by the output of the pointing error detector. The reduction in received signal intensity fluctuations obtained by activating the fast beam steerers will be described in the next section.

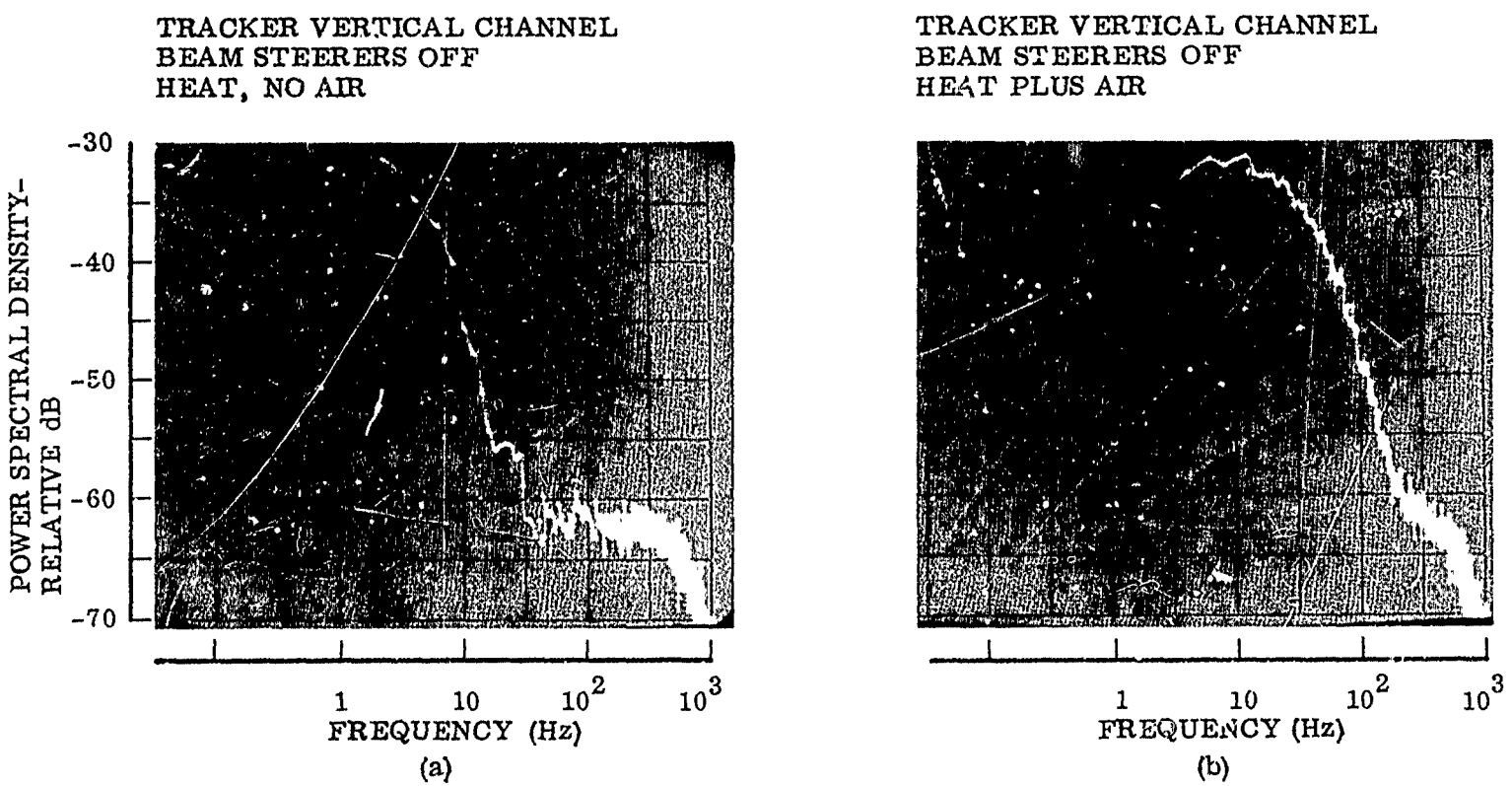


Figure 28 Power Spectral Density of Indicated Beacon Direction Fluctuations Caused by Simulated Atmospheric Turbulence (Beam Steerers Off) – (a) Heat Input to Turbulence Generator, (b) Heat Plus Air Input

Figure 29 demonstrates the reduction in random pointing jitter of the beacon laser beam and of the communication (pointing) laser beam that was realized when the fast-beam steerers were energized. The traces at the left are the error signals produced in the horizontal channels of the pointing and tracking detectors (upper pair) and the vertical channels (lower pair) by the standard turbulence condition when the beam steerers are inactive. Activating the fast steerers, without any other change, produced the traces at the right. It is seen that a very substantial reduction in the indicated pointing and tracking errors is obtained in each channel shown in Figure 29.

Power spectra of the vertical channel signals from the tracking and pointing detectors are shown in Figures 30 and 31. Here the spectral plots produced by the Fourier Analyzer for the two conditions – fast steerers off and on – have been traced to allow them to be superimposed. It is seen that activation of the fast-beam steerers has two effects – it reduces the peak spectral density of the error signal, and it moves the peak of the curve from about 10 Hz to the vicinity of 50 Hz. Further, activation of the fast beam steerers did not reduce the tracking and pointing errors at all frequencies. Above about 100 Hz, the errors are somewhat increased.

Because of the shift in the peak of the spectra toward higher frequencies, and the actual increase in high-frequency tracking errors, when the beam steerers are activated, the reduction in rms (total) pointing and tracking errors is not as great as the reduction in peak spectral density. Table 3 presents a summary of the measurement results.

Table 3. Summary of Measurement Results

Beam	Channel	Reduction of RMS Angle Error
Beacon	Horizontal	3.57 (11.1 dB)
Beacon	Vertical	4.16 (12.4 dB)
Communication	Horizontal	2.33 (7.4 dB)
Communication	Vertical	3.50 (10.9 dB)

(2) Intensity Fluctuations at Receiving Detector. Figure 21 shows the intensity detector that simulates the communication detector as being operative simultaneously with the pointing (angle error) detector. The system was diagrammed in that way for simplicity in description but, in actuality, the intensity detector was not in place initially, and was substituted for the pointing detector after completion of the angle error measurements. In view of the substantial reduction in angle error due to turbulence, obtained when the beam steerers were activated, it was confidently expected that a similar reduction in intensity variation would be observed. Initially, however, this was not the case. At most, reductions of only a few decibels in the total intensity variance were obtained, and correspondingly small reductions in power spectral density of the intensity fluctuations were observed.

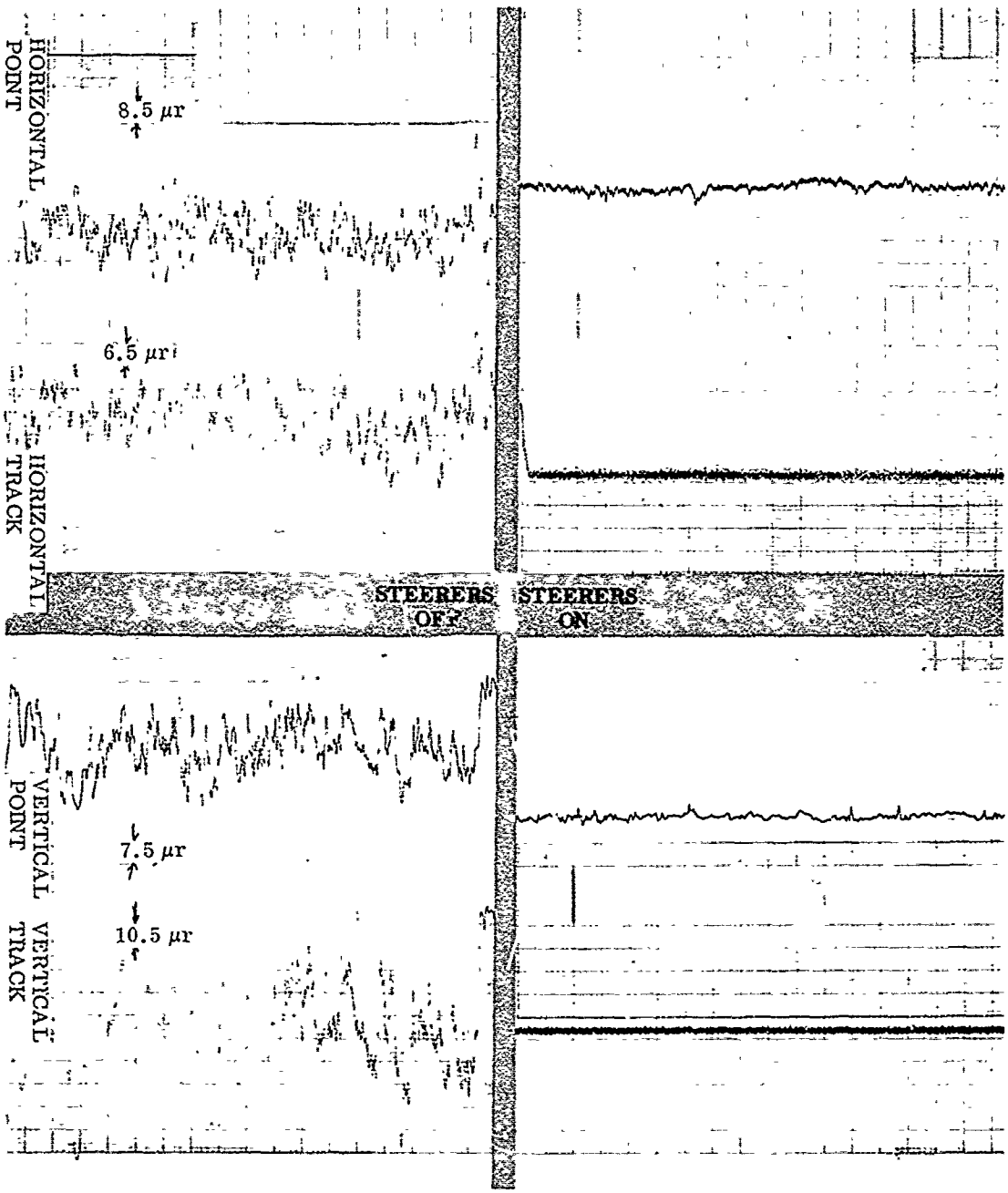


Figure 29 Pointing and Tracking Detector Outputs With Simulated Atmospheric Turbulence – (a) Beam Steerers Off, (b) Beam Steerers On

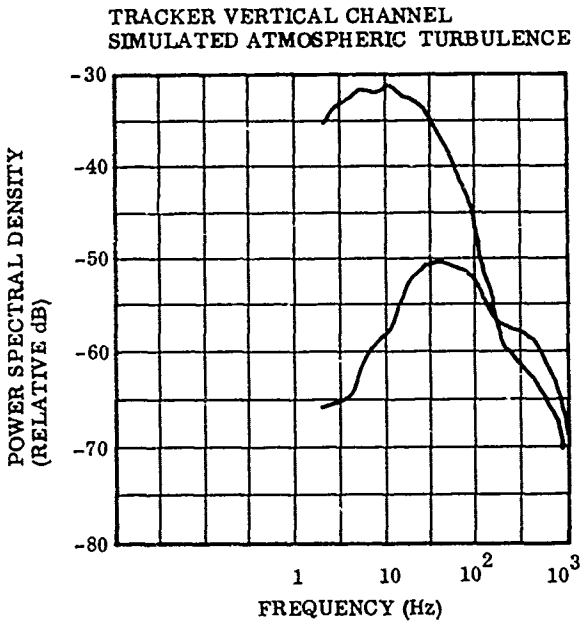


Figure 30 Comparison of Power Spectra of Tracker Vertical-Channel Error Signals With Beam Steerers Off (Upper Trace) and On (Lower Trace)

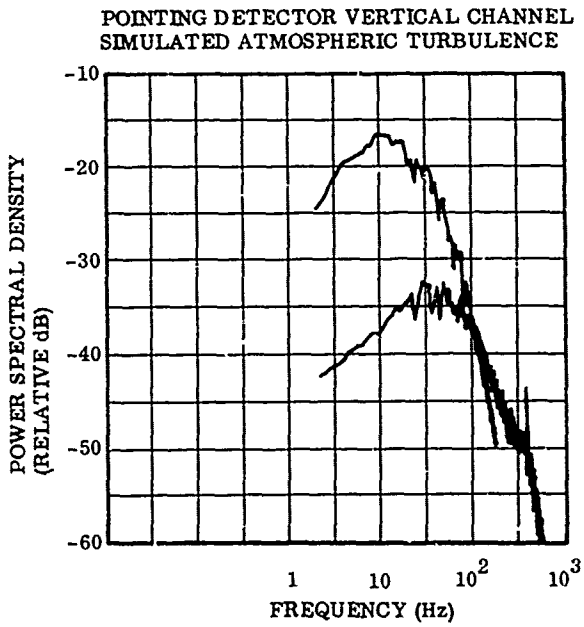


Figure 31 Comparison of Power Spectra of Pointing Detector Vertical-Channel Angle Error Signals With Beam Steerers Off (Upper Trace) and On (Lower Trace)

After careful realignment and readjustment of the optical system failed to correct the problem, it was decided that a critical examination should be made of the quality of the beam focus at both the tracking detector and the intensity detector. For this purpose, an alignment telescope and a microscope were used, respectively, to produce enlarged images of the collimated beams or focal spots at various points in the system. These tests indicated that beam quality was being affected adversely by several components, notably the principal beamsplitters at each of the link terminals, and the beam-converging lens ahead of the intensity detector. Once these deficient components were identified, high quality components were procured and substituted, and the system was readjusted and realigned.

After these improvements were completed, the system was again tested, using the standard turbulence conditions described earlier (heat plus air) in Section III,4,b,(1) and greatly improved performance was obtained. Figure 32 shows the effectiveness of fast beam steering under these new conditions in reducing intensity fluctuations at the receiving detector caused by simulated turbulence. In this test, a 25-μm-diam. pinhole was located just in front of the intensity photodetector. As indicated, fading of the downward signal to one-half of the maximum signal level (V_{max}) or below occurs quite frequently when the beam steerers are off (left). With the beam steerers on (right) the depth of fading is reduced markedly.

The power spectral density of the signals represented in Figure 32 was determined by means of the Fourier Analyzer and is shown in Figure 33. There, the original CRT display photographs have been traced to allow display of the two spectra on a single graph for comparison. Similar tracings in Figure 34 show the reduction in intensity fluctuation observed when the detector pinhole was 10 μm.[12]

For both pinhole sizes, activation of the beam steerers reduced the peak spectral density and shifted the peak toward higher frequency, much as in the case of tracking and pointing error signals (Figures 30 and 31, respectively). The measured rms values of intensity fluctuation (expressed as a fraction of mean intensity) for the two conditions – beam steerers off and beam steerers on – are given in Table 4. Also shown are reductions in intensity variance obtained by activating the beam steerers.

Table 4. Intensity Detector Output Fluctuation Magnitude and Variance Reduction with Beam Steering

Detector Pinhole Diameter (μm)	RMS Intensity Fluctuation / Mean Intensity		Intensity Variance Reduction (dB)
	Beam Steerers Off	Beam Steerers On	
25	0.072	0.0055	23.2
10	0.047	0.0055	18.7

[12]The spectra of Figure 33 cannot be compared with those of Figure 34 as to absolute level because of the change in signal level associated with the change of pinhole size.

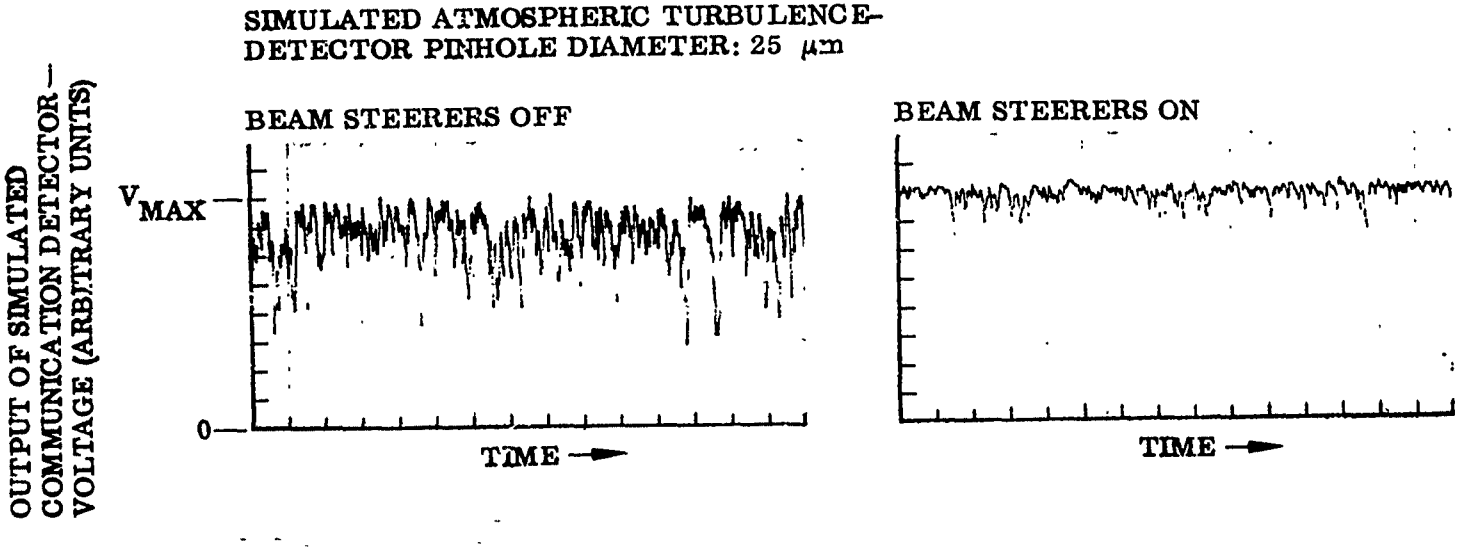


Figure 32 Output Fluctuations of Intensity Detector Communication Receiver Due to Simulated Atmospheric Turbulence – (a) Beam Steerers Off, (b) Beam Steerers On

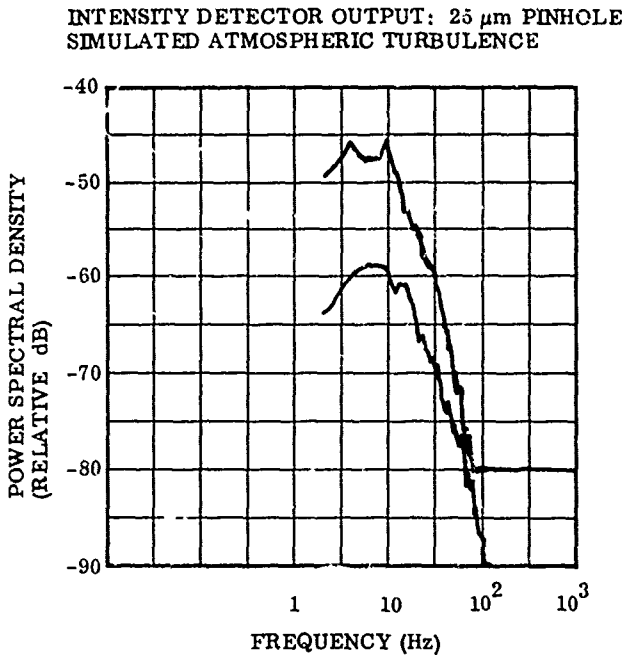


Figure 33 Intensity Detector Output Signal Power Spectra – Beam Steerers Off (Upper Trace), Beam Steerers On (Lower Trace); 25-μm Pinhole

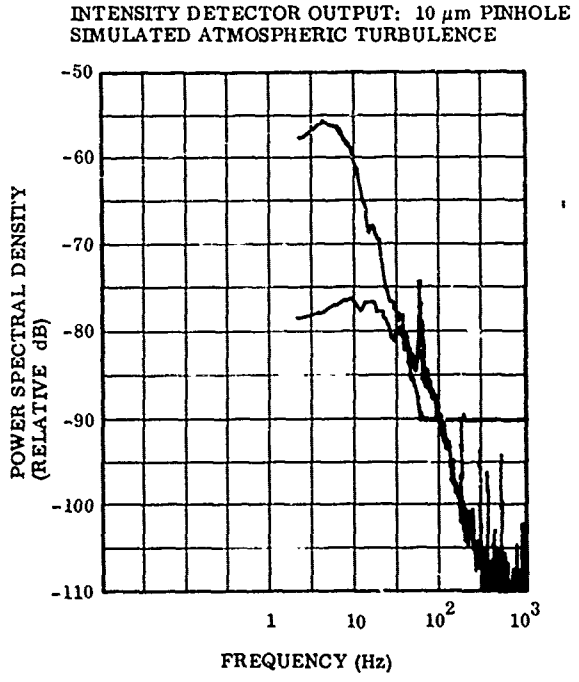


Figure 34 Intensity Detector Output Signal Power Spectra – Beam Steerers Off (Upper Trace), Beam Steerers On (Lower Trace); 10-μm Pinhole

Comparing the reduction factors in this table with those in Table 3 for the pointing and tracking detectors, it is seen that greater reductions in variance are obtained in the intensity detector case.

e. Turbulence Effect on Frequency Response of Fast Tracking Loop

When the beacon beam quality (direction and wave-front uniformity) is perturbed by turbulence, the focal spot at the tracking photodetector pinhole is also perturbed to the extent that the fast steerers fail to counteract the turbulence effect. It is conceivable, therefore, that the focal spot will be randomly deflected away from the tracking detector pinhole, or simply defocused, with a consequent loss of signal strength. This in turn could cause a change in tracker sensitivity with a corresponding change of the beam steering loop bandwidth.[13]

In order to determine whether turbulence causes any such effect, the frequency response of the steering servo loop was measured. With reference to Figure 35, a sinusoidal test signal was introduced into the inner fine steering loop at the point shown, and the signal appearing at the test point was measured after transmission around the loop. The ratio of the latter signal (output) to the input signal at a given test signal frequency is the desired measure of beam-steering loop servo gain.

When frequency was varied over the range from 0.1 to 600 Hz, the response was constant up to frequencies somewhat above 100 Hz. At still higher frequencies, the response dropped rapidly, reaching -3 dB (0.707 relative amplitude) at 340 Hz for the horizontal channel and 270 Hz for the vertical channel. These frequencies are taken as the measure of beam-steerer servo bandwidth.

To determine whether servo bandwidth was affected by turbulence, similar measurements were made with the turbulence generator both on and off. No change in bandwidth between the two conditions was detected. It is therefore concluded that turbulence does not have any effect on beam-steerer servo bandwidth, at least up to level of turbulence used in these experiments.

f. Effect of Aperture Size on Fading Reduction by Fast Tracking

In Reference 1 (Appendix L) it was predicted theoretically that the reduction in intensity variance obtainable with a fast-tracking/fast-steering transmitter would vary as a function of the ratio of transmitter (and tracker) aperture size D to a quantity r_o that characterizes the strength of optical inhomogeneity. In particular, as discussed more fully later in this report (Section IV, 1, b), there is a value of aperture diameter beyond which the intensity variance begins to increase rapidly. This value is given by $D \simeq 1.5\ r_o$.

[13] It is a characteristic of a servo system that the effective servo bandwidth is directly related to the gain of the servo loop.

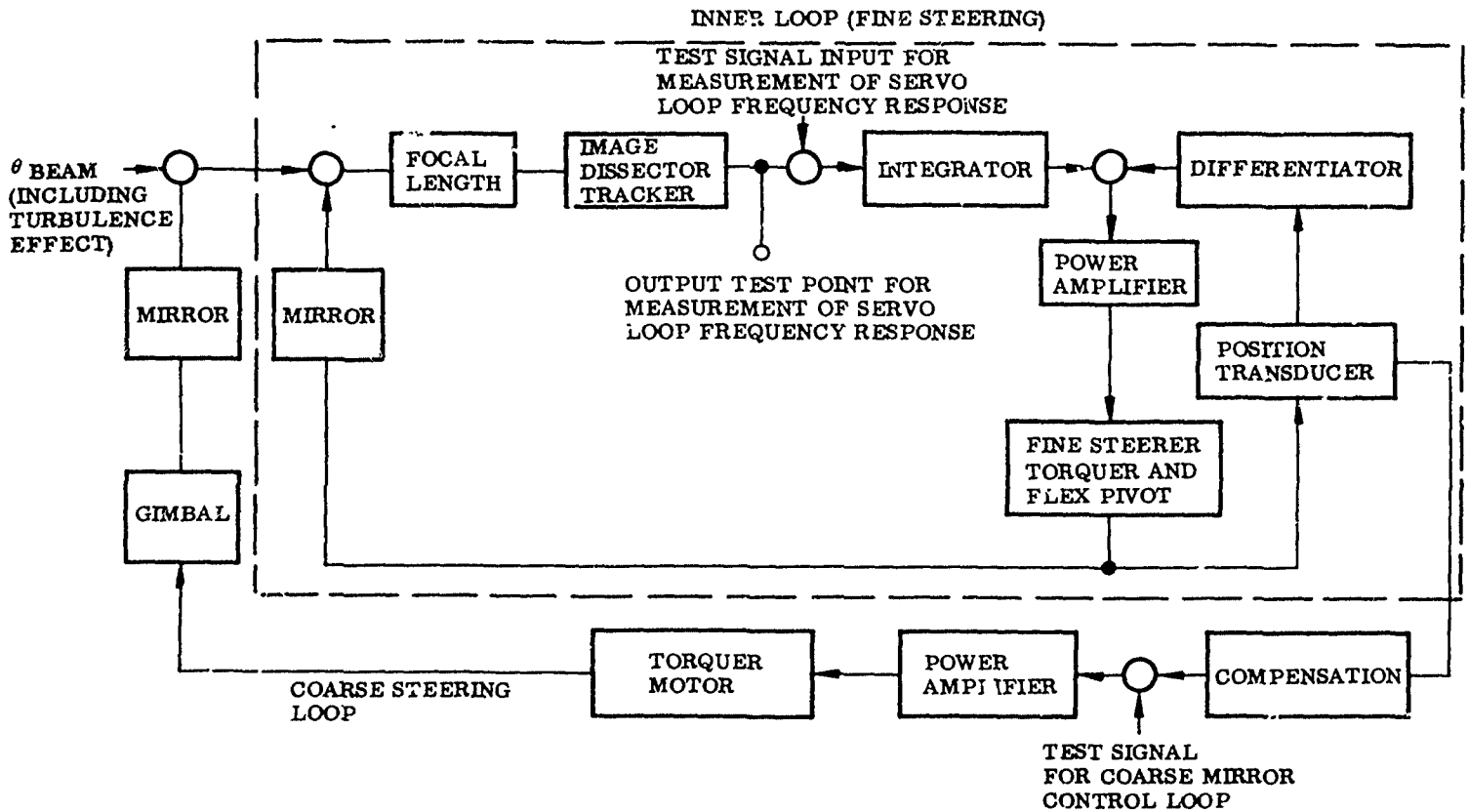


Figure 35 Component Relationships in Tracking and Beam Steering System – With Only Portion of System Within Dashed Line Active in Fast-Tracking Experiment

It was intended, as part of this experiment, to vary the diameter of the transmitter/tracker aperture in an attempt to determine the validity of the predicted dependence of intensity variance on aperture diameter. However, this test was not accomplished for the following reasons:

- The availability of the test system for this program was severely limited because of the high priority of the Acquisition and Tracking System Evaluation Program.
- The period scheduled for the test of aperture size effect was consumed in making the optics refinements found necessary in order to complete the test of fading reduction by fast tracking, the primary objective of that experiment. (See Section III, 4, d.)

Since predicted dependence of intensity variance on aperture size has not been verified experimentally, it is pertinent to mention that an independent theoretical analysis of the action of a fast-steering transmitter, also based on the concept of reciprocity, has recently been reported and the predictions of that theory are consistent, at least in a qualitative sense, with the previously developed theory that formed the basis for the concept of a fast-tracking transmitter as studied in this program. (See Reference 8.)

g. Boresight Tolerance

An underlying assumption of the fast-tracking/fast-steering concept is that the transmitter be accurately boresighted to the tracking receiver. In other words, disregarding point-ahead correction, when the receiving detector is tracking an incoming plane wave beam and the fast beam steerers have been positioned by servo action to minimize angle errors at the tracking detector, then alignment of the transmitting optics will be such that the transmitted beam axis is co-linear with that of the incoming beam. If this condition is not satisfied, then the transmitter signal strength at the other (communication receiver) end of the link will not, on average, be maximal. Even worse, random tracking errors due to turbulence that tend to deflect the transmitter beam farther away from the receiver than its mean position will produce exaggerated fading (as compared to a boresighted beam) because of the steepness of the sides of the transmitter beam pattern. However, the basic action of the fast beam steerers is to position the received beacon beam at the tracking detector so as to maximize the average received signal strength, and at the same time to minimize fluctuations of signal strength at that detector. Boresight misalignment therefore tends to increase signal fluctuation strength at the receiver end of the link relative to the signal fluctuation strength at the transmitter (tracker) end.

On the other hand, if the boresight condition is satisfied, reciprocity theory states that fluctuations seen at one end of the link will be duplicated at the other end; that is, signals at the two ends of the link will be highly correlated. Conversely, in view of the discussion of the previous paragraph, boresight misalignment will degrade correlation. Therefore, correlation of the two signals is a direct and pertinent measure of boresight accuracy.

The question now remains as to what constitutes an acceptably small boresight error. In Appendix IV, the correlation of intensity fluctuations is calculated as a function of boresight error using an approach based on reciprocity theory. One of the principal results of that calculation, applicable to the fast-tracking transmitter, is presented in Figure 36 where correlation C_T is plotted as a function of boresight error θ. Here θ is measured in units of transmitter beamwidth λ/D. It is seen, for example, that if the boresight error is less than 0.2 beamwidths, the correlation will be 95 percent or greater. If the boresight error can be kept that small, virtually all of the improvement in average transmitting antenna gain and reduction of up-link fading predicted for the fast tracking/fast steering technique will be realized.

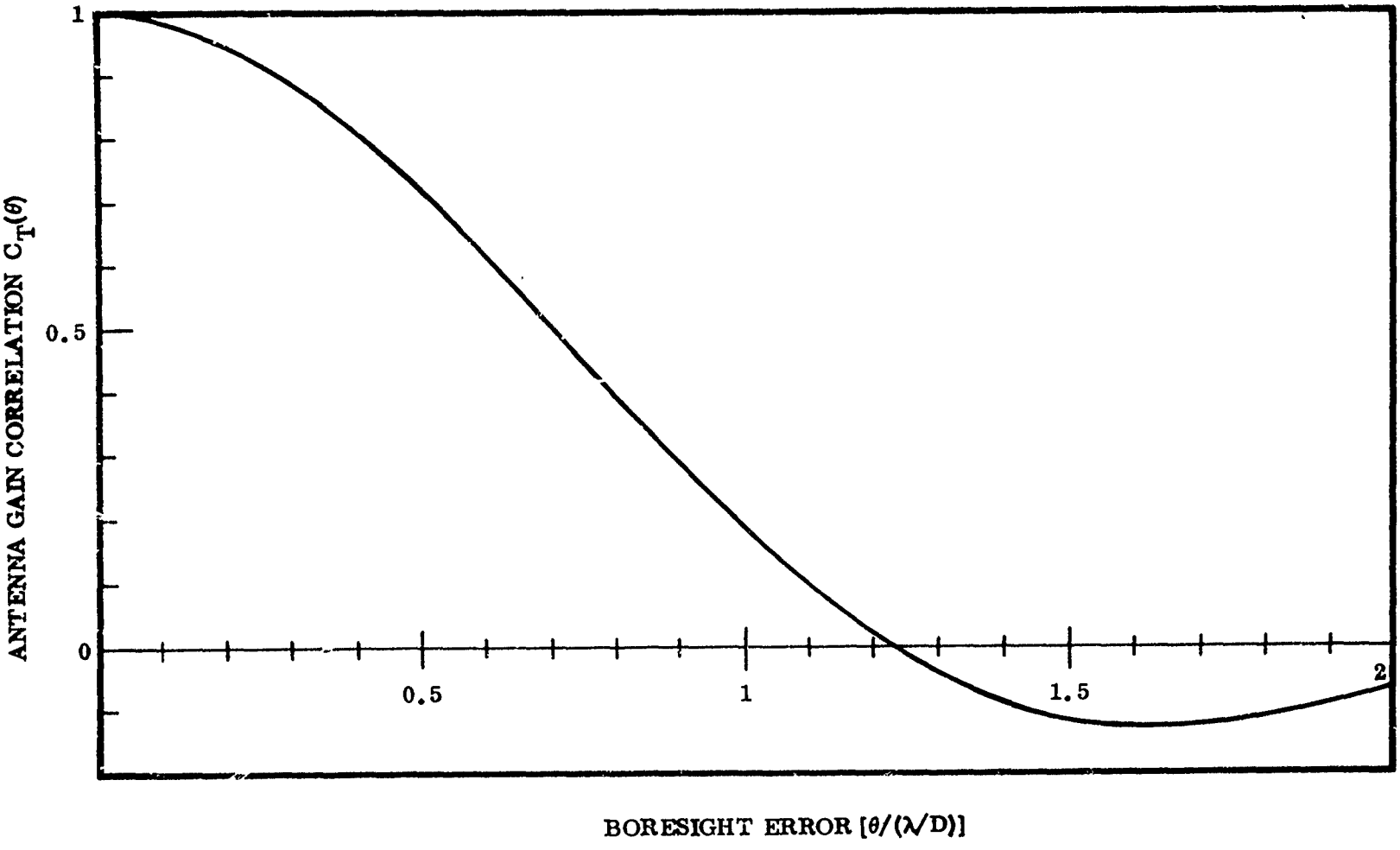


Figure 36 Antenna Gain Correlation $C_T(\theta)$ for a Tracking/Pointing System Employing Fast Beam Steering – Aperture Diameter: $D = 1.5r_d$

SECTION IV

ATMOSPHERIC TRANSMISSION MEASUREMENT SYSTEM DESIGN

1. GENERAL CONSIDERATIONS

In conjunction with the experimental and theoretical work performed during this program to establish the nature of the reciprocity phenomena, work has also been performed with the objective of exploiting reciprocity as a basis for a measurement program to determine the actual limitations on antenna gain set by atmospheric turbulence.[14] This work has concerned itself with defining the equipment necessary for such a measurement program, establishing the data recording and processing procedures for the experiment, and laying out a program plan and schedule. This section is devoted to a presentation of this work.

a. Summary Discussion of Atmospheric Turbulence Effects on Ground-To-Space Link Design

Atmospheric turbulence will affect the properties of a laser beam passing through the atmosphere by inducing wavefront distortions and intensity variations across the beam. In an up-link, i.e., from ground-to-space, the dominant effect is wave-front distortion which will cause the average antenna gain of the transmitter to be degraded. The laser beam wobbles (i.e., tilts) and spreads. Therefore, on average, less energy will be collected by the receiver at the space-end of the link. This is itself a significant degradation in link characteristics. In addition, it must be considered that not only does atmospheric turbulence reduce the average power that the receiver will collect, but it also makes the amount of power collected at any instant a random variable. This means that, in a data transmission link, there is a potential problem of fading and information dropout. To avoid this phenomenon, the fading must somehow be suppressed, or more laser power must be transmitted than would be needed with a non-fading signal of the same average power. Altogether, the atmospheric turbulence causes a reduction in effective antenna gain by reducing the average gain, and by requiring excess average power to be transmitted to accommodate fading.

Depending on the wavelength and aperture diameter of the transmitter, the strength of turbulence, and the zenith angle at which the transmitter is operating, the loss due to atmospheric turbulence can be quite severe. In general, the longer the wavelength and the smaller the transmitter aperture diameter, the less of a problem there will be

[14] The main importance of reciprocity remains the added 10-dB performance offered in an atmospheric-turbulence limited laser transmitter. In this effort, however, the purpose was to exploit one of the side benefits, namely, an opportunity to make simplified field measurements.

PRECEDING PAGE BLANK-NOT FILM

with atmospheric turbulence. The effect of turbulence on the antenna gain is determined in part by the quantity r_o, which has the dimensions of length, and is a function of the wavelength and of the integrated optical strength of turbulence along the propagation path. This parameter is a measure of the amount of wave-front distortion caused by the turbulence. (See Reference 1, Appendix M). If the transmitter antenna diameter D is much less than r_o, atmospheric turbulence will have virtually no effect on the antenna gain. If the diameter D is less than but comparable to r_o, then turbulence effects will be noticeable, slightly in terms of average antenna gain and more substantially in terms of antenna gain fading. If the diameter D is comparable to but larger than r_o, the atmospheric turbulence will significantly degrade the average antenna gain and, more importantly, introduce very large and quite unacceptable antenna gain fading. For transmitter antenna diameter D very much larger than r_o, the average antenna gain will be limited by atmospheric turbulence to a value about equal to what a diameter equal to r_o would yield in free space propagation, quite independent of the actual value of D. Moreover, the antenna gain fading with such a large diameter will be so severe as to render any hope of transmitting useful amounts of information entirely outside the realm of possibility.

In discussing the effect of atmospheric turbulence on a laser beam, brief reference was made previously to the fact that part of the beam spreading produced by atmospheric turbulence corresponded to a wobbling or tilting of the beam. On an average, this spreads the beam but, at any instant, it only tilts the beam. If the laser transmitter is designed, using reciprocity, to take advantage of the possibility of compensating for this tilt by fast-pointing adjustment, then about three times as large an antenna could be used compared to that possible with a static slow tracking system, before turbulence effects on the effective antenna gain (taking into account both fading and average gain) become significant (Reference 1, Appendix M). Analysis indicates that while a static laser transmitter will have the maximum possible effective antenna gain when its diameter is about $0.5\ r_o$, a fast-pointing laser transmitter will achieve its optimum performance when its diameter is about $1.5\ r_o$. There is about a 10-dB improvement in effective antenna gain to be obtained by using fast pointing. Even with fast pointing, however, the best possible effective antenna gain is only about equal to what an ordinary laser transmitter of diameter r_o would achieve in free space propagation.

b. Need for Atmospheric Transmission Measurements for Ground-To-Space Link Design

Probably the most significant area of uncertainty in attempting to estimate the effect of atmospheric turbulence on a laser ground-to-space link is the lack of adequate data on the value of r_o. Some data, based on estimates of the vertical distribution of the optical strength of atmospheric turbulence, are available, and there are some other data based on astronomical observations. (See Reference 1, Appendix M.) However, the data computed from estimates of the vertical distribution of the strength of turbulence are at best questionable, while those derived from astronomical observations are limited to night-time, and to special sites only.

It would be desirable to have a more extensive and reliable data base for values of r_o as a function of location, time of day and year, and climatic conditions for use in estimating link performance and in defining link design parameters. Analysis of expected performance of a laser ground-to-space link performed on the Space Data Relay Subsystem program (Reference 1) showed that if nominal values are assumed for r_o, in

general agreement with estimates developed under the program, the desired link characteristics could, for most conditions, be achieved with a portable ground laser transmitter terminal, by making use of reciprocity and the fast-pointing laser transmitter concept. The margin was not wide, however, and to achieve the desired performance, it was necessary to introduce the complexity not only of fast-pointing but also of four parallel but independent transmitter units, each with its own fast pointing.

In view of the lack of a firm data base for r_o , and considering the implications of different values of r_o relevant to achieving the required link performance within practical constraints on the ground station, it would seem critical that more complete and reliable data for r_o should be obtained. Data that is reliable in nature and that covers a wide variety of locations and conditions are needed. On the basis of such data, it would then be possible to specify more reliably the performance to be expected from a ground-to-space laser data link and to design the ground terminal to ensure this performance within required reliability limits. (The reliability aspect of the question depends on obtaining valid statistics for the occurrence of various values of r_o.)

In addition to obtaining data on r_o , it would be desirable to obtain data on the frequencies associated with laser beam tilt so that the servo system for a fast pointing laser transmitter can be properly designed. At present, only very rough estimates of the frequencies associated with this phenomena are available. It would be desirable to obtain experimental data on this subject as an aid in later system design.

As mentioned above, about 10-dB better performance is expected from a fast pointing laser transmitter than from a static unit. It would be desirable to obtain experimental measurement of the expected performance of a laser transmitter in each mode of operation, not merely to confirm the expected 10-dB improvement, but also to yield a clear and unambiguous measure of the level of system performance that can be achieved in practice.

c. Advantages of Approach Based on Star Image Sensing

In order to obtain the desired data base just discussed, consideration has been given to the use of a star image sensor (SIS) based on the use of an image dissector tube. This sensor is described in Section IV, 2.

Making use of the reciprocity concept as developed in Section II, it follows that measurement of the performance of diffraction-limited optics looking at starlight coming down to a ground-based telescope can be directly equated with the performance of a ground-to-space laser transmitter along the same path. By using a tracking image-dissector in the focal plane of diffraction limited optics (with the image dissector aperture smaller than the Airy disk), and measuring signal strength and tracking voltages as the telescope diameter is varied with an iris, all of the desired data can be obtained. Interestingly, the data produced in this manner are almost directly interpretable, and not subject to any of the possible inaccuracies of most of optical propagation theory for random media.

Specifically, the following quantities relating to up-link performance can be directly determined:

- Wavefront coherence parameter r_o
- Average antenna gain and gain variance for any antenna diameter up to 8-in.
- Optimum antenna aperture size
- Optimum tracking loop bandwidth and gain
- Antenna gain probability distribution and fluctuation spectrum
- Pointing error variance and fluctuation spectrum

The basic measurement for determining r_o consists of varying the aperture diameter and observing how the signal strength varies. A plot of signal strength versus diameter should show a break from a fourth-power dependence at small diameters to second power at large diameters, with the knee of the curve at a diameter r_o . Measurements of average signal strength when (1) the image dissector tracking servo is fully operational with a wide servo bandwidth, or (2) the bandwidth is reduced to about 1 Hz, should show the expected 10-dB difference in performance (at optimum aperture sizes) expected from used of fast pointing. Measurements of average signal strength with various servo bandwidths will indicate without ambiguity the required servo bandwidth to achieve, say, 90 percent of the full potential of the fast-pointing concept. Much the same data can also be obtained by measuring the servo voltage power spectrum. The fluctuation statistics of the detected signal strength can be measured and correlated with telescope aperture diameter to check predictions of fading statistics, for both static and fast pointing (in this case, of course, fast tracking). More important, however, is the fact that, whether or not measured fluctuation statistics confirm theoretical predictions, they are useful in their own right. Based on the fluctuation statistics observed, the extent of the potential antenna gain fading problem can be determined.

Three features of the star image sensor (SIS), particularly deserve comment. First, because of its very small instantaneous field-of-view, the unit can function just about as well during daytime as during the night (except that it will take somewhat longer for initial acquisition of the target star during daylight hours). This means that both day and nighttime data can be obtained.

Second, the unit allows a single-ended link experiment. Since the star is available without cost and does not require maintenance, the experiment would be rather easy to perform, requiring only a few people, perhaps as few as two persons, during the data taking; this facilitates planning for many continuous hours of data gathering. A small crew could, over a period of several weeks, obtain as much as a few hundred hours of data at quite low operational cost. The actual amount of data taken would be limited mostly by such practical considerations as recording tape length and data handling. This ensures that adequate statistical coverage of the subject can be obtained.

The third feature of the SIS is the relative ease of being transported to and set up at various sites, including mountain-top observatory sites, if desired. This means data on atmospheric turbulence effects at a variety of sites can be obtained. The only limit on the number of sites surveyed will be the duration of the measurement program, and the amount of time it is desired to spend at each site.

It is worth noting that, beyond its use as a data gathering unit prior to detailed design of the ground laser transmitter, the SIS may prove to be useful as a diagnostic instrument during the shake-down phase of operation of the laser ground-to-space communications link. However, this potential application is beyond the scope of the present program.

d. Overall System Description and Operational Concept

(1) Measurement Equipment. The equipment required for the measurement program is depicted in Figure 37. The principal unit is a small (i.e., 16-in.-diam.) astronomical-quality telescope, modified by the addition of an image dissector that is servo-tracking-loop controlled at the telescope's focal plane. The telescope and operator console are enclosed in a portable observatory dome that can be disassembled. The telescope pier and dome base are cast concrete and are not portable. Their installation is part of site preparation. The telescope and dome are easily movable from one prepared site to another, as required. A trailer van will be used to house the data recording and preliminary processing equipment and will provide shelter for the field-site crew during data-acquisition periods. It will also supply space and suitable supports for use during transport of the disassembled telescope from one measurement site to another.

The tracking SIS will employ a modified cruciform pattern when the image dissector is in the tracking mode. This modified cruciform approach will provide for a portion of the total scan waveform during which there is zero a-c deflection, so that the star can be sampled without its image being modulated by the normal scan pattern. The background will be sampled during periods of time when the instantaneous field-of-view of the SIS is purposely scanned off the target. Provision for varying both the tracker bandwidth and sample time (i.e., the time when the a-c deflection scan voltage is zero) will be incorporated. The SIS will work with an external rather than an internal clock in order to provide synchronization between it and the data processing system. This is necessary in order to assure availability of data when required by the computer. The sensor in the SIS will be an F4012 image dissector which ITT Gilfillan has utilized in previously designed star trackers. The instantaneous aperture in the image dissector will be 0.0017 in. in radius. Optical magnification will be adjusted as the telescope primary aperture is varied so that the instantaneous aperture remains appreciably smaller than the star image size. In this way, the SIS will be able to measure the intensity at the center of the star image, this being the quantity that corresponds to up-link transmission, according to reciprocity theory.

The telescope will be a modification of a standard 16-in. Cassegrain system. Figure 38 is a photograph of the (unmodified) telescope selected. An effective telescope diameter of 8 inches, which will be the maximum aperture in this application, will be achieved

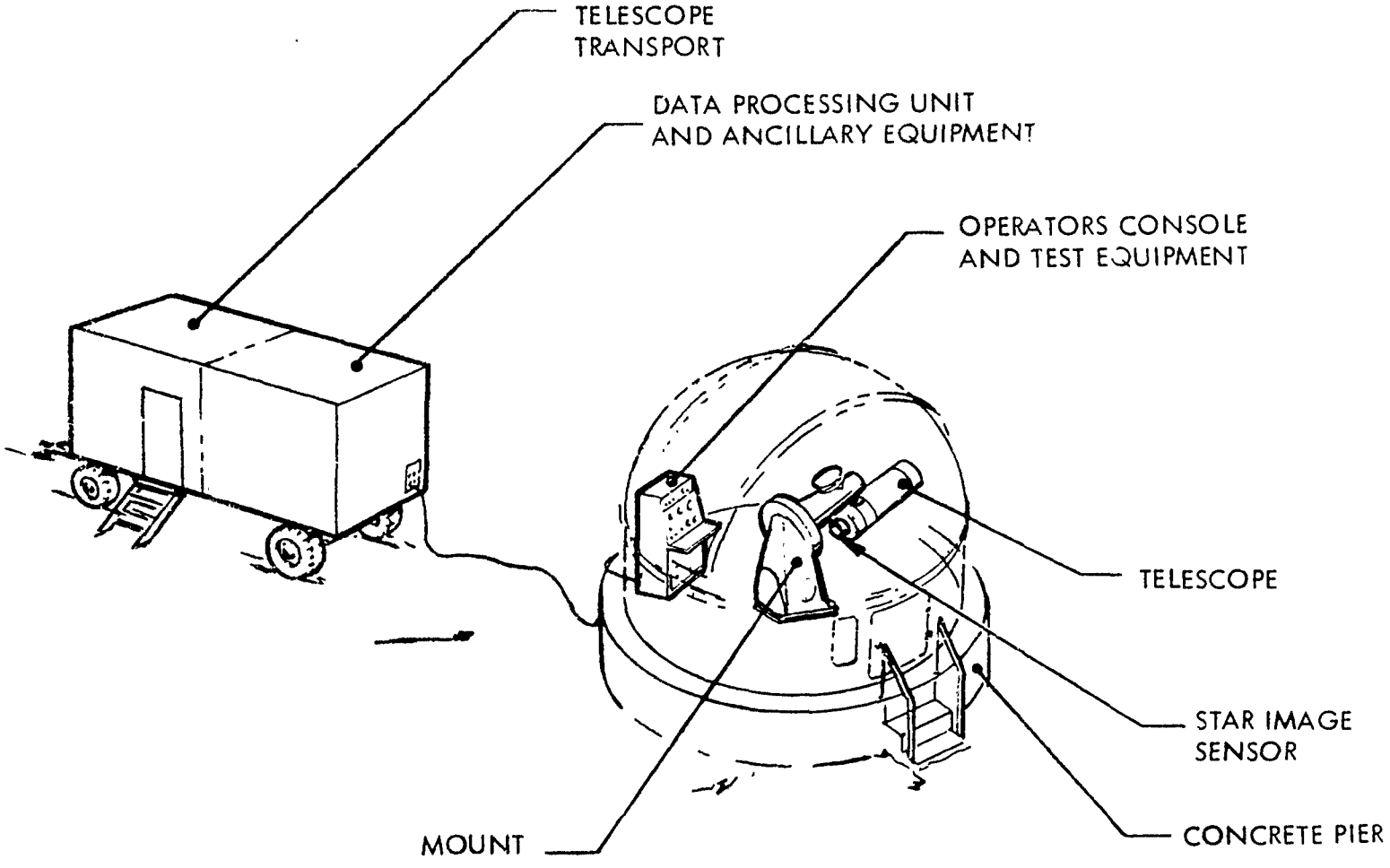


Figure 37 System Configuration

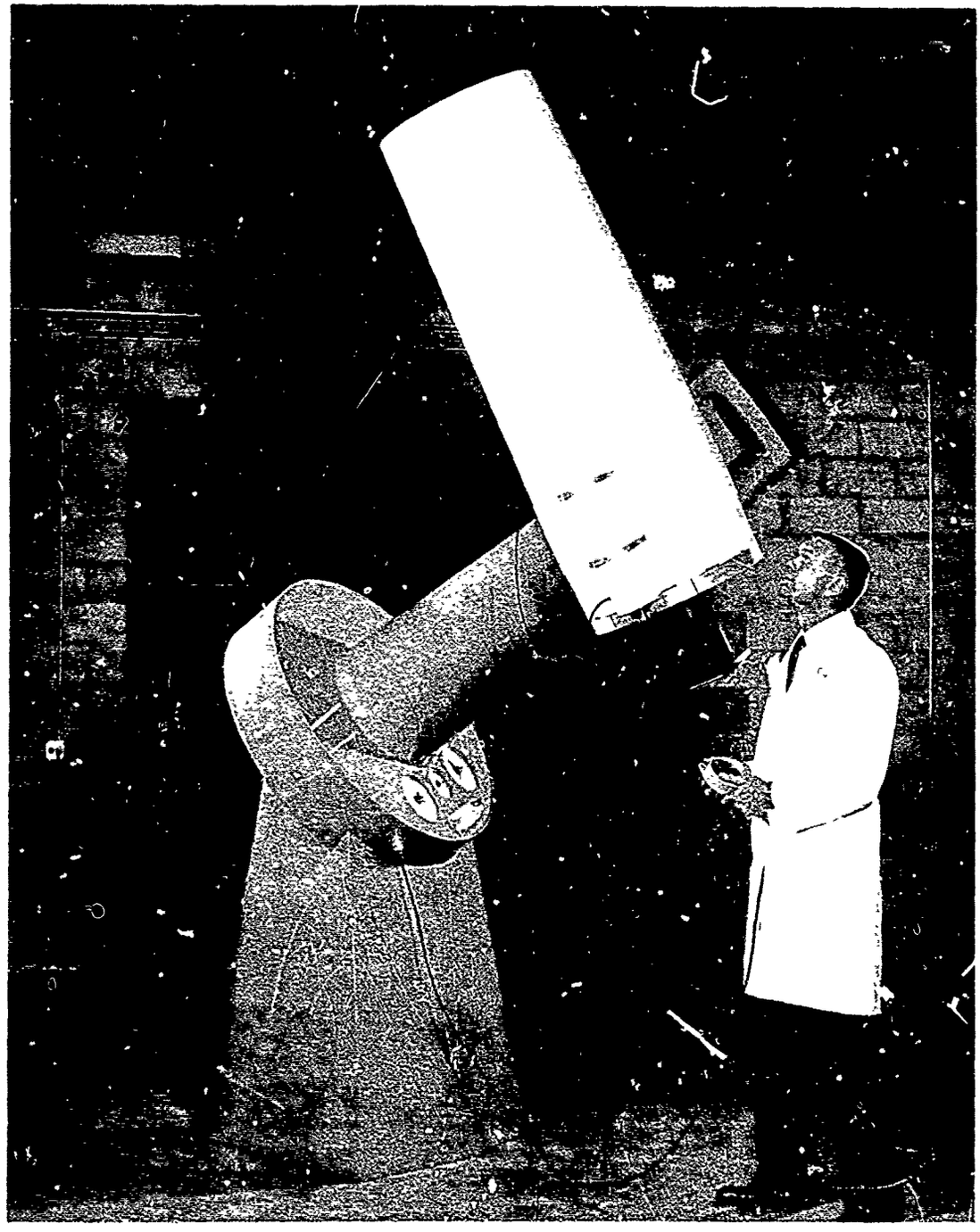


Figure 36 Cassegrain Reflector Telescope – 16 in.

using a mask. This will result in a small amount of obscuration at one edge of the 8-in. diameter aperture, but this obscuration will be no more than 2 in. in diameter. Since most observations will be made with smaller apertures, this compromise is not considered detrimental to the validity of the measurements. The effective aperture of the system will be adjustable, by use of a variable iris from the nominal 8-in. diameter to approximately 1 inch. To maintain an approximately constant focal spot size as the aperture diameter is varied, the focal length of the telescope will be varied from approximately 1,084 to 136 in. using a turret arrangement of lenses in the optical path of the telescope. Provision will be made for chromatic correction of atmospheric chromatic aberration (dispersion) as a function of zenith angle. Since the telescope rotates during operation, a provision will be incorporated to counterrotate the chromatic correction in order to maintain adequate correction.

In addition to the chromatic correction, it will be necessary to correct telescope pointing for refraction and cumulative errors arising from mount misalignment, axis nonorthogonality, or improper drive speed of the right ascension axis. All corrections to realign the telescope so that the star image remains within the tracking range of the SIS will be performed manually at appropriate intervals. Data acquisition will be interrupted during these correction periods because of the likelihood of mechanical pointing jitter being caused by the chromatic correction drive and, especially, by the declination drive. With this method, called "open-loop" correction, only the right ascension (sidereal) drive runs during data taking periods. As discussed later, great care is taken in the design of astronomical telescope to make disturbances from this source insignificant.(see Section IV, 2, c.)

It should be emphasized that, although the telescope is operated "open-loop," the star image nevertheless, is "closed-loop" tracked by the SIS at all times following star acquisition. [See Section IV, 2 d (2).] Therefore, there is no need for continuous correction of telescope pointing errors as long as the image remains within the tracking range of the SIS. However, chromatic correction will be required at predetermined intervals.

The measurement system will be housed in a 12-ft-diam. astrodome. This unit can be disassembled to permit transport from site-to-site, using standard moving equipment and without requiring special wide-load permission for use on roads and highways. The telescope will be removed from the mount before transport in order to assure that the integrity of the optical system is maintained. The mount will be partially disassembled to prevent bearing damage during transport. It is estimated that the system can be set up in two days at a prepared site.

(2) Operational Concept. A measurement program designed to provide definitive data on atmospheric transmission characteristics obviously must extend over a period of many months in order to take account of all major weather patterns and conditions that can occur at any given site. It is essential, therefore, that adequate provision be made for accommodating the field-site crew, not only during data acquisition periods, but during "in-between" hours. Because of this consideration, it is assumed that test sites will be selected at which year-round living accommodations will be available, either on site, or within driving distance. Established observatory sites have obvious advantages in this connection. Provision has been made for pertinent site survey and selection. (See Section IV, 4.)

Based on the assumption that sites at established observatories will be selected, the further assumption is made that electrical power adequate to operate the measurement system will be available, i.e., that a portable power source will not be needed. Power requirements are assumed to include those needed for air-conditioning – primarily heating, but also air cooling if required, for example, for a low altitude site.

Transport of the measurement system will be accomplished with the help of contract moving services. The radome will be transported in a conventional moving van or other suitable vehicle. The equipment van will be hauled by means of a tractor supplied by the moving contractor. Field personnel will have available at all times a leased utility vehicle, such as a small van or station wagon, and will travel from site-to-site in that vehicle.

e. Summary of Measurement System Performance Characteristics

The major performance characteristics of the Atmosphere Transmission Measurement (ATM) system can be summarized as follows:

- Image Acquisition and Tracking
  - Day and night operation
  - Automatic acquisition
  - Maximum acquisition time:
    Full field of view (FOV) – 105 sec
    Reduced field of view – 26 sec
    Tracking loop bandwidth – 1 to 500 Hz (selectable)
- Data Sampling
  - Image sampling time – 0 to 35 μsec (selectable)
  - Background sampling time – 2 μsec
- Optics (Cassegrain type)
  - Adjustable focal length – 1084 in. (2754 cm) to 136 in. (344 cm) (selectable)
  - Adjustable diameter – 8.15 in. (20.71 cm) to 0.68 in. (1.7 cm) (selectable)
  - Adjustable chromatic correction
- Field of View (function of telescope focal length)
  - Acquisition field of view
    Full field – 0.7 to 6 mrad
    Reduced field – 0.35 to 3 mrad
  - Instantaneous field of view (IFOV)
    3.1 to 25 μrad diam.
- Tracking Precision of SIS (random error)
  - $\leq$0.125 IFOV[15] (1 - σ) for first-magnitude star when using 20-cm telescope aperture and a 250-Hz tracking bandwidth, or 500-Hz bandwidth for a zero magnitude star
- Telescope Pointing Accuracy[16]
  - Ten percent of full acquisition field

---

[15]For the tracking system used, this precision is approximately equal to an rms noise equivalent angle (NEA) referred to object space of 0.1 λ/d, where D is the diameter of the primary aperture.

[16]The only requirement on telescope pointing accuracy is that the star image remain well within the quality FOV. The latter is at least as large as the full acquisition field specified above for the Cassegrainian telescope selected. (See Section IV, 2, b.)

- Computing and Data Analysis Subsystem
  - Generation of telescope pointing commands for measurement initiation
  - Assistance to system operator in maintaining proper instrument settings during measurement
  - Processing and digital recording of star image measurement data during measurement
  - Provision at quick-look on-line analysis and display of selected measurement data
  - Performance at off-line analysis of all measurement data within 8 hr
- Operation
  - Transportable
  - Short setup and teardown time (2 days each)
  - Output data synchronized to data recording and processing equipment

f. Measurement System Design Study Approach

As initially conceived, the measurement system was to be a combination of standard, well developed components which, at most, would require only minor modification. Minimizing cost, commensurate with achieving major objectives of the program also was an important goal. With special reference to the latter goal, it was considered essential that the design be one capable of producing data with a validity not subject to serious question. Otherwise, the ultimate objective of making measurements serving to verify theoretical system design concepts and provide needed design data would not be met. This consideration, and the obvious importance of pointing jitter (Section IV, 2,c.), was a strong influence in the choice of a high-quality astronomical telescope for the program, rather than, for example, a gimbal-mounted telescope of the type widely used for satellite tracking cameras. (Appreciable tracking jitter can be tolerated in a satellite tracking camera because the star background is available as a direction reference for data reduction. This is not the case for the measurement system.)

The study effort can be divided into the following major phases:

Phase 1 Initial concept formulation and preliminary definition of system parameters
Phase 2 Design of telescope and image-sensing subsystems
Phase 3 Design of data recording and analysis subsystem

As previously indicated in Section I, the Phase 1 effort was carried out primarily by Dr. D. L. Fried of Optical Science Consultants, in consultation with LMSC and ITT project personnel; the work on Phase 2 was performed by ITT-Gilfillan under a subcontract from LMSC; and the Phase 3 work on the design study was carried out by Dr. R. D. Merrill of the LMSC Information Sciences Laboratory.

2 OPTICAL SENSOR DESIGN

a. Measurement System Overview

(1) System Parameters. The fundamental system parameters, which are germain to this effort and which were used as the basis for developing hardware concepts were

derived by Optical Science Consultants (Appendix V). These may be summarized as follows:

• Pinhole radius	0.0017 in.
• Telescope f-number	f/200 to f/133
• Telescope effective diameter	8.15 in. (20.71 cm) to 0.68 in. (1.722 cm), no central obscuration
• Telescope focal length	1084 in. (2754 cm) to 136 in. (344 cm) in seven steps if zoom system is not used
• Diffraction limit	2.5 μrad (f/133)
• All other aberrations	< 0.75 μrad (includes saggital coma and atmospheric dispersion) -30 percent of diffraction limit
• Baffles	Maximum practical reduction of stray radiation
• Target sample rate	40,000 measurements/sec (all channels)
• Spectral range	0.4 to 0.6 μ

Additional system parameters have been developed in the course of the study and will be discussed in other sections of this document.

(2) Functional Description of System. A general functional description of the system is presented in this section. Figure 39 shows the major system elements.

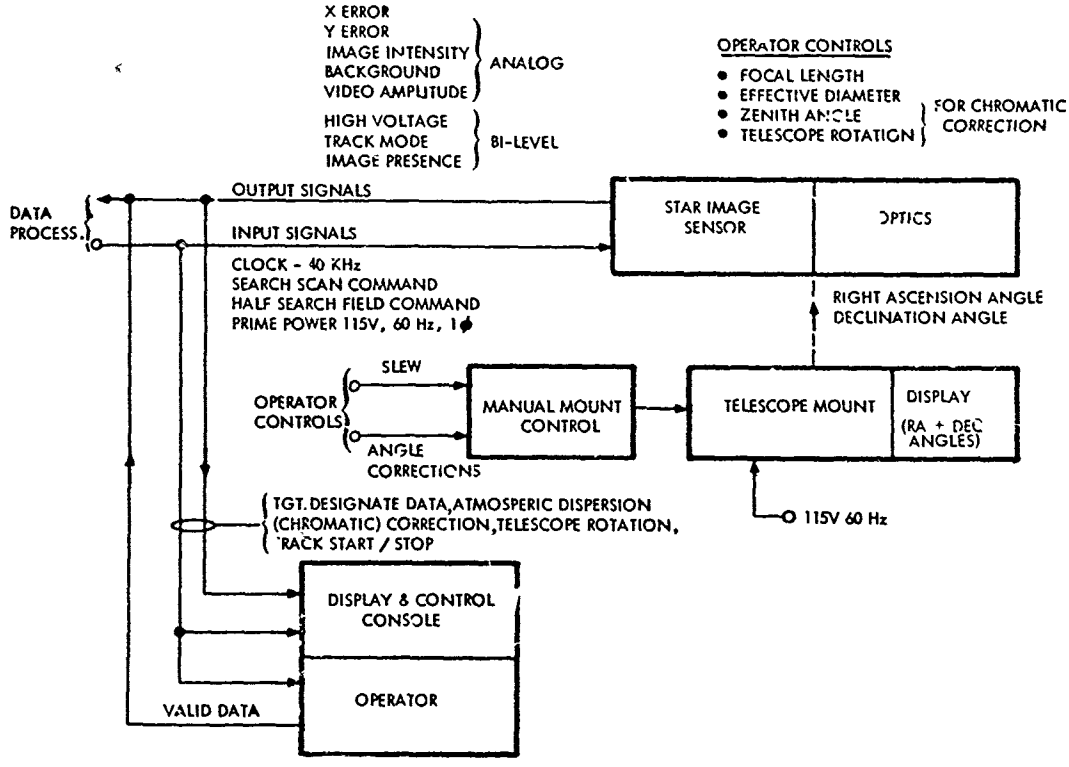


Figure 39 Major Elements of Measurement System – Functional Block Diagram

In order to simplify the mechanical design of the mount and the electronic interfaces, many of the operational adjustments and settings will be performed manually by the operator. Prior to the start of a measurement run, the operator will set the focal length and effective diameter of the telescope, and enter these settings into the data recording system via a keyboard. From computer generated information, he will adjust the magnitude and direction of the chromatic correction control for the particular star to be tracked. The computer will also provide the operator with pointing information (i.e., right ascension and declination angle) which he will manually enter into the telescope mount. The data processing system will compute this information on the basis of star position information and will make corrections for atmospheric refraction.

With the tracker turned on, a star should be acquired within 26 sec. The star acquired will be somewhere off-axis, and the operator will make appropriate corrections to the right ascension and declination angles to bring the target close to the optical boresight. This is the same procedure that is commonly used for all astronomical telescopes. The controls will have three sensitivity settings to facilitate adjustment, namely, 6 deg/sec, 2 $\widehat{\text{min}}$/sec, and 3 $\widehat{\text{sec}}$/sec. The operator will then check to determine that the level of the video output is consistent with the brightness of the star selected. When the operator observes that the system is tracking properly, he will depress the Data Valid button, thereby permitting the data processing system to record the appropriate signals from the star image sensor. When a star is being tracked, no further operator intervention is necessary. Should the tracker lose its target, the data valid signal will change its state so that the computer knows that any subsequent data is not valid. The operator, during the acquisition process or re-acquisition (should the target be momentarily lost), can select either the full or half of the search field for acquisition or re-acquisition. It may be necessary, at approximately 5-min intervals, to adjust the chromatic correction (because of telescope rotation and elevation angle changes) and the mount axes if the target is not close to boresight. Telescope rotation and elevation angle needed for this adjustment will be computed by the data processor. The performance of these adjustments should take no longer than 1 min, during which period data will not be collected. During operation, a display console will present the data that are being sent to the data processing system. As a consequence, the operator will always be able to monitor all of the pertinent system outputs and perform any necessary remedial action, should problems occur.

On being moved from site to site, the system will be disassembled by removal of the telescope from its mount and disassembly of the mount to avoid a load on the bearings. The astrodome will be capable of being disassembled so that each of the pieces can be transported using common commercial carriers without wide-load restrictions. The other components of the system are reasonably small and are easily transported in an equipment van. The reverse procedure will be performed to assemble the system at the new site.

Some preparation is necessary before a site can be used. This includes construction of a concrete pier to support the telescope mount. Mounting provisions for the telescope mount will be imbedded in the concrete and designed to provide the proper base angle for the particular latitude of the site. The system will be completely self-contained except for the input raw power and air-conditioning to be supplied from a separate portable unit or through a duct from a van.

b. Telescope

(1) General Considerations for Telescope Selection. The basic optical parameters for the telescope are outlined in Section IV, 2, a, (1). In addition to the functional requirements, operational requirements must also be considered. These factors include size, weight, ease of alignment, stability, and cost. With the constraints of the functional and operational considerations, various telescope configurations were evaluated for possible use in the measurement system.

The first optical system considered was a refractive telescope. The advantages of this type include:

- No obscuration
- Ability to seal the telescope tube to avoid air turbulence which could generate erroneous measurements
- Minimum diameter

The major disadvantage to this optical system is the cost of the optics. It is quite difficult to obtain for the first element an 8-in. blank that is of sufficiently high quality for a diffraction-limited system. Several estimates for this first element were generated in the course of discussions with various optical designers and suppliers. The estimated cost for the glass alone range between $10,000 and $15,000.

The other choice for the optical system consists of reflective optics. With this type, large-diameter mirror surfaces can be ground to a very high degree of precision, as evidenced by the variety of diffraction-limited astronomical telescopes available as standard products at reasonable cost for a complete telescope. The conventional reflective telescope has a central obscuration which would be objectionable in this application because of its effect on antenna gain. Use of an off-axis optical system which does not have a central obscuration therefore was considered.

Since an off-axis optical system is actually a section of a conventional symmetrical telescope, the question arises as to whether there is an advantage to an off-axis system compared to the use of an off-axis portion of a larger (16-in.) telescope. The obvious advantages of an off-axis system are minimum size and weight; however, an off-axis system of a given size will be more costly because the primary mirror is from a large source mirror, so that additional work is involved. Standard telescope mounts are usually designed to carry reasonably large loads so that weight is not a major factor. Unless a specially designed mount were to be considered, there is no benefit gained by reducing size and weight below that of a standard 16-in. telescope. It was therefore considered appropriate to investigate the use of available astronomical telescopes rather than a unique design. The simple paraboloidal reflector, e.g., Cassegrain, Schmidt-Cassegrain, and Ritchey-Cretian designs, were considered.

(2) Basic Considerations for Telescope Selection. A simple parabola design has the advantage of simplicity, but suffers the disadvantage of a very low-quality field of view. It is desirable to have as large a quality-field-of-view as practically possible in order to simplify atmospheric refraction corrections and to increase the off-axis distance a star can be tracked for valid data. These considerations will be discussed in other parts of this section. A paraboloid reflector of low focal ratio falls far short of providing an adequate field of good definition. The distance L off-axis of a paraboloid at which the comatic image reaches a size C is given by the following equation, in which F is the focal ratio:

$$L = \frac{16\,F^2 C}{3}$$

At a focal ratio of F = 5, L = 133C, therefore, the diameter of the field over which the comatic image has a size under 0.75 μrad is only 0.1 mrad. This field is unacceptably small. (See Section IV, 1, e.)

The Schmidt system makes use of a thin glass plate figured aspherically to correct all orders of spherical aberration at the stop at the center of the curvature of the mirror. The theory and residual aberrations of the Schmidt camera have been treated extensively by Stromgren, Caratheodory, Bouwers, Linfoot, and Bowen. (References 9 through 13, respectively) Near the axis, the chief aberration arises from the chromatic aberration of the corrector plate, which is normally made of one material, either crown glass or fused silica. There is some question as to the ability of the corrector plate to maintain its integrity in operational uses, even though the corrector plate contains a rather mild correction. Another disadvantage of the Schmidt camera is that it requires a longer tube than the Cassegrain or Ritchey-Cretian types.

The Ritchey-Cretian system is somewhat better corrected than a Cassegrain. However, like the Cassegrain, the Ritchey-Cretian has field curvature and astigmatism which, when spherical aberration and coma have been eliminated, become the dominant aberrations. It also suffers the need for very precise alignment in order to maintain its performance. This could present a problem for field operation.

The Cassegrain system is reasonably simple and many standard designs exist. The coma of a two-mirror Cassegrain system may be calculated as follows: Assume that the primary mirror is a surface of revolution, the radius of curvature of whose intersection with a plane through optic axis is given by the following equation for a point at a distance y from the axis:

$$R = 2f\left(1 + \frac{\alpha y^2}{f^2}\right)$$

The focal length of the primary is f , and α is a constant. The secondary is given the figure that eliminates spherical aberration at the Cassegrain focus. The maximum dimension C of the comatic image at a distance L from the axis of such a Cassegrain system is given to a first approximation by

$$\frac{C}{L} = \frac{3}{16m^2F^2} + \left(\frac{3}{8} - \alpha\right)\left(\frac{m+1-K}{K}\right)\frac{1}{4F^2}$$

The focal ratio of the primary is F; for the Cassegrain, system it is mF . The distance between the focus of the primary and of the Cassegrain system divided by the focal length of the primary is K . The value of K is normally slightly larger than 1, except in the case of the coude' focus, where it may be as large as 2 or 3.

For a spherical primary, α is 0. For a paraboloid primary, α is 3/8, and the last term vanishes. In the latter case, the expression for the coma of a Cassegrain system with a paraboloid primary of focal ratio F is the same as that for a paraboloid alone with a focal ratio mF; that is:

$$\frac{C}{L} = \frac{3}{16\,m^2\,F^2}$$

A 16-in. Cassegrain system (Boller and Chivens Division, Perkin-Elmer Company) is available which has an f/3 primary mirror and a system f-number of 60. The size of the comatic image (sagittal coma) for the full mirror is $L \times 5.2 \times 10^{-5}$ μrad. The nominal focal length of this Cassegrain is 2400 cm and, at this focal length, the farthest point from the center of the SIS field-of-view is approximately 0.3×10^{-3} radians. Correspondingly, the size of the comatic image at the edge of the field-of-view is 0.0016 μrad, which is considerably smaller than the size of the diffraction-limited image (≈ 1.2 μrad). For an 8-in-diam. portion of the primary mirror and for different focal lengths, the comatic aberration will be even smaller and, therefore, small compared to the diffraction-limited focal spot size (2.5 μrad). Therefore, tracking need not be restricted to boresight or near boresight; this is a significant advantage.

The combined rms wave-front distortion for both mirror surfaces of the telescope being considered is $\lambda/10$ for the full 16-in. diameter. For any 8-in. diameter, the wave-front distortion will obviously be considerably smaller.

The approach of using a 16-in. -diam. standard astronomical reflector, and masking all but an 8-in. diameter, is considered to be feasible. Some modifications to the standard unit will be necessary to provide a variable focal length and effective diameter, chromatic aberration correction (including telescope rotation), and baffling. Figure 40 illustrates the telescope configuration.

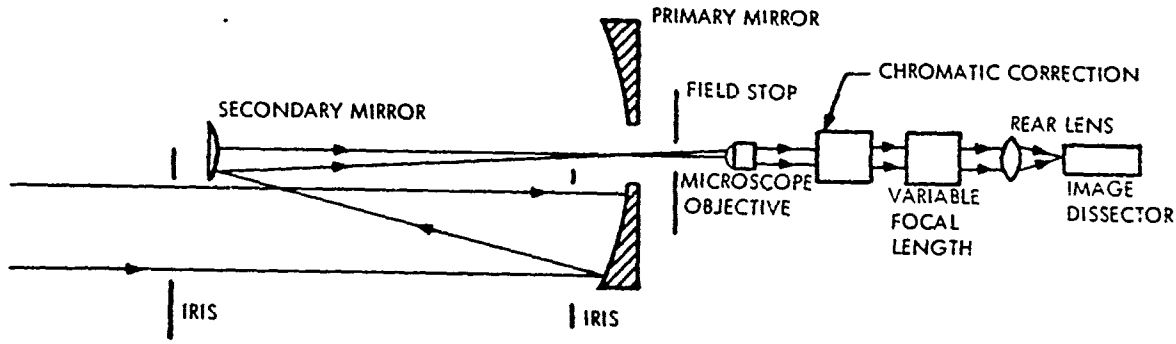


Figure 40 Optical System – Schematic

Since the primary portion of the mirror used is half the size of the mirror, the secondary mirror protrudes into the entrance aperture. This is of possible significance only when the system is used with its full 8-in. diameter aperture, and even then is of only minor importance so far as its effect on antenna gain. The obscuration could be avoided by using a primary mirror 18 inches in diameter, but this size is not a standard design.

(3) Description of the Optical System. Tracing the light through the optical chain shown in Figure 40, it can be seen that, after the folding mirror, the light is brought to focus at the field stop. The field stop is fixed for the maximum field of view. The light passing through the field stop is collected by a microscope objective and thereby collimated. The field stop and all the optical components behind it will be aligned to the optical axis of the unmasked area of the primary mirror, not the entire 16-inch mirror. The collimated light then passes into the chromatic elements box. Chromatic correction is necessary since the incoming beam will have different propagation directions for the various wavelengths in the spectrum. The function of the chromatic elements is to assure that the beam is collimated for all wavelengths of interest. This is discussed in greater detail in Section IV, 2, b, (4). This box contains the bandpass filter which limits the spectral range of the signal to the 0.4 to 0.6 μ spectral range. It also contains a pair of prisms designed to compensate for the chromatic dispersion of the atmosphere.

The light leaves the chromatic element box, still collimated, and enters the variable magnification unit. The variable magnification unit contains a seven-position magnifier wheel. Each of the positions (except the 1X position, which is empty) contains a pair of microscope objectives arranged nose-to-nose and adjusted so that a collimated beam entering (the rear of) one lens leaves the (rear of the) other in a collimated condition, but having been subjected to an MX magnification. By rotating the wheel, the beam can be made to pass through different pairs and receive different magnifications. It is important to note that, because the beam entering and leaving the magnification unit is collimated, there is no tight tolerance on the positioning of the magnification optics in the beam. The only serious tolerance concerns the alignment of the pair of microscope objectives with respect to each other. Placement in the beam has a tolerance of thousandths of an inch rather than a fraction of a micron. After leaving the magnification unit, the beam falls on a lens which focuses the collimated beam onto the photocathode of the SIS.

The first elements in the optical train are actually the irises – one just in front of the primary mirror and one at the front of the telescope tube. Each iris is adjustable over the range of 2- to 20-cm diameter from a fixed central point, with the two adjusted in synchronism, except that the rear iris is taken as the defining aperture. It is necessary that the opening of the forward iris be slightly greater than that of the rear iris. The function of the forward iris is to cut down on stray radiation. Its placement is dictated by the requirement that it be forward of the folding mirror so that it will not block the converging beam coming from the primary mirror.

(4) Correction of Atmospheric Aberrations. In using the Cassegrain system, there are no difficulties in operating over the entire field of view of the tracker as far as

sagittal coma is concerned, as already indicated. The major aberration of concern is that due to dispersion of the atmosphere. Because of the very high angular resolution involved in the measurements, atmospheric dispersion can be significant as an aberration mechanism. Over the operational spectral band from $\lambda = 4000$ Å to $\lambda = 6000$ Å, the atmosphere refractive index varies from $n = 1 + 298.1 \times 10^{-6}$ at $\lambda = 4000$ Å to $n = 1 + 291.9 \times 10^{-6}$ at $\lambda = 6000$ Å, a difference in refractive index of $dn = 6.2 \times 10^{-6}$). It can be shown that for a star at zenith angle θ, its apparent position will be spread over the angular range of $d\theta$ due to this spread in refractive index given by

$$d\theta = -\frac{dn}{n} \tan \theta \approx - dn \tan \theta$$

If a spread of 2.5×10^{-6} radians is allowed (which is obviously excessive for the 20-cm-diam. aperture and is possibly too much even when working with a 5-cm-diam. aperture), the zenith angles would then be restricted to 23 deg or less. If as much as 5×10^{-6} radian dispersion, could be allowed, there would still be a restriction to zenith angles of less than 40 deg; this is still an excessive limitation.

For this reason, the chromatic dispersion compensating prism pair mentioned previously have been incorporated into the chromatic element box of the optical train. This consists of two pairs of prisms with very small wedge angles, – one pair of crown and one pair of flint glass. (The important factor in the choice of glass is that different types have different dispersions.) By rotating the two wedges of one type of glass about the beam direction, it is possible to adjust the effective wedge angle and thereby the chromatic dispersion introduced by the pair. With a proper setting of the two pairs of wedges with respect to each other and in terms of each of their effective angles, it is then possible to introduce a negatively oriented chromatic dispersion that will just cancel the effect of the atmospheric dispersion. These angles can be adjusted to allow cancellation at any zenith angle.

The prism pair will deviate the light bundle from the optical axis. However, this deviation will be less than ±0.1 mrad (with respect to object space) and is small enough to be inconsequential. A single-prism pair will be adequate.

During normal target tracking, the telescope tube rotates about its own axis relative to a local gravity gradient. This angle, denoted by R, is calculated in Appendix VII in terms of declination and right ascension angles. The method used for chromatic correction will obviously require a fixed orientation with respect to an earth reference. Therefore, the chromatic corrector will require two inputs – one for the zenith angle and the second for telescope rotation. Both will be entered manually, during a period of time when data are not being corrected. Very little correction time will be lost since it will take only about 1 min to make these corrections. The rationale for this approach is discussed in Section IV,2,c. The chromatic correction input will be calibrated in dn and will have a range of 0 to 6.2×10^{-6}. It may, however, be more convenient to calibrate the dial in elevation angle. The telescope rotation input will be calibrated in degrees for a range of 0 to 360.

c. Telescope Mount and Astrodome

(1) Basic Considerations for Mount Selection. A sidereal mount is required for the telescope in order to facilitate star tracking. Since the objective of the measurements made by the equipment is to determine atmospheric scintillation precisely, the mount cannot be allowed to introduce mechanical vibration in the frequency range of interest. Beam wander is not a problem because the SIS will be able to track image motion. Peak scintillation frequencies between 20 and 30 Hz are anticipated, and significant components can be expected to extend over the range of 2 to 100 Hz. Extraneous mechanical inputs in the latter frequency range cannot therefore be tolerated without the possibility of invalidating the measurement data. The IFOV of the SIS will be between 0.3 and 3 arc-sec, depending on the telescope focal length selected. The rms value of all the transmitted extraneous mechanical frequencies summed over the range of 2 to 100 Hz therefore should be less than 0.1 arc-sec so as to avoid degrading the tracking precision of the system.

Various manufacturers of professional astronomical telescope mounts were contacted in order to ascertain the performance of their product relative to the vibration transmitted through the mount to the telescope. Unfortunately, little definitive information is available concerning mechanical noise over the frequency spectrum of concern. The mount manufacturers were able to present star field photographs taken with long exposures that do not show image motion. These photographs are relatively insensitive to high frequency motion because of the long integration time of the photographic exposure, but they would be expected to show effects of low-frequency disturbances. Since it is fairly evident that there are no low frequency components in the mount of sufficient amplitude to be objectionable, it may be conjectured, in view of the mass of the mount, that there are no higher frequencies as well. The photographic data presented by the suppliers are not sufficiently conclusive to remove all doubt concerning the performance of the various mounts but are adequate to establish a reasonable expectation that the mechanical noise experienced in operation will be acceptably small.

Because of the many sidereal mounts available or which to make measurements, the possibility of determining mechanical noise experimentally was considered. The sensitivity of the accelerometers required for such a measurement was calculated and found to be on the order of 0.003 g. This was based on achieving a measurement of 0.1 arc-sec at the end of a 24-in. arm. Although accelerometers capable of this sensitivity are available, the work attendent to procurement, and complexity of performing the measurements were considered as involving too extensive an effort for the scope of this study.

It was considered inappropriate to specify a mount that would have to be designed and manufactured to particular specifications, since it would differ from a standard unit only with respect to mechanical noise. Reliable manufacturers already use techniques for minimizing mechanical noise as part of their design. These techniques include large spring-loaded drive gears, precision gears, best available bearings, and large masses. Manufacturers have utilized these approaches because freedom from mechanical vibration is of major concern to professional astronomers who are the main users of these mounts. As a consequence, none of the manufacturers of quality mounts that were contacted was able to offer any assurance that significant reduction in vibration levels (from the already low levels) could be achieved without a major development program. In view of this situation, it is believed that, rather than emphasizing design improvement, the greatest payoff would result from concentrating on choosing the best available mount. For this purpose, the manufacturer's background and length of experience were given considerable weight. In addition, the following design features were considered

important to assure acceptable performance:

- Unit Mass. The greater the weight, the less likely the transmission of mechanical vibration to the telescope
- Large Main Gear Drive. Should lower the vibration frequency
- Preloaded Gears. Considered an important design feature

Based on these considerations, the 16-in. sidereal mount manufactured by Boller & Chivens (division of Perkin-Elmer) was selected. A data sheet describing this mount is included as Figure 41.

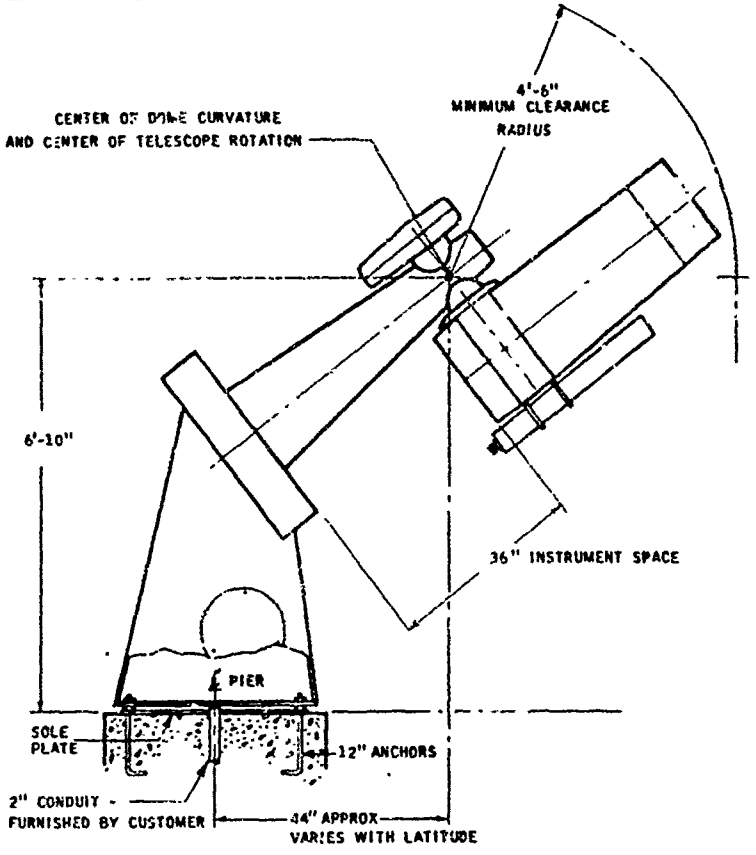
(2) Consideration of Additional Noise Sources. Although great care is exercised in attempting to assure a smooth drive along the right ascension angle axis, the declination axis is not as well designed. The reason for this is found in examining the mechanical configuration of a sidereal mount, where it can be seen that it would be difficult to design the declination axis to achieve the same smoothness of motion as the right ascension axis. Some mechanical noise can be expected if the declination angle is changed during star tracking. Another possible source of noise can be expected from the chromatic corrector, which has two adjustments (the magnitude and direction of the chromatic correction) if corrections are made during the track mode. Still another possible source of noise, although of a lower magnitude, can result from correcting the sidereal rate during target tracking. On the basis of mount manufacturer's data and field experience, once the mount has been properly aligned, the open-loop tracking accuracy is expected to be within 5 arc-sec over a tracking period of at least 1 hr.

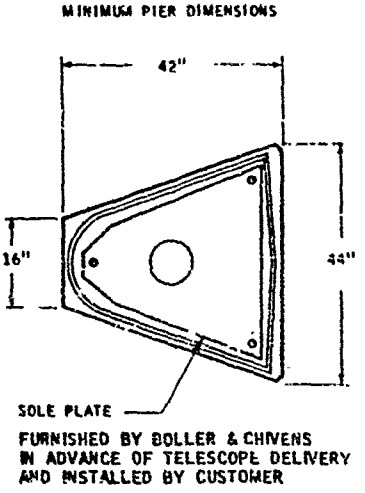
(3) Telescope Operational Considerations. As a result of examining the various sources of noise, it appears evident that it is desirable not to change the sidereal rate, declination angle, or the chromatic correction during the time data are being collected. The sidereal mount is sufficiently accurate in the open loop mode so that no corrections are necessary in the rate or the declination angle for periods up to an hour of tracking. However, chromatic corrections are necessary more frequently because of changes in elevation and telescope rotation. Computations (presented in Section IV, 2, e) indicate that the minimum time between corrections under worst case conditions (assumed previously) is 5 min. It is assumed acceptable to interrupt data for approximately 1 min to make the corrections at 5-min intervals. The baseline approach therefore is to operate the mount and chromatic correctors on an open-loop basis. The required chromatic corrector adjustments will be supplied by the computer. The operator will correct the mount manually when necessary to bring the target to boresight.

The base angle of the mount is selected for the latitude of the site where observations are to be made. Since measurements are planned for a variety of sites, adjustments must be provided in the mount for this variation. It is expected that measurements will be made within a 500-mi distance so that the difference in the base angle is reasonably small (approximately 7 deg). Different sole plates for mounting will have to be procured compatible with the different locations. In addition, the mount will be provided with fine adjustments.

BOLLER & CHIVENS
16-INCH CASSEGRAIN REFLECTOR

DIMENSIONS





GENERAL DESCRIPTION

The 16-inch Cassegrain reflector, smallest of Boller & Chivens standard line of professional observatory instruments, is a fine primary instrument for the small observatory. It also finds extensive use in major observatories in relieving the work load of larger telescopes. The totally enclosed mount is designed for maximum rigidity. The polar axle's thick-walled cone shape and wide bearing spacing give an extremely stiff support. Adjusting the controls of accessory instruments does not affect the telescope pointing. The base is custom-fabricated for each location to provide the correct polar axis inclination. Convenient provisions for adjusting the base in azimuth and elevation are built in.

The primary worm of either drive can be partially disengaged for sensing balance after instruments are changed. Balance about the declination axis is achieved by moving the entire telescope tube parallel to the optical axis. Built-in pivoted counterweights balance the telescope about the polar axis. Individual weights at the mirror cell permit balancing unsymmetrical instruments.

The primary mirror is mounted on a rigid central support of proven design, with provisions for centering and tilting. The secondary mirror also has centering and tilting adjustments, and has motor-driven focusing to move the final focus through a range of 16 inches along the optical axis.

Figure 41 Cassegrain Reflector Telescope Mount – Supplier Specifications

The right ascension and declination drives are completely powered by electric motors. The tracking drive is powered by a synchronous motor, driving through a gear train to give correct sidereal rate. Maximum tracking accuracy is assured by the use of a large, high-precision worm gear, preloaded with an electric torque motor. The telescope is prewired for connecting an optional external variable-frequency power supply to the tracking motor.

All drive components, gears, bearings and electrical wiring are completely enclosed. A junction box on the telescope tube has outlets for 115V AC and 6.3V AC power for instrument use.

The telescope is completely assembled, tested and adjusted at the factory. Shipping and installation service is available and is recommended.

Boller & Chivens is one of the nation's leading manufacturers of large astronomical telescopes—from 16-inches upward.

OPTICAL SPECIFICATIONS

PRIMARY MIRROR	*16-inch clear aperture f/3 paraboloid, Pyrex or equivalent*
SECONDARY MIRROR	*4-inch diameter hyperboloid, Pyrex or equivalent*
CASSEGRAIN FOCAL RATIO	*f/18, optional f/13.5*
FIELD SIZE	*2.5-inch diameter*
FOCUSING	*Electric drive at secondary mirror ± ½-inch travel*
OPTICAL QUALITY	*80% of incident light, from geometrical considerations, will fall within 0.1 arc seconds*
MIRROR COATINGS	*Aluminized with Silicon Monoxide overcoat; optional — Silicon Dioxide, Magnesium Fluoride or no overcoat*
FINDER	*4-inch aperture 34-inch focal length with illuminated reticle*

MOUNT SPECIFICATIONS — *mount available with or without telescope*

TYPE OF MOUNT	*Equatorial, off-axis*
SLEW DRIVE RATE	*6 degrees per second of time*
SET DRIVE RATE	*2 minutes of arc per second of time*
GUIDE DRIVE RATE	*3 seconds of arc per second of time*
TRACKING DRIVE GEAR	*20-inch diameter, 360 tooth, preloaded*
TRACKING ACCURACY	*2 arc seconds in 5 minutes* *6 arc seconds in 1 hour*
POSITION READOUTS	*Illuminated clock-type dials; right ascension to 10 seconds of time, hour angle to 1 minute of time, declination to 2 arc minutes*
OPERATING CONTROLS	*Hand paddle with pushbuttons for slew, set, and guide motions*
INSTRUMENT MOUNTING	*Threaded hole pattern to accommodate instruments up to 50 pounds in weight and 3 feet in length. Additional counterweights can be provided for heavier instruments*
POWER REQUIREMENTS	*115 volts, 60 cps at 10 amperes*
FINISHES	*Exterior—durable automotive plastic enamel* *Interior—optical flat black enamel*
SHIPPING WEIGHT	*3,500 pounds—with telescope*

TYPICAL OPTIONAL FEATURES

available at extra cost

Fused Silica Optics
Ritchey-Chretien Type Optics
Alternate Focal Ratios
Continuously Variable Set-Guide Rates
Variable Tracking Rate for Planetary and Lunar Rates
Remote Digital Readouts
Additional Counterweights for Heavier Instruments

TYPICAL OPTIONAL EQUIPMENT

available at extra cost

Model 14753 3¼ x 4¼ Plate Holder Camera with or without shutter
6-inch aperture f/10 finder telescope
4-inch or 6-inch f/15 guide telescope
Direct reading zenith angle indicator
Instrument rotator
Spectrograph

Figure 41 (Cont.)

The standard telescope mount includes a readout of the right ascension and declination angles that are necessary for designating the telescope to a star in order to achieve acquisition. These data will be computed in the data processing system from standard star position and atmospheric refraction data. With the exception of a readout of the declination and right ascension angles, no other data interface with the mount is necessary.

The particular mount selected can be disassembled for transportation from one site to another. The disassembly and reassembly can be performed in one day each and require either a fork lift or small crane for lifting the parts. It is desirable to disassemble the mount although it can be shipped as an assembled unit. The purpose for disassembly is to protect the main bearings from damage caused by shock and vibration during transportation, which could result in the generation of subsequent mechanical noise. The added time and cost required for assembly and disassembly are considered worthwhile to achieve confidence in the integrity of the mount.

(4) Detailed Description of the Telescope Mount. The Boller & Chivens mount has been selected during the execution of this study. However, other suppliers should be investigated further before a mount is ordered so as to confirm the initial judgment. The following description is based on information regarding the mount that was received from Boller & Chivens.

(a) Structure. The mount is of a modern single pier, off-axis type. It is designed to support the basic telescope plus instruments projecting up to 36 in. behind the Cassegrain instrument mounting surface and weighing up to 50 lb.

(1) Tube. The telescope tube supports and aligns the optical components. The shell section is a slightly tapered aluminum cylinder. It supports a secondary shell at the upper end and is bolted to the center section (saddle) at the lower end. The center section consists of a double-walled aluminum weldment mounted solidly to a flange provided on the end of the declination axle. It is fastened to the flange in such a way that it may be moved up or down by the loosening of four screws. This provides a means of accurately balancing the telescope tube assembly about the declination axis. A lead screw for ease in making this adjustment is conveniently accessible at the lower end of the telescope tube assembly. The secondary shell supports the secondary mirror assembly and provides a means of holding a cover for protection of the inside of the tube and reflecting surfaces from dust when the telescope is not in use. When the end cover is removed, a baffle plate can be installed to carry the various aperture stops. As the tube is an enclosed type, it has ventilation openings at the lower end. Electrical wiring is carried into the tube and to an electrical junction box located on the center section for connection of power to instruments.

(2) Declination Axle. The declination axle is a hollow, fabricated steel weldment to allow passage of electrical power leads through its center. It is supported by two 4-in.-i.d. precision ball bearings, one at either end, 12 in. apart. A flange is provided on one end to accommodate the mounting surface of the tube center section, allowing for 3 in. of axial adjustment of the telescope tube.

(3) Polar Axle. The polar axle assembly is a double tube, consisting of a rigid inner axle on which an outer housing rotates. The inner axle is bolted to the mount and supports the outer housing through two precision ball bearings 43.5 in. apart. The upper bearing has 6-in. i.d. and the lower bearing has an i.d. of 12-in. Attached to the lower end of the axle is a 20-in.-diameter, 360-tooth worm gear against which a right ascension drive mechanism rotates the outer housing. The outer housing supports the declination axle and its associated drive mechanism. Both axle systems accommodate a means of carrying uninterrupted electrical power (115 Vac, 10 A) to the telescope tube center section. Because continuous rotation is not required of either axle, and because slip rings are known to be much noisier than good bearings, continuous flexible leads will be used for this purpose.

(4) Pedestal. The base or pedestal is a hollow, fabricated, heavy-gage, steel weldment to which the polar axle is bolted. Its upper surface is accurately machined to correspond to the telescope median observing site latitude angle. The bottom of the pedestal attaches to a sole plate and has adjustments in elevation and azimuth, each with a range of ±0.5 deg for precise alignment of the polar axle. Within the pedestal is a single-pole circuit breaker for electrical protection of main power, with the switch accessible from outside. Size of the pedestal is limited to a trapezoidal floor plan with an altitude of 42 in., and a major base of 44 in.

(5) Sole Plate. A steel sole plate is provided by the telescope contractor in advance of the delivery of the telescope to be cast into a concrete mounting pier by the observatory. The pier is provided as part of the telescope building by the observatory. The sole plate is a triangular, 3/4-in.-thick, steel plate, provided with three mounting studs extending upward from the top surface. One stud is located at the rear of the telescope on the north/south line, and the remaining two in the opposite corners corresponding to east and west. Each stud is supplied with two nuts, one for adjusting vertical alignment of the polar axle and one for locking the base. The studs are actually extensions of J-bolts which protrude 12 in. below the bottom surface of the plate. An 8-in.-diameter hole is provided in the center of the sole plate to allow for entrance of electrical conduit through the bottom of the telescope mounting. Additional sole plates can be provided at a nominal cost as required for other observing sites.

(6) Site Latitude Adapter. An adapter can be provided to permit operation of the telescope at all latitudes within the continental United States. This adapter will interface with the sole plate and the telescope pedestal and will retain all adjustable features of the basic mount for alignment of the polar axis.

(b) Drives. Electrical motor drives are used for all motions about the polar and declination axes. All motions are smooth with no abrupt starts and stops and are free of objectionable vibration. All motions are continuous within the limits specified below. Couplings or clutches, where used, are completely free of backlash.

Tracking rates are smooth and free from mount noise and vibration from approximately 0.1 Hz upward, with an amplitude not to exceed 0.1 to 0.2 arc-sec. The manufacturer states that these performance specifications have been verified on mounts of this design through actual observation and test.

(1) Drive Rates. Following are drive rate specifications:

- Slew 6 deg/sec of time
- Set 2 min of arc/sec of time
- Guide 5 sec of arc/sec of time
- Track 15 sec of arc/sec of sidereal time when driven by 60-cycle/solar-second power

(2) Main Drive Worms. The right ascension and declination drives are designed so that the primary worm in each is preloaded against its respective worm gear to eliminate backlash from the mechanisms. Preload torque of 8 to 10 ft-lb is provided for each axis and is developed by stalled d-c torque motors.

(3) Balance Provisions. The right ascension and declination drives have provision for quick release of the worm-to-worm gear mesh in order to allow sufficient backlash for sensing telescope balance about either axis for any position of the telescope tube. An electrical interlock is provided in each drive to prevent operation of the drive motors in the released position.

(4) Right Ascension Drive. The right ascension drive assembly is mounted at the lower end of the polar axle housing and covered by an appropriate flange. Tracking speed is produced by a 115-Vac synchronous motor, geared to produce sidereal rate output when driven by a 60-Hz/solar-second power source. Wiring for this motor is such that it may be driven directly from a standard power line. Alternatively, a separate terminal strip is located in the base to which power of variable or stabilized frequency may be furnished if the frequency of the local power source proves to be insufficiently stable. The right ascension tracking drive has no errors exceeding 2 arc-sec in 5 min of time, or 5 arc-sec in 1 hr. The guide-set motor is a 115-Vac servo motor with a 36-Vac control winding to which a tachometer-generator is attached. Power for this servo motor is provided by a servo amplifier which compares the output voltage of the tachometer-generator with the command voltage from a pushbutton control paddle. The servoamplifier is mounted at the lower end of the polar axle housing also covered by the flange for the right ascension drive assembly. A separate 115-Vac slew motor is provided with acceleration control so that it offers no sudden forces to the worm and worm gear, but supplies smooth power when speed it increased and decreased.

(5) Declination Drive. The declination drive assembly is mounted in a housing on the upper end of the polar axle housing opposite the telescope tube. Motors are of the same type used to perform the functions described for the right ascension drive with the exception of the tracking drive. The worm gear is 12 in. in diameter. The servo-amplifier for the guide-set motor is mounted on the flanged area at the lower end of the polar axle housing.

(c) Position Indicators. Illuminated dial indicators for right ascension angle and declination are mounted in the upper surface of the flange on the lower end of the polar axle housing. The intensity of illumination is variable by means of a control knob located adjacent to the indicators. Each dial is adjustable in setting by insertion of a hex key through a hole in the center of the dial face which is normally sealed by means of a removable rubber plug.

(5) Astrodome. Figure 42 is a data sheet describing various astrodomes produced by Paraboan, whose product was determined to be the best available. The selected unit is indicated in this figure. The unit will be procured without the servo drives since manual operation of the unit is considered acceptable as a cost-effective measure. Also, the omission of the servo drives simplifies assembly and disassembly. Umbrellas may be attached to the astrodome to eliminate potential problems caused by the sun during daylight tracking.

d. Star Image Sensor (SIS)

(1) Summary of Star Image Sensor Requirements. The star image sensor (SIS) is essentially a pinhole detector designed to measure the intensity modulation and angular motion of the star image. The special requirements that this sensor must satisfy will be discussed before proceeding with the description and analysis of the SIS. A more complete discussion of requirements is contained in Appendixes IV and V.

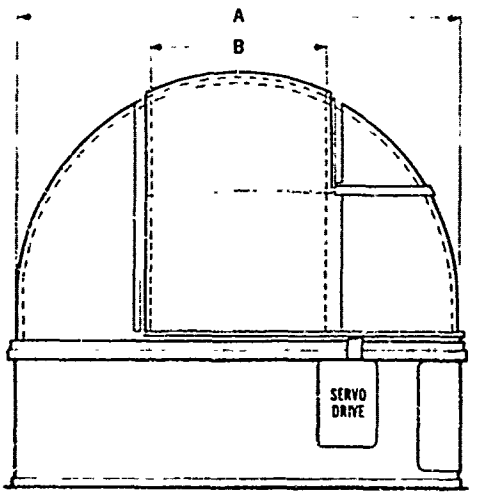
The pinhole radius is required to be approximately 0.0017 in. (Appendix V, p. 1.). The FOV of this pinhole will depend on the focal length of the telescope, which can vary from 1084 to 136 in. (2754 cm to 344 cm.) The pinhole FOV (full width) can therefore vary from approximately 0.8 to 6 arc sec. The rather small size of this field of view results in the generation of unique design requirements because the image will be larger than the pinhole.

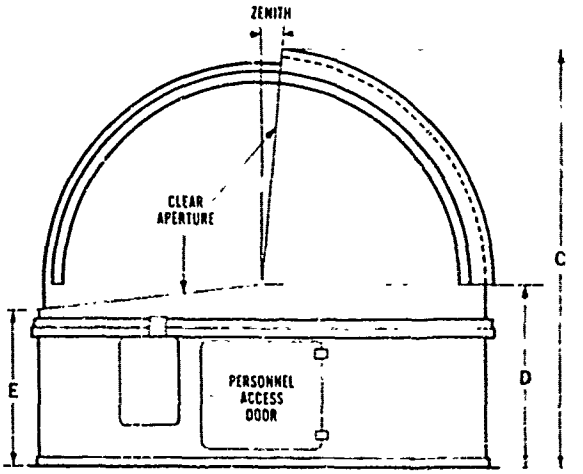
The SIS must have an automatic acquisition mode capable of locating a star within a large FOV (up to 3 mrad). It is not practical to locate the image manually or by using a-priori data because of the small pinhole size and image size.

A stellar image will move in angle due to atmospheric effects when it is being tracked. The image motion will be a function of atmospheric conditions (including time of day, wind, temperature, etc.) and the telescope diameter. The magnitude of the angular excursions can vary up to 20 arc-sec with scintillation frequencies to 100 Hz. (The most probable values of these quantities is around 8 to 10 arc-sec and 20 to 30 Hz respectively). As a consequence, the pinhole must be able to follow (i.e., track) the image in order to prevent it falling outside the FOV or observing modulation effects that could not be separated from image intensity variation.

An image dissector tracker will provide capability for reliably acquiring and tracking a star image. In addition, off-axis tracking can be accomplished with an image dissector tracker, which approach simplifies the design of the system because the design is not restricted to boresight tracking. It is believed that no other tracker can supply the necessary capability for this system except at greater cost and complexity. Although the quantum efficiency of an image dissector is less than that of a solid-state detector, less internal noise is generated, resulting in a greater detectivity for the image dissector.

Noise components will be present in the system, primarily because of shot noise generated from the image and background photocathode current. This will cause an angular variation in the apparent position of the signal (or noise equivalent angle – NEA).





ASTRODOME SHELTER DIMENSIONS AND WEIGHTS

Model Size (ft)	9	10	10	12	12	12	14	16	16	16	16	17
Aperture Opening Beyond Zenith (deg)	6 1/2	5	14	5	15	5	18.5	5	5	18	18	10
(a) Outside Diameter (in.)	108	121 5/8	121 5/8	144 15/16	144 15/16	144 15/16	170	191 3/8	191 3/8	191 3/8	191 3/8	201 3/4
(b) Width of Aperture (in.)	40 3/4	50	76	64	78	64	96	72	86	96	96	96
(c) Overall Shelter Height (in.)	100	125	125	137 1/4	137 1/4	167 1/4	169	158 1/2	158 1/2	158 1/2	209	205
(d) Height to Centroid of Sphere (in.)	44	62 1/8	62 1/8	62 1/8	62 1/8	94 3/4	82	60	60	60	111	101 1/8
(e) Height to Aperture Base (in.)	39	49 7/8	49 7/8	49 7/8	49 7/8	49 7/8	54	42 5/8	42 5/8	42 5/8	65 5/8	56 7/8
Approximate Shelter Weight (lb)	3000	4000	4000	4500	4500	5000	5500	5500	5500	5500	6000	7000

Selected Unit

ENVIRONMENTAL PERFORMANCE:

Ambient Temperature Range: Operating . . . . . -40° to 125°F
Non-operating . . . . . -65° to 160°F

Wind Load: Operating . . . . . 30 mph steady, gusts to 50 mph
Non-operating . . . . . 130 mph

Thermal Conductivity . . . . . Less than 0.4 Btu/hr/sq ft/°F

Figure 42. Selected Astrodome Chart (Parabam, Inc.)

The magnitude can be calculated if the background is known. For this reason, separate outputs for image intensity and background are desirable.

The tracking loop bandwidth and image sampling time should be variable in order to provide flexibility in gathering experimental data. The SIS must have day and night star-tracking capability in order to permit data collection under a variety of atmospheric conditions. Finally, synchronization between an external data processor and the SIS is desirable in order to assure minimum delay and dead time in recording data and to simplify system timing.

(2) Fundamentals of the Star Image Sensor Operation. The SIS will be a modification of an existing ITT/Gilfillan design with proven ability to track stars precisely, both at night and during daytime. Design changes are necessary in order to achieve the particular performance required to perform the atmospheric effects measurements.

The SIS is a two-axis, dual-mode star tracker designed to measure precisely the angle between its boresight axis and the line of sight to a target and to provide image intensity data. It has the unique features of previous ITT/Gilfillan Electro-Optical trackers, namely:

- Use of electronic scanning that needs no moving parts
- Ability to scan a large FOV
- Ability to select a specific star in the FOV
- Position information of excellent resolution and accuracy
- Automatic switching between track and acquisition mode of operation
- Linear image intensity indication

A tracker is made up of three basic building blocks – the optics, the image dissector tube, and the electronics.

The optics of a tracker determines its angular FOV and image brightness. The purpose of the optics is to focus an image on the photocathode of the image dissector tube.

The heart of the tracker is the image dissector tube. Figure 43 shows an image being focused on the photocathode to form an electron image of the target. Behind the photocathode there is an aperture mask and secondary emission dynodes capable of amplifying a signal up to 10^7 times. The image dissector is constructed so that, when an accelerating voltage is applied between the photocathode and a mechanical limiting aperture, only electrons leaving a specific area on the photocathode will pass through the limiting aperture. This area is called the instantaneous photocathode diminsion (IPD). When a target image is positioned on the photocathode by the lens, a very small stream of electrons is formed by the electron optics of an electromagnetic focusing field.

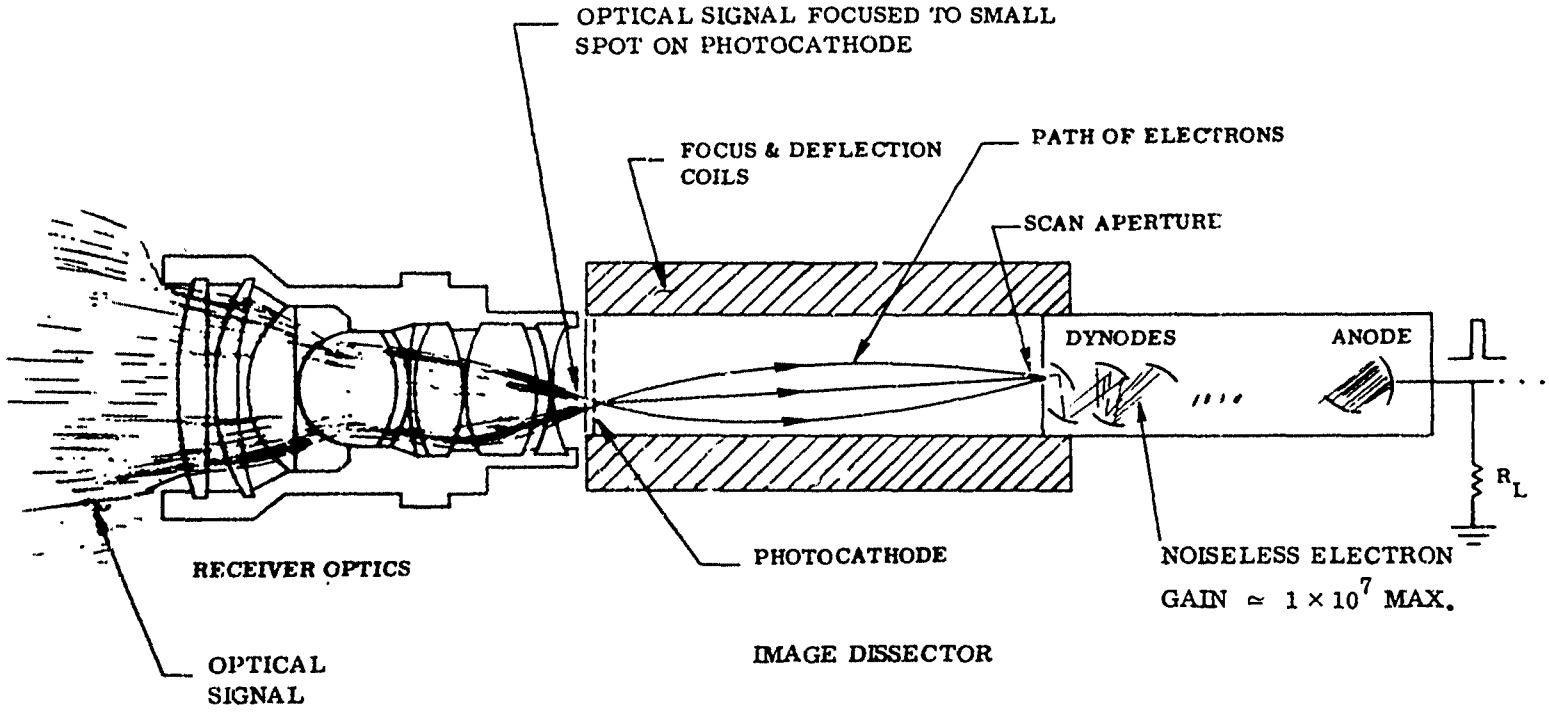


Figure 13 Typical Star Tracker

A deflection coil positioned around the image section provides magnetic deflection of the target image electron beam. By applying proper deflection coil currents, the electron beam is swept back and forth across the limiting aperture, causing a modulation of the electron beam. Deflection coil current centers the IPD on the target image.

The IPD [See Section IV, 2d (2)] , when projected forward through the optics, represents a region in space defined as the instantaneous field-of-view (IFOV). It is defined by the geometric relationship:

$$\tan\frac{\text{IFOV}}{2} = \frac{\text{IPD}}{2 \times \text{lens focal length}}$$

The region of space covered when scanning deflection currents are applied represents the total search or acquisition field-of-view.

Electronics drive the deflection coils in either a search mode (scanning the acquisition field-of-view) or in the track mode (scanning about a target). In the track mode, the modulated tube output signal is processed to produce internal X and Y error outputs. These errors are used as feedback to the deflection coils to correct for target position and velocity errors. Image intensity, target presence, and X and Y position voltages are generated by the electronic processing circuits as information outputs.

(3) Detailed Operational Description. An explanation of the SIS (Figure 44) is best presented by describing a sequence that will be encountered in operation. The basis for selections of the various parameters is contained in Section IV, 2, d, (4). A pertinent detailed performance specification is presented in Section IV, 3.

(a) Acquisition Sequence. The search scan is digital with the central portion of the photocathode being sampled in a 256 × 256 element format. Sweep waveforms are generated in the search scan logic and D/A converter boxes of Figure 44 by converting the outputs of an 16-stage ripple counter to analog current. The first 8 bits (highest frequency) are converted to generate an X-axis staircase sweep and the last 8 bits are converted to generate the Y-axis staircase sweep. The waveforms are shown in Figure 45. The step rate will be 625 Hz, thereby giving a dwell time of 1 6 ms and a frame time of less than 105 sec. Normally, a 10-percent overlap of the elemental IPD areas throughout the scan is used to assure target acquisition. However, since the stellar image will be larger than the IFOV, the overlap can be eliminated and the number of acquisition steps decreased to reduce the acquisition time, if desired. A half-field search scan will be available on command, which will reduce the acquisition time to 26 sec. This feature can be utilized when the image is known to be close to boresight.

In the acquisition mode, the SIS is in an open loop configuration as compared to the track mode in which the video signal is demodulated to obtain position information. Offsets and/or drifts that might affect the acquisition sweep are prevented by use of solid state switches on the track loop and track sweep circuits.

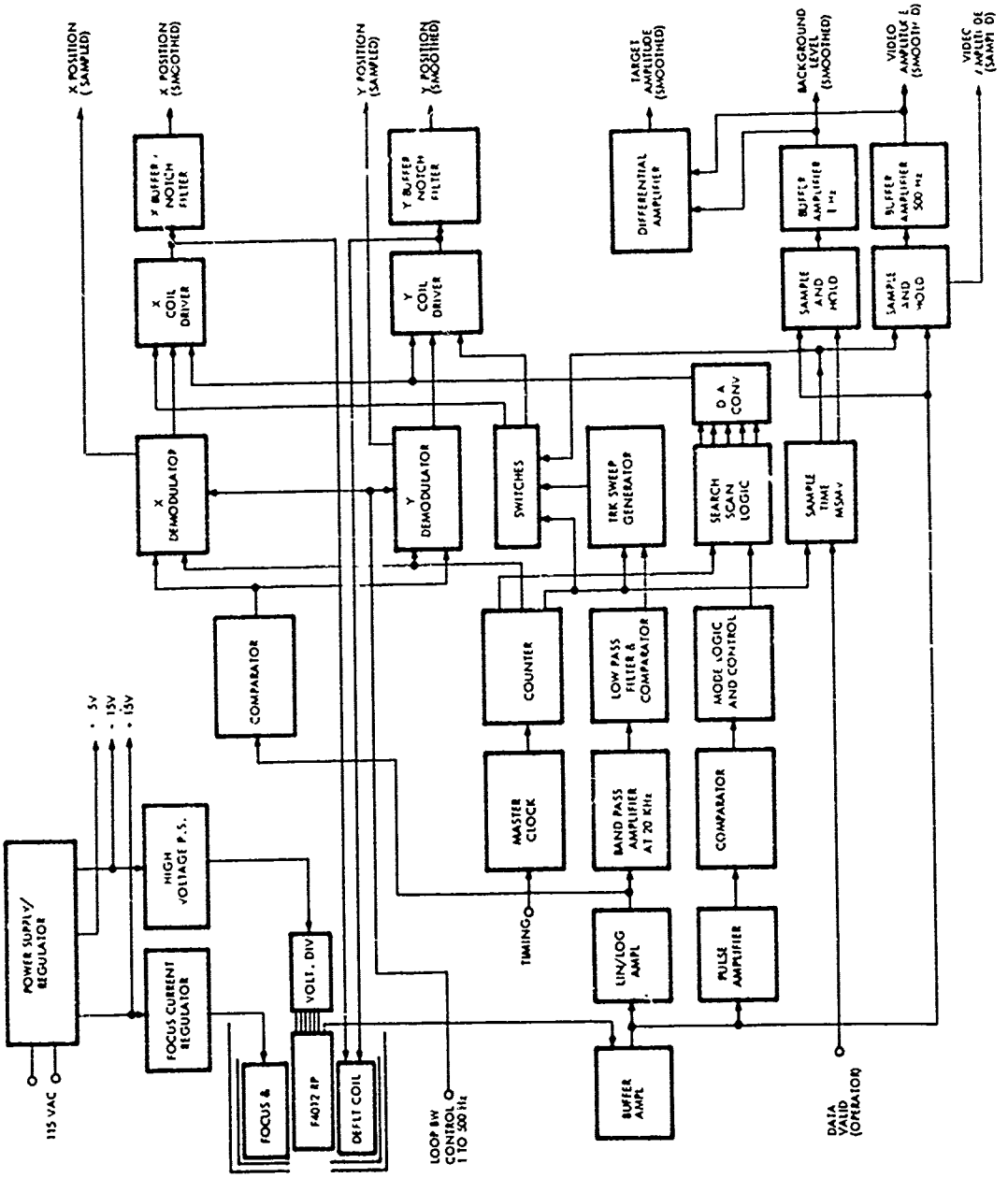


Figure 44 Star Image Sensor – Block Diagram

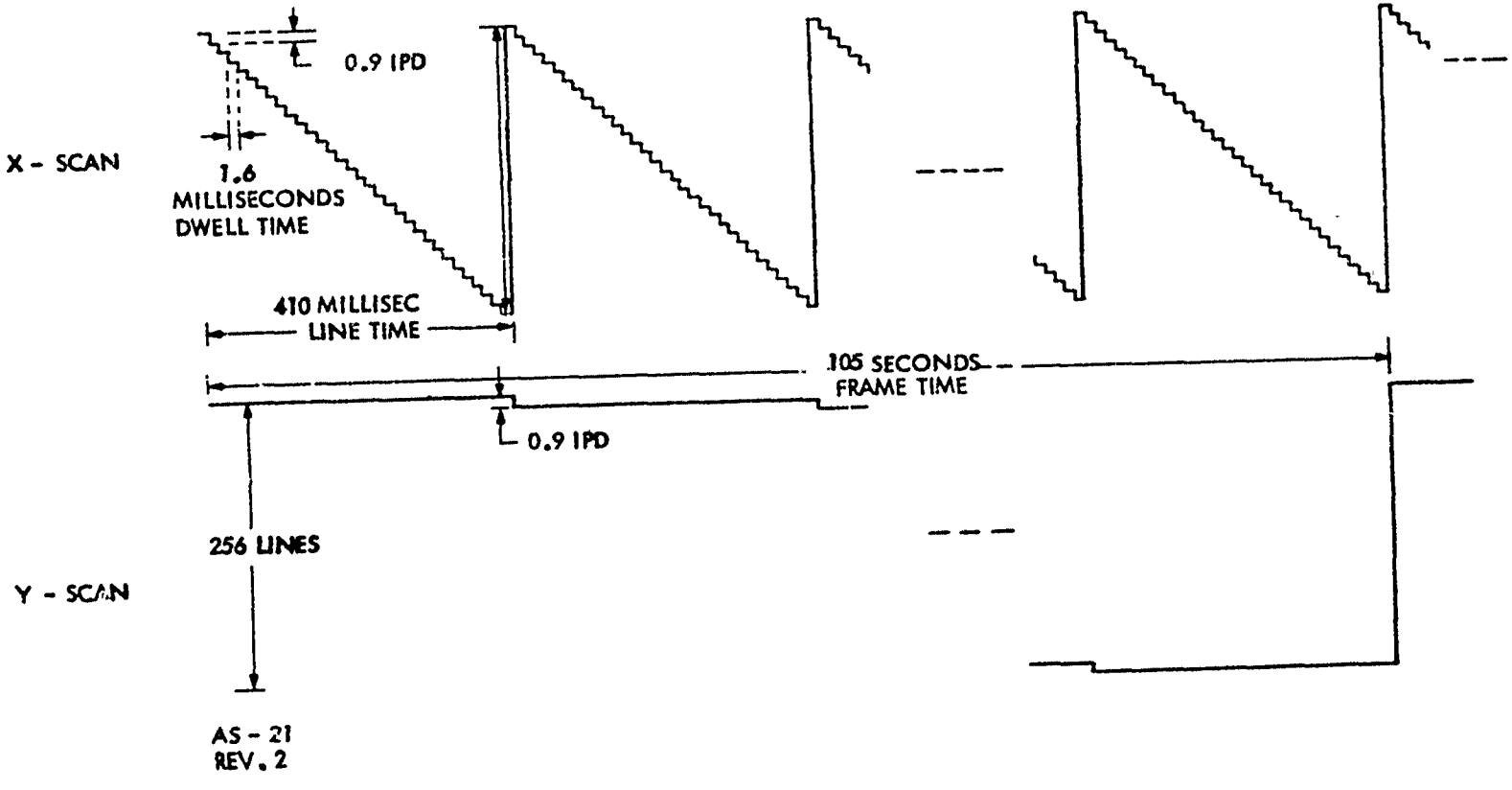


Figure 45 Search-Scan Waveforms

Video from stellar targets will be pulses of 1.6 ms duration with the magnitude dependent on the source brightness. The amplified video will then be compared to a constant threshold level in an operational amplifier comparator, and an initiation of acquisition will be generated when the video signal exceeds the threshold setting. An acquisition video bandwidth of approximately 200 Hz will pass the information while greatly attenuating noise pulses of short duration (high frequency).

When a pulse is received from the acquisition video comparator and the SIS is in the acquisition mode, operation in that mode stops, and track mode operation commences. The acquisition video-pulse resets a flip-flop in the mode control section, and the logic levels freeze the acquisition counter so that the deflection coil currents remain at the value that produced the video pulse. Simultaneously through electronic switches (FET's) the logic levels enable all circuits pertinent to tracking, namely, the sweep, demodulator and integrator.

(b) Operation in the Track Mode. The track sweep is an analog cruciform scan of 5 kHz with individual X- and Y-axis waveforms as shown in Figure 46. A 5-kHz scan frequency has been selected because experience has indicated that it should be at least 10 times the 500-Hz tracking loop bandwidth. The scan amplitude is ± 3 IFOV to ensure that the scan extends beyond the Airy disc. (The disc may be four or five times the IFOV.) Background sampling is taken near the end of the scan while the IFOV is beyond the Airy disc. The scan causes a pulse width and pulse position modulation of the video signal. The image intensity is sampled during the time t_s when the deflection current is zero so that the sampled signal will not be modulated. This sampling period will be range from 0 to 35 μsec under the operator's control.

The track-video signal is a waveform of approximately 50-percent duty cycle at 20 kHz (four times the track scan frequency). The video is amplified and limited, thereby providing a position and duration modulated pulse train to the demodulator. The track video amplifier will utilize a lin-log amplifier to ensure that the limiting takes place only in the comparator. In this way, the amplifier bandwidth is predictable and delays and slew rate variations, which are potential sources of position indication shifts, are eliminated.

The video pulse train is synchronously demodulated to obtain output analog error signals proportional to the angular distances (in two orthogonal directions) between the center of the scan cross and the center of the star image. The synchronous demodulators use logic gates to steer the video. The gates are controlled by the waveforms that generate the track and sweep. The transition to track takes place when a video pulse is received. The IPD can be anywhere within the image and most probably is not at the exact center. The demodulator error signals are fed,after amplification and integration, to summing amplifiers that generate target position correction to the initial cross scan position. The integral drive forces a correction until the demodulator error is zero. The cross scan is then centered on the star.

The track mode is characterized by a Type-1 control loop, where any movement within the IFOV results in an automatic correction to the d-c deflection coil current so that the cruciform scan remains centered on the star image. This loop will have a bandwidth controllable from 1 to 500 Hz. Track lock is maintained by detecting the 20-kHz

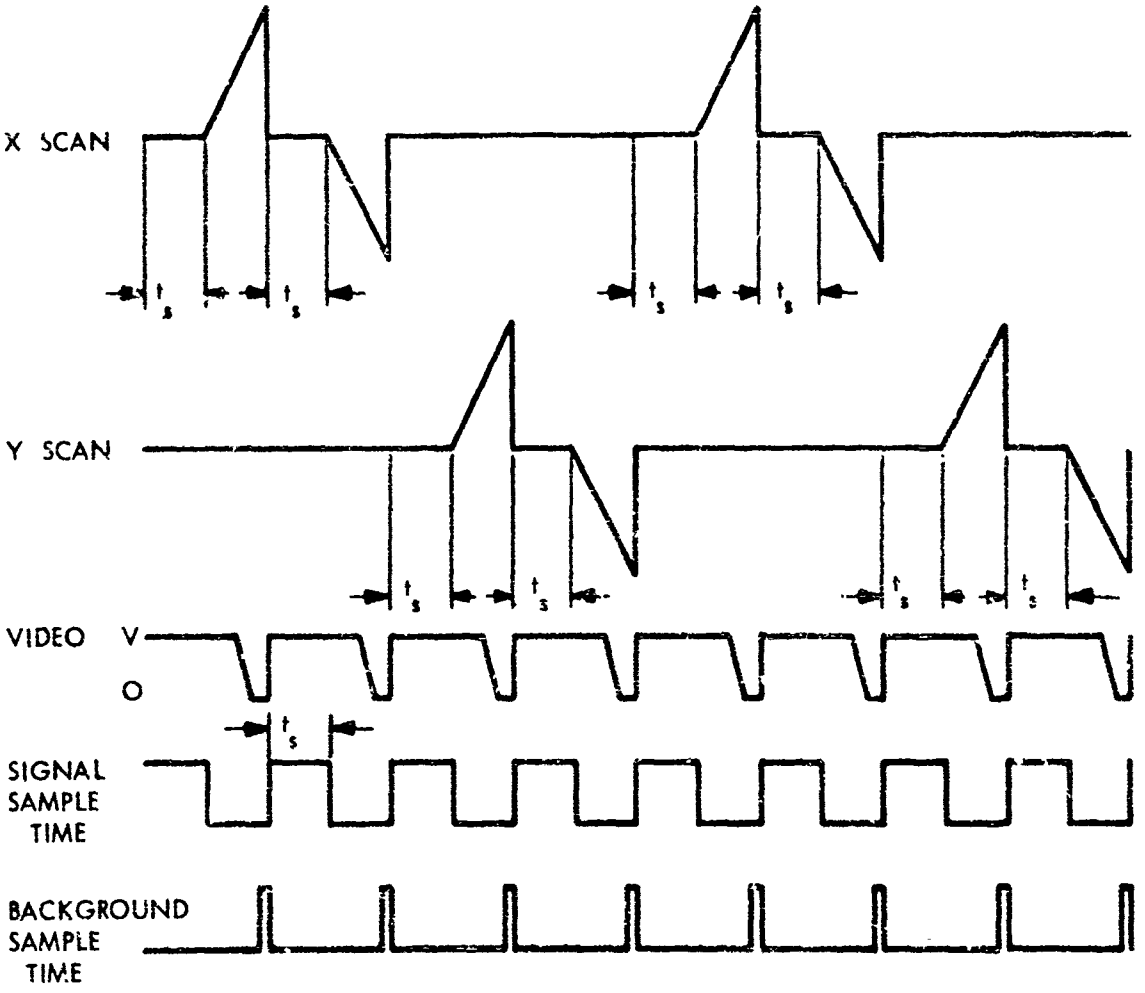


Figure 46 SIS Spatial Relationship

frequency component of the video. The video is filtered in a bandpass amplifier centered at 20 kHz. The output is envelope-detected and averaged. The analog level is compared to a set threshold value, and a digital star-presence signal is generated. The star-presence level indicates that meaningful position outputs are being generated. The loss of the star-presence signal automatically returns the SIS to the acquisition model. In like manner, if the track mode is initiated on a noise pulse, a star-presence signal will not be generated, and the acquisition mode will commence within milliseconds.

The background will be sampled during a 2-μsec interval when the star image is not in the IFOV, as shown in Figure 46. The background level will be available as an output which will have a 1-Hz bandwidth. The difference between the video and background signals is the image intensity output.

Because the effective integration time of a 1-Hz bandwidth filter is $\simeq 0.5$ sec, and because the sampling rate is 20 kHz (see above, this section) the effective number of samples integrated is 10,000. Assuming that the S/N ratio for individual samples will not be less than 1 to 1, the background measurement channel output will have an S/N ratio $\geq 1 \times \sqrt{10,000} = 100$. As this S/N ratio value is much greater than that of the star intensity samples, subtraction of the smoothed background value will contribute negligibly to overall measurement error. This conclusion would not be valid if the background level fluctuated appreciably during the 0.5-sec effective integration time, but the background is expected to remain constant during such short periods. Over longer periods, background variations will be sensed and, because the background value is subtracted from the star intensity sample values, such longer term variations will not affect the accuracy of star intensity measurements. As a precaution against the possibility of errors due to unusually rapid background fluctuations, additional circuitry will be provided to sense short-term (~ 0.01 sec) fluctuations of background and produce an alerting signal (data invalid) if the fluctuation magnitude exceeds a preset threshold.

(4) Analysis of SIS Operation. An analysis of the factors that define the performance characteristics of the SIS is presented in this section. First, the background photo current for daytime operation is calculated because the latter imposes a much more severe restriction than does night-time background. Next the signal current is determined as a function of lens diameter. Using these, the noise equivalent angle and signal-to-noise ratio for two different scanning patterns are calculated. These two factors, taken together, provide a good measure of the performance capabilities of a given SIS configuration. In order to establish operational limits for the system, a determination is then made of the minimum lens diameters, for given bandwidths, necessary to achieve tracking. Finally, the results of the analysis are briefly summarized.

(a) Preliminary Considerations. One of the requirements of the SIS is to separate the background signal from that of the target. Initially a two-aperture image dissector, with one aperture for the signal and the other for background, was considered. However, a preliminary analysis of such a dual-aperture arrangement showed that the background current collected in the larger tracking aperture was of the same magnitude as the signal current collected in the smaller tracking aperture. As the background current was present even when measuring the signal intensity, this scheme was judged to be unworkable and was ruled out. Instead, a single aperture will be used, and the SIS will be instrumented to sample the background during periods when the instantaneous photocathode diameter is not on target. The background signal will be subtracted from the total signal to generate the target signal of interest.

Initially, the analysis in this section parallels that presented in Appendix IV. It then extends into the consideration of the star tracker design parameters. The pinhole aperture size defined in Appendix IV, Eq. (28), will be used in this analysis. From Eq. (28) of Appendix IV, therefore:

$$\alpha = 0.294\, f\lambda$$

where

α = the desirable aperture radius

f = optics f-number

λ = spectral wavelength in meters
$\equiv 0.5 \times 10^{-6}$ m

(In order to stay consistent with nomenclature used by ITT/Gilfillan, IPD (instantaneous photocathode diameter) will be used subsequently instead of α).

Therefore,

$$IPD = 0.588\, f\lambda$$

$$\text{and IFOV} = \frac{588\, f\lambda}{F} = 0.588\, \lambda/D$$

where F = optics focal length (m) and D = primary aperture diameter (m).[17]

(b) Calculation of Background and Signal Current. The ability to track stars during daylight is much more difficult to achieve than under nighttime conditions. The analysis therefore will be directed toward the more severe conditions. In order to analyze various performance characteristics, the stellar and background signals must be determined.

(1) Background Current. The P(photocathode) current due to the background is:

$$I_{BG} = N\omega\Delta\lambda\, kg \frac{\pi D^2}{4} T_o$$

where

N = background radiance (blue sky)
$\equiv 3 \times 10^{-3}$ w cm^{-2} ster^{-1} micron^{-1}

ω = IFOV in steradians
$\equiv (\pi/4)\left(\frac{0.588\lambda}{D}\right)^2$

$\Delta\lambda$ = spectral bandwidth (μ)
$\equiv 0.2\ \mu$

[17] D. L. Fried (See Appendix IV) indicated a preference for a round pinhole aperture during a meeting on 8 Aug 1972, and the round type will be used instead of the square aperture conventionally used in star trackers.

kg = S-20 responsivity (including mesh)
$\equiv$ 0.021 A/W

D = optics diameter (cm)

T_o = optics transmission
$\equiv$ 0.7

Therefore

$$I_{BG} = 4.7 \times 10^{-15} \text{ (amperes)}$$

(2) Signal Current. Based on the ITT/Gilfillan ODC Daylight Study (Reference 14), 57 percent of the available power from a G0 star (6000-K blackbody) is within the S-20 spectral band and 26.5 percent is within the 0.4 to 0.6 micron band. Based on the measurements of Forbes and Mitchell (References 15 and 16), the former case (57 percent) corresponds to 9×10^{-13} w·cm^{-2} for a 0^m star.

Therefore, H_o (stellar irradiance) in the tracker spectral bandwidth is

$$H_o = 9 \times 10^{-13} \left(\frac{26.5}{57}\right)$$

$$= 4.18 \times 10^{-13} \text{ w cm}^{-2}$$

The PC signal current for this source is

$$I_s = H_o \frac{\pi D^2}{4} T_o T_a \, kg \, K_i$$

where

D = optics diameter (cm)

T_a = atmospheric transmission
$\equiv$ 0.5

K_i = fraction of image energy in IPD
$\equiv$ 0.175 (from the report)

Therefore

$$I_s = 4.22 \times 10^{-16} D^2 \text{ (amperes)}$$

In order to compare these results with results shown in Appendix IV, I_s is calculated for a D of 10 cm, as follows:

$$I_s = 4.22 \times 10^{-14} \text{ A}$$

From this

$$\frac{I_s}{I_{BG}} = \frac{4.22 \times 10^{-14}}{4.7 \times 10^{-15}}$$

$$= 8.98$$

From Eqs. (34) and (37) of Appendix IV:

$$\frac{I_s}{I_{BG}} = 25.1$$

The primary reasons for the difference between these two results are use of a 0.5 atmospheric transmission and 1.5 times less signal irradiance than that used in Appendix IV.

Based on the present analysis, a graph of the currents for the optics diameter range can be constructed as shown in Figure 47.

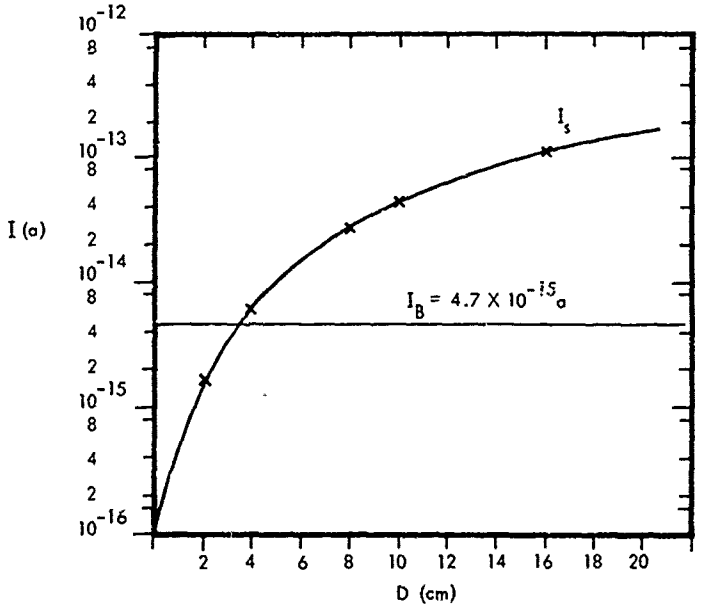


Figure 47 Signal Current as a Function of Lens Diameter

(c) Determination of Noise Equivalent Angle (NEA). It is considered desirable to have an NEA no larger than 0.125 IFOV in order to avoid dilution of atmospheric measurements by noise. A calculation of NEA is presented below to determine the conditions under which this criterion can be satisfied.

The NEA formula used is a model developed by ITT-G which has been verified by empirical means on a number of trackers. The factor 0.707 accounts for the 50-percent duty cycle of the video. In parametric form

$$NEA = 0.707 \frac{\left[2\, e \frac{\sigma}{\sigma - 1} (I_s + I_{BG})\, \Delta f\right]^{1/2}}{I_s} (IFOV \cdot D_1)^{1/2}$$

where

e = electronic charge
$\equiv 1.6 \times 10^{-19}$ coulombs

σ = F4012 individual dynode gain
$\equiv 3$

Δf = tracker bandwidth (Hz)

D_1 = image size (arc-sec)

IFOV = instantaneous field-of-view (arc-sec)

Since the IFOV changes as the optics diameter and focal length change, NEA will be expressed in terms of IFOV. The factor $(IFOV\, d_1)^{1/2}$ for diffraction limited optics can be expressed as

$$(IFOV\, d_1)^{1/2} = (IFOV \frac{2.44}{0.588} IFOV)^{1/2}$$

$$\simeq 2.04\, IFOV$$

The expression for NEA can now be written as

$$NEA = 1.4 \times 10^{-9} \left(\frac{I_s + I_{BG}}{I_s}\right)^{1/2} (\Delta f)^{1/2}\, IFOV$$

Using this expression and the values for I_S and I_{BG} previously computed (Section IV, 2, d(4)), a set of parametric curves can be drawn for NEA/IFOV versus tracking loop bandwidth (Figure 48). Although these curves are for daylight tracking conditions, one curve for nighttime ($I_{BG} << I_S$) has been included. For lens diameters greater than 10 cm, the background is much less than the signal current, as can be seen in Figure 47, and day and night performance will be comparable.

From Figure 48 it is seen that an optics diameter of at least 5 cm will be required to attain an NEA of 0.125 IFOV or less with a bandwidth of 100 Hz or greater.

(d) Analysis of Image Intensity Information. The amplitude at the center of the Airy disc is the output of the SIS of primary interest. With a cross-scan pattern, the center of the image is crossed or sampled four times each cross scan cycle. First, the performance of a tracker using a cross-scan pattern of the type normally employed in in ITT-G star trackers will be analyzed. The scanning waveform is shown in Figure 49. Referring to this figure:

$$t_s = S_d \frac{t_{cs}}{4}$$

where

t_s = sample time (sec)

S_d = ratio of sample time to the maximum possible sample time

The number of samples (N) related to the track loop BW Δf is

$$N = \frac{1}{\Delta f} \times 4 f_{cs}$$

$$= \frac{4 f_{cs}}{\Delta f}$$

The composite integration time for the information is

$$t_i = N t_s$$

$$= \frac{4 f_{cs}}{\Delta f} \times S_d \frac{t_{cs}}{4}$$

$$= \frac{S_d}{\Delta f}$$

The bandwidth of the video samples, denoted by f_i, can be expressed as

$$f_i = \frac{\Delta f}{S_d}$$

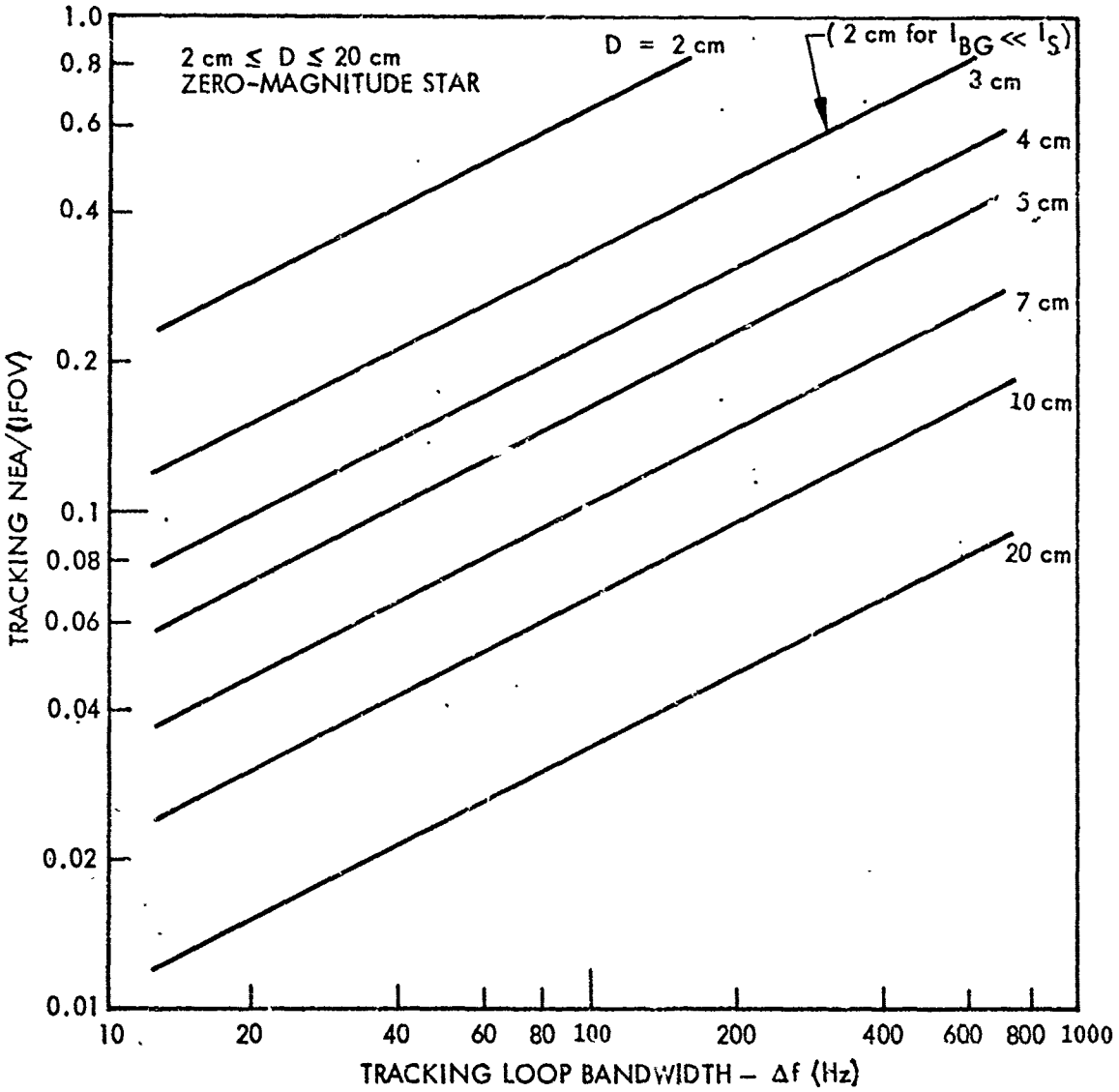


Figure 48 Tracking NEA Vs. Tracking Loop BW

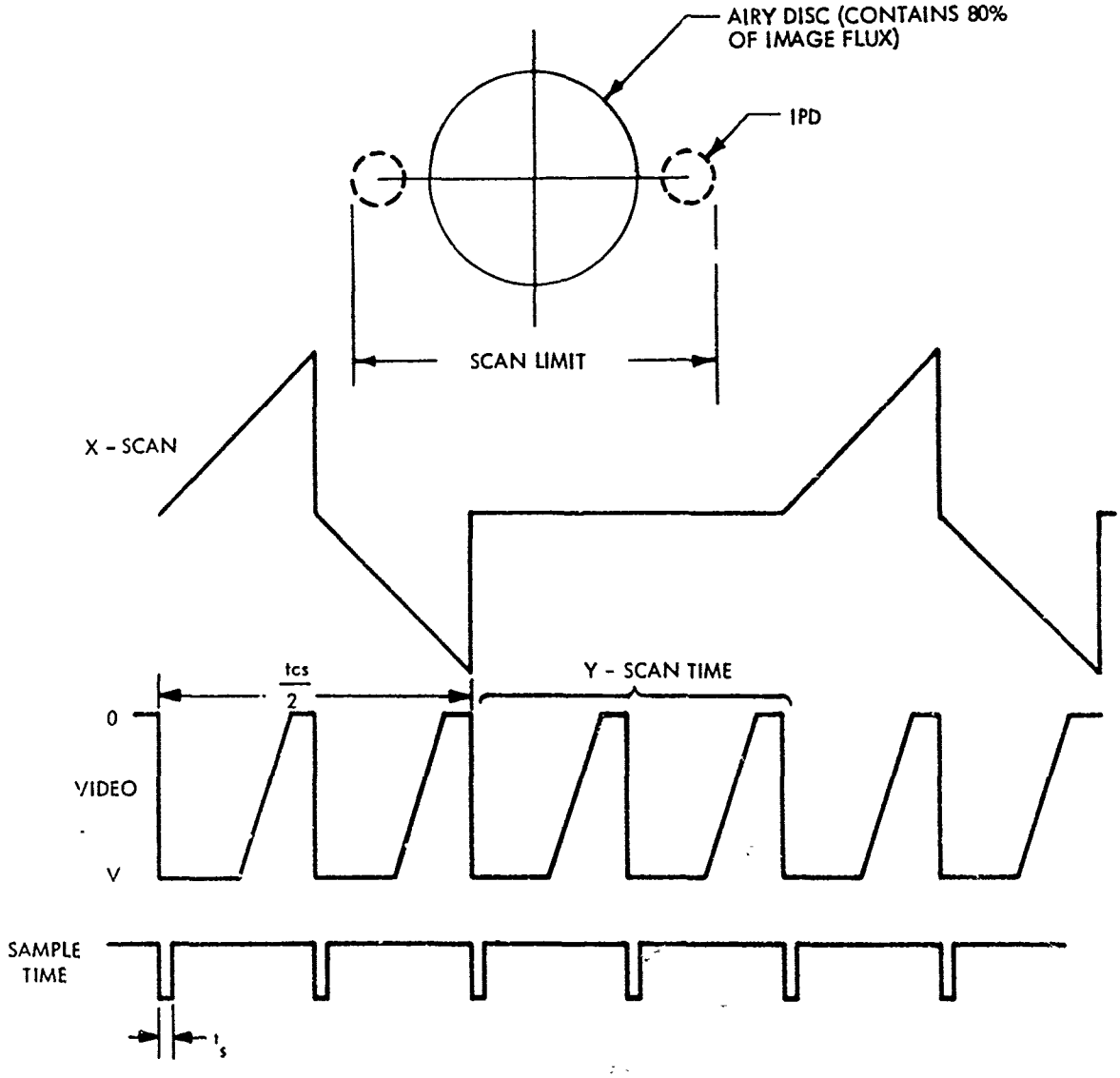


Figure 49 Spatial Relationship

The video S/N ratio is

$$\frac{S}{N} = \frac{I_s}{\left[2\, e \frac{\sigma}{\sigma - 1}\left(I_s + I_{BG}\right) f_i\right]^{1/2}}$$

where

f_i = video amplitude bandwidth

If $D > 10$ cm so that $I_{BG} << I_s$,

$$S/N = \left(\frac{I_s}{2\, e \frac{\sigma}{\sigma - 1}\, f_i}\right)^{1/2}$$

$$= \left(\frac{4.22 \times 10^{-16}}{2 \times 1.6 \times 10^{-19} \times 3}\right)^{1/2} D\left(\frac{S_d}{\Delta f}\right)^{1/2}$$

$$S/N = 21 \frac{D\left(S_d\right)^{1/2}}{\Delta f^{1/2}}$$

The next step is to sample the image at the center of the Airy disc. Because the pinhole moves three IPDs during the time interval ($t_{cs}/4$), the maximum possible sampling ratio S_d is 1/3 . However, it is probable the S_d will have to be 1/9 or less ($0.33 \times 1/3$) in order to assure that only the center and not the skirts of the image are sampled. On the basis of this rather arbitrary assumption:

$$S/N = \frac{7D}{\Delta f^{1/2}}$$

A graph of S/N versus Δf for various values of D is shown in Figure 50.

From the preceeding analysis, it is evident that a longer sampling time is desirable. Therefore, the scanning pattern will be modified, shown in Figure 51, to include a period for sampling during which the scan deflection is zero.

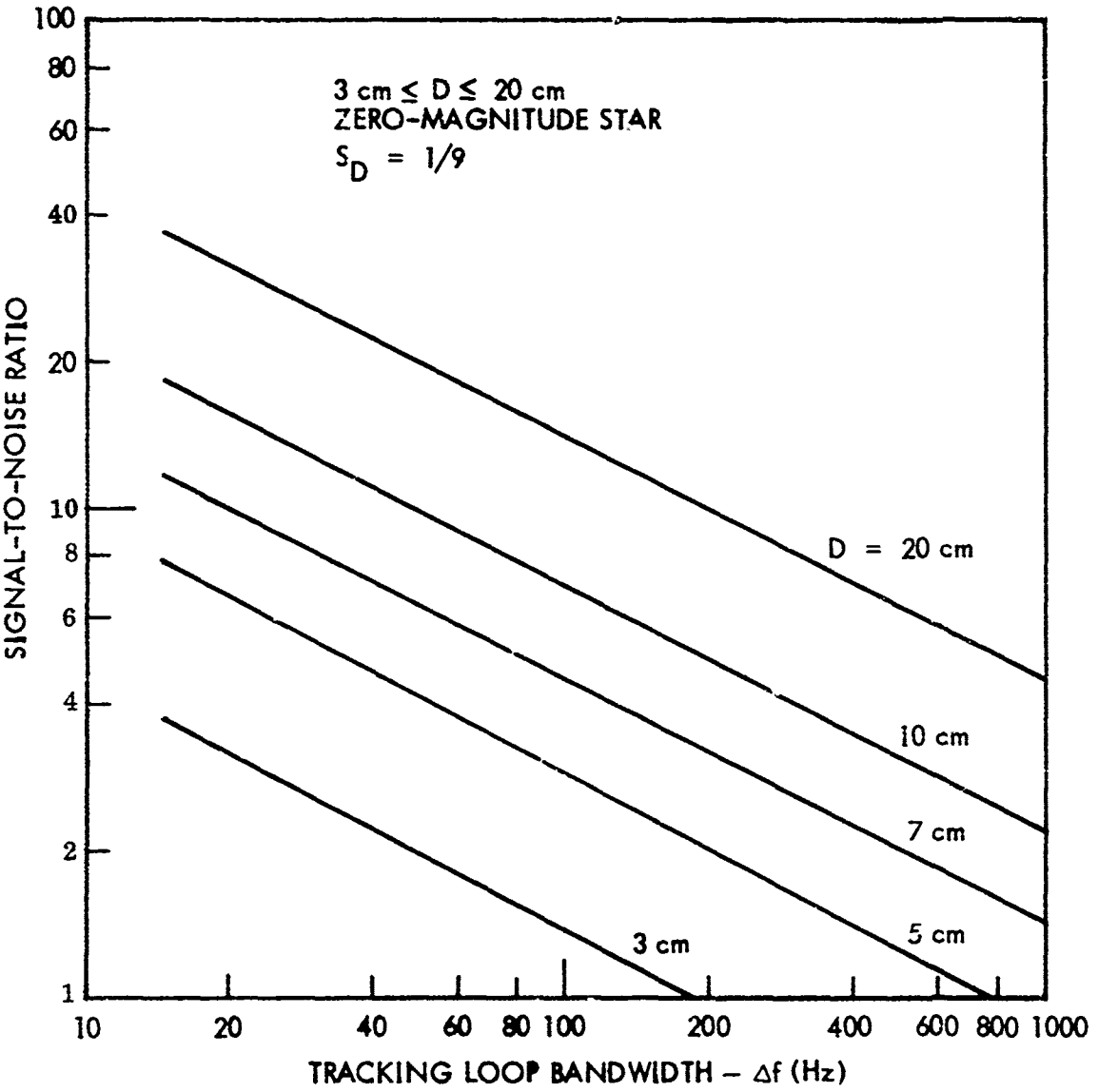


Figure 50 Amplitude S/N Ratio Vs. Sample BW

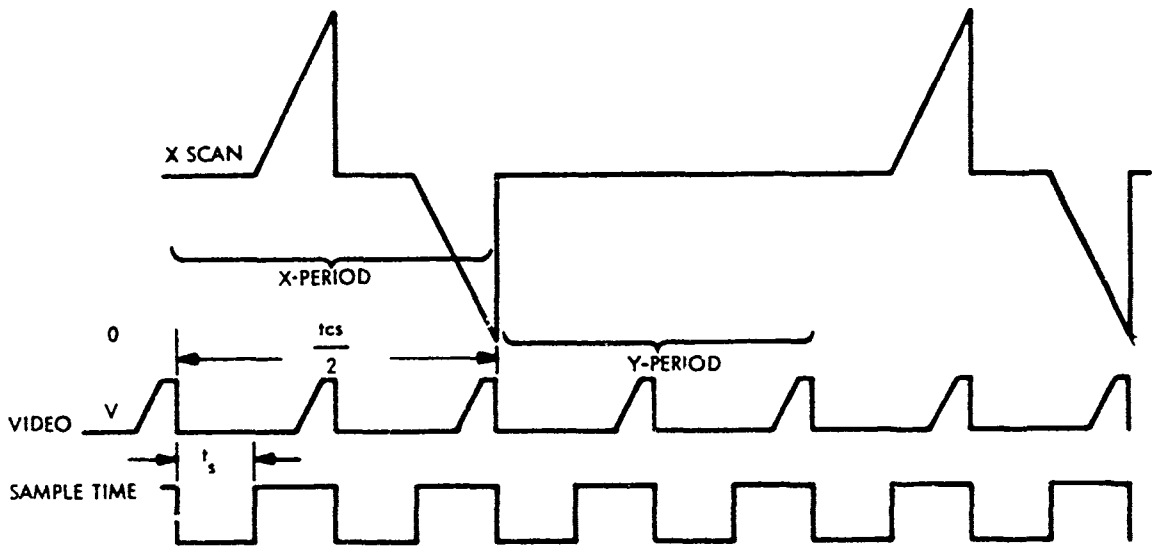


Figure 51 Spatial Relationship to Provide a Sampling Period With Zero Scan Deflection

Where previously an $S_d = 1/9$, it now can become 1/2 (which is again arbitrary). Therefore, the video S/N ratio is increased by the factor $\sqrt{4.5}$ or 2.12. These results are shown on a new plot shown on Figure 52.

It should be noted that the NEA increases,due to loss in angle S/N ratio. The loss is the result of crossing the image edge faster than before. Comparison of the video rise times for the sweeps shown on Figures 49 and 51 indicates a factor of two difference. Therefore, the NEA will increase by a factor of $\sqrt{2}$ or 1.4. The new NEA is shown in Figure 53.

(e) Determination of Minimum Usable Lens Diameter. It is useful to determine the constraints imposed on the selection of lens diameter and tracking loop bandwidth, when the only requirement on the tracker is that it be capable of acquiring and maintaining track. In other words, no requirement as to tracking accuracy is imposed. Experience has shown that approximately 20 electrons per sample period are required for reliable tracking. During each scan period, 1/4 of the time is utilized to develop tracking information,because the total signal is divided between two channels and half of the time is used for intensity measurement. (See Figure 51). Therefore, the sample period is

$$t \approx \frac{1}{4} \times \frac{1}{\Delta f}$$

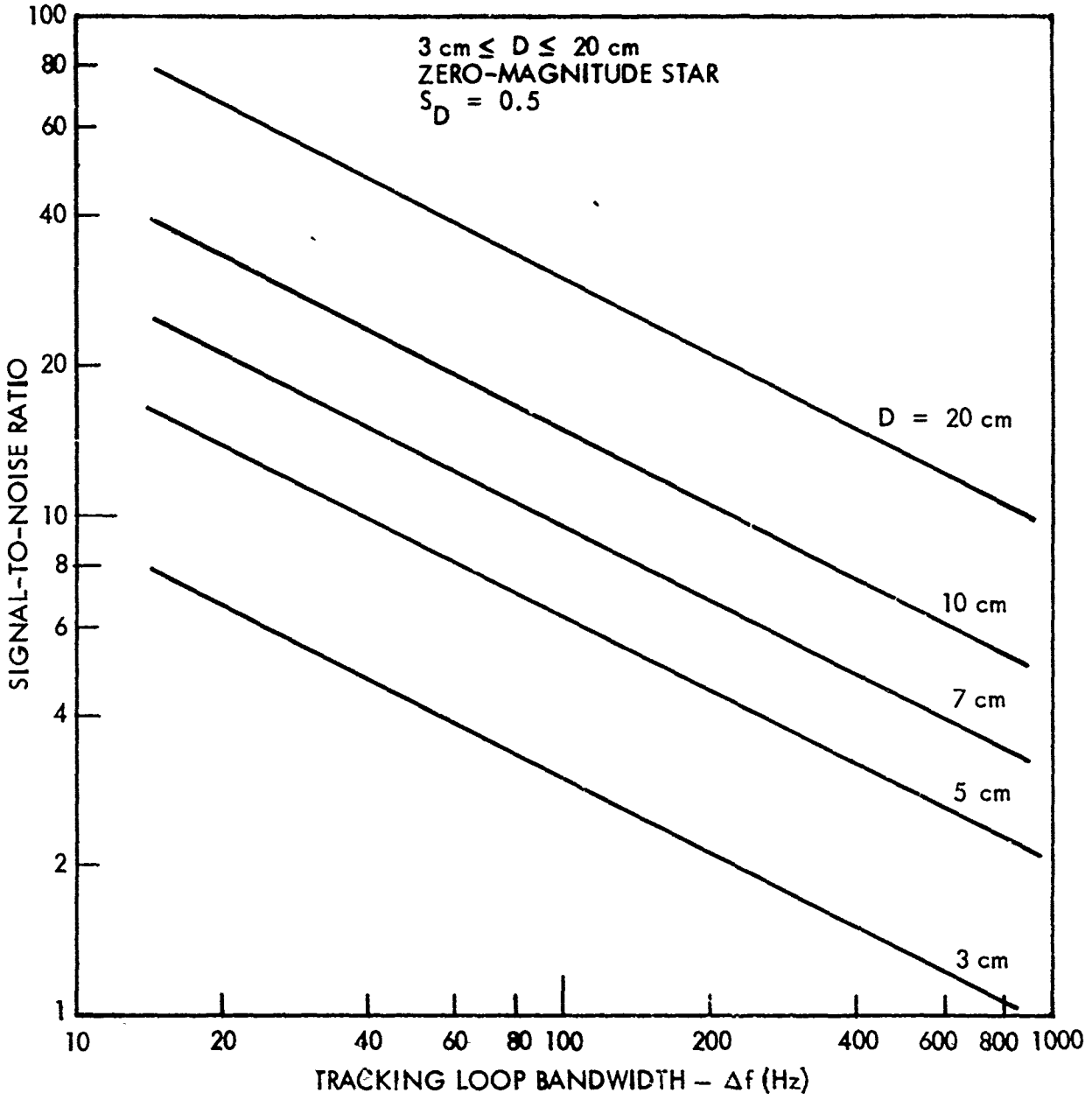


Figure 52 Amplitude S/N Ratio Vs. Sample BW — Modified Scanning Pattern of Figure 51

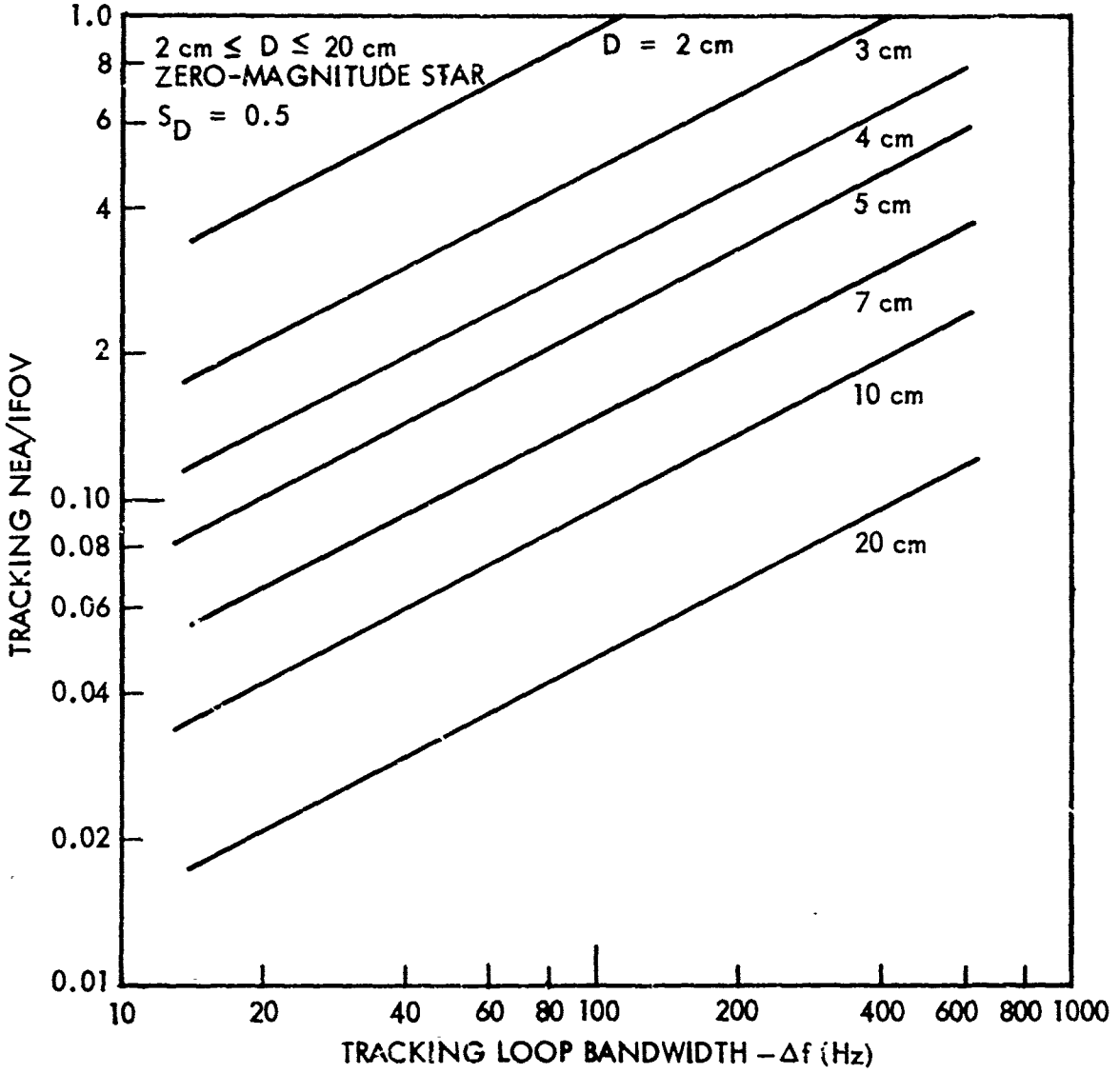


Figure 53 Tracking NEA Vs. Tracking Loop BW for Modified Scanning Pattern of Figure 51

where

Δf is the tracking loop bandwidth (Hz)

The number of electrons N_e collected during the sample period is equal to

$$N_e = \frac{I_s \Delta t}{1.6 \times 10^{-19}}$$

This expression has been calculated for various stellar targets and is presented graphically in Figure 54.

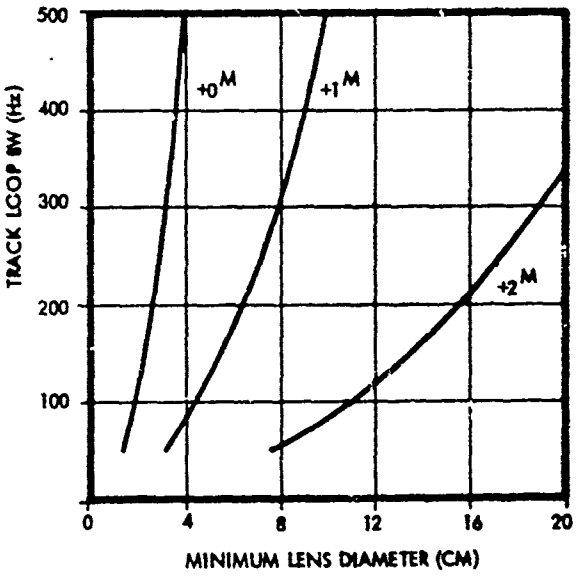


Figure 54 Minimum Lens Diameter Vs. Tracking Loop Bandwidths for Different G-0 Star Magnitudes

(f) Summary of Conclusions From Analysis. Of the two implementation techniques considered, the one in which the sampling time can be adjusted has been selected for an operational system because of the experimental flexibility it provides.

Since it is considered desirable for the NEA to be less than 0.125 IFOV when data are being collected, the curves in Figure 53 define the limiting telescope aperture for a zero magnitude star. Information regarding the number and brightness of stars and definition of stellar magnitude may be found in Reference 17. For a 20-cm lens diameter and a 500-Hz tracking loop bandwidth, the NEA is approximately 0.125 IFOV. Therefore, no star that is dimmer than a zero magnitude can be tracked during daylight and yet permit achievement of an NEA of 0.125 IFOV under these conditions. With smaller bandwidths, dimmer stars can be tracked or smaller lens apertures used.

Figure 53 can be used to calculate the NEA for other than zero magnitude stars. For lens diameters greater than about 10 cm, the signal current is greater than the background. (See Figure 47.) Therefore, the NEA for an M magnitude star can be obtained by multiplying the NEA from the curves of Figure 53 by $(2.5^{M})^{1/2}$. For example, a first-magnitude star can be tracked with an acceptable NEA, provided that a 20-cm lens diameter is used and the tracking bandwidth is no more than 270 Hz. For lens diameters greater than 10 cm, there is essentially no difference in the NEA for day and night conditions. For lens apertures less than 10 cm it will be necessary to construct additional curves using the expressions for NEA, I_s and I_{BG} as shown in Section II, 2, d, (4).

By comparing Figures 53 and 54, it can be seen that the system is not signal-electron limited in that there is a sufficient number of electrons for tracking even when the NEA is too large for the data collected to be very useful.

The requirements for the SIS that tracking precision (NEA) be better than 0.125 IFOV will be met for first-magnitude stars when using 20-cm optics and a 250-Hz tracking loop bandwidth. The same requirements are met with a 500-Hz bandwidth for zero-magnitude stars.

(5) Peripheral and Test Equipment. The measurement system will be self-contained, relying only on external power for operation. In addition to the major components described in the previous sections, the following equipment is required:

- Pulse oscillator (simulating external clock)
- Auto-collimator-Kollmorgen Model K222
- Simulated target source

- Oscilloscope – Tektronix Model 454
- Digital voltmeter – Non-Linear Systems Model 2900
- Microvolt-Ammeter – Hewlett Packard Model 425A
- Multimeter

An operator control console will be a part of the equipment supplied and will contain displays and controls as required to control and monitor the operation of the system.

e. Operational Considerations

(1) Data Interface. In this section, the telescope pointing and parameter settings that must be calculated by the digital computer in the data processing subsystem before experiment initiation will first be outlined and the mathematical functions to be evaluated will be stated. Then, the control and data signal flow between the SIS and the data processing system will be described.

(a) Target Acquisition. In order to acquire a known star as the target, the telescope must be pointed to the target with sufficient accuracy to assure that it will be within the FOV of the SIS. Although the field-of-view can be in the range of 1.4 to 11.8 arc-min, target designation accuracy must be such as to assure acquisition for the smallest FOV (1.4 arc-min). The computation required involves starting with star position data available in standard star catalogs and then extrapolating the position based on the location of the site and time (GMT). The atmospheric refraction at elevation angles from 20 to 70 deg is sufficiently large (Table 5) so that the computation of the star position must take into account the difference between the true and the apparent star position. The data contained in Table 5 or mathematical model must be used in the computation.

At least two fully developed programs for performing these computations are available. One is the advanced radar calibration system (ARCS) developed by SAMTEC at Vandenberg Air Force Base and the second is the portable automatic calibration tracker (PACT) from the NASA Goddard Research Center. The computations used at Vandenberg AFB are contained in Appendix VI. This approach cannot be used without modification in this application because of the differences in mounts. An estimate of the required computer memory is difficult to achieve because of differences in computers. However, based on discussion with the personnel at Vandenberg AFB, it is fairly safe to assume that no more than 500 to 600 30-bit words will be required. This includes storing position data for 75 stars.

(b) Aberration Correction. In accordance with the development in Section IV, 2, b(4), the chromatic corrector in the optical train must introduce the angular dispersion $d\theta$ given by the following expression:

$$d\theta = 6.2 \times 10^{-6} \tan (90 \text{ deg} - E)$$

where E is the elevation angle of the telescope axis relative to the horizontal. This correction must be applied in a vertical plane, but the chromatic corrector must be positioned with respect to the axes of the telescope body in which it is mounted. Because the telescope body will rotate relative to the vertical during normal operation, a counter-rotation R must, therefore, be applied to the corrector.

Table 5. Astronomical Refractions[a]

Apparent Elevation Angle (Deg)	Astronomical Refraction (Min)	Apparent Elevation Angle (Deg)	Astronomical Refraction (Min)
2	18.2	10	5.3
2.5	16.0	11	4.8
3	14.3	12	4.6
3.5	12.8	14	3.8
4	11.6	16	3.3
4.5	10.7	18	2.9
5	9.8	20	2.6
5.5	9.0	25	2.0
6	8.4	30	1.7
6.5	7.8	40	1.2
7	7.3	50	0.8
7.5	6.9	60	0.6
8	6.5	70	0.4
8.5	6.1	80	0.2
9	5.8	90	0.0
9.5	5.5		

(a) See Reference 17.

Accordingly, to properly adjust the chromatic corrector, the elevation angle E must be known so that $d\theta$ can be calculated from the above expression. Also, the telescope rotation angle R must be known so that the corrector element can be properly oriented with respect to the telescope barrel.

Expressions for angles E and R are derived in Appendix VII in terms of the following principal mount angles:

- Site latitude base tilt angle = β
- Right ascension angle = γ
- Declination angle = α

These expressions are as follows:

$$E = \tan^{-1} \frac{\sin\alpha \cos\beta \cos\gamma + \sin\beta \sin\gamma}{(\cos^2\alpha \cos^2\gamma + \sin^2\alpha \sin^2\beta \cos^2\gamma + \cos^2\beta \sin^2\gamma - 2 \sin\alpha \sin\beta \cos\beta \sin\gamma \cos\gamma)^{1/2}}$$

$$R = \cos^{-1} \frac{\cos\alpha \cos\beta}{[(\sin\alpha \cos\beta \cos\gamma - \cos\beta \sin\gamma)^2 + \cos^2\alpha \cos^2\gamma]^{1/2}}$$

The zero reference for angle R is established in the telescope body by setting α, β, and γ to zero and rotating the chromatic corrector so that its angular dispersion axis is vertical. (See Appendix VII for an exact definition of angle R.)

In normal operation the chromatic corrector will be adjusted at intervals rather than continuously. As discussed subsequently, these adjustments can be made at the same intervals as those required for diffraction correction.

It is assumed that no targets below a 20-deg elevation angle will be tracked. The maximum chromatic correction will be required at the smaller elevation angles; at zenith, no correction is required. In going from a 20- to 25-deg elevation, d θ changes in 20 min by 0.635 μ radians. If the proper correction is made at 20 deg, this spread is sufficiently small to avoid the need for correction at 25 deg. Since both rotation and elevation angle are involved, an update once every 5 min is considered adequate. The computation therefore should be performed at 5-min intervals, and the data communicated to the measurement equipment operator.

For the 20- to 25-deg case discussed, the change in atmospheric refraction will change the apparent position of the target by 0.6 arc min. In the 5-min increment selected for updating the chromatic corrector, the target will remain within the quality field of view. Therefore, when the chromatic correction is made, the SIS should be bore-sighted. This can be accomplished manually by observing the SIS error outputs while the mount angles are changed. It may be easier to recompute the declination and right ascension angles, using the error outputs at 5-min intervals, if boresighting is found difficult.

It should be noted that near zenith, corrections are not necessary and computation will not be required for elevation angles ±5 deg from 90 deg. The chromatic correction will be set at zero when tracking stars in this cone angle.

(c) SIS Signal Outputs. The interface signals between the measurement equipment and the data processor were previously shown in Figure 39. With the exception of the "valid data" signals, all of the signals are generated in the SIS. The "valid data" signal will be generated in an OR circuit. One input will come from the SIS (target presence signal), and the other will come from an operator-controlled switch which will be activated at the discretion of the operator in response to system outputs. The various signal outputs from the SIS are described in detail in Section IV, 5, c, (2).

(d) System Timing. System timing, with respect to data, will employ a 40-kHz ±10-percent clock in the data processor. The SIS output signals will be synchronized to this signal. Adequate delays will be incorporated to assure that data are available when the SIS is interrogated. The timing details will be worked out during the implementation phase. In addition, an accurate clock in GMT, maintained to an accuracy of 1 sec, is necessary for the data processing unit to provide target pointing data.

(2) Equipment Setup. Prior to setting up the equipment at a site, some preparation will be required to provide a pier for the mount. Since the measuring equipment is extremely sensitive, the site selected should be located at a reasonable distance from roads which are subject to heavy vehicular traffic or other sources of potential acoustic and mechanical vibration. The location of the site must be fairly accurately known; a second-order survey is considered adequate.

The pier should be in the order of 3 ft deep, depending on local geological conditions. An overall pad approximately 14 ft-in.-diameter is required for the astrodome but need not be of uniform depth. Figure 41 indicates the mounting provisions required for the telescope. The sole plate (designed for the latitude of the site) on which the mount will be placed will be imbedded in the concrete, leveled, and oriented for the particular site. Mounting studs for the astrodome should also be imbedded in the concrete to facilitate assembly. Approximately 30 A of 60-Hz, 120-V power will be required. If a motor-generator set is used to supply the prime power, a "quiet" unit should be selected and located at least 100 ft from the mount.

The measurement equipment will be delivered to the site in disassembled form. The astrodome can be assembled in one day using local labor and an equal amount of time will be required for the telescope and mount. If the mount and telescope should be procured from Boller and Chivens, it is considered desirable to have their personnel perform the assembly and alignment. Lifting equipment, either a fork lift or small crane, will be necessary since some of the components cannot be safely lifted and put in place without mechanical assistance.

The optical and mechanical alignment procedures will be similar to those employed when setting up a conventional astronomical telescope. Some additional alignment will be necessary because of the added complexity of the optical system and the use of the SIS. The overall alignment is considered to be well within accomplishment by means of standard techniques and instrumentation. The detailed alignment procedures will be developed during the implementation phase of the program.

(3) Equipment Operation. After the equipment has been installed, aligned, and checked out, the operator will proceed as follows:

(a) Set the experimental initial parameters (i.e., focal length into the system.)

(b) Turn on measurement equipment 1 hr before start of data taking.

(c) Enter data on declination angle, right ascension angle, telescope rotation, and chromatic correction, using mount hand paddle and calibrated dials on the telescope for this purpose.

NOTE: These data are computed to be valid after a short period (e.g., 2 min) to allow sufficient time to make the above settings.

(d) On receipt of a signal from the computer, indicating time tracking must start, switch the mount into its tracking mode.

(e) If the target presence signal (indicating target acquisition and usually received within 30-sec of operation) is not received after approximately 2 min have elapsed, repeat steps (c) and (d) above. If a target is not acquired after a third attempt, check the system to determine reason for nonacquisition. Check functional alignment and obtain computational verification; also determine if cloud coverage or other weather conditions are preventing target acquisition.

(f) During data-gathering periods, monitor output signals; notify data-processing system (by means of DATA-VALID switch) if a tracking problem should occur.

(g) Tracking will continue for 5 min or more until computer determines that the initial system settings require change. At that time, the computer will transmit a Stop signal and updated data for target designation and telescope rotation. Reset telescope controls accordingly.

(h) Shut down system at end of scheduled data acquisition period.

3. DATA ANALYSIS AND RECORDING SUBSYSTEM

a. General Considerations

This section presents the results of the effort to define the data processing and recording requirements of the Atmospheric Transmission Measurement (ATM) System, and to prepare a preliminary design of a facility to meet these requirements. A further function of the facility was to perform certain computations required for experiment initiation, such as generation of telescope pointing commands, and for monitoring and altering measurement system parameters during the course of an experiment.

Because the atmospheric measurements will be made at mountain-top locations possibly remote from data processing facilities, it was considered essential to provide for on-side preliminary quick-look data analysis of selected data segments. Only in this way could a rapid assessment be made of the success or adequacy of the data-gathering operations just completed. Then, as necessary, the measurement conditions for subsequent operations could be modified appropriately. In addition, the data processing system should be capable of preprocessing the raw star-sensor data so that it could be recorded in a form suitable for subsequent detailed analysis at an established computing center. These considerations together with the need for rather complex computations to be performed in conjunction with experiment initiation led to a decision early in the study program to employ an all-digital approach to quick-look processing, data recording, and ancillary on-site computation requirements.

Section IV, 3, b details the Processing System Concept; Section IV, 3, c presents an overall description of a preliminary system design including both the hardware and software elements. Section IV, 3, d delineates the key system functions, describes the required performance characteristics, and presents computer configurations which will meet these requirements. Section IV, 3, e summarizes the processor system characteristics and cost tradeoffs.

b. Data Processing System Concept

The data processing system interfaced with the star-sensor will be used for the following:

- Assist in setting up and initiating the star tracking experiments
- Convert, process, and record the star image measurements during the experiments; assist the experimenter in maintaining the proper instrument settings during the experiments
- Retrieve, playback, analyze, and display selected intervals in the recorded data to provide a quick-look processing capability

(1) Setting Up and Initiating The Experiments. Prior to each experiment, the following functions must be performed:

(1) Select the star.

(2) Select the time to begin the star measurements.

(3) Adjust the telescope parameters so that the star image is properly sized in the sensing aperture.

(4) Set the telescope and optics parameters to correct for atmospheric dispersion.

(5) Point the telescope at the star and center the star image in the sensor.

(6) Initiate the measurements.

The data processor system will be programmed so that the experimenter can log the following necessary star and measurement parameters:

- Star identity
- Star astro table for which data may be logged at program load time
- Tracker station location
- Experiment initiation time
- Telescope aperture diameter and effective focal length
- Data scale factors

These will be used to carry out the experiment and document the experimentation conditions of the recorded measurement data.

Following the entry of the experimental parameters, a computer program will be called to determine the telescope pointing commands (i.e., right ascension and declination angles) on the basis of the astro table, site location, and initiation time, taking into account corrections for atmospheric refraction.

The program will also determine the chromatic correction control direction and magnitude settings. The experimenter will point the telescope manually and perform the chromatic correction settings. If the star is somewhere off-axis, the experimenter will adjust the right ascension and declination angles manually to place the star image close to the optical boresight. The computer will display the time-to-zero pointing error so that the experimenter will know when to turn on the telescope sidereal drive. The star should be acquired by the tracker within 26 sec after the mount is activated. When the experimenter observes that the star is being tracked properly, he will signal

the processor that the SIS measurements are valid (i.e., the acquisition procedure was successful). The processor will then initiate the experiment and commence processing and recording the SIS data.

(2) Processing and Recording the SIS Measurements. During the experiment, the processor will convert and record the SIS data together with a running voice commentary. Data will not be recorded while the sidereal rate, declination angle, or chromatic corrections are being changed. Sidereal rate and declination angle are sufficiently accurate in the open-loop mode so that corrections should not be necessary for periods up to an hour of tracking. However, if target lock-on is lost or the image moves to an area of poor optical quality, the SIS will alert the processor and the operator. Data recording will be interrupted by the processor while reacquisition is accomplished. The reacquisition procedure is essentially the same as the acquisition procedure.

Chromatic corrections may be necessary as often as every 5 min. The processor will compute a new correction every 5 min. on the basis of current telescope elevation and rotation conditions. If the correction is significantly different from the current settings, the processor will alert the operator and display the new settings. The operator will make the adjustments manually. This adjustment should take no more than 1 min. During this interruption, the data status line to the processor will be in the "invalid" state.

During an experiment, the processor will be recording SIS data in either a slow or a fast mode. Most of the data collected during an experiment, which could last 1 to 2 hr, will be recorded in the slow mode (at 1 to 2 kHz). At selected times, however, the mode will be changed under control of the experimenter to the fast mode (20 to 40 kHz) which will extend over a 1- to 3-min interval. At the end of this interval, the processor will return to the slow mode. The fast-mode operation is to be conducted while SIS data status is "valid," i.e., between chromatic corrections or mount axes updates.

If more data are received during an experiment than can be recorded on one magnetic tape, data recording will be interrupted (i.e., the data status will be made invalid) while a new reel is mounted manually; the mounting should require no more than a 5-min pause.

During the initiation and execution of an experiment, the output of an external clock source of 40,000 Hz will be supplied to the SIS system and the sensor data multiplexer. This basic clock rate could be set at any frequency in a ±10% range.

During the experiment, a display will be available to selectively examine SIS data being sent to the processing system. With this equipment the experimenter will be able to continuously monitor the pertinent system outputs and perform remedial action as necessary.

The characteristics of the SIS and voice signals to be processed and recorded are shown in Table 6 :

Table 6 . SIS and Voice Signal Characteristics

Symbol	Signal[a]	(V)	Digitizing Accuracy (bits)	Sampling Rate (kHz)[b]	
				Slow Mode	Fast Mode
A_i	Tracker Azimuth Error	±2.5	7	1	20 ±5
E_i	Tracker Elevation Error	±2.5	7	1	20 ±5
I_i	Star Intensity	0 to 5	10	2	40 ±10
B_k	Background Intensity	0 to 5	7	1 Hz	1 Hz
V_i	Voice Commentary	±5	7	3	3000

(a) A_i, E_i, I_i and B_K are referred to as X-error, Y-error, target amplitude (or star intensity), and background, respectively, in Section IV, 2.

(b) These rates were selected as a basis for initial design of the data processing system as being representative of the maximum rate of probable interest. System designs using 75 and 50 percent of these rates will be developed later in this section.

(3) Post-Experiment Quick-Look Processing. An on-site quick-look processing capability will be required following the completion of an experiment. This provision will enable the experimenter to select an interval of the recorded measurements on the basis of the Greenwich Mean Time (GMT) at which it actually started and request that it be played back, analyzed, and displayed. Following are analyses which may be performed on the data collected during the fast recording mode:

I. 1-msec Averaging Interval (500-Hz Effective Bandwidth)

(a) Azimuth rms tracking error $\overline{A}_j = \frac{1}{20} \sum_{i=1}^{20} A_i$

(b) Elevation rms tracking error $\overline{E}_j = \frac{1}{20} \sum_{i=1}^{20} E_i$

where the A_i and E_i, $i = 1(1)20$, are the tracker error signals sampled at the nominal 20K sample/sec rate over a 1-msec interval.

(c) Star intensity $\bar{I}_j = \frac{1}{40} \sum_{i=1}^{40} I_i - B_k$

(d) Log Star intensity $\bar{L}_j = \text{Log}_e \bar{I}_j$

where the I_i, $i = 1(1)40$, are the tracker video output samples taken at the nominal 40K samples/sec rate over a 1-msec interval.

II. 100-msec Averaging Interval:

(a) Azimuth rms noise[17]

$$\sigma_A \cong \left\{ \frac{1}{2000} \sum_{i=1}^{2000} A_i \cdot A_{i+1} - (\bar{A})^2 \right\}^{1/2}$$

$$\bar{A} = \frac{1}{100} \sum_{j=1}^{100} \bar{A}_j \qquad \text{from item I, (a) above.}$$

(b) Elevation rms noise

$$\sigma_E \cong \frac{1}{2000} \left\{ \sum_{i=1}^{2000} E_i \cdot E_{i+1} - (\bar{E})^2 \right\}^{1/2}$$

$$\bar{E} = \frac{1}{100} \sum_{j=1}^{100} \bar{E}_j \qquad \text{from item I, (b) above}$$

(c) Star mean intensity

$$\bar{I} = \frac{1}{100} \sum_{j=1}^{100} \bar{I}_j \qquad \text{from item I, (c) above}$$

[17] This method of calculating σ_A avoids biasing of the result by uncorrelated photocurrent noise, as demonstrated in the addendum to Appendix V. The quantity actually calculated is the covariance of the sampled output variable A with a time shift of one sample period. When precautions are taken in the measurement system to avoid artificially introducing correlation over this period of the photocurrent noise, this method averages out the contribution to σ of this noise.

(d) Mean log intensity

$$\overline{L} = \frac{1}{100} \sum_{j=1}^{100} \overline{L}_j \qquad \text{from item I, (d) above}$$

(e) Variance of log intensity

$$\sigma_L^2 \cong \frac{1}{100} \sum_{j=1}^{100} \overline{L}_j \cdot \overline{L}_{j+1} - (\overline{L})^2$$

where $\overline{A}_j$, $\overline{E}_j$, $\overline{I}_j$, and $\overline{L}_j$ are averages computed every 1 msec as specified in items I, (a) through (d) above. The summations extend over a 100-msec interval.

c. Overall Description of Data Processing System

The data processing needs of the ATM system can be met by use of a computer facility with the conversion, processing, recording, and display capabilities depicted in Figure 55. The physical size of a typical implementation of this facility is suggested in Figure 56.

(1) Functional Elements and Data Flow. The computer with adequate internal memory to handle program code and data buffers will be interfaced with a number of peripheral equipment units as shown in Figure 55. The SIS analog data and experimenter voice commentary will be converted to digital form by a multiplexer and A/D converter under control of an external clock with frequency dividers which generate interleaved timing pulses at the nominal rates of 40, 20, and 3 kHz and at 1 Hz, respectively, on separate lines. These lines will control the multiplexer's selection of the SIS and voice data (I at 40 kHz, A and E at 20 kHz, V at 3 kHz, and B at 1 Hz) so that they are periodically sampled and digitized in an interleaved systematic manner. The 40 kHz line will also be fed to the SIS to control its cruciform scan pattern.

The SIS operating status will be indicated on the tracker status line: successful target acquisition or reacquisition will produce a "true" state on the line; otherwise, there is a "false" state on the line. The experimenter can override the SIS indication by controlling the state of his experiment status line. These lines are ANDed together so that the data status line is in a true state only if both the SIS and experimenter agree that the SIS analog data is valid. The computer interface sends an interrupt to the computer whenever the data status line state changes from false to true or true to false.

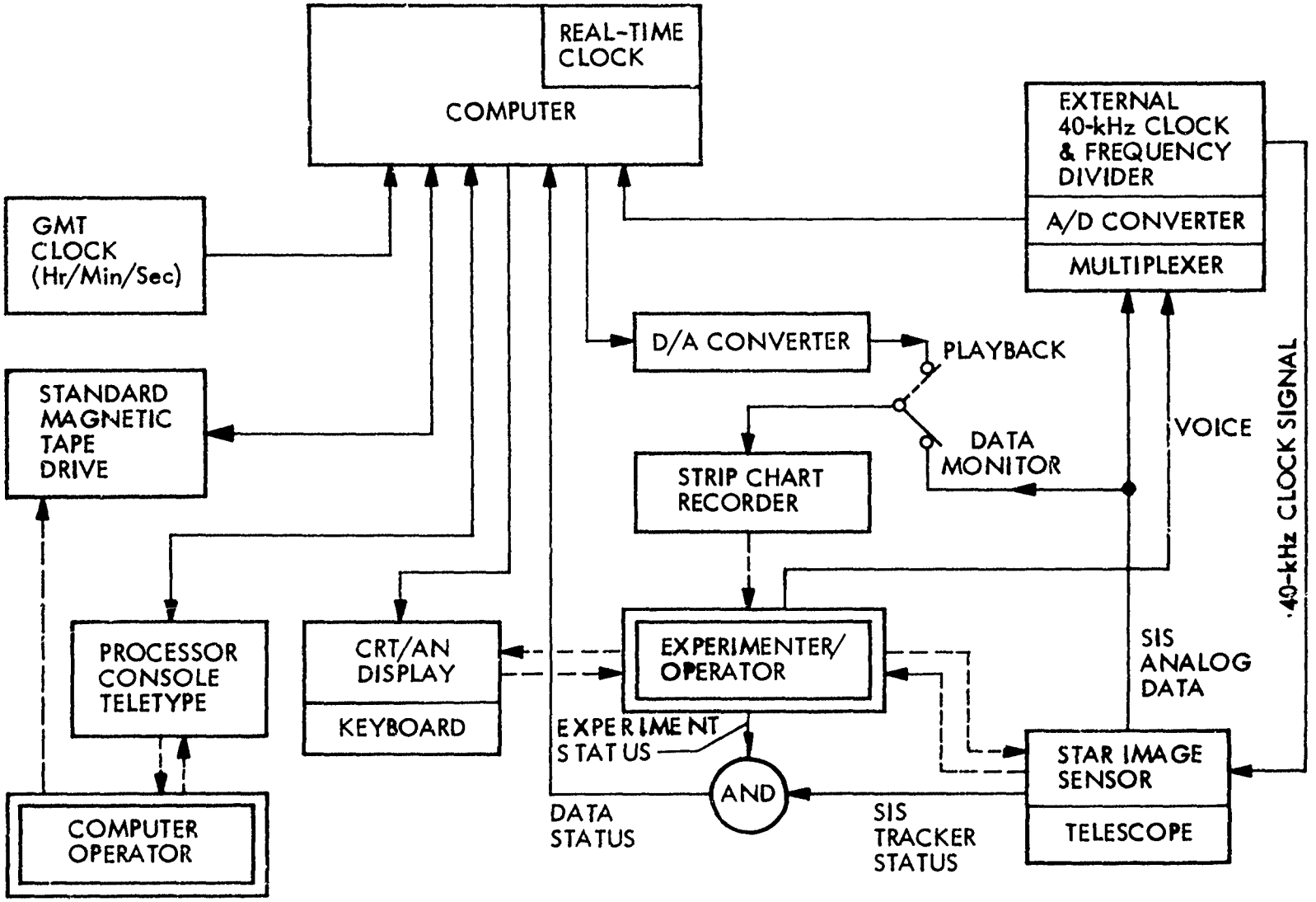


Figure 55 Data Processor System Hardware

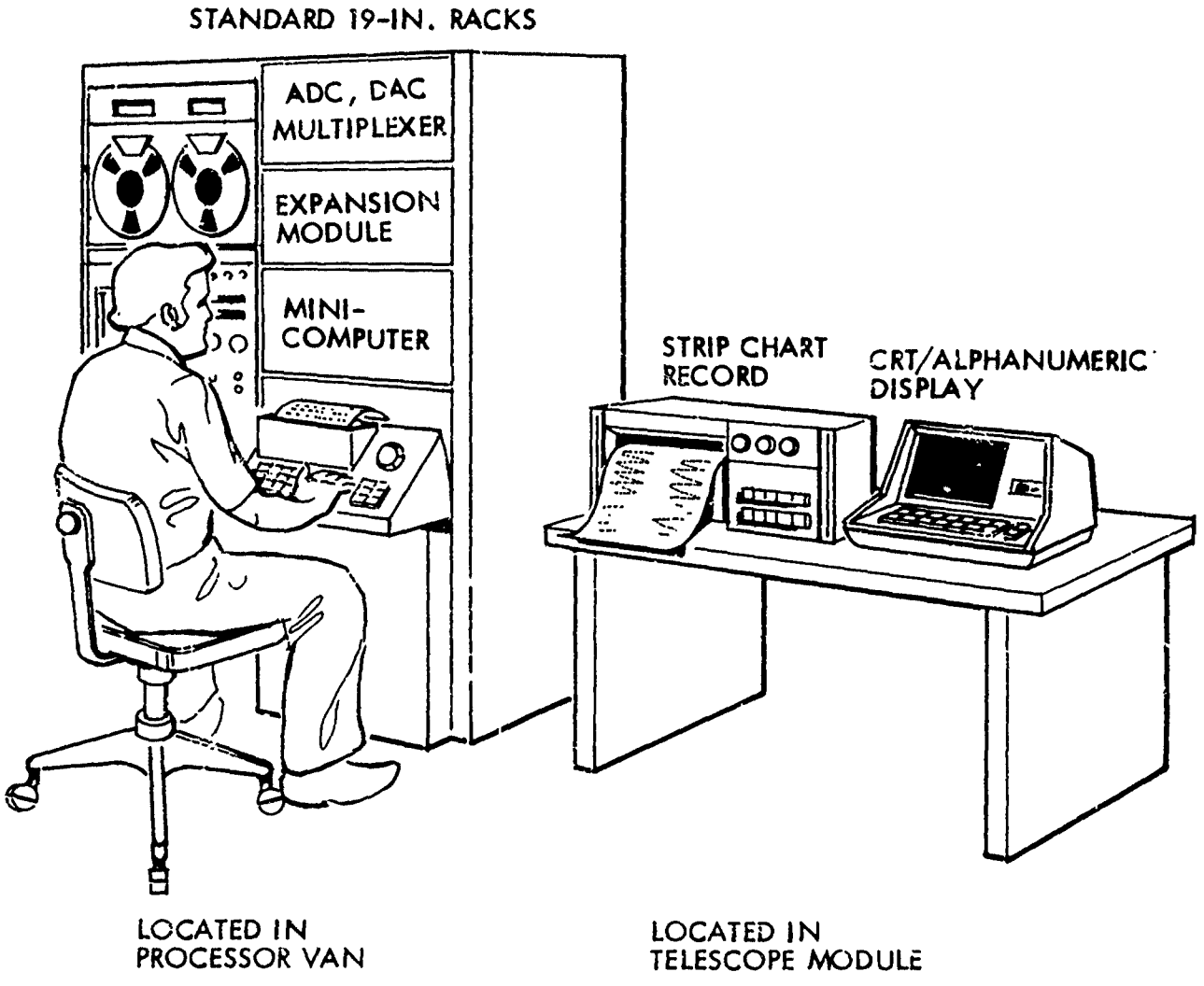


Figure 56 Typical Processor Hardware Configuration

A CRT alphanumeric (CRT/AN) display situated near the SIS displays the telescope pointing commands and chromatic correction adjustments to the experimenter for setting up an experiment. It is also used during an experiment to alert the experimenter that a chromatic correction update is required. If the tracker loses the star image, or requires pointing adjustments to recenter the star on the SIS boresight, the SIS tracker status is changed to the false state. The computer then interrupts the data recording and alerts the experimenter that the SIS requires attention. This CRT/AN display will also have a keyboard so that the experimenter can control the computer at his telescope module location; that is, he will be able to set up and initiate the experiment, monitor its progress, and carry out varied post-experiment data analyses if desired.

A GMT clock is interfaced with the computer and, when interrogated, will output the current time in hr/min/sec. During slow-mode data recording, the computer will regularly read the GMT (when interrupted by the real-time clock interval timer) so that it can check for possible chromatic correction updates at regular 5-min intervals. These readings will also be used to time-tag the data being recorded on magnetic tape. These time tags will occur regularly on slow-mode data records, and on the first and last records of the sequences resulting from fast-mode data.

The magnetic tape drive is used to record the digitized SIS data and voice commentary. The SIS data is averaged before being stored on the magnetic tape, the averaging time depending upon the recording mode (fast or slow) and the type of data. (See Section IV, 3, b.) (The program procedure for performing these averaging operations will be discussed later in Section IV, 3, d.) The tape drive will also be used to load the various executive and operating programs and certain control parameters. Specifically, before experiment initiation, a software program tape will be mounted on the drive. Programs necessary to initiate and execute the experiment will be loaded. The astro tables may be included with these programs. The software tape will then be dismounted and a data recording tape mounted. Following the termination of the experiment, the software tape will be interchanged with the data tape; the data analysis programs will be loaded into the computer; and the data tape then will be remounted. (By adding a second tape drive to the processor, this mounting and remounting procedure could be eliminated; however, the additional expense of a second tape drive does not appear to be justified.)

A strip chart recorder, driven by selected SIS data lines, provides the experimenter with graphic displays by which he can monitor the progress of the experiment. It can also be used in conjunction with the digital-to-analog (D/A) converter during post-experiment analysis to view selected graphic displays of the processed SIS data.

The D/A converter can also be used to drive an oscilloscope or speaker under timing control from the external clock so that selected SIS data or voice commentary can be output with respect to a particular time base.

(2) Computer Facility Programs and Software. Facility programs can be divided into three groups: pre-experiment, experiment, and post-experiment. Some program routines will appear in two of these groups, and some will appear in all three groups.

The executive program will be resident in the computer memory during all three phases of an experiment. This program will include routines to perform the following:

- Index, read, and format programs from the program library on magnetic tape.
- Service interrupts from the real-time clock, SIS data status line, operator console requests, and A/D converter channel.
- Control program routine initiation and termination transitions.

Pre-experiment programs will include the following routines:

- Control and service operator-computer interaction via either of the consoles. This includes responding to requests for machine attention, providing guide lines for setting up the experiment, and inputting the experimental parameters.
- Compute the telescope pointing commands (using the Vandenberg AFB program, Appendix VI, would require approximately 1000 minicomputer words of memory, which would also include the astro tables for 75 stars).
- Compute chromatic correction.
- Interrogate the GMT clock.
- Control D/A conversion of standard signal levels for calibration purposes.
- Display sidereal mount switch-on count-down time.
- Execute experiment initiation.

Experiment programs will include routines as follows:

- Control and service interaction via consoles.
- Compute chromatic corrections every 5 min (which also requires computation of telescope pointing commands using star data and GMT).
- Interrogate the GMT clock.
- Handle double buffer switching as required to store the A/D converter data.
- Handle double buffer switching for magnetic tape output records.
- Control data handling rates, depending on slow- or fast-mode recording conditions and valid or invalid SIS data status.

- Perform data averaging as a function of data handling rates. For example, control of the recording mode can be carried as a function of how the input data from the ADC channel are processed and transferred to the output buffers. The ADC can continue at the nominal 83-kHz rate, independent of the recording conditions.

- Format and store output data on tape.

Post-experiment programs will include routines to perform the following:

- Control and service user "quick-look" data analysis requests as determined by the GMT measurement interval desired, the SIS signals of interest, the analysis processes desired, the output mode of display, etc.

- Perform the signal analysis functions as previously described.

- Retrieve the tape records for a given GMT interval.

- Control D/A converter output, and hard copy printer or CRT/AN display outputs.

The executive routines, and those which will be run during the experiment will be programmed in assembly language to produce compact code and fast execution times. The other routines, where possible, will be programmed in FORTRAN IV or BASIC.

d. Performance Characteristics

The hardware configuration shown in Figure 55 has all the equipment features necessary to carry out the ATM measurement function. The capabilities of this equipment will depend on the input data sampling rates and the data analyses requirements imposed on the processing system. The two key requirements that most affected the system design were: (1) providing the experimenter with a way of obtaining quick-looks at the measured data at the measurement site, and (2) enabling the experimenter to sample the SIS data at a nominal 80-kHz rate (100-percent sampling rate, all data) at selected 1- to 3-min intervals during an experiment. To meet the first requirement, a recording procedure was adopted that produces results that can be easily accessed, processed, and displayed. Real-time A/D conversion was used, and the reduced results recorded with GMT tags.

To meet the second requirement, a data averaging process is to be carried out concurrently with the data sampling process. In this way the quantity of data which must be recorded during the fast mode is reduced by a factor of 80. Such a reduction is possible because post-experiment analysis uses SIS data averaged over no less than 1 msec.

(1) Data Conversion, Processing and Recording. In the high-speed mode, there are three crucial data conversion, processing, and recording functions, that is, functions to be accomplished in real time. These are as follows:

- Conversion – SIS signals A_i, E_i, and I_i will be periodically sampled at 20, 20, and 40 kHz, respectively, and quantized to 7, 7, and 10-bit accuracy, respectively. Also, the voice commentary V_i will be sampled at 3 kHz with 7-bit accuracy, and the background B_k will be sampled at 1 Hz with 7-bit accuracy.

- Processing – SIS signals will be averaged in the following way over consecutive 1-msec intervals:

$$\sum_{i=1}^{20} A_i, \quad \sum_{i+1}^{20} A_i * A_{i+1}, \quad \sum_{i=1}^{20} E_i, \quad \sum_{i=1}^{20} E_i * E_{i+1}, \text{ and } \sum_{i=1}^{40} I_i.$$

  In the post-experiment analyses, other arithmetic must be performed on the averages as specified in Section IV, 3, b(3).

- Recording – At regular intervals, the above averages must be blocked together with the sampled voice signal and the GMT tags, then written out on magnetic tape.

The tradeoff between sampling rate and facility cost has been established for 100, 75 and 50 percent of the nominal sampling rate requirements. For the 100-percent case, three minicomputers were considered. One of the better of these designs was reconfigured for the 75- and 50-percent cases.

(2) 100-Percent Sampling Rate Requirement. The Data General NOVA, Digital Equipment PDP 11, and Varian Model 73 minicomputers with supporting peripherals were considered. The NOVA and PDP 11 designs cost approximately the same. The Varian Model 73 configuration cost is 30 percent higher. Following is a description of the NOVA design, itemized to illustrate the method used to establish system costs.

(a) NOVA Design. The operating approach in this design provides for organizing the main memory into two pairs of buffers – one pair to handle the input ADC data from the tracker and voice commentary and the other pair to handle the output data being written on magnetic tape. The data are transferred on the high-speed data channel which is operated so as to have direct access to the main memory. In this mode, the central processor sets up the controls to transfer a data word from the A/D converter to the memory, or from the memory to the magnetic tape controller on a "cycle-stealing" basis without interrupting the problem program. Thus the data channel is multiplexed under control of the converter and magnetic tape controllers to accommodate the input and output data streams, respectively. The operation of the problem program is unaffected by this cycle stealing and continues computing the averages and performing certain bookkeeping functions.

Two buffers are used on the input data so that the data channel can be filling up one buffer while the problem program averages data from the other buffer. When the first buffer is filled, the problem program, if suitably coded, will have completed the averages for data in the latter buffer. The roles of the buffers are then switched.

A similar dual-buffer switching technique is used for the output data. The size of these buffers depends on the bookkeeping overhead in the time budget dictated by real-time operation. A detailed analysis of timing is given in Appendix VIII from which the following equipment requirements were determined. Since a considerable variety of computation and processing will be carried out before and after an experiment, the core memory is configured to support FORTRAN programs. The NOVA FORTRAN compiler needs at least 8,000 words of main memory to compile and run such a program.

An external clock with frequency dividers will be required in order to generate commands for sampling of the tracker, voice and background signals at appropriate interleaved times and for control of SIS timing.

The NOVA configuration (Table 7) will meet the crucial conversion, processing, and recording requirements for the 80-kHz sampling rate case with a 40-percent design margin. (See Appendix VIII, Section 4.)

Table 7 . NOVA (Data General) Configuration and Costs

Model	Description	Cost	Discount Cost
	Central Processor		
8C01	Supernova SC Central Processor	$5,600	$ 5,040
8012(2)	Semiconductor (SC) Memory (2048-Word)	5,600	4,760
8003	Core Memory (4096-Word)	3,650	3,285
8025	Supernova SC Memory Expansion Chassis	1,850	1,665
8007	High-Speed Multiply/Divide Unit	1,600	1,440
8009	High-Speed Data Channel	950	855
	Subtotal		$17,045
	TTY Console With Interface		
4007	I/O Interface Subassembly	$ 200	$ 180
4010/SN	Teletype I/O Interface for 33ASR, 33KSR, 35KSR	150	128
4010A/SN	Teletype	1,250	1,250
	Subtotal		$ 1,558

Table 7 (Cont.)

Model	Description	Cost	Discount Cost
	CRT Console With Interface		
4007	I/O Interface Assembly	$ 200	$ 180
4010/SN	Teletype Interface	150	128
4023	Voltage I/O Interface (EIA-type)	100	90
4010X	Keyboard CRT for Alphanumeric Display and Input	2,400	2,160
	Subtotal		$ 2,558
	Interfaces for Digital Clock, Status Line, Etc.		
4040	General-Purpose Interface Board	$ 450	$ 405
4041X	Dual 16-Bit Input Register	100	90
4045/SN	General-Purpose I/O	200	180
	Subtotal		$ 675
	A/D and D/A Converter Subassembly		
4014(2)	I/O Interface Subassembly	$ 400	$ 340
4032(2) SN	Basic A/D Interface	1,400	1,190
4055A(2)/SN	A/D, D/A Chassis and Power Supply	1,800	1,800
4055K	Timing and Control	230	230
4055M	Multiplexer (8-channel)	160	160
4055D	A/D Converter (10 bits)	600	600
4055C	A/D Converter (8 bits)	450	450
4055I	Buffer Amplifier	400	400
4037/SN	D/A Converter Control	300	270
4056A	Timing and Control for All D/A Converters in Chassis	350	350
4056B	D/A Converter (8 bits)	250	250
	Subtotal		$ 6,040
	Magnetic Tape Transport		
4030/SN	Magnetic Tape Control	$4,000	$ 3,600
4030J	Transport 9 (or 7) track (45 ips, 800 bpi; WANG 1045)	5,900	5,900
	Subtotal		$ 9,500
	Total Cost		$37,378[a]

(a) With 10-percent discount; approximately 60 days delivery

(b) Other Equipment. Computer costs for PDP 11 and Varian 73 Equipment are summarized in Table 8 for the 100-percent sampling rate.

Table 8 . PDP 11 and Varian 73 Equipment Description and Cost

Model	Description	Cost
PDP 11	PDP 11/40 with 16-K word memory	$19,995
	CRT/AN Console	3,195
	Interfaces	800
	A/D and D/A Assemblies	5,040
	Magnetic Tape Drive	9,950
	Total Cost (5-percent Discount)	$36,080
Varian 73	Varian 73 with 12K work memory	$30,250
	CRT/AN Console	3,610
	Interfaces	1,100
	A/D and D/A Assemblies	8,140
	Magnetic Tape Drive	9,000
	Total Cost (without Discount)	$52,100

(3) 75-Percent Sampling Rate Requirement. The NOVA solution for the 100-percent case provides a 40-percent safety margin. A comparable margin can be achieved for the 75-percent case by replacing the semiconductor memory with a core memory. (See Appendix VIII, Section 4.) Specifically, with respect to the previous NOVA itemization:

	Model	Cost
Replace:	2 ea 8012 SC memory	$5,600
	1 ea 8003 core memory	3,650
		$9,250
With:	1 ea 8015 core memory	$4,900

The new total cost (discounted) would then be $33,463.

(4) 50-Percent Sample Rate Requirement. A 40-percent margin can be achieved by replacing the super NOVA with a NOVA 800. (See Appendix VIII, Section 4.) With respect to the first NOVA itemization:

	Model	Cost
Replace:	1 ea 8001 Super NOVA	$5,600
	2 ea 8012 SC	5,600
	1 ea 8003 core	3,650
		$14,850
With:	1 ea 8201 NOVA 800	$3,600
	1 ea 8215 Core memory	4,400
		$8,000

The new total cost (discounted) would then be $31,213.

(5) Clock Reference. Greenwich Mean Time in hrs/min/sec is to be used within the computer to document each experiment and to determine tracker pointing commands, and atmospheric refraction and dispersion corrections from the star almanac or astro tables.

One instrument that will adequately satisfy this need is the Model 30031200 clock built by Chrono-log Corp., 2583 West Chester Pike, Broomall, Pa. 19008. A brief itemized description is given in Table 9 .

Table 9 . Clock Description and Cost

Model Code		Description	Cost
Clock Ranges	A = 0	23 hr, 59 min, 59 sec	$495
Time Base	C = 3	External 1- to 5-MHz	142
Power Supply	D = 1	115VAC	115
Digital Output	E = 2	Serial BCD characters, one for each clock range digit	
		Total Cost	$752

(6) Strip Chart Recorder. There is a need to record and display the four tracker signals for azimuth, elevation, intensity, and background, with an instrument which will operate independently of the computer facility. This instrument is to be used in setting up each experiment and in monitoring the experiment during critical intervals. One which will adequately satisfy this need is built by the Honeywell Test Instrument Division, Sunnyvale, Ca. A brief description and costs are shown in Table 11.

Table 10. Strip-Chart Recorder Description and Cost

Model	Description	Cost
1508B	Visicorder oscillograph; uses UV writing, nonpermanent 0.1 in. to 150 in/sec frequency response-dc to 24 kHz	$4,975
117-04 (4)	Interface Modules and Amplifiers	860
	Total Cost	$5,835

e. Summary

The computer facility which will meet the data analysis and recording requirements of the Atmospheric Transmission Measurement System is shown in Figure 55. Hardware itemizations using NOVA minicomputer configurations for the 100%, 75% and 50% of nominal (80 kHz) sample rate are given in Section 4.3.4. These configurations were derived on the basis of the key input/output bound and compute bound functions. Analysis for the computer bound functions are given in Appendix G. Table 11 summarizes the cost/performance tradeoff for this application:

Table 11. Cost/Performance Tradeoff

Nominal Sampling Rate	NOVA Computer ($)	GMT Clock ($)	Strip Chart Recorder ($)	Total Cost ($)
100 percent (80 kHz)	$38,378	$905	$5,835	$45,118
75 percent (60 kHz)	34,462	905	5,835	41,202
50 percent (40 kHz)	32,213	905	5,835	38,953

4. EXPERIMENTAL PROGRAM DEFINITION

a. Measurement Procedure

The first measurement, once the SIS has been turned on and is tracking the star of interest, will be to obtain an estimate of r_o. This result will then be used to determine the instrument settings that will be used in all other measurements. This determination will be made once every half hour while the system is working. To determine r_o, the operator will adjust the SIS tracking bandwidth to 1 Hz so that the system will be functioning essentially in the static mode. The telescope aperture

diameter D will then be varied, and the average signal output of the photodetector I will be measured. The signal processing system will calculate and plot the ratio I/D^2 against D to determine where the "knee" of this curve falls. This will be used as an estimate of r_o. The operator will then make 30-sec runs at diameter settings of 0.3 r_o, 0.5 r_o, 0.7 r_o, 1.0 r_o, 1.2 r_o, 1.5 r_o, 1.8 r_o, and 2.2 r_o, respectively, first with a servo bandwidth setting of 1 Hz, and then at a 500-Hz setting. The 16 runs should just fit into two 5-min tracking blocks. During each of these runs, the signal intensity I will be recorded, as well as the servo control voltages for both tracker channels. Background intensity also will be recorded.

After these data are taken, the operator will set the telescope aperture to 1.5 r_o and will determine the average signal intensity I at the full 500-Hz servo bandwidth setting. He will then determine the servo bandwidths, $f_{.5}$, $f_{.7}$, $f_{.9}$, $f_{.95}$ and $f_{.98}$, which reduce the average signal intensity to 0.5 $\bar{I}$, 0.7 $\bar{I}$, 0.9 $\bar{I}$, 0.95 $\bar{I}$, and 0.98 $\bar{I}$, respectively.[18] Five minutes is allotted to these measurements. The operator will then make 60-sec data recording runs with the servo bandwidth set to $f_{.5}$, $f_{.7}$, $f_{.9}$, $f_{.95}$, and $f_{.98}$, as well as for a 500-Hz bandwidth. This will take approximately two more 5-min tracking periods. Subsequently, there will be an approximate 5-min pause before the basic measurement cycle starts over with a redetermination of r_o.

During data taking, the operator will keep a running voice log on one track of the data tape, indicating what is being recorded and making any appropriate comments as to the conditions. He will also enter onto the tape, by means of the data processor remote keyboard, a log number for each data section which can be read by a computer, and will tag the data sections for appropriate computer processing. During the scheduled 3-week data-taking period at each site (see Section IV, 4, b), this process will be conducted on a continuous basis, day and night, whenever weather permits, up to a 50-percent duty cycle.

b. Measurement Schedule

As shown in Figure 57, the program is divided into five distinct phases. The first phase consists of equipment procurement (i.e., the SIS) and preparation of a test site at the Lockheed Palo Alto Research Laboratory.

The second phase consists of operation of the equipment at the Palo Alto site for acceptance testing and operational shakeout of the equipment. During this phase, data taking will be performed, and data reduction procedures will be established.

The third phase of the program, which will start at the same time as the first phase, but completed in a period of 6 weeks thereafter, will be concerned with the selection of three sites at which to gather continuous field data. Site selection early in the program will be essential to ensure that proper facilities will be available, when needed, at the test sites.

[18] Rather than use fractions of $\bar{I}$ as a basis for selecting frequency, the operator may use percentage modulation as a criterion. This choice will have to be determined later.

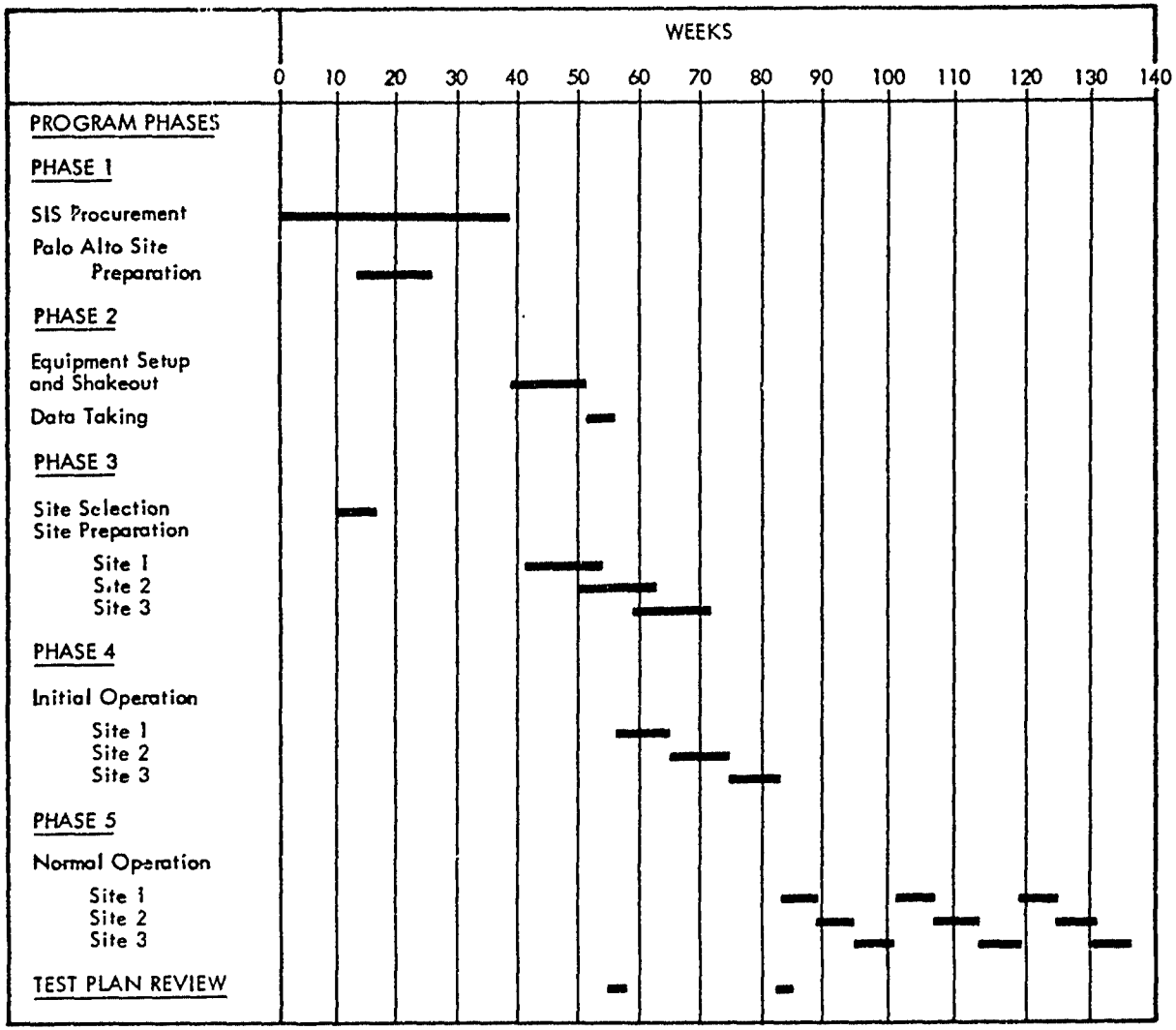


Figure 57 Program Schedule

The fourth phase will consist of initial operation of the equipment at each of the three sites, establishing procedures for transport and travel to and from each site, and for working at each site. It will result in the first regular block of field data for each site.

The fifth phase will consist of three cycles of operation at each of the three sites, in the manner established during Phase 3, but with less time spent at each site since all of the procedures will have been worked out previously. The data gathered during this phase, in combination with that produced during Phase 3, will constitute the basic field results of the program.

The schedule for this program has a duration of 137 weeks, the last 54 of which are the routine data production of Phase 4. The first 39 weeks are devoted to the equipment procurement of Phase 1. The schedule is shown in Figure 57. In Figures 58 and 59 the subschedules for operation at the sites during Phase 4 and during Phase 5, respectively, are presented.

c. Test Plan Review

At the end of Phase 2, the test plan for subsequent data-gathering operations will be reviewed in the light of experience gained in operating the system at the Lockheed Palo Alto Research Laboratory. A second review at the end of Phase 4, before the start of the main data-production period, will be held to take advantage of experience gained during initial field operation of the equipment.

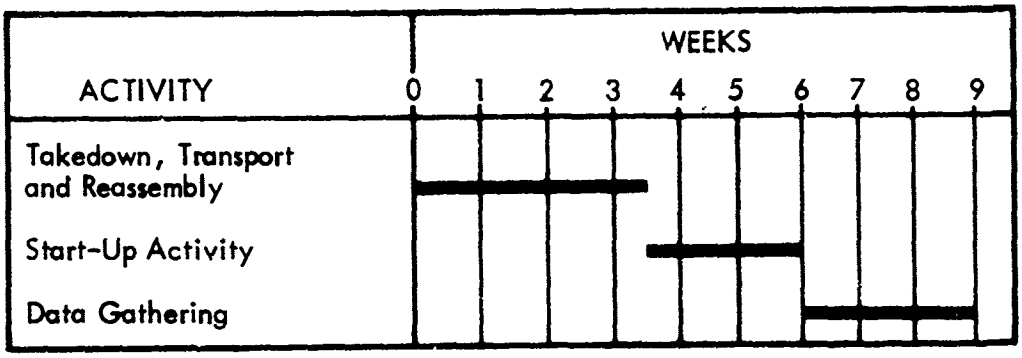


Figure 58 Site Operation Schedule for Initial Operation

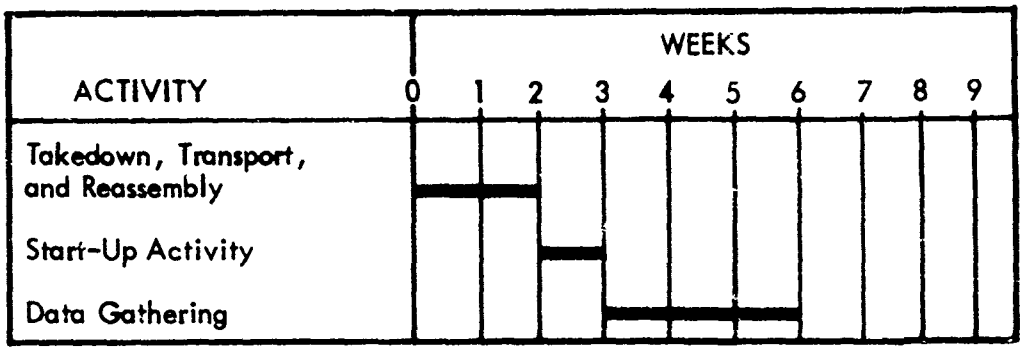


Figure 59 Site Operation Schedule for Normal Operation

5. MAJOR COMPONENT SPECIFICATIONS

a. General Considerations

This section presents detailed specifications for the star image sensor and the telescope. Although the sidereal mount is also a major component, at least one commercially available unit for which specifications can be obtained is considered satisfactory for this application, and specifications for the sidereal mount have therefore not been included in this section. Other components, such as the astrodome and standard test equipment, are also not covered because they are not considered major components of the ATM system.

b. Specification for Star Image Sensor

(1) Scope. This specification defines the requirements of star image sensor (SIS). The SIS will interface with an experimental, astronomical quality telescope on a precision sidereal mount. The SIS will provide two-axis analog angle error signals, image intensity signals and background intensity signals on selected stellar targets in dark or daylight environments.

(2) Applicable Documents. The following specifications and drawings are required:

- Specification for experimental telescope
- Specification for sidereal mount
- System mechanical interface drawing
- System electrical interface drawing

(3) Requirements

(a) General Background Information and Operational Description. The SIS is a multimode target tracker with the primary function of providing target image position and intensity information in real time. The position information is also used to aid sidereal mount pointing. A typical data-taking sequence is as follows:

(1) The SIS is interfaced with the telescope on the sidereal mount – mount is designated to R.A. and declination of stellar target.

(2) The SIS searches an area 1.17-cm square (460 μradians square with optics focal length of 25.4 meters) on the detector photocathode for the target image.

(3) Acquisition of the target image is effected on receipt of the initial video pulse. A tracking mode characterized by a cruciform scan and a control loop that maintains the scan on the target image begins at the position of acquisition. Track-lock is maintained as the target image moves within the 1.17-cm-square area.

(4) The target image is boresighted by applying the SIS position signals to the sidereal mount drive. This type of closed-loop pointing will not be continuous but will be used only when necessary to move the image into the quality area of the optics.

(5) During track lock, two coordinates of image position information at a 10-kHz sample rate each, image amplitude information at a 20-kHz sample rate, and the ambient background level information in a 1-Hz bandwidth are provided by the SIS.

(6) A limited acquisition scan centered at the final target position will be initiated upon non commanded loss of track lock in order to minimize reacquisition time.

(b) Physical Measurements. Following are pertinent physical measurements:

- Weight: < 20 lb
- Size: 8 × 8 × 14 in.

- Mounting: TBD
- Alignment: Electrical and mechanical adjustments
- Connector: TBD

(c) Electrical Interface. Following are the electrical interface element specifications:

(1) Power. Power will be made available to the SIS from a 115 ±10 V, single-phase, 60-Hz power line.

(2) Signals

(a) Inputs – The following input signals will be provided to the SIS:

1. Search scan command
2. Half search field command
3. External clock – 40 kHz ± 10 percent

(b) Adjustments – The following adjustments will be available and calibrated:

1. Amplitude sample time
2. Track loop bandwidth

(c) Outputs – The following output signals will be provided by the tracker and synchronized to an external master clock:

1. X analog error signal samples
2. Y analog error signal samples
3. Target presence (data valid) digital level
4. Track mode digital level
5. High voltage analog signal
6. Image intensity analog signal samples
7. Background analog signal
8. Video amplitude analog signal.

(d) Photodetector Characteristics. The detector of the SIS will be an F4012 RP image dissector manufactured by ITT Electron Tube Division.

(1) Photocathode Surface. The photocathode surface will be an S-20 with a minimum responsivity of 0.055 A/W at 0.5 μ.

(2) Multiplier. The detector multiplier will be a 12-stage type with a minimum gain of 5×10^5 at 1400 V.

(3) Dark Noise. The maximum dark current at 5×10^5 multiplier gain will be 5×10^{-9} A.

(4) Aperture. The internal limiting aperture will be round with a radius of 0.0043 cm (0.0017 in.).

(5) Photocathode Blemishes. To be determined.

(e) Acquisition Performance Requirements. Following are requirements for acquisition performance.

(1) General. The SIS will have three acquisition modes, i.e., modes in which the operational objective is to search a large field for the target image. In all acquisition modes, the element dwell time will be 1.6 msec.

(2) Full Field. The search scan will be a 256×256 element raster covering a 1-cm-square area of the photocathode. The frame time will be 105 sec.

(3) Half Field. This search scan can be commanded in lieu of the full-field scan. The scan will be a 128×128 element raster covering a 0.58-cm-square area of the photocathode. The frame time will be 26 sec.

(4) Limited Field. This search scan will be automatically used upon loss of tracklock, except when commanded. The scan will be a 32×32 element raster covering a 0.15-cm square of the photocathode centered at the last tracklock position. The frame time shall be 6 sec.

(f) Tracking Performance Requirements. The following requirements have been set up for the SIS.

(1) General. In the tracking mode, the SIS will provide information of the target image position and amplitude in its central Airy disc. A background level outside of the image will also be provided. A sweep scan timing format as shown in Figure 46 will be used to modulate the incoming video.

(2) Track Scan. The track scan frequency will be approximately 5 kHz. The amplitude shall be set to minimize the video off time consistent with measurement of background without interference from star image.

(3) Track Loop Bandwidth. The track loop bandwidth will be at least 500 Hz. An external control to allow setting of the loop bandwidth between 1 Hz and 500 Hz shall be provided.

(4) Track Loop Gain. The track loop gain will be such that the steady-state error due to a position change is less than 10 percent of the limiting aperture. The position change amplitude will be equivalent to 50 percent of the full-acquisition field or to the size of the optics-quality circle, whichever is smallest.

(5) Signal Amplitude Sample Time. The signal amplitude sample will be taken during the time at which the ac scan currents are zero. By means of an external control, the sample time t_s setting (Figure 46) will be variable between 0 to 35 μsec.

(6) Background Sample Time. The background sample time t_b, (Figure 46) will be approximately 2 μsec.

(g) Output Signal Characteristics

(1) X Error and Y Error. These signals will be analog voltages proportional to the distance between the image position and SIS boresight position. The error gradients will be 0.020 V/0.001 in. (one-half limiting aperture). The error bandwidth will be the track loop bandwidth and therefore selectable over a range of 1 to 500 Hz. The following characteristics will apply:

(a) Accuracy. Data taking periods will probably not exceed 15 min. During this interval, drifts will be less than 10 percent of the limiting aperture following a 1-hr warmup interval. Long-term drifts will be less than two limiting apertures (such that optics/SIS alignment will not be required more frequently than monthly).

(b) Precision. The tracking precision (noise angle) will be less than 10 percent of the limiting aperture under the following conditions:

1. Zero visual magnitude or brighter; Class G-0 star
2. Track loop bandwidth of ≤ 500 Hz
3. Optics collecting aperture diameter of 20 cm
4. Amplitude sensing sample time of 25 μsec

(2) Video Amplitude. The video amplitude will be an analog signal proportional to the total radiant intensity (signal and background) in the central area of the image Airy disc. The signal will be 0 to 5 V and have a 500-Hz bandwidth. For the same conditions as those noted just above under "Precision," the video amplitude S/N ratio will be ≥ 15.

(3) Background Level. The background will be an analog signal proportional to the background radiance near the target. The signal will be 0 to 5 V and have a 1-Hz bandwidth.

(4) Image Intensity. The image intensity will be an analog signal proportional to the target radiant intensity (without background) in the central area of the image Airy disc. The signal will be 0 to 5 V, and derived from the differential amplification of samples taken during periods t_s (Figure 46) and the background level.

(5) High Voltage. The high voltage signal will be an analog voltage proportional to the detector voltage divider current. The signal will be 5 ± 0.5 V when the SIS is in operating condition.

(6) Track Mode. The track mode signal will be a digital signal in which a high state indicates that the SIS is operating in the track scan mode.

(7) Target Presence. This signal will be a digital type in which a high state indicates that the SIS is locked onto a target image and that valid position, amplitude, and background signal are available.

(h) Environmental Conditions

(1) Temperature. The SIS with alignment will meet performance specifications for a temperature range of 0° to 100° F. The SIS will meet performance specifications without alignment for any 20° F temperature range (i.e., ±10°F about the alignment temperature) within the overall temperature range. Temperature changes will not be considered for short-term drifts.

c. Specification for Telescope

(1) General Description. This specification describes a telescope that will be used in an atmospheric effects investigation in conjunction with other equipment to analyze star images. A pinhole smaller than the size of the diffraction-limited image will be used in the measurement system. In order to achieve valid results, diffraction limited operation with correction for aberrations is required. The equipment will be mobile and therefore the telescope design must be such as to maintain its integrity over temperature and vibration. Adjustments to compensate for temperature variations and other environmental factors will be permitted, providing that they can be made under normal field operating conditions and do not degrade overall optical performance. The design will minimize the effects of atmospheric turbulence within the telescope tube.

(2) Effective Focal Length. The focal length will be variable from 136 to 1084 in. (344 to 2754 cm). Either zoom or discrete stepping can be used. If discrete stepping is employed, at least seven positions are required to provide effective focal lengths at approximately 1084, 813, 542, 361, 271, 181, and 126 inches.

(3) Effective Diameter. The maximum effective aperture diameter will be 8 in. (20.7 cm). Provision will be incorporated to reduce the aperture diameter to 0.6 in. (1.7 cm) to maintain a speed (f/no.) of either 133 or 200 for the effective focal lengths specified in Section IV, b, (2) above. Suitable calibration dials will be provided for this purpose. Central obscuration is not allowed. However, an obscuration at the edge of the aperture is acceptable if it is less than 8 percent of the total area for the 8-in. diameter. There will not be any obscuration for effective aperture diameters less than 4 in.

(4) Total Field of View. The total field of view will be 0.72 in. in diameter at the focal plane.

(5) Quality Field of View. The quality field of view will be at least ± 5 mrad from the optical boresight with respect to object space. The quality field of view is the region where diffraction limited operation and aberration correction is required over the spectral range of 0.4 to 0.6 μ. The total allowable aberration will be less than 50 percent of the diffraction angle.

(6) Wave-Front Distortion. The spherical wave front distortion will be less than $\lambda/20$ rms and $\lambda/3$ peak-to-peak in the spectral range of 0.4 to 0.6 μ in the quality field of view, including residual errors due to atmospheric dispersion.

(7) Correction for Atmospheric Dispersion. Atmospheric dispersion will result in significant chromatic aberration and a means must be provided to correct for this effect. The maximum difference in the index of refraction of the atmosphere between 0.4 and 0.6 μ is $dn = 6.2 \times 10^{-6}$. A manual adjustment will be incorporated to correct this aberration. The adjustment will have a range of dn from 0 to 6.2×10^{-6} and a suitably calibrated dial will be provided. During normal operation, the telescope will rotate about the optical axis and, provision therefore must be made for rotating the subassembly used for dispersion correction. A manual control with a suitably calibrated dial for rotating the subassembly through 360 deg will be provided.

The quality field of view will not be degraded from that specified in Section IV, b, (5) for all values of $d\theta$. The optics required to correct the chromatic aberration may be located anywhere in the optical path of the telescope, including a location in front of the first element. If placed after the first element, the chromatic correction is not to change the path of the light beam by more than ± 0.1 mrad with respect to object space. If it is placed in front of the first element, it is desirable to correct for atmospheric bending as well. Astronomical refraction is shown in Table 5 . The value of $d\theta$ is determined using the following expression:

$$d\theta = 6.2 \times 10^{-6} \tan \theta$$

Note that θ is the angle from zenith and the angles in Table 5 are elevation angles.

(8) Baffle Requirements. The telescope will be designed to minimize light entering the telescope from outside the field of view. The baffling will be adjustable so that, as the effective lens focal length and diameter are varied, background radiation outside the total field of view is effectively attenuated. The baffling techniques used should include field stops, baffles, irises, and blackened internal surfaces.

(9) Operating Environment. The telescope will meet all of the performance requirements for an ambient temperature range of 0° to 100°F. Vibration levels will be those normally encountered during transport in a pick-up truck over improved (but not necessarily paved) roads. A transportation case shall be provided to afford protection as necessary during transit.

(10) Size and Weight. Minimum size and weight are desirable because the telescope will be mounted on a sidereal mount during operation. Also, it will be transported from site to site. As a first estimate, it is considered that the telescope weight should be on the order of 60 lb. It should be 6-ft long by 16 in. in diameter. Mounting pads are to be provided as required.

(11) Ancillary Equipment. Any nonstandard tools, jigs, fixtures, etc., required for alignment, focusing, mounting, and operation will be provided.

(12) Transportability. The entire system will be designed to withstand the shock, vibration, and temperature environment that may be encountered during transportation between measurement sites.

SECTION V

CONCLUSIONS AND RECOMMENDATIONS

1. CONCLUSIONS

The overall objectives of the Atmospheric Transmission Measurement program, as defined in the statement of work (Section I), have been met as follows:

(1) Experimental studies have established the validity of the technique of fast tracking, as called for in the preliminary subsystem design for the optical space data relay system presented in Reference 1. This conclusion is based on the positive results obtained in two sets of experiments, namely, critical, quantitative tests of the theory of optical antenna gain reciprocity, and demonstration in the laboratory (by means of an experimental laser link with a fast-tracking capability) of the effectiveness of the transmitter fast-steering technique in reducing pointing and tracking errors and signal fading due to simulated atmospheric turbulence.

(2) The feasibility of a measurement system suitable for field use and capable of experimentally evaluating atmospheric turbulence effects on a laser space communication system has been demonstrated. The measurement technique is based on the optical reciprocity theory and makes use of a fast-tracking star sensor coupled to a standard astronomical telescope. The system is capable of day-or-night operation with zero or first-magnitude stars, depending upon the measurement accuracy required. The measurement system uses only ground-based equipment; it does not require flyable hardware.

(3) A measurement program plan for obtaining adequate evaluation of three field sites chosen as possible locations for a laser communications transmitter will require a period of 32 months, including equipment procurement. Measurements of atmospheric up-link transmission should be made at each site for at least four periods spaced over a 20-month period.

2. RECOMMENDATIONS

The following recommendations for future effort are based on the foregoing conclusions:

(1) Because of the relatively long time period required to accomplish an adequate measurement and evaluation program, it is recommended that the engineering, procurement, and equipment integration phases of the program be started as soon as possible.

(2) Budgetary provision should be made at the outset for field site preparations so that firm commitments for space and facility arrangements at selected test sites can be negotiated.

(3) Further evaluation of the fast-tracking technique for combating atmospheric turbulence effects should be made to verify the theoretically predicted dependence of fading reduction on transmitter and receiver aperture size. The tests preferably should be conducted through use of an outdoor path. The evaluation program should also be designed to test the validity of the theoretical criterion for boresight tolerance in a fast-tracking transmitter with respect to atmospheric effects.

APPENDIXES

APPENDIX I

FORMAL PROOF OF OPTICAL ANTENNA GAIN RECIPROCITY FOR PROPAGATION THROUGH A TURBULENT MEDIUM

by D. L. Fried

The material in this Appendix has been excerpted as submitted from Optical Science Consultants Report No. TR-080 (November 1972).

PRECEDING PAGE BLANK-NOT FI

Introduction

In this report, we wish to present the concept of propagation reciprocity in a randomly inhonogeneous medium in a complete form, and discuss its implications and applications. It is the objective of this paper to make clear the foundation and nature of the reciprocity results.

In the next section, we define the concept of reciprocity and explain, in general terms, its basis and implications. In the section after that, we present the foundations of the reciprocity analysis, in a form sufficiently rigorous and yet compact as to allow a judgment of the sureness of the analysis to be formed. Finally, in the concluding section we discuss the practical implications of these results for up-link laser communications.

Reciprocity Concept

The concept of propagation reciprocity in its most commonly used form relates to microwave antenna gain, and put in its simplest terms, states that an antenna will perform equally well, i.e., provide the same antenna gain, whether used as part of a transmitter system or as part of a receiver system. The emphasis in the claim of reciprocity for microwave antennas is on the effect of imperfections and misalignments in the instrument. In applying the term "reciprocity" to the subject of optical propagation, we emphasize the effect of the medium on the performance of an instrument. It is not imperfections in the antenna per se, which we assume to be ideal, that concerns us, but rather the effect of the atmosphere in distorting the wave launched by the antenna if it is acting as part of a transmitter system, or the wave received by the antenna if it is part of a receiver system. The concept of reciprocity as applied to optical propagation asserts that the degradation effects of atmospheric inhomogeneities on the performance of an optical antenna is quantitatively the same whether the antenna functions as part of a transmitter or a receiver.

PRECEDING PAGE BLANK-NOT F

One item which almost "goes without saying" in the microwave case, but needs to be carefully pointed out in the optical case, pertains to the fact that we are considering a coherent, i. e., a wavefront distortion sensitive system. In this sense, we distinguish between a laser transmitter and a searchlight transmitter, and between an optical heterodyne receiver and a photon bucket type of receiver. Initially, we restrict our attention to the laser transmitter and the optical heterodyne receiver, for which devices performance is dependent on wavefront distortion.

When we claim reciprocity for optical system performance in the presence of atmospheric turbulence, we are, in essence, saying that if we had an optical link between a laser transmitter and an optical heterodyne receiver, with atmospheric turbulence somewhere in the propagation path, and if we then interchanged the role of the two ends of the link, leaving the antenna apertures as they were, the signal strength developed over the link will remain the same. It should be noted that our claim of reciprocity is to be understood on an instantaneous, random sample basis, as well as on a statistical basis.

Implications of Reciprocity

The significance of the reciprocity concept lies in two areas. First, as a practical computational aid, it allows us to apply the well developed body of knowledge that has been developed for the performance of an optical heterodyne receiver in the presence of atmospheric turbulence to the problem of estimating the expected performance of a laser transmitter in the presence of atmospheric turbulence. This is particularly important since the subject of laser transmitter performance appears to be in a rather weak condition, with essentially no meaningful results available for average antenna gain, and only limited certainty for the results on antenna-gain variance.

The second significant point to be recognized relative to the matter of reciprocity is that since reciprocity applies on an instantaneous, random

sample basis, then if the same aperture is used for both reception and transmission, alignment of the aperture to maximize the received signal will simultaneously result in maximization of the transmitter antenna gain. This is particularly interesting not simply because it takes care of the normal alignment problem, but also because it offers an opportunity for application of the concept of fast tracking in the transmitter. It has been shown that to a significant extent atmospheric turbulence induced wavefront distortion can be considered to be simply a matter of random tilting of the wavefront. This means that a large part of the effect of wavefront distortion can be cancelled by alignment of the antenna to follow the random tilt, i.e., by fast tracking. In fact, analysis of the performance of such a fast tracking optical heterodyne receiver system shows that its performance can be about 10 dB better than what the atmosphere will allow a static optical heterodyne receiver system to achieve. For an optical heterodyne receiver, or for a diffraction limited optical tracker, the approach to fast tracking is straightforward. There is a meaningful signal wavefront being collected and its tilt can be tracked. It is just a matter of implementing the necessary servo capabilities. On the other hand, for a laser transmitter, there is no straightforward method of obtaining the necessary information for controlling a servo system to compensate for a tilt which the atmosphere will put into the beam after it leaves the transmitter. However, because of reciprocity, it follows that if the receiver at the other end of the link is sending out some sort of coherent laser beacon, then if the laser transmitter shares its aperture with a beacon tracking receiver (either an optical heterodyne receiver or a diffraction limited imaging receiver), then the appropriate tilt for the aperture can be derived from tracking of the beacon and then also be used for the laser transmitter. Because of reciprocity, we know that the tilt developed from the beacon tracker is exactly the right tilt to use to achieve the benefits of fast tracking for a laser transmitter.

Reciprocity Proof - General Discussion

It is a particularly interesting feature of the proof of reciprocity that it is rather simple in form and remarkably free of the approximations and infinite series truncations that bring into question so much of the main body of optical propagation theory. The theory can be separated into two parts. The first is a proof of point-to-point propagation reciprocity. This result, which is originally due to Lutomirski and Yura*, is dependent only on the nature of the wave equation and the general radiation properties associated with the Green's function in classical electromagnetic theory. The proof is rather elegant and brief, and we shall reproduce it in the next section.

The second part of the proof follows in a straightforward manner from writing down the equations governing signal strength for a laser transmitter and for an optical heterodyne receiver. It is convenient to first consider the propagation between a point and either a laser transmitter or an optical heterodyne receiver, and then consider the propagation between a laser transmitter and an optical heterodyne receiver -- although clearly reciprocity in the first pair of cases follows from reciprocity in the latter case. We take this up later. Now we turn our attention to the proof of point-to-point propagation reciprocity.

Reciprocity Proof -- Point-to-Point

If $\psi(\vec{r}_i, \vec{r}_j)$ is the Green's function for Maxwell's equation that relates the field at $\vec{r}_i$ to a point excitation of unity strength at $\vec{r}_j$, then it obeys the equation

$$(\nabla_i^2 + k^2 n_i^2)\,\psi(\vec{r}_i, \vec{r}_j) = -4\pi\,\delta(\vec{r}_i - \vec{r}_j) \quad . \tag{1}$$

Here ∇_i^2 is the Laplacian in $\vec{r}_i$-space, k is the optical wave-number for the radiation, and n is the refractive-index of the propagation medium. Normally n_i is taken to be a constant independent of position. However, in

* R. F. Lutomirski and H. T. Yura, Appl. Opt. 10, 1652, (1971)

this case we can consider n_i to be a true function of $\vec{r}_i$, without affecting the validity of the equation.

Our proof of reciprocity proceeds by rewriting Eq. (1) with j replaced by j′

$$(\nabla_i^2 + k^2 n_i^2)\, \psi(\vec{r}_i, \vec{r}_{j'}) = -4\pi\, \delta(\vec{r}_i - \vec{r}_{j'}) \quad . \tag{2}$$

We then multiply Eq. (1) by $\psi(\vec{r}_i, \vec{r}_{j'})$, giving

$$\psi(\vec{r}_i, \vec{r}_{j'})\, \nabla_i^2\, \psi(\vec{r}_i, \vec{r}_j) - k^2 n_i^2\, \psi(\vec{r}_i, \vec{r}_{j'})\, \psi(\vec{r}_i, \vec{r}_j)$$
$$= -4\pi\, \delta(\vec{r}_i - \vec{r}_j)\, \psi(\vec{r}_i, \vec{r}_{j'}) \quad , \tag{3}$$

and multiply Eq. (2) by $\psi(\vec{r}_i, \vec{r}_j)$ giving

$$\psi(\vec{r}_i, \vec{r}_j)\, \nabla_i^2\, \psi(\vec{r}_i, \vec{r}_{j'}) + k^2 n_i^2\, \psi(\vec{r}_i, \vec{r}_j)\, \psi(\vec{r}_i, \vec{r}_{j'})$$
$$= -4\pi\, \delta(\vec{r}_i - \vec{r}_{j'})\, \psi(\vec{r}_i, \vec{r}_j) \quad . \tag{4}$$

If we subtract Eq. (4) from Eq. (3), the n_i^2-dependence will drop out, yielding

$$\psi(\vec{r}_i, \vec{r}_{j'})\, \nabla_i^2\, \psi(\vec{r}_i, \vec{r}_j) - \psi(\vec{r}_i, \vec{r}_j)\, \nabla_i^2\, \psi(\vec{r}_i, \vec{r}_{j'})$$
$$= -4\pi\, [\delta(\vec{r}_i - \vec{r}_j)\, \psi(\vec{r}_i, \vec{r}_{j'}) - \delta(\vec{r}_i - \vec{r}_{j'})\, \psi(\vec{r}_i, \vec{r}_j)] \quad . \tag{5}$$

Now if we integrate both sides of Eq. (5) over all $\vec{r}_i$-space, we get

$$\int_V d\vec{r}_i\, [\psi(\vec{r}_i, \vec{r}_{j'})\, \nabla_i^2\, \psi(\vec{r}_i, \vec{r}_j) - \psi(\vec{r}_i, \vec{r}_j)\, \nabla_i^2\, \psi(r_i, r_{j'})]$$
$$= -4\pi\, [\psi(\vec{r}_j, \vec{r}_{j'}) - \psi(\vec{r}_{j'}, \vec{r}_j)] \quad , \tag{6}$$

where V is the volume bounding our region of integration, and we have used the well known properties of the delta function to allow us to perform the integration giving us the result on the right hand side of Eq. (6). If the volume defined by V is bounded by the surface S, then using Green's theorem, we can transform the volume integration in Eq. (6) into the form

$$\int_S d\vec{s}_i \cdot \left[\psi(\vec{r}_i, \vec{r}_{j'}) \vec{\nabla}_i \psi(\vec{r}_i, \vec{r}_j) - \psi(\vec{r}_i, \vec{r}_j) \vec{\nabla}_i \psi(\vec{r}_i, \vec{r}_{j'})\right]$$
$$= -4\pi \left[\psi(\vec{r}_j, \vec{r}_{j'}) - \psi(\vec{r}_{j'}, \vec{r}_j)\right] \quad , \tag{7}$$

where $d\vec{s}_i$ is associated with an element of area on the surface S, and has a magnitude equal to the area of the element and has a vector orientation normal to the surface element and oriented outward, $\vec{\nabla}_i$ denotes the gradient operator in $\vec{r}_i$-space.

Now if we choose the surface S to correspond to a sphere of radius R (where R is very large), we get

$$\int_{4\pi} R_i^2 \, d\Omega_i \left[\psi(\vec{r}_i, \vec{r}_{j'}) \frac{\partial}{\partial R_i} \psi(\vec{r}_i, \vec{r}_j) - \psi(\vec{r}_i, \vec{r}_j) \frac{\partial}{\partial R_i} \psi(\vec{r}_i, \vec{r}_{j'})\right]$$
$$= -4\pi \left[\psi(\vec{r}_j, \vec{r}_{j'}) - \psi(\vec{r}_{j'}, \vec{r}_j)\right] \quad , \tag{8}$$

where we have used the element of solid angle $d\Omega_i$ to replace $|d\vec{s}_i|$ according to the equation

$$R_i^2 \, d\Omega_i = |d\vec{s}_i| \quad , \tag{9}$$

and taken note of the fact that

$$d\vec{s}_i \cdot \vec{\nabla}_i = |d\vec{s}_i| \frac{\partial}{\partial R_i} \quad . \tag{10}$$

Now if we add and subtract $-i k n_i \psi(\vec{r}_i, \vec{r}_j) \psi(\vec{r}_i, \vec{r}_{j'}) R_i^2$ from the integrand in Eq. (8), we get

$$\int_{4\pi} d\Omega_i \left\{ \left[R_i \psi(\vec{r}_i, \vec{r}_{j'})\right] \left[R_i \left(\frac{\partial}{\partial R_i} \psi(\vec{r}_i, \vec{r}_j) - i k n_i \psi(\vec{r}_i, \vec{r}_j) \right) \right] \right.$$
$$\left. - \left[R_i \psi(\vec{r}_i, \vec{r}_j)\right] \left[R_i \left(\frac{\partial}{\partial R_i} \psi(\vec{r}_i, \vec{r}_{j'}) - i k n_i \psi(\vec{r}_i, \vec{r}_{j'}) \right)\right]\right\}$$
$$= -4\pi \left[\psi(\vec{r}_j, \vec{r}_{j'}) - \psi(\vec{r}_{j'}, \vec{r}_j)\right] \quad . \tag{11}$$

At this point, we introduce the condition of regularity at infinity* which

* J. A. Stratton, "Electromagnetic Theory," McGraw-Hill, New York (1941), p. 485(c).

requires that " ψ vanishes in such a way that lim $R\psi$ is bounded as $R \to \infty$," and the radiation condition† that

$$\lim_{R \to \infty} \quad R \left(\frac{\partial \psi}{\partial R} - i k n \psi \right) = 0 \quad . \tag{12}$$

It follows by inspection, from these two conditions, that the integrand on the left hand side of Eq. (11) becomes vanishingly small for large values of R . It follows from this that

$$\boxed{\psi(\vec{r}_j , \vec{r}_{j'}) = \psi(\vec{r}_{j'} , \vec{r}_j)} \quad . \tag{13}$$

When we consider that $\psi(\vec{r}_1 , \vec{r}_2)$ defines the field at $\vec{r}_1$ due to a point source at $\vec{r}_2$, we see that Eq. (13) is an explicit statement of point-to-point reciprocity. It states that quite independent of the nature of the refractive-index distribution, n_i , the phase and amplitude at $\vec{r}_j$ due to a unit point source at $\vec{r}_{j'}$ is exactly equal to the phase and amplitude at $\vec{r}_{j'}$ due to a unit point source at $\vec{r}_j$! It is especially significant to note that this result is completely rigorous and requires no approximations in its derivation.

With this result in hand, we are now ready to turn our attention to the nature of laser transmitter and optical heterodyne receiver performance. We take this up in the next section.

Reciprocity Proof -- Point-Aperture System

In this section, we shall demonstrate the existence of reciprocity for antenna gain between a laser transmitter propagating a signal to a point in space, and an optical heterodyne receiver collecting a signal from a source located at that same point in space. We assume that the heterodyne receiver antenna aperture is coincident with the laser transmitter's aperture.

† ibid., p. 486 (d) .

We let the point in space be denoted by $\vec{r}$, and let the aperture plane for either system be defined by the vector $\vec{x}_1$. We let the effective aperture be defined by the function $W(\vec{x}_1)$. Generally $W(\vec{x}_1)$ is taken to be a physical aperture, presumably circular in shape, so that its value is restricted to unity (within the circle) and zero (outside the circle). However, to be entirely general in our treatment, we will consider the aperture per se to be infinite in extent and take $W(\vec{x})$ as referring to the amplitude distribution of a laser beam at the aperture plane. In the case of a laser transmitter, this is the amplitude distribution for the transmitted laser beam at the aperture plane. (This distribution is, for our purposes, the definition of the aperture.) For the case of an optical heterodyne receiver, we can project the local oscillator laser beam backwards through the optical system, the other way through the beam splitter, so that it can be visualized as having a distribution over the aperture plane. For an optical heterodyne receiver, we take $W(\vec{x})$ as referring to the amplitude distribution of the laser local oscillator in terms of its virtual distribution at the aperture plane. In both cases, i.e., for both the laser transmitter and the optical heterodyne receiver, it is convenient to also introduce a phase function $\Phi(\vec{x})$ which carries information about any phase variations in the laser wavefront at the aperture. Thus for a tilt $\vec{\theta}$, $\Phi(\vec{x}) = \exp(-i k \vec{\theta} \cdot \vec{x})$. We note then that $\Phi(\vec{x})$ incorporates any laser beam focusing or tilting in our laser transmitter or optical heterodyne receiver, except that because the laser beam must be considered as going in opposite directions for the local oscillator of an optical heterodyne receiver and for a laser transmitter, if $\Phi(\vec{x})$ describes the wavefront shape for the optical heterodyne receiver, then $\Phi^*(\vec{x})$ defines the same shape surface for the laser transmitter. For the two cases, the aperture of the system can be considered to be fully defined by $W(\vec{x})\,\Phi(\vec{x})$, or by $W(\vec{x})\,\Phi^*(\vec{x})$.

What we wish to show is that the signal amplitude, S_{LT} at the space point $\vec{r}$ will vary with propagation conditions and the function $W(\vec{x})\,\Phi(\vec{x})$ for a laser transmitter, in exactly the same way that the signal amplitude, S_{OHR}, for an optical heterodyne receiver will vary with the propagation conditions and the choice of $W(\vec{x})\,\Phi(\vec{x})$. The proof of this, as we shall see, will derive from the point-to-point propagation reciprocity we demonstrated in the previous section, and the similarity in the nature of the equations for laser transmitter performance and for optical heterodyne receiver performance. We start by writing down a formal expression for laser transmitter performance.

In calculating the signal amplitude at $\vec{r}$ due to the laser transmitter, we start by noting that the signal amplitude, S_{LT}, is just the sum of the amplitudes at $\vec{r}$ due to the laser excitation at all of the various regions $d\vec{x}$ on the aperture. Thus, making use of the Maxwell's equation Green's function, we get

$$d\,S_{LT} = \psi(\vec{r},\vec{x})\,W(\vec{x})\;\Phi^{*}(\vec{x})\,d\vec{x} \quad , \tag{14}$$

where the Green's function $\psi(\vec{r},\vec{x})$ takes account of the propagation effects associated with some particular instantaneous sample of the random atmospheric turbulence induced refractive-index variation pattern in the propagation path. The total signal amplitude at $\vec{r}$ is just

$$\begin{aligned}
|S_{LT}| &= \left|\int d\,S_{LT}\right| \\
&= \left|\int d\vec{x}\;W(\vec{x})\;\psi(\vec{r},\vec{x})\;\Phi^{*}(\vec{x})\right| \\
&= \tfrac{1}{2}\left\{\left[\int d\vec{x}\;W(\vec{x})\;\psi(\vec{r},\vec{x})\;\Phi^{*}(\vec{x})\right]^{*} + \left[\int d\vec{x}\;W(\vec{x})\;\psi(\vec{r},\vec{x})\;\Phi^{*}(\vec{x})\right]\right\} \\
&= \tfrac{1}{2}\left\{\int d\vec{x}\;W(\vec{x})\;\psi^{*}(\vec{r},\vec{x})\;\Phi(\vec{x}) + \int d\vec{x}\;W(\vec{x})\;\psi(\vec{r},\vec{x})\;\Phi^{*}(\vec{x})\right\} \\
&= \tfrac{1}{2}\int d\vec{x}\;W(\vec{x})\left[\psi^{*}(\vec{r},\vec{x})\;\Phi(\vec{x}) + \psi(\vec{r},\vec{x})\;\Phi^{*}(\vec{x})\right] \quad .
\end{aligned} \tag{15}$$

This rather simple and intuitively obvious result is all we need in the way of analysis for the laser transmitter. We are now ready to turn our attention to the performance of the optical heterodyne receiver.

In treating the optical heterodyne receiver, we note first that the signal amplitude at the point $\vec{x}$ in the aperture plane due to a unity strength point source at $\vec{r}$ is $\psi(\vec{x},\vec{r})$. In the optical heterodyne receiver, this signal is added to the local oscillator signal $W(\vec{x})\,\Phi(\vec{x})$ and the magnitude squared is formed on a square law photodetector, i.e., we form

$$\tfrac{1}{2}\,\left|\,\psi(\vec{x},\vec{r}) + W(\vec{x})\,\Phi(\vec{x})\,\right|^2 = \tfrac{1}{2}\,\psi(\vec{x},\vec{r})\;\psi^*(\vec{x},\vec{r})$$
$$+ \tfrac{1}{2}\,[\psi(\vec{x},\vec{r})\;W(\vec{x})\,\Phi^*(\vec{x}) + \psi^*(\vec{x},\vec{r})\,W(\vec{x})\,\Phi(\vec{x})\,]$$
$$+ \tfrac{1}{2}\;W(\vec{x})\;\;W(\vec{x})\;\;\Phi^*(\vec{x})\;\;\Phi(\vec{x}) \qquad . \tag{16}$$

For the optical heterodyne receiver, a detectable beat frequency representing the difference between the optical frequency of the local oscillator and of the received signal from the point source at $\vec{r}$ is generated only by the cross-terms contained in the square brackets on the right hand side of Eq. (16). Thus, for the optical heterodyne receiver, the beat frequency signal associated with the element of aperture $d\vec{x}$ is

$$d\,S_{OHR} = \tfrac{1}{2}\,[\psi(\vec{x},\vec{r})\;W(\vec{x})\;\;\Phi^*(\vec{x}) + \psi^*(\vec{x},\vec{r})\;W(\vec{x})\;\Phi(\vec{x})\,]\;d\vec{x} \quad , \tag{17}$$

so that the total optical heterodyne receiver signal, obtained by integrating over the aperture plane is

$$S_{OHR} = \tfrac{1}{2}\int d\vec{x}\;W(\vec{x})\;[\psi^*(\vec{x},\vec{r})\;\Phi(\vec{x}) + \psi(\vec{x},\vec{r})\;\Phi^*(\vec{x})\,] \quad . \tag{18}$$

Now if we apply point-to-point reciprocity, as expressed in Eq. (13), we see that

$$S_{OHR} = \tfrac{1}{2}\int d\vec{x}\;W(\vec{x})\;[\psi^*(\vec{r},\vec{x})\;\Phi(\vec{x}) + \psi(\vec{r},\vec{x})\;\Phi^*(\vec{x})\,] \quad , \tag{19}$$

which is identical to $|S_{LT}|$ as given in Eq. (15). From this exact equivalence in magnitude, we can conclude that reciprocity exists between the performance of a laser transmitter to a point in space and an optical heterodyne receiver collecting a signal from that point in space, providing that the

two units have equivalent laser-aperture functions, namely $W(\vec{x})\,\phi(\vec{x})$ and $W(\vec{x})\,\phi^*(\vec{x})$. It is particularly interesting to note that if a change in $\phi^*(\vec{x})$ will improve the laser transmitter's performance by some fractional amount, then the corresponding change in $\phi(\vec{x})$ will produce the exact same fractional improvement in the optical heterodyne receiver's performance. This means that the same improvement in performance that could be achieved by an optical heterodyne receiver through the use of fast tracking can also be achieved by a laser transmitter, if it can obtain a tracking command signal. Moreover, the exact equivalence inherent in the above reciprocity proof makes it clear that if an optical heterodyne receiver is allowed to share the aperture with a laser transmitter, the receiver can generate the appropriate fast tracking commands both for itself and for the laser transmitter.

Reciprocity Proof -- Aperture-Aperture System

In the preceding two sections, we have gone exhaustively through the analytic details of the reciprocity proofs, perhaps sometimes expanding to a paragraph and several equations a portion of the proof that could have been covered with a single sentence.* This was done to insure ease in following the smallest details of the proof. In this section, we wish to demonstrate the validity of the reciprocity concept for a laser transmitter system operating into an optical heterodyne receiver. However, a detailed analysis of such a two-aperture system would be excessively cumbersome and we therefore shall attempt to simply describe how such a proof would proceed.

We may consider the proof of reciprocity in the two-aperture system to have been demonstrated if we can show that when we interchange the roles of the transmitter and the receiver, we retain the same expression for the

* Consider, for example, the much briefer coverage provided in R. F. Lutomirski and H. T. Yura, op cit , and in D. L Fried and H. T. Yura, J. Opt. Soc. Am. 62, 600 (1972)

signal strength. Our analysis would start by writing an expression for the aperture functions on the $\vec{x}$-plane , $W(\vec{x})\,\Phi(\vec{x})$ for a receiver, and $W(\vec{x})\,\Phi^*(\vec{x})$ for a transmitter, and introducing the $\vec{y}$-plane corresponding to the point in space at $\vec{r}$ in our previous section, so that $\vec{y}$ represents two components of $\vec{r}$, and introducing the aperture functions on the $\vec{y}$-plane, which we denote by $w(\vec{y})\,\phi(\vec{y})$ for the receiver, and $w(\vec{y})\,\phi^*(\vec{y})$ for the transmitter. For the receiver in the $\vec{x}$-plane and the transmitter in the $\vec{y}$-plane, the signal at $d\vec{x}$ due to an element of the transmitter at $d\vec{y}$ is

$$d^2 S_{xy} = d\vec{x}\,\{\,\psi(\vec{x},\vec{y})\;w(\vec{y})\;\phi^*(\vec{y})\;d\vec{y}\,\}\quad , \tag{20}$$

while for the transmitter in the $\vec{x}$-plane and the receiver in the $\vec{y}$-plane, the corresponding element of signal is

$$d^2 S_{yx} = d\vec{y}\,\{\psi(\vec{y},\vec{x})\;W(\vec{x})\;\Phi^*(\vec{x})\;d\vec{x}\,\}\quad , \tag{21}$$

In the heterodyne receiver at $\vec{x}$, the detection process multiplies $d^2 S_{xy}$ by $W(\vec{x})\,\Phi^*(\vec{x})$ and its complex conjugate by $W(\vec{x})\,\Phi(\vec{x})$. Then integrating over the $\vec{x}$-plane and over the $\vec{y}$-plane to obtain the total signal S_{xy} for propagation from a laser transmitter in the $\vec{y}$-plane to an optical heterodyne receiver in the $\vec{x}$-plane, we get an expression of the nature of

$$S_{xy} = \tfrac{1}{2}\int d\vec{x}\int d\vec{y}\;W(\vec{x})\;w(\vec{y})[\psi(\vec{x},\vec{y})\;\Phi^*(\vec{x})\,\phi^*(\vec{y}) + \psi^*(\vec{x},\vec{y})\;\Phi(\vec{x})\,\phi(\vec{y})]. \tag{22}$$

When we consider the aperture at $\vec{y}$ to define an optical heterodyne receiver, and the one at $\vec{x}$ to define a unit that functions as a laser transmitter, and integrate over the $\vec{x}$-plane and over the $\vec{y}$-plane, we get for the signal received at $\vec{y}$

$$S_{yx} = \tfrac{1}{2}\int d\vec{x}\int d\vec{y}\;W(\vec{x})\;w(\vec{y})\;[\psi(\vec{y},\vec{x})\,\phi^*(\vec{y})\;\Phi^*(\vec{x}) + \psi^*(\vec{y},\vec{x})\,\phi(\vec{y})\;\Phi(\vec{x})\;]\,. \tag{23}$$

It is immediately apparent, considering the point-to-point reciprocity expressed in Eq. (13), that S_{xy} is identically equal to S_{yx} . This

demonstrates aperture-to-aperture reciprocity. If we have an optical signal link consisting of two apertures and a propagation path between then, with one aperture representing a laser transmitter and the other an optical heterodyne receiver, then the signal generated at the receiver is the same, no matter which aperture we consider to be the receiver.* The effect of atmospheric turbulence and of aperture wave function variations is the same, no matter which way the optical signal is flowing. We have exact reciprocity.

* Note that we are talking about interchanging the aperture functions, i.e., transmission and reception, but not interchange of the physical apertures. That latter is a distinctly different matter (involving replacement of $W(\vec{x})\,\phi(\vec{x})$ by $W(\vec{y})\,\phi(\vec{y})$, for which our proof does not apply and for which, in general, we would not expect reciprocity to hold.

APPENDIX II

EQUIVALENCE OF RECEIVERS

by D. L. Fried

The material in this Appendix has been excerpted from Optical Science Consultants Report No. TR-083 (November 1972) and is included as received from that organization.

PRECEDING PAGE BLANK-NOT FI

Introduction

The concept of Optical Antenna Gain Reciprocity for Propagation Through a Turbulent Medium states that for certain classes of optical transmitters and of optical receivers, the performance of the link between a transmitter and a receiver is independent of whether the antenna at one end of the link is functioning as part of the transmitter system or as part of the receiver system (with the antenna at the other end, naturally, functioning in the reverse role). This means that if at both ends of an optical link the antennas are used in the dual role of transmitter and receiver, then we expect that any fade in the signal level going one way will be exactly mimicked by a fade in the signal level going the other way; and moreover, any adjustment in the pointing of one of the antennas will have the same effect on both links -- if it improves (or harms) the signal level in one direction, it will similarly improve (or harm) the signal level in the other direction.

The concept of reciprocity as just described has a potentially important practical implication in an optical communications system, operating through the atmosphere. For an uplink, i.e., transmitter on the ground and receiver in space, atmospheric turbulence can severely degrade the expected performance of the system by affecting the transmitter antenna gain. Following reciprocity concepts, however, we find that if the ground transmitter antenna is also used as a receiver viewing a beacon on the space vehicle, then by adjusting the ground antenna's pointing so as to maximize the received signal, the uplink signal is improved to the extent that about 10 dB better performance can be achieved than would be possible without beacon tracking.

In Optical Science Consultants Report No. TR-080, we provided a formal proof of the concept of reciprocity. However, that treatment emphasized the relationship between a laser transmitter and an optical heterodyne receiver. That report only touched briefly on other somewhat less coherent types of receivers and their relationship to the concept of reciprocity as we plan to use it. However, in fact, all plans for the use of reciprocity as a basis for

PRECEDING PAGE BLANK-N

"beacon tracking" aid in uplink transmitter pointing, and all intermediate experimental measurement programs related to this, avoid the use of an optical heterodyne receiver, and instead rely on some sort of less than fully coherent (sub-coherent) detection system.

It is the objective of this report to establish the relationship between the optical heterodyne receiver and the sub-coherent receiver, and show that with a reasonable degree of accuracy, the results derived for reciprocity in relationship to the optical heterodyne receiver also apply for a sub-coherent receiver. We do this by showing that the signal to be expected from either type of receiver under various conditions is essentially the same.

Receiver Performance

For a circular aperture of diameter D, defined by the function

$$W_o(\vec{x}) = \begin{cases} 1, & \text{if } |\vec{x}| \leq \frac{1}{2} D \\ 0, & \text{if } |\vec{x}| > \frac{1}{2} D \end{cases} . \qquad (1)$$

Collecting a randomly distorted signal wave function $u(\vec{x})$ and mixing it with a local oscillator wave function $u_{LO}(\vec{x})$, it can be shown that the beat frequency signal will have an amplitude

$$A_{OHR} = \alpha \int d\vec{x}\ W_o(\vec{x})\, u(\vec{x})\, u_{LO}^*(\vec{x}) \quad , \qquad (2)$$

where α is a constant of proportionality, and where we have everywhere suppressed any explicit time dependence. The power associated with this optical heterodyne receiver signal is

$$P_{OHR} = \tfrac{1}{2} |A_{OHR}|^2$$

$$= \tfrac{1}{2} \alpha^2 \iint d\vec{x}\, d\vec{x}' W_o(\vec{x})\, W_o(\vec{x}')\, u^*(\vec{x})\, u(\vec{x}')\, u_{LO}(\vec{x})\, u_{LO}^*(\vec{x}') \quad . \qquad (3)$$

This random variable, P_{OHR}, which is dependent on the random function

$u^*(\vec{x})$, measures the receiver signal strength. In a normal optical heterodyne receiver, the local oscillator wave function is uniform across the aperture and has some (slight) tilt $\vec{\theta}$ relative to the nominal line of sight direction. Hence we can write

$$u_{LO}(\vec{x}) = \exp(i k \vec{\theta} \cdot \vec{x}) \quad , \tag{4}$$

where we have, without loss of generality, arbitrarily assigned an amplitude of unity to the local oscillator, and have used k to denote the optical wave number. Thus

$$P_{OHR} = \tfrac{1}{2} \alpha^2 \iint d\vec{x}\, d\vec{x}'\, W_o(\vec{x}) W_o(\vec{x}')\, u^*(\vec{x})\, u(\vec{x}')\, \exp[i k \vec{\theta} \cdot (\vec{x} - \vec{x}')] \quad . \tag{5}$$

This completes the basic formulation for the coherent receiver.

We start our treatment of the signal obtained from a sub-coherent receiver by first considering the signal amplitude in the focal plane of some perfect lens. For convenience, we shall assume, without loss of generality, that the lens focal length is unity. This will allow us to treat focal plane position and angular coordinates interchangeably, and in fact we shall only work with the angular coordinate version. Rather than go through the details of calculating the pattern, ab initio , we make use of the well known fact that the focal plane amplitude pattern is the Fourier transform of the pupil function, in this case $W_o(\vec{x})\, u(\vec{x})$. Thus the amplitude in the focal plane at $\vec{\theta}$ is

$$A_{FP}(\vec{\theta}) = \beta \int d\vec{x}\, W_o(\vec{x})\, u(\vec{x})\, \exp(i k \vec{\theta} \cdot \vec{x}) \quad , \tag{6}$$

where β is a constant of proportionality. The power in the focal plane is just

$$P_{FP}(\vec{\theta}) = \tfrac{1}{2} |A_{FP}(\vec{\theta})|^2$$

$$= \tfrac{1}{2} \beta^2 \iint d\vec{x}\, d\vec{x}'\, W_o(\vec{x})\, W_o(\vec{x}')\, u^*(\vec{x})\, u(\vec{x}')\, \exp[i k \vec{\theta} \cdot (\vec{x} - \vec{x}')] \quad . \tag{7}$$

The obvious equivalence of the right hand sides of Eq.'s (5) and (7) makes it clear that if we could measure its power density at $\vec{\theta}$ in the focal plane, then even though our measurement would be sub-coherent (as compared to the heterodyne receiver, since we could not determine the optical frequency), it would be an entirely adequate measure of received power to let us replace the heterodyne receiver with this lens and focal plane point power density measurement unit and still expect transmitter-receiver reciprocity to apply. The problem is that we can not measure power density at a point in the focal plane. We must measure it over some solid angle region, $d\vec{\theta}$. If $d\vec{\theta}$ is small enough, there should be no problem -- but how small is small enough. We provide some estimates in the next section.

Solid Angle Averaging

The sub-coherent receiver collects the focal plane power in some small angular region in the focal plane. This region may nominally be taken to be a circle centered about $\vec{\theta}_o$ with radius $\delta\theta$. Thus the sub-coherent receiver power would be

$$P_{SCR} = \int_{|\vec{\psi}| \le \delta\theta} d\vec{\psi}\ P_{FP}\ (\vec{\theta}_o + \vec{\psi}) \quad . \tag{8}$$

The simplest criteria we could apply to determine an allowable value for $\delta\theta$ is to note that if we substitute Eq. (7) into Eq. (8), and note that we have to consider both positive and negative values of $\vec{\psi}$, for each value of $\vec{x}$ and $\vec{x}'$, then what we are concerned about is the introduction of an extra factor of $\cos\,[k\vec{\psi}\cdot(\vec{x}-\vec{x}')]$ in the integrand.

$$P_{SCR} = \tfrac{1}{2}\beta^2 \int_{|\vec{\psi}| \le \delta\theta} \iint d\vec{x}\, d\vec{x}'\ W_o(\vec{x})\, W_o(\vec{x}')\, u^*(\vec{x})\, u(\vec{x}')\, \{\exp[i k \vec{\theta}_o \cdot (\vec{x}-\vec{x}')] \times \exp[i k \vec{\psi}\cdot(\vec{x}-\vec{x}')]\}$$

$$= \tfrac{1}{2}\beta^2 \int_{|\vec{\psi}| \le \delta\theta} \iint d\vec{x}\, d\vec{x}'\ W_o(\vec{x})\, W_o(\vec{x}')\, u^*(\vec{x})\, u(\vec{x}')\{\exp[i k \vec{\theta}_o \cdot (\vec{x}-\vec{x}')] \times \cos[k\vec{\psi}\cdot(\vec{x}-\vec{x}')]\} \quad . \tag{9}$$

If this extra factor were always unity, as it would be if $\delta\theta$ were essentially zero, then obviously P_{SCR} would be identical to P_{FP} (and thus to P_{OHR}). In practice, $\delta\theta$ can not be allowed to be too small or there will be no signal-to-noise ratio available. If, for example, we were willing to allow the cosine factor to introduce a correction to the integral of 10%, then we have some criteria for stating how large $\delta\theta$ can be. Taking first a worst case analysis for which $|\vec{x} - \vec{x}'| = D$, and assuming $\vec{\psi}$ is parallel (or anti-parallel) to $\vec{x} - \vec{x}'$, and further that $|\vec{\psi}| = \delta\theta$, we get

$$\cos(k\,\delta\theta\,D) = .9$$

$$\approx 1 - \tfrac{1}{2}\left(\frac{2\pi}{\lambda}\,\delta\theta\,D\right)^2 + \ldots \qquad (10)$$

so that

$$\delta\theta \approx 0.0712\frac{\lambda}{D} \quad , \qquad (11)$$

implying that the angular diameter of the focal plane pinhole over which the signal was being collected could only be $\frac{1}{14}\,\lambda/D$ if we wished to insure 90% accuracy in the relationship between the sub-coherent receiver signal thus generated and the signal we would get from an optical heterodyne receiver. While this provides a lower bound for our work, we shall, however, see that it is a quite pessimistic answer. We shall show that a more appropriate value is about $0.6\,\lambda/D$ for the focal plane aperture diameter. The reason for this large discrepancy follows from several considerations. First, most values of $\vec{x}$ and $\vec{x}'$ in the ranges of integration defined by $W_0(\vec{x})$ and $W_0(\vec{x}')$ give rise to an $\vec{x} - \vec{x}'$ whose magnitude is very much less than D. Secondly, there is a significant angle between $\vec{x} - \vec{x}'$ and $\vec{\psi}$ reducing their dot-product by about $\sqrt{2}$ on an average. Finally, only the largest values of $|\vec{\psi}|$ are as large as $\delta\theta$ -- most are noticeably smaller.

An easy way to combine these various factors into a single properly weighted result is not obvious, and in fact, considering the random nature of $u(\vec{x})$, it is not clear that there is a meaningful explicit answer to the

question of how large a focal plane area can we average over and still get a sub-coherent receiver signal power within ± 10% of what we would expect from a focal plane point detector, or an optical heterodyne receiver. When we examine Eq. (9) and note that for the cases we shall be interested in*, the wavefront as defined by $u(\vec{x})$ will be essentially flat and uniform, although possibly tilted in a way that is matched by θ_o . This suggests that we ought to consider as a measure of signal measurement performance as a function of focal plane pinhole size, the function

$$\eta = \frac{P_{SCR} \Big/ \int_{|\vec{\psi}| < \delta\theta} d\vec{\psi}}{P_{OHR}}$$

$$= \frac{\int_{|\vec{\psi}| < \delta\theta} d\vec{\psi} \iint d\vec{x}\, d\vec{x}'\, W_o(\vec{x})\, W_o(\vec{x}') \cos\left[k\vec{\psi} \cdot (\vec{x} - \vec{x}')\right] \Big/ \int_{|\vec{\psi}| < \delta\theta} d\vec{\psi}}{\iint d\vec{x}\, d\vec{x}'\, W_o(\vec{x})\, W_o(\vec{x}')} \qquad (12)$$

The use of the ratio of P_{SCR} to P_{OHR} in the definition of η needs no comment. However, the presence of the $\vec{\psi}$-integral deserves note. It is introduced to take account of the fact that P_{SCR} increases as we increase $\delta\theta$ just because the pinhole area increases and we collect more flux. The ratio of P_{SCR} to the $\vec{\psi}$-integral gives us a measure of the sub-coherent receiver's performance which is independent of this effect and only relates to the diffraction image extent. Because we have considered an aperture size for which the wavefront distortion is very small, the $u(\vec{x})$ and θ_o dependencies disappear from the integrand. Their values combine to unity. Hence the final form of Eq. (12). Some simple procedures allow us first to perform the $\vec{\psi}$-integration, yielding

* We shall not be particularly interested in cases in which the aperture diameter is large enough to subtend a noticeably distorted region of the wavefront. (Over small enough regions, the wavefront may appear tilted, but will not appear to be distorted.)

$$\eta = \frac{\iint d\vec{x}\, d\vec{x}'\, W_0(\vec{x})\, W_0(\vec{x}') \left[\frac{2 J_1(k|\vec{x}-\vec{x}'|\delta\theta)}{k|\vec{x}-\vec{x}'|\delta\theta}\right]}{\iint d\vec{x}\, d\vec{x}'\, W_0(\vec{x})\, W_0(\vec{x}')} \tag{13}$$

and then introducing sum and difference coordinates on $\vec{x}$ and $\vec{x}'$, and allowing

$$\vec{\rho} = (\vec{x} - \vec{x}')/D \quad , \tag{14}$$

we get

$$\eta = \frac{16}{\pi} \int_0^1 \rho\, d\rho \left[\cos^{-1}\rho - \rho(1-\rho^2)^{\frac{1}{2}}\right] \left[\frac{2 J_1(k\rho\,\delta\theta)}{k\rho\,\delta\theta}\right] . \tag{15}$$

This function has been evaluated numerically* and is shown plotted in Fig. 1. It can be seen from this data that we require that the pinhole be about equal to $0.6\,\lambda/D$ in diameter if the sub-coherent receiver and the optical heterodyne receiver signals are to be generated to be within 10% of each other.

* OSC Report No. TR-067

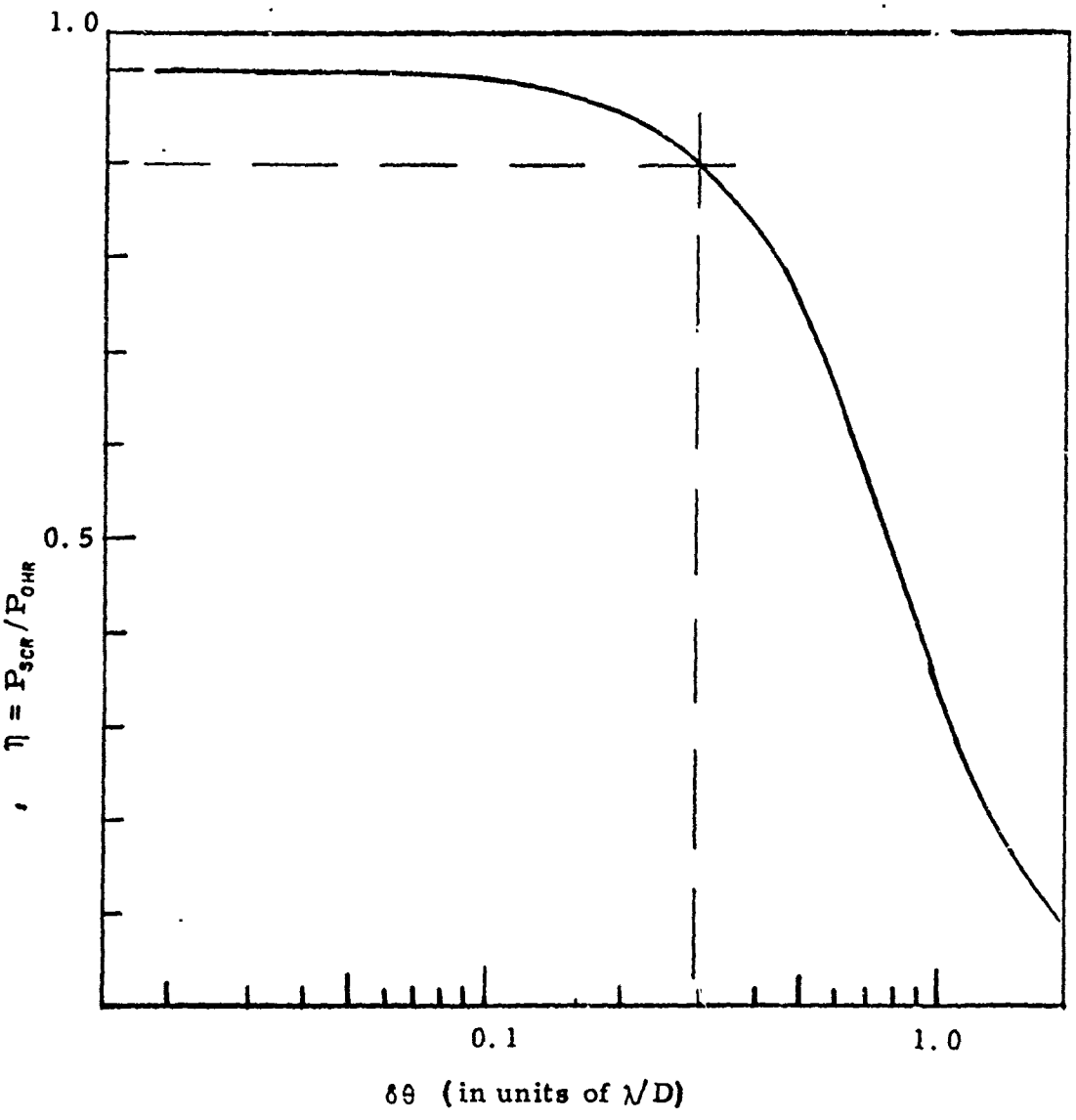


Figure 1. Ratio of Sub-Coherent Receiver Signal Power to Optical Heterodyne Receiver Signal Power as a Function of Focal Plane Aperture Radius, $\delta\theta$, in the Sub-Coherent Receiver.

APPENDIX III

BORESIGHT REQUIREMENTS FOR APPLICABILITY OF ANTENNA GAIN RECIPROCITY

by D. L. Fried

This Appendix is a reproduction of Optical Science Consultants Report No. TR-091 (January 1973) as provided by that organization.

Introduction

The concept of antenna gain reciprocity for propagation through a turbulent medium asserts that if a laser transmitter and a near coherent laser receiver, both operating at (nearly) the same wavelength share a common aperture, then the antenna gain of the transmitter will vary due to atmospheric turbulence in exactly the same way that the antenna gain of the receiver varies, provided that the two units are perfectly boresighted.[1] It is assumed that at the other end of the link is a similarly arranged transmitter-receiver unit, or that if the other end is in the distant far field*, then the two units are at least close together. In this paper we wish to take up the question of how precisely the boresight condition must be met if reciprocity is to apply. To put the question in quantitative terms, we start by noting that for perfect boresighting, the correlation between transmitter and receiver fluctuations is 100%, i.e., unity -- and we then ask how the correlation will vary as a function of the angular deviation from boresight.

Problem Formulation

Our procedure in formulating the problem of calculating the dependence of the correlation function on angular misalignment is to start by noting that while the correlation function is defined in terms of the correlation between the antenna gain of a heterodyne receiver and of a laser transmitter, we can by reciprocity replace the antenna gain of the laser transmitter by the antenna gain of a second optical heterodyne receiver that is perfectly boresighted with the laser transmitter. This means that we can calculate the boresight misalignment effect by calculating the correlation of the antenna gain of two optical heterodyne receivers whose local oscillators are misaligned with respect to each other. Both receivers share a common aperture and, of course, are receiving transmissions from the

* The distant far field region must be well removed from the region of turbulence and must be far field in terms of the size of the apertures at both ends if the relaxation to the condition of side-by-side units is to apply.

PRECEDING PAGE BLANK-NOT FILM

same source, i.e., they both collect the same atmospheric turbulence distorted wavefront.

One of the more interesting implications of the concept of antenna gain reciprocity is that it makes possible the fast tracking transmitter concept with an expected 10 dB improvement in atmospheric limit on performance of a laser transmitter. Key to this is the fact that reciprocity implies that the angular pointing adjustment that optimizes the performance of a coherent (or a subcoherent) receiver will also optimize the performance of a laser transmitter that shares the use of the aperture with the receiver. It is appropriate here to concern ourselves not only with the correlation of antenna gain as a function of boresight error for an ordinary, i.e., a non-tracking system, but also to inquire into the dependence of the correlation of antenna gain on boresight error for a fast tracking system. For this latter case, we will treat the problem as one of two optical heterodyne receivers with a common aperture where one of the two adjusts its local oscillator wavefront to follow the apparent tilt of the incident wave, while the second receiver tilts its local oscillator in perfect synchronism with the first receiver -- but with some constant additional angle corresponding to the boresight error.

Allowing the presence of a random phase as well as amplitude, we can say that the antenna gain of an optical heterodyne receiver is proportional to

$$G(\vec{\theta}) = \int d\vec{x}\, W(\vec{x}) \exp\left[\ell(\vec{x}) + i\phi(\vec{x}) - i k \vec{\theta} \cdot \vec{x}\right] \quad , \qquad (1)$$

where $\vec{x}$ is a two-dimensional vector on the aperture plane, and $W(\vec{x})$ is an aperture defining function which is equal to unity if the magnitude of $\vec{x}$ is less than one-half the diameter of the aperture, and is equal to zero if the magnitude of $\vec{x}$ is greater than one-half the diameter. $\ell(\vec{x})$ is the so-called log-amplitude variance induced by atmospheric turbulence, $\phi(\vec{x})$ is the random phase perturbation induced by atmospheric turbulence, k is the optical wave number, (i.e., $2\pi/\lambda$), and $\vec{\theta}$ is the tilt of the local oscillator relative to the plane against which $\phi(\vec{x})$ was defined. The angle

brackets $\langle\ \rangle$ denote an ensemble average. For the static case, we can write for the correlation function $C_s(\vec{\theta})$ for a boresight error $\vec{\theta}$

$$C_s(\vec{\theta}) = \langle \mathrm{Re}\,[G(\vec{\theta}_0)\, G(\vec{\theta}_0+\vec{\theta})]\rangle \,/\, \langle \mathrm{Re}\,[G(\vec{\theta}_0)]^2\rangle \quad , \tag{2}$$

where we assume that $\vec{\theta}_0$ has been set at a value which optimizes $G(\vec{\theta}_0)$. For the static case, $\vec{\theta}_0$ is not a random variable. The use of the real-part operator, Re , insures that we will consider amplitude only and ignore phase in determining the correlation.

Without loss of generality, we can assume that the plane against which $\phi(\vec{x})$ is measured is so oriented that the mean tilt of the phase distortion, as represented by $\phi(\vec{x})$, is zero. This means that $\vec{\theta}_0$ will be equal to zero. Thus

$$C_s(\vec{\theta}) = \langle \mathrm{Re}[G(0)\, G(\vec{\theta})]\rangle \,/\, \langle \mathrm{Re}[G(0)]^2\rangle \quad . \tag{3}$$

For the fast tracking case, we have to consider $\vec{\theta}_0$ to be a random variable which is continuously changing to follow the apparent tilt of the received wavefront, inherent in $\phi(\vec{x})$. The adjustment of $\vec{\theta}_0$ is such as to, at every instant, maximize $G(\vec{\theta}_0)$. For the tracking heterodyne receiver, the correlation of antenna gain as a function of a boresight error $\vec{\theta}$ is

$$C_T(\vec{\theta}) = \langle \mathrm{Re}\,[G(\vec{\theta}_0)\, G(\vec{\theta}_0+\vec{\theta})]\rangle \,/\, \langle \mathrm{Re}[G(\vec{\theta}_0)]^2\rangle \ , \quad (\vec{\theta}_0 \text{ random variable}) \ . \tag{4}$$

Making use of Eq. (1), we can show that

$$\langle \mathrm{Re}[G(0)\, G(\vec{\theta})]\rangle = \mathrm{Re}\left(\iint d\vec{x}\, d\vec{x}'\, W(\vec{x})\, W(\vec{x}')\, \exp(i\,k\,\vec{\theta}\cdot\vec{x}) \times \langle \exp\{\ell(\vec{x}) + \ell(\vec{x}') + i[\phi(\vec{x}) - \phi(\vec{x}')]\}\rangle \right) \ . \tag{5}$$

We have shown elsewhere[2] that for atmospheric turbulence induced phase

and log-amplitude variations

$$\langle \exp[\ell(\vec{x}) + \ell(\vec{x}') + i\,[\phi(\vec{x}) - \phi(\vec{x}')]]\rangle = \exp\,[-\tfrac{1}{2}\mathcal{D}(|\vec{x} - \vec{x}'|)]\quad , \tag{6}$$

where $\mathcal{D}$ is the so-called wave structure function and can be written as

$$\mathcal{D}(r) = 6.88\,(r/r_0)^{5/3}\quad , \tag{7}$$

where r_0 is a length which measures the "strength" of the atmospheric turbulence effect on the coherence of the wave.

If we now make the change of variables from $\vec{x}$ and $\vec{x}'$ to $\vec{r}$ and $\vec{r}'$, where

$$\vec{r} = \vec{x} - \vec{x}'\quad , \tag{8a}$$

$$\vec{r}' = \tfrac{1}{2}(\vec{x} + \vec{x}')\quad , \tag{8b}$$

then combining Eq.'s (5) and (6), we get

$$\langle \mathrm{Re}[G(0)\,G(\vec{\theta})]\rangle = \iint d\vec{r}\,d\vec{r}'\,W(\vec{r}' + \tfrac{1}{2}\vec{r})\,W(\vec{r}' - \tfrac{1}{2}\vec{r})\,\exp[-\tfrac{1}{2}\mathcal{D}(r)]$$
$$\times\,\mathrm{Re}\,(\exp\,[i\,k\,\vec{\theta}\cdot(\vec{r}' + \tfrac{1}{2}\vec{r})])\quad . \tag{9}$$

The real part of the exponential in Eq. (9) is, of course, just the cosine. We can expand this cosine, as its argument is the sum of $k\vec{\theta}\cdot\vec{r}'$ plus $\tfrac{1}{2}k\vec{\theta}\cdot\vec{r}$, into a cosine × cosine minus a sine × sine form. If this is put into Eq. (9), we recognize that the rest of the integrand is even in $\vec{r}$, so that the sine × sine contribution must vanish on integration, inasmuch as sine is odd. This means that we can rewrite Eq. (9) as

$$\langle \mathrm{Re}[G(0)\,G(\vec{\theta})]\rangle = \iint d\vec{r}\,d\vec{r}'\,W(\vec{r}' + \tfrac{1}{2}\vec{r})\,W(\vec{r}' - \tfrac{1}{2}\vec{r})\,\exp[-\tfrac{1}{2}\mathcal{D}(r)]$$
$$\times\,\cos\,(k\vec{\theta}\cdot\vec{r}')\,\cos(\tfrac{1}{2}k\vec{\theta}\cdot\vec{r})\quad . \tag{10}$$

The formulation of the denominator in Eq. (2) is obtained simply as a sub-case of Eq. (10), with $\vec{\theta} \equiv 0$. In this case we have

$$\langle \mathrm{Re}[G(0)]^2 \rangle = \iint d\vec{r}\, d\vec{r}\,' \, W(\vec{r}\,' + \tfrac{1}{2}\vec{r})\, W(\vec{r}\,' - \tfrac{1}{2}\vec{r}) \exp[-\tfrac{1}{2}\mathcal{D}(r)] \quad . \tag{11}$$

For the case of the tracking heterodyne receiver, we have to treat $\vec{\theta}_0$ as a random variable. In this case, we get

$$\langle \mathrm{Re}[G(\vec{\theta}_0)\, G(\vec{\theta}_0 + \vec{\theta})] \rangle = \mathrm{Re} \left(\iint d\vec{x}\, d\vec{x}\,' \, W(\vec{x})\, W(\vec{x}\,') \exp(i k \vec{\theta} \cdot \vec{x}) \right.$$
$$\left. \times \langle \exp\{\ell(\vec{x}) + \ell(\vec{x}\,') + i[\phi(\vec{x}) - \phi(\vec{x}\,') - k^2 \vec{\theta}_0 \cdot (\vec{x} - \vec{x}\,')]\} \rangle \right) \quad . \tag{12}$$

It has been shown[3] that so long as $\vec{\theta}_0$ is a random variable which on an instantaneous basis matches the random tilt of the wavefront, as embodied in the linear part of the dependence of $\phi(\vec{x})$ on $\vec{x}$, then

$$\langle \exp\{\ell(\vec{x}) + \ell(\vec{x}\,') + i[\phi(\vec{x}) - \phi(\vec{x}\,') - k^2 \vec{\theta}_0 \cdot (\vec{x} - \vec{x}\,')]\} \rangle$$
$$= \exp\left[-\tfrac{1}{2}\mathcal{D}(|\vec{x} - \vec{x}\,'|) + \tfrac{1}{4} k^2 |\vec{x} - \vec{x}\,'|^2 \langle |\vec{\theta}_0|^2 \rangle\right] \quad . \tag{13}$$

If we substitute Eq. (13) into Eq. (12), and replace the variables $\vec{x}$, $\vec{x}\,'$ by $\vec{r}$, $\vec{r}\,'$, as defined in Eq. (8a and b), we get

$$\langle \mathrm{Re}[G(\vec{\theta}_0)\, G(\vec{\theta}_0 + \vec{\theta})] \rangle = \iint d\vec{r}\, d\vec{r}\,' \, W(\vec{r}\,' + \tfrac{1}{2}\vec{r})\, W(\vec{r}\,' - \tfrac{1}{2}\vec{r})$$
$$\times \exp\left[-\tfrac{1}{2}\mathcal{D}(r) + \tfrac{1}{4} k^2 r^2 \langle |\vec{\theta}_0|^2 \rangle\right] \mathrm{Re}\left(\exp[i k \vec{\theta} \cdot (\vec{r}\,' + \tfrac{1}{2}\vec{r})]\right) \quad . \tag{14}$$

It has been shown[3] that for a circular aperture of diameter D

$$\langle |\vec{\theta}_0|^2 \rangle = \frac{64}{D^4} \int_0^D r\, dr\, [\mathcal{F}_c(r, D) - \mathcal{F}_L(r, D)]\, \mathcal{D}(r) \quad , \tag{15}$$

where

$$\mathcal{F}_c(r, D) = \pi^{-1} \{2 \cos^{-1}(r/D) - 2(r/D)[1 - (r/D)^2]^{\frac{1}{2}}\} \quad , \tag{16a}$$

$$\mathcal{F}_L(r, D) = \pi^{-1} \{6 \cos^{-1}(r/D) - [14(r/D) - 8(r/D)^3][1 - (r/D)^2]^{\frac{1}{2}}\} \quad . \tag{16b}$$

Applying Eq. (7), it is then possible to show by simply carrying out the integration that

$$k^2 \langle |\vec{\theta}_0|^2 \rangle = 2 \times 6.88\, r_0^{-5/3}\, D^{-\frac{1}{3}} \quad . \tag{17}$$

With this expression in hand, we can consider the performance of the integral in Eq. (14) as a straightforward numerical matter, except that it is first convenient to replace the real part of the exponential by a cosine-function, and then expand this as the cosine of a sum, and then drop the sine part of the expansion on the basis that it gives rise to an odd integrand which must vanish on integration. Then we can write

$$\langle \mathrm{Re}[G(\vec{\theta}_o)\, G(\theta_o+\vec{\theta})]\rangle = \iint d\vec{r}\, d\vec{r}\,'\, W(\vec{r}\,'+\tfrac{1}{2}\vec{r})\, W(\vec{r}\,'-\tfrac{1}{2}\vec{r})$$

$$\times \exp\left[-\tfrac{1}{2}\mathcal{D}(r)+\tfrac{1}{2}k^2 r^2 \langle|\vec{\theta}_o|^2\rangle\right] \cos(k\vec{\theta}\cdot\vec{r}\,') \cos(\tfrac{1}{2}k\vec{\theta}\cdot\vec{r}) \quad . \qquad (18)$$

The denominator for Eq. (4) is obtained from Eq. (18) by simply letting $\vec{\theta}$ vanish, in which case we get

$$\langle \mathrm{Re}[G(\vec{\theta}_o)]^2\rangle = \iint d\vec{r}\, d\vec{r}\,'\, W(\vec{r}\,'+\tfrac{1}{2}\vec{r})\, W(\vec{r}\,'-\tfrac{1}{2}\vec{r}) \exp\left[-\tfrac{1}{2}\mathcal{D}(r)+\tfrac{1}{4}k^2 r^2\langle|\vec{\theta}_o|^2\rangle\right] . \qquad (19)$$

With these expressions in hand, we are now ready to turn our attention to the problem of numerical evaluation of the quadruple integrals in Eq.'s (10), (11), (18), and (19). We take this up in the next section.

Numerical Evaluation

In previous papers, we have encountered quadruple integrals of the form of Eq.'s (10), (11), (18), and (19), and have been able to reduce them to single integrations which had to be performed numerically. However, in the case of Eq.'s (10) and (18), the presence of the dot products, i.e., $\vec{\theta}\cdot\vec{r}$ and $\vec{\theta}\cdot\vec{r}\,'$ so complicates the problem that we do not seem to be able to carry out any of the integrations analytically.* In this section we shall therefore be concerned with recognition of those symmetries in the integrands that can be used to reduce the magnitude of the numerical

---

* An attempt to attack the problem by use of Hankel transforms reduced the number of integrations by one, but replaced that integration by an infinite sum over coefficients obtained from a Gegenbauer-function expansion, as well as introducing Bessel-functions into the integrand and replacing the finite integral limits with infinite limits.

integration problem.

We start by representing in Eq.'s (10) and (18) with $\vec{r}'$ in rectangular coordinates as (r_x', r_y') and with $\vec{r}$ in polar coordinates as (r, ϕ_r). Moreover, we choose the r_x'-axis to be parallel to $\vec{\theta}$, and orient the (r, ϕ_r) polar coordinates so that ϕ_r is zero for $\vec{r}$ parallel to $\vec{\theta}$. Thus we can write for Eq. (10)

$$\langle \mathrm{Re}[G(0)\, G(\vec{\theta})] \rangle = \int_0^D r\, dr \int_0^{2\pi} d\phi_r \int_{-\frac{1}{2}D}^{\frac{1}{2}D} dr_x' \int_{-\frac{1}{2}D}^{\frac{1}{2}D} dr_y'\, W\left(\sqrt{(r_x' + \tfrac{1}{2}r\cos\phi_r)^2 + (r_y' + \tfrac{1}{2}r\sin\phi_r)^2}\right)$$

$$\times\, W\left(\sqrt{(r_x' - \tfrac{1}{2}r\cos\phi_r)^2 + (r_y' - \tfrac{1}{2}r\sin\phi_r)^2}\right) \exp[-3.44(r/r_0)^{5/3}]$$

$$\times\, \cos(k\,\theta\, r_x') \cos(\tfrac{1}{2}k\,\theta\, r\cos\phi_r) \quad , \qquad (20)$$

where we have introduced the explicit representation for $\mathcal{P}(r)$ given in Eq. (7), and have shown explicitly the limits on the r and ϕ integrations which are inherent in the product of the aperture functions, W. The limits shown for the r_x'- , and r_y'-integrations are excessive in that for some combinations of values of r_x' and r_y' allowed by these limits, the product of the W's will vanish. For Eq. (18), the equivalent expression is

$$\langle \mathrm{Re}[G(\vec{\theta}_0) G(\vec{\theta}_0 + \vec{\theta})] \rangle = \int_0^D r\, dr \int_0^{2\pi} d\phi_r \int_{-\frac{1}{2}D}^{\frac{1}{2}D} dr_x' \int_{-\frac{1}{2}D}^{\frac{1}{2}D} dr_y'\, W\left(\sqrt{(r_x' + \tfrac{1}{2}r\cos\phi_r)^2 + (r_y' + \tfrac{1}{2}r\sin\phi_r)^2}\right)$$

$$\times\, W\left(\sqrt{(r_x' - \tfrac{1}{2}r\cos\phi_r)^2 + (r_y' - \tfrac{1}{2}r\sin\phi_r)^2}\right) \exp\{-3.44(r/r_0)^{5/3}[1 - (r/D)^{\frac{1}{3}}]\}$$

$$\times\, \cos(k\,\theta\, r_x') \cos(\tfrac{1}{2}k\,\theta\, r\cos\phi_r) \quad , \qquad (21)$$

where here we have also made use of Eq. (17).

At this point, viewing Eq.'s (20) and (21), we note that it would be convenient to separate out the ϕ_r- , r_x'- , and r_y'-integrations. We get the same quantity from either Eq. (20) or (21), which we define as the function $F(\theta, r)$, which we can write as

$$F(\theta, r) = \int_0^{2\pi} d\phi_r \int_{-\frac{1}{2}D}^{\frac{1}{2}D} dr_x' \int_{-\frac{1}{2}D}^{\frac{1}{2}D} dr_y' \; W\left(\sqrt{(r_x' + \tfrac{1}{2}r\cos\phi_r)^2 + (r_y' + \tfrac{1}{2}r\sin\phi_r)^2}\right)$$

$$\times \; W\left(\sqrt{(r_x' - \tfrac{1}{2}r\cos\phi_r)^2 + (r_y' - \tfrac{1}{2}r\sin\phi_r)^2}\right) \cos(k\theta r_x') \cos(\tfrac{1}{2}k\theta r\cos\phi_r) \,. \quad (22)$$

With this function in hand, we can write in place of Eq.'s (20) and (21),

$$\langle \mathrm{Re}[G(0)\, G(\vec{\theta})] \rangle = \int_0^D r\, dr\, F(\theta, r) \exp[-3.44(r/r_0)^{5/3}] \,, \quad (23)$$

$$\langle \mathrm{Re}[G(\vec{\theta}_0)\, G(\vec{\theta}_0 + \vec{\theta})] \rangle = \int_0^D r\, dr\, F(\theta, r) \exp\{-3.44\,(r/r_0)^{5/3}[1 - (r/D)^{\frac{1}{3}}]\}, \quad (24)$$

Examining Eq. (22), we note that the integrand is even in r_x' and in r_y'. This means that we can replace the limits on these integrations, which were $-\frac{1}{2}D$ to $+\frac{1}{2}D$, with the limits 0 to $+\frac{1}{2}D$, by simply introducing a factor of 4. We also note that the integrand is unchanged if ϕ_r is replaced by $\pi + \phi_r$. This means that by introducing another factor of 2, we can reduce the range of the ϕ_r-integration from 0 to 2π to 0 to π. Thus we can write

$$F(\theta, r) = 8 \int_0^{\pi} d\phi_r \int_0^{\frac{1}{2}D} dr_x' \int_0^{\frac{1}{2}D} dr_y' \; W\sqrt{(r_x' + \tfrac{1}{2}r\cos\phi_r)^2 + (r_y' + \tfrac{1}{2}r\sin\phi_r)^2}$$

$$\times \; W\left(\sqrt{(r_x' - \tfrac{1}{2}r\cos\phi_r)^2 + (r_y' - \tfrac{1}{2}r\sin\phi_r)^2}\right) \cos(k\theta r_x') \cos(\tfrac{1}{2}k\theta r\cos\phi_r) \,. \quad (25)$$

As a practical matter in carrying out the integrations, it is convenient to cast the integral of ϕ_r over the range $\frac{1}{2}\pi$ to π as an integration over the range 0 to $\frac{1}{2}\pi$, but with a somewhat different integrand. Furthermore, it is convenient to introduce the unit circle aperture function, $\bar{W}(\rho)$ which is unity for ρ less than one-half, and zero for ρ greater than one-half. Then we can write

$$F(\theta, r) = 8\, D^2 \int_0^{\frac{1}{2}\pi} d\phi_r \int_0^{\frac{1}{2}} dr_x' \int_0^{\frac{1}{2}} dr_y' \cos\left[2\pi\left(\frac{\theta}{\lambda/D}\right) r_x'\right] \cos\left[\pi\left(\frac{\theta}{\lambda/D}\right)\left(\frac{r}{D}\right)\cos\phi_r\right]$$

$$\times \{\bar{W}\left(\sqrt{[r_x' + \tfrac{1}{2}(r/D)\cos\phi_r]^2 + [r_y' + \tfrac{1}{2}(r/D)\sin\phi_r]^2}\right)$$

$$\times \; \bar{W}\left(\sqrt{[r_x' - \tfrac{1}{2}(r/D)\cos\phi_r]^2 + [r_y' - \tfrac{1}{2}(r/D)\sin\phi_r]^2}\right)$$

$$+ \; \bar{W}\left(\sqrt{[r_x' + \tfrac{1}{2}(r/D)\cos\phi_r]^2 + [r_y' - \tfrac{1}{2}(r/D)\sin\phi_r]^2}\right)$$

$$\times \; \bar{W}\left(\sqrt{[r_x' - \tfrac{1}{2}(r/D)\cos\phi_r]^2 + [r_y' + \tfrac{1}{2}(r/D)\sin\phi_r]^2}\right)\} \,, \quad (26)$$

where we have replaced k by $2\pi/\lambda$. At this point, we note that actually we can do the r_y'-integration now. Each of the two products of $\overline{W}$-functions gives rise to an allowed range of r_y' over which the value of the product is unity, and outside which it is zero. The first $\overline{W}$-function in Eq. (26) gives rise to the condition

$$[r_x'+\tfrac{1}{2}(r/D)\cos\phi_r]^2 + [r_y'+\tfrac{1}{2}(r/D)\sin\phi_r]^2 \le \tfrac{1}{4} \quad , \tag{27}$$

which is an equality when

$$r_y' = -\tfrac{1}{2}(r/D)\sin\phi_r \pm\sqrt{\tfrac{1}{4} - [r_x'+\tfrac{1}{2}(r/D)\cos\phi_r]^2} \quad . \tag{28}$$

Only for values of r_y' that fall between the two values of r_y' given by Eq. (28) will the first $\overline{W}$-function in Eq. (26) be non-vanishing. The second $\overline{W}$-function in Eq. (26) gives rise to the boundary points

$$r_y' = \tfrac{1}{2}(r/D)\sin\phi_r \pm\sqrt{\tfrac{1}{4} - [r_x' - \tfrac{1}{2}(r/D)\cos\phi_r]^2} \quad . \tag{29}$$

We see that for the product of the first two $\overline{W}$-functions in Eq. (26), the upper bound is the lesser of the two upper values in Eq.'s (28) and (29), which since $0 \le \phi_r \le \tfrac{1}{2}\pi$, is

$$(r_y')_{ub,1} = \begin{cases} -\tfrac{1}{2}(r/D)\sin\phi_r + \sqrt{\tfrac{1}{4} - [r_x'+\tfrac{1}{2}(r/D)\cos\phi_r]^2} \\ 0 \end{cases} \text{, whichever is greater} \tag{30}$$

The possible value of zero is introduced in Eq. (30) to take account of the fact that the lower limit on the r_y'-integration in Eq. (26) is zero.

Similarly, for the product of the first two $\overline{W}$-functions in Eq. (26), the lower bound is the greater of the two lower values in Eq.'s (28) and (29), which is

$$(r_y')_{lb,1} = \begin{cases} \tfrac{1}{2}(r/D)\sin\phi_r - \sqrt{\tfrac{1}{4} - [r_x' - \tfrac{1}{2}(r/D)\cos\phi_r]^2} \\ 0 \end{cases} \text{, whichever is greater .} \tag{31}$$

Here again the zero is introduced to take account of the lower limit on the r_y'-integration in Eq. (26). The allowed range of r_y' in the r_y'-integration, for which the product of the first two $\bar{W}$-functions is non-vanishing, is

$$Y_{\ell,1} = \begin{cases} (r_y')_{ub,1} - (r_y')_{\ell b,1} \\ 0 \end{cases} \text{, whichever is greater .} \qquad (32)$$

The introduction of the possibility of a zero value in Eq. (32) takes account of the fact that nothing in the above formulation precluded the possibility of an upper bound less than the lower bound, in which case the allowed range of the r_y'-integration is zero, not negative.

If we go through exactly the same procedures for the product of the second two $\bar{W}$-functions in Eq. (26), the corresponding results are

$$UB = \begin{cases} -\frac{1}{2}(r/D)\sin\phi_r + \sqrt{\frac{1}{4} - [r_x' + \frac{1}{2}(r/D)\cos\phi_r]^2} \\ \frac{1}{2}(r/D)\sin\phi_r + \sqrt{\frac{1}{4} - [r_x' - \frac{1}{2}(r/D)\cos\phi_r]^2} \end{cases} \text{, whichever is less} \qquad (33')$$

$$(r_y')_{ub,2} = \begin{cases} UB \\ 0 \end{cases} \text{, whichever is greater} \qquad (33)$$

$$(r_y')_{\ell b,2} = \begin{cases} \frac{1}{2}(r/D)\sin\phi_r - \sqrt{\frac{1}{4} - [r_x' + \frac{1}{2}(r/D)\cos\phi_r]^2} \\ 0 \end{cases} \text{, whichever is greater} \qquad (34)$$

$$Y_{\ell,2} = \begin{cases} (r_y')_{ub,2} - (r_y')_{\ell b,2} \\ 0 \end{cases} \text{, whichever is greater} \qquad (35)$$

where $Y_{\ell,2}$ is the allowed length of the r_y'-integration over which the product of the second two $\bar{W}$-functions in Eq. (26) is non-vanishing. (Note that Eq.'s (33) and (33') do not exactly correspond to Eq. (30), since for Eq. (30) the selection performed in Eq. (33') is trivial.)

We now can rewrite Eq. (26) in the form

$$F(\theta, (r/D)) = 8\,D^2 \int_0^{\frac{1}{2}\pi} d\phi_r \int_0^{\frac{1}{2}} dr_x' \cos\left[2\pi\left(\frac{\theta}{\lambda/D}\right) r_x'\right] \cos\left[\pi\left(\frac{\theta}{\lambda/D}\right)\left(\frac{r}{D}\right)\cos\phi_r\right] Y_\ell, \qquad (36)$$

where

$$Y_{\ell} = Y_{\ell,1} + Y_{\ell,2} \quad , \tag{37}$$

and where we have taken the liberty of replacing r by r/D in the argument of F, since it is only (r/D) that appears in the right hand side of Eq. (27).

Now we can rewrite Eq.'s (23) and (24) as

$$\langle \mathrm{Re}[G(0)\, G(\vec{\theta})]\rangle = D^2 \int_0^1 r\, dr\, F(\theta, r) \exp\left\{-3.44\left[\frac{r}{(r_0/D)}\right]^{5/3}\right\} , \tag{38}$$

$$\langle \mathrm{Re}[G(\vec{\theta}_0)\, G(\vec{\theta}_0+\vec{\theta})]\rangle = D^2 \int_0^1 r\, dr\, F(\theta, r) \exp\left\{-3.44\left[\frac{r}{(r_0/D)}\right]^{5/3}(1-r^{\frac{1}{3}})\right\} , \tag{39}$$

where here $F(\theta, r)$ corresponds literally to the definition in Eq. (36). I.e., r as used here runs from zero to one and corresponds to (r/D) in Eq. (36), which also runs over the range of zero to one.

We have prepared computer programs to carry out the calculations corresponding to Eq.'s (36), (37), (38), and (39). These programs are listed at the end of this appendix. It should be noted that actually, rather than calculate $\langle \mathrm{Re}[G(0)\, G(\vec{\theta})]\rangle$ and $\langle \mathrm{Re}[G(\vec{\theta}_0)\, G(\vec{\theta}_0+\vec{\theta})]\rangle$ from Eq.'s (38) and (39), we calculated a quantity equal to $(2/\pi)$ times these quantities. This represents "diameter normalization" in that it scales the results so that for the case $\vec{\theta} = 0$, for which we are calculating the mean square antenna gain, the asymptotic limit for very large diameters equals unity. The actual rms antenna gain in this limit is equal to the free space value for an antenna with diameter $D = r_0$. In Table 1, we list the values of $F(\theta, r)$ calculated according to Eq. (36). In Table 2, we list the values of $(2/\pi)\langle \mathrm{Re}[G(0)\, G(\vec{\theta})]\rangle$, and in Table 3, we list the values of $(2/\pi)\langle \mathrm{Re}[G(\vec{\theta}_0)\, G(\vec{\theta}_0+\vec{\theta})]\rangle$, each shown as a function of both θ and D/r_0, calculated on the basis of Eq.'s (38) and (39). In Tables 4 and 5, we show the values of the correlation of antenna gain for static and tracking systems, i.e., $C_s(\theta)$ and $C_T(\theta)$, calculated from Eq.'s (3) and (4), each as a function of θ and D/r_0. In the next section, we discuss the significance of these results.

Discussion of Results

All of the important results of our work are contained in Tables 4 and 5. These tables tell us how well antenna gain is correlated between two units with a common aperture when there is a boresight error. The results in Table 5 apply for the case in which fast tracking is used, while those in Table 4 apply for a system without such tracking. If the correlation is high, then the antenna gain of a transmitter unit using the fast tracking signal from a nearly coherent receiver to which it is nominally, but somewhat inaccurately boresighted, will be nearly as good as that of the receiver. We take the correlation in this case from Table 5. The results in Table 4 are of use in estimating the boresight achieved in a reciprocity experiment in which less than 100% correlation is observed. For an experiment in which the correlation is 95%, the boresight error is apparently about $0.2\ \lambda/D$, as can be seen from Table 4.

It is particularly interesting to consider the boresight requirements between the laser transmitter and the beacon tracker in a fast tracking laser transmitter in a laser communications link. In this case, as a practical matter, we are interested in a diameter of about $1.5\ r_0$. We have taken the appropriate data on $C_t(\theta)$ from Table 5, and plotted it in Fig. 1. As can be seen from Fig. 1, a boresight misalignment of $\frac{1}{4}\ \lambda/D$, corresponding in a sense to the standard Rayleigh criteria, will assure a correlation of antenna gains of $92\frac{1}{2}\%$. This means that to a close approximation, we can expect a fast tracking transmitter system to achieve nearly its full expected performance, even though its alignment is less than perfect.

In general, we expect no significant limitation to the applicability of reciprocity due to boresight alignment problems.

Computer Programs Used in Preparing Appendix II

Program 1

This program calculates tables of $F(\theta, r)$ as a function of θ and r, From Eq. (36).

```
1010 *     TILT WEIGHTED APERTURE ØVERLAP PRØGRAM - MAIN PRØGRAM
1020      $MAP
1030      $DEBUG
1040       REAL THETA(14),R(41),RP(41),C(14,41),F(14,41),
1050      +DF(14),PHI(41),CPHI(41),SPHI(41)
1060 *
1070 *
1080       DATA F,DF,PI/588*0,3.141592653/,THETA/0,.03,.1,.2,
1090      +.3,.5,.7,1,1.3,1.6,2,2.4,2.8,3.3/
1100 *
1110       DØ 1 INDEX=1,41
1120       PHI(INDEX)=(INDEX-1)*PI/80.
1130       CPHI(INDEX)=CØS(PHI(INDEX))
1140       SPHI(INDEX)=SIN(PHI(INDEX))
1150       R(INDEX)=(INDEX-1)/40.
1160       RP(INDEX)=(INDEX-1)/80.
1170    1  CØNTINUE
1180       DØ 2 I=1,14
1190       DØ 3 K=1,41
1200       C(I,K)=CØS(2*PI*THETA(I)*RP(K))
1210    3  CØNTINUE
1220    2  CØNTINUE
1230       WRITE(1,0) ††,"CØNDITIØN SET TIME = ", TIM(0.0)
1240 *
1250       DØ 4 J=1,41
1260       WRITE(1,0) †,"J = ",J,"     TIME = ",TIM(0.0)
1270       DØ 5 M=1,41
1280       IF(J.NE.1) GØ TØ 6
1290       IF(M/5.NE.M/5.) GØ TØ 6
1300       WRITE(1,0) "M = ",M,"     TIME = ",TIM(0.0)
1310    5  CØNTINUE
1320       RX=R(J)*CPHI(M)
1330       HRX=RX/2
1340       HRY=R(J)*SPHI(M)/2
1350       DØ 7 K=1,41
1360       CALL YLENGTH(RP(K),HRX,HRY,YL)
1370       DØ 8 I=1,14
1380       DF(I)=DF(I)+YL*C(I,K)
1390    8  CØNTINUE
```

Program 1 (Continued)

```
1400        IF(K.NE.1) GØ TØ 9
1410        DØ 10 I=1,14
1420        DF(I)=DF(I)/2
1430   10   CØNTINUE
1440    9   CØNTINUE
1450    7   CØNTINUE
1460        DØ 11 I=1,14
1470        F(I,J)=F(I,J)+DF(I)*CØS(PI*THETA(I)*RX)
1480        IF(M.NE.41) DF(I)=0
1490   11   CØNTINUE
1500        IF(M.NE.1) GØ TØ 12
1510        DØ 13 I=1,14
1520        F(I,J)=F(I,J)/2
1530   13   CØNTINUE
1540   12   CØNTINUE
1550        IF(M.NE.41) GØ TØ 15
1560        DØ 16 I=1,14
1570        F(I,J)=F(I,J)-.5*DF(I)*CØS(PI*THETA(I)*RX)
1580        DF(I)=0
1590   16   CØNTINUE
1600   15   CØNTINUE
1610    5   CØNTINUE
1620    .   DØ 14 I=1,14
1630        F(I,J)=F(I,J)*PI/1600
1640   14   CØNTINUE
1650        WRITE(1,20) (F(I,J),I=1,14)
1660   20   FØRMAT(14F5.4)
1670    4   CØNTINUE
1680  *
1690        ØPEN(3,ØUTPUT FIJ
1700        WRITE(3,0) F
1710        CLØSE
1720        STØP
1730        END
```

Program 2

This program is used as a subroutine for Program 1. It calculates Y_ℓ from Eq. (37).

```
1010        SUBRØUTINE YLENGTH(RPXK,HRX,HRY,YL)
1020       $MAP
1030       $DEBUG
1040  *
1050  *
1060        YL=0
1070        X2M=(RPXK-HRX)↑2
1080        X2P=(RPXK+HRX)↑2
1090        IF(X2P.GE..25) GØ TØ 1
1100        SRM=SQRT(.25-X2M)
1110        SRP=SQRT(.25-X2P)
1120        YMAX=AMAX(0,-HRY+SRP)
1130        YMIN=AMAX(HRY-SRM,0)
1140        YL=AMAX(YMAX-YMIN,0)
1150        YMAX=AMAX(0,AMIN(-HRY+SRM,HRY+SRP))
1160        YMIN=AMAX(0,HRY-SRP)
1170        YL=YL+AMAX(0,YMAX-YMIN)
1180     1  CØNTINUE
1190        RETURN
1200        END
```

Program 3

This program prepares a formated output of the values of $F(\theta, r)$ prepared by Program 1. Its output is shown as Table 1.

```
1010 *     PRINT FIJ -- MAIN PRØGRAM
1020      $MAP
1030      $DEBUG
1040       REAL F(14,41)
1050 *
1060 *
1070       ØPEN(3) INPUT FIJ
1080       READ(3,0) F
1090       CLØSE
1100 *
1110       WRITE(1,0) ††††
1120       DØ 1 J=1,41
1130       WRITE(1,9) ((J-1.)/40.),(F(I,J),I=1,7)
1140    1  CØNTINUE
1150       WRITE(1,0) ††
1160       DØ 2 J=1,41
1170       WRITE(1,9) ((J-1.)/40.),(F(I,J),I=8,14)
1180    2  CØNTINUE
1190       WRITE(1,0) ††
1200    9  FØRMAT(F4.3,2X,7(X,F8.6))
1210       STØP
1220       END
```

Program 4

This program calculates tables of $(2/\pi)\langle \mathrm{Re}[G(0)\, G(\vec{\theta})]\rangle$ and $(2/\pi)\langle \mathrm{Re}[G(\vec{\theta}_0)\, G(\vec{\theta}_0+\vec{\theta})]\rangle$, as a function of D/r_0 and θ, from Eq.'s (38) and (39).

```
1010 *     BØRESIGHT TØLERANCE EVALUATIØN - MAIN PRØGRAM
1020       $MAP
1030       $DEBUG
1040        REAL F(14,41),CHI1(14,26),CHI2(14,26),DRN(26)
1050 *
1060 *
1070        DATA DRN,CHI1,CHI2,PI/.01,.03,.1,.2,.3,.5,.7,1,1.3,1.5,
1080       +1.7,2,2.3,2.6,3,3.5,4,4.5,5,5.5,6,6.5,7,8,9,10,728*0,
1090       +3.141592653/
1100 *
1110        ØPEN(3)INPUT FIJ
1120        READ(3,0) F
1130 *
1140        ↄØ 1 K=1,26
1150        WRITE(1,0) "K= ",K,"    TIME = ",TIM(0.0)
1160        Q=32*(DRN(K)/PI)↑2
1170        C=.1/3
1180        DØ 2 J=2,41
1190        P1=(DRN(K)*(J-1)/40.)↑(5./3.)
1200        P2=P1*(1-((J-1)/40.)↑(1./3.))
1210        E1=EXP(-3.44*P1)
1220        E2=EXP(-3.44*P2)
1230        DØ 3 I=1,14
1240        TEMP=C*((J-1)/40.)*Q*F(I,J)
1250        CHI1(I,K)=CHI1(I,K)+TEMP*E1
1260        CHI2(I,K)=CHI2(I,K)+TEMP*E2
1270     3  CØNTINUE
1280        IF(C.NE..1/3) C=.1/3 ; GØ TØ 4
1290        C=.05/3
1300     4  CØNTINUE
1310     2  CØNTINUE
1320     1  CØNTINUE
1330        DØ 5 K=1,26
1340        WRITE(1,6) (CHI1(I,K),I=1,14)
1350     5  CØNTINUE
1360     6  FØRMAT(14F5.4)
1370        WRITE(1,0)↑↑
1380        DØ 7 K=1,26
1390        WRITE(1,6) (CHI2(I,K),I=1,14)
1400     7  CØNTINUE
1410        ØPEN(4)ØUTPUT CHI12
1420        WRITE(4,0) CHI1,CHI2
1430        CLØSE
1440        STØP
1450        END
```

Program 5

This program prepares formated outputs of the results of Program 4, constituting Tables 2 and 3. It then calculates the normalized antenna gain angular dependence $C_s(\theta)$ and $C_r(\theta)$, from Eq.'s (3) and (4) and the outputs of Program 4, and prepares formated outputs of these results, as Tables 4 and 5.

```
1010 *     PRINT BØRE-SIGNAL DATA -- MAIN PRØGRAM
1020       $MAP
1030       $DEBUG
1040        REAL DRN(26),CHI1(14,26),CHI2(14,26)
1050 *
1060 *
1070        DATA DRN/.01,.03,.1,.2,.3,.5,.7,1,1.3,1.5,
1080       +1.7,2,2.3,2.6,3,3.5,4,4.5,5,5.5,6,6.5,7,8,9,10/
1090        ØPEN(4) INPUT CHI12
1100        READ(4,0) CHI1,CHI2
1110        CLØSE
1120 *
1130        WRITE(1,0) ††††
1140        DØ 1 J=1,26
1150        WRITE(1,9) DRN(J),(CHI1(I,J),I=1,7)
1160     1  CØNTINUE
1170        WRITE(1,0) ††
1180        DØ 2 J=1,26
1190        WRITE(1,9) DRN(J),(CHI1(I,J),I=8,14)
1200     2  CØNTIN'JE
1210        WRITE(1,0) ††††
1220        DØ 3 J=1,26
1230        WRITE(1,9) DRN(J),(CHI2(I,J),I=1,7)
1240     3  CØNTINUE
1250        WRITE(1,0) ††
1260        DØ 4 J=1,26
1270        WRITE(1,9) DRN(J),(CHI2(I,J),I=8,14)
1280     4  CØNTINUE
1290        WRITE(1,0) †††††
1300     9  FØRMAT(F4.2,X,7(X,F8.6))
1310        DØ 5 J=1,26
1320        WRITE(1,8) DRN(J),((CHI1(I,J)/CHI1(1,J)),I=2,14)
1330     5  CØNTINUE
1340        WRITE(1,0) ††††
1350        DØ 6 J=1,26
1360        WRITE(1,8) DRN(J),((CHI2(I,J)/CHI2(1,J)),I=2,14)
1370     6  CØNTINUE
1380        WRITE(1,0) †††††
1390     8 FØRMAT(F4.2,X,13F5.3)
1400        STØP
1410        END
```

References

1. D. L. Fried and H. T. Yura, "Telescope Performance Reciprocity for Propagation in a Turbulent Medium," J. Opt. Soc. Am. 62, 600 (1972).

2. D. L. Fried, "Optical Resolution Through a Randomly Inhomogeneous Medium for Very Long and Very Short Exposures," J. Opt. Soc. Am., 56, 1372 (1966).

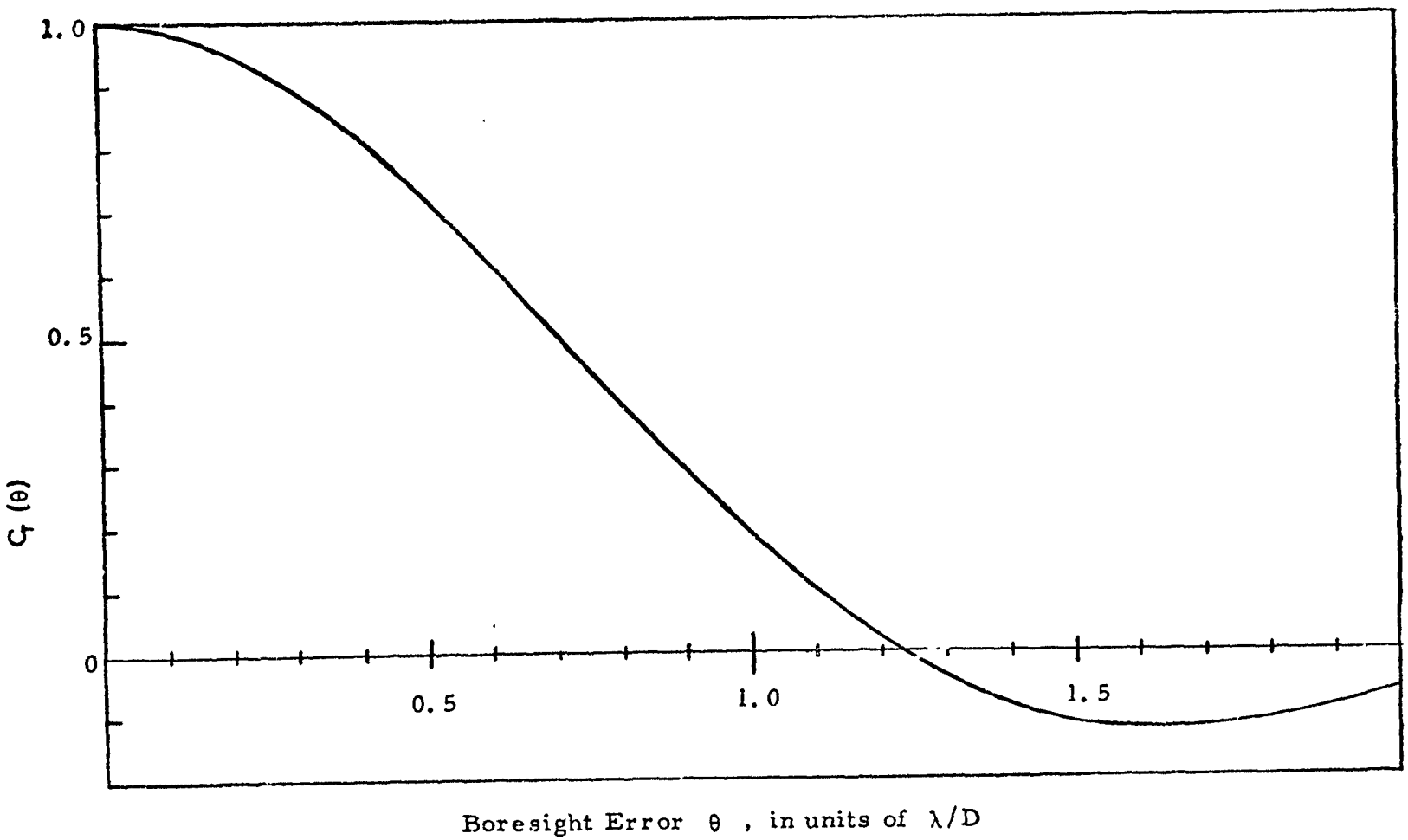


Figure 1. Antenna Gain Correlation, $C_T(\theta)$, for a Tracking System. The aperture diameter in this case is $D = 1.5\ r_o$.

Table 1

$F(\theta, r)$

r \ θ	0.0	0.03	0.1	0.2	0.3	0.5	0.7
*0.0	2.468623	2.465897	2.438454	2.349420	2.205844	1.784893	1.253626
.025	2.391071	2.388498	2.362587	2.278490	2.142769	1.744011	1.238560
.050	2.312629	2.310210	2.285850	2.206760	2.079021	1.702927	1.224131
.075	2.234207	2.231930	2.209004	2.134546	2.014216	1.659353	1.206034
.100	2.155945	2.153800	2.132192	2.062001	1.948517	1.613441	1.184298
.125	2.555800	2.553332	2.528469	2.447688	2.317024	1.930741	1.434699
.150	1.998007	1.996095	1.976834	1.914253	1.813025	1.513746	1.129356
.175	1.920535	1.918724	1.900484	1.841218	1.745346	1.461852	1.097576
.200	1.843320	1.841602	1.824301	1.768088	1.677158	1.408292	1.062838
.225	1.766459	1.764827	1.748389	1.694983	1.608602	1.353254	1.025331
.250	1.690312	1.688758	1.673104	1.622249	1.540008	1.297009	.985228
.275	1.614490	1.613008	1.598081	1.549592	1.471193	1.239670	.942940
.300	1.539227	1.537812	1.523556	1.477251	1.402399	1.181485	.898706
.325	1.464654	1.463300	1.449662	1.405369	1.333786	1.122658	.852773
.350	1.390840	1.389543	1.376477	1.334050	1.265499	1.063448	.805525
.375	1.317584	1.316341	1.303817	1.263154	1.197467	1.003977	.757305
.400	1.245261	1.244067	1.232051	1.193038	1.130033	.944553	.708401
.425	1.173506	1.172362	1.160836	1.123421	1.063008	.885253	.659196
.450	1.102903	1.101805	1.090745	1.054845	.996890	.826460	.609967
.475	1.033441	1.032387	1.021776	.987336	.931749	.768371	.561082
.500	.964676	.963667	.953505	.920526	.867307	.710966	.512816
.525	.897301	.896336	.886615	.855068	.804171	.654735	.465564
.550	.831190	.830268	.820987	.790871	.742292	.599754	.419559
.575	.766189	.765312	.756480	.727827	.681618	.546124	.375083
.600	.702667	.701836	.693460	.666291	.622489	.494156	.332437
.625	.640510	.639725	.631820	.606182	.564862	.443913	.291801
.650	.579888	.579152	.571733	.547677	.508922	.395600	.253416
.675	.521142	.520455	.513535	.491101	.454975	.349483	.217504
.700	.464256	.463620	.457215	.436457	.403048	.305643	.184196
.725	.409094	.408511	.402645	.383638	.353067	.264092	.153582
.750	.356099	.355571	.350260	.333056	.305407	.225099	.125799
.775	.305172	.304702	.299966	.284634	.260014	.188665	.100886
.800	.256768	.256356	.252209	.238788	.217256	.155023	.078902
.825	.211060	.210707	.207157	.195675	.177273	.124246	.059805
.850	.168166	.167874	.164928	.155406	.140164	.096384	.043566
.875	.128434	.128201	.125859	.118290	.106192	.071568	.030128
.900	.092225	.092051	.090300	.084646	.075621	.049895	.019372
.925	.060136	.060018	.058829	.054992	.048878	.031523	.011131
.950	.032894	.032826	.032148	.029964	.026488	.016671	.005256
.975	.011674	.011649	.011399	.010592	.009312	.005713	.001575
*1.0	.000000	.000000	.000000	.000000	.000000	.000000	-.000000

Note: θ is measured in units of λ/D .

Table 1 (Continued)

$F(\theta, r)$

r \ θ	1.0	1.3	1.6	2.0	2.4	2.8	3.3
*0.0	.453540	-.113367	-.323536	-.168462	.095566	.153026	-.018867
.025	.470116	-.086627	-.308995	-.182171	.073068	.147889	-.003144
.050	.489265	-.055180	-.288677	-.191958	.049918	.140069	.014318
.075	.504918	-.024184	-.264631	-.195988	.027533	.126202	.026958
.100	.516671	.005452	-.237793	-.193927	.007972	.108075	.032770
.125	.658161	.053970	-.248417	-.229689	-.016743	.101091	.039744
.150	.527207	.057551	-.179970	-.172739	-.016536	.068843	.023409
.175	.526201	.078646	-.151485	-.155385	-.019790	.052733	.011396
.200	.520908	.095795	-.124681	-.135157	-.017109	.041497	-.001840
.225	.511348	.108586	-.100534	-.113446	-.009259	.036039	-.013449
.250	.497443	.116555	-.079983	-.091684	.002527	.036374	-.021101
.275	.479785	.119949	-.063578	-.071529	.016362	.041624	-.023469
.300	.458536	.118705	-.051794	-.054191	.030470	.050173	-.020612
.325	.433955	.112958	-.044819	-.040577	.043182	.060020	-.013803
.350	.406542	.103120	-.042591	-.031416	.052890	.068980	-.005137
.375	.376880	.089776	-.044792	-.027026	.058577	.075404	.003144
.400	.345295	.073362	-.050923	-.027148	.059770	.077865	.008764
.425	.312549	.054771	-.060204	-.031304	.056679	.076220	.010620
.450	.278882	.034409	-.071959	-.038658	.049832	.070440	.008252
.475	.244943	.013168	-.085143	-.048088	.040346	.061594	.002527
.500	.211373	-.008136	-.098890	-.058538	.029663	.051508	-.004816
.525	.178602	-.028780	-.112055	-.068596	.019218	.041488	-.012046
.550	.147084	-.048140	-.123884	-.077191	.010329	.033181	-.017309
.575	.117347	-.065538	-.133628	-.083501	.004061	.027874	-.019307
.600	.089772	-.080402	-.140491	-.086600	.001181	.026075	-.017646
.625	.064660	-.092420	-.144237	-.086362	.001752	.027680	-.013016
.650	.042318	-.101227	-.144508	-.082607	.005571	.032019	-.006623
.675	.022934	-.106643	-.141167	-.075467	.011966	.037793	-.000255
.700	.006645	-.108657	-.134461	-.065633	.019810	.043536	.004380
.725	-.006444	-.107342	-.124798	-.054003	.027935	.048081	.006402
.750	-.016402	-.102953	-.112631	-.041369	.035169	.050144	.005183
.775	-.023245	-.095744	-.098579	-.028771	.040474	.049212	.001268
.800	-.027196	-.086200	-.083344	-.017099	.043018	.044961	-.004438
.825	-.028551	-.074926	-.067785	-.007212	.042515	.038093	-.010214
.850	-.027536	-.062396	-.052557	.000349	.039059	.029557	-.014676
.875	-.024534	-.049263	-.038384	.005231	.033114	.020574	-.016702
.900	-.019995	-.036181	-.025862	.007405	.025476	.012355	-.015873
.925	-.014522	-.023908	-.015491	.007198	.017225	.005922	-.012537
.950	-.008711	-.013130	-.007593	.005178	.009452	.001826	-.007731
.975	-.003337	-.004631	-.002346	.002235	.003255	.000104	-.002892
*1.0	-.000000	-.000000	.000000	.000000	.000000	-.000000	-.000000

Note: θ is measured in units of λ/D .

Table 2

$(2/\pi)\,\langle \mathrm{Re}[G(0)\,G(\vec{\theta})]\rangle$

(D/r_c) \ θ	0.0	0.03	0.1	0.2	0.3	0.5	0.7
.01	.000101	.000100	.000099	.000096	.000090	.000073	.000051
.03	.000903	.000902	.000892	.000859	.000807	.000652	.000457
.10	.009847	.009836	.009726	.009371	.008797	.007117	.004998
.20	.037580	.037539	.037123	.035775	.033601	.027227	.019183
.30	.079291	.079205	.078336	.075517	.070970	.057633	.040786
.50	.186778	.186580	.184578	.178082	.167601	.136827	.097869
.70	.301405	.301092	.297940	.287709	.271195	.222653	.161053
1.00	.450618	.450166	.445608	.430811	.406913	.336556	.246970
1.30	.561720	.561169	.555620	.537601	.508486	.422667	.313119
1.50	.618030	.617429	.611383	.591745	.560009	.466410	.346793
1.70	.663749	.663108	.656650	.635675	.601771	.501742	.373800
2.00	.717850	.717158	.710193	.687568	.650995	.543045	.404868
2.30	.759653	.758920	.751539	.727561	.688798	.574364	.427833
2.60	.792828	.792060	.784328	.759212	.718606	.598724	.445199
3.00	.827465	.826658	.818537	.792154	.749503	.623586	.462347
3.50	.859736	.858891	.850379	.822731	.778035	.646104	.477227
4.00	.883215	.882340	.873522	.844882	.798586	.661964	.487169
4.50	.900263	.899363	.890306	.860888	.813339	.673057	.493682
5.00	.912522	.911604	.902359	.872331	.823801	.680665	.497749
5.50	.921245	.920313	.910919	.880411	.831110	.685740	.500080
6.00	.927424	.926479	.916967	.886077	.836164	.689029	.501222
6.50	.931846	.930895	.921286	.890086	.839677	.691118	.501598
7.00	.935138	.934176	.924488	.893029	.842206	.692463	.501534
8.00	.940053	.939078	.929258	.897373	.845870	.694195	.500986
9.00	.944474	.943487	.933554	.901303	.849217	.695883	.500723
*10.	.949315	.948319	.938279	.905684	.853049	.698153	.501142

Note: θ is measured in units of λ/D .

Table 2 (Continued)

$(2/\pi)\ \langle \mathrm{Re}[\,G(0)\ G(\vec{\theta})\,]\rangle$

(D/r_o) \ θ	1.0	1.3	1.6	2.0	2.4	2.8	3.3
.01	.000018	-.000005	-.000013	-.000007	.000004	.000006	-.000001
.03	.000164	-.000042	-.000118	-.000061	.000034	.000054	-.000008
.10	.001810	-.000445	-.001278	-.000666	.000369	.000585	-.000086
.20	.007064	-.001539	-.004771	-.002534	.001356	.002196	-.000310
.30	.015353	-.002799	-.009759	-.005319	.002720	.004528	-.000602
.50	.038761	-.003977	-.021181	-.012341	.005609	.010058	-.001125
.70	.067074	-.001836	-.030984	-.019519	.007706	.015176	-.001336
1.00	.109257	.006358	-.039953	-.028358	.008870	.020583	-.001069
1.30	.143770	.015503	-.044672	-.035025	.008508	.023781	-.000431
1.50	.161400	.020128	-.047316	-.038913	.007857	.025247	.000085
1.70	.175148	.023148	-.050238	-.042676	.007048	.026453	.000645
2.00	.189976	.024971	-.055387	-.048241	.005748	.028056	.001553
2.30	.199781	.024433	-.061160	-.053582	.004582	.029628	.002522
2.60	.206223	.022475	-.067079	-.058464	.003738	.031284	.003520
3.00	.211450	.018780	-.074597	-.064007	.003236	.033658	.004817
3.50	.214689	.013629	-.082845	-.069305	.003536	.036759	.006229
4.00	.215767	.008607	-.089661	-.073011	.004577	.039781	.007278
4.50	.215544	.003995	-.095172	-.075474	.006049	.042545	.007932
5.00	.214513	-.000148	-.099596	-.077022	.007724	.044974	.008229
5.50	.212989	-.003839	-.103151	-.077915	.009455	.047058	.008242
6.00	.211195	-.007120	-.106029	-.078356	.011156	.048823	.008045
6.50	.209296	-.010036	-.108387	-.078493	.012780	.050314	.007704
7.00	.207412	-.012632	-.110348	-.078437	.014301	.051575	.007270
8.00	.203995	-.017009	-.113450	-.078039	.017012	.053571	.006269
9.00	.201291	-.020512	-.115859	-.077542	.019297	.055073	.005236
*10.	.199348	-.023343	-.117861	-.077108	.021213	.056255	.004261

Note: θ is measured in units of λ/D .

Table 3

$(2/\pi)\,\langle \mathrm{Re}[G(\vec{\theta}_0)\,G(\vec{\theta}_0+\vec{\theta})]\rangle$

(D/r_0) \ θ	0.0	0.03	0.1	0.2	0.3	0.5	0.7
•01	•000101	•000101	•000099	•000096	•000090	•000073	•000051
•03	•000905	•000904	•000894	•000862	•000809	•000654	•000458
•10	•010028	•010017	•009905	•009542	•008957	•007240	•005076
•20	•039794	•039750	•039306	•037864	•035541	•028731	•020145
•30	•088532	•088434	•087446	•084240	•079071	•063924	•044824
•50	•238479	•238214	•235553	•226921	•213093	•172214	•120782
•70	•449020	•448523	•443515	•427269	•401075	•324310	•227513
1•00	•849809	•848868	•839399	•808679	•759148	•613989	•430941
1•30	1•310903	1•309454	1•294863	1•247528	1•171206	•947526	•665444
1•50	1•629525	1•627725	1•609603	1•550813	1•456022	1•178206	•827837
1•70	1•943274	1•941130	1•919540	1•849497	1•736562	1•405560	•988093
2•00	2•383536	2•380910	2•354471	2•268698	2•130397	1•725035	1•213732
2•30	2•765691	2•762650	2•732028	2•632685	2•472500	2•002969	1•410660
2•60	3•074616	3•071242	3•037269	2•927054	2•749335	2•228376	1•571102
3•00	3•363439	3•359760	3•322709	3•202506	3•008674	2•440427	1•723335
3•50	3•537930	3•534076	3•495270	3•369368	3•166335	2•571024	1•819527
4•00	3•545675	3•541831	3•503122	3•377532	3•174989	2•581000	1•830868
4•50	3•441642	3•437929	3•400540	3•279230	3•083574	2•509655	1•784522
5•00	3•277146	3•273628	3•238201	3•123250	2•937834	2•393816	1•706096
5•50	3•091410	3•088106	3•054841	2•946899	2•772771	2•261738	1•615352
6•00	2•909698	2•906602	2•875418	2•774226	2•610971	2•131719	1•525188
6•50	2•745330	2•742418	2•713092	2•617926	2•464376	2•013501	1•442578
7•00	2•603165	2•600411	2•572671	2•482649	2•337386	1•910747	1•370254
8•00	2•382261	2•379747	2•354424	2•272239	2•139606	1•749920	1•255878
9•00	2•225593	2•223244	2•199589	2•122811	1•998895	1•634738	1•172859
*10•	2•109894	2•107665	2•085210	2•012329	1•894697	1•548969	1•110370

Note: θ is measured in units of λ/D .

Table 3 (Continued)

$(2/\pi)\,\langle \mathrm{Re}[G(\vec{\theta}_o)\, G(\vec{\theta}_o+\vec{\theta})]\rangle$

(D/r_o) \ θ	1.0	1.3	1.6	2.0	2.4	2.8	3.3
.01	.000018	-.000005	-.000013	-.000007	.000004	.000006	-.000001
.03	.000165	-.000043	-.000119	-.000061	.000034	.000054	-.000008
.10	.001824	-.000472	-.001315	-.000679	.000382	.000600	-.000090
.20	.007239	-.001872	-.005216	-.002694	.001515	.002382	-.000359
.30	.016113	-.004155	-.011595	-.005990	.003371	.005298	-.000799
.50	.043464	-.011123	-.031175	-.016108	.009079	01425[illegible]	-.002157
.70	.081988	-.020773	-.058550	-.030259	.017090	.026808	-.004073
1.00	.155716	-.038699	-.110284	-.057022	.032317	.050609	-.007748
1.30	.241252	-.058521	-.169123	-.087512	.049779	.077814	-.012022
1.50	.300893	-.071624	-.209285	-.108373	.061790	.096473	-.015007
1.70	.360149	-.083943	-.248351	-.128723	.073548	.114703	-.017975
2.00	.444461	-.099956	-.302133	-.156894	.089862	.139954	-.022191
2.30	.519259	-.112101	-.347416	-.180876	.103708	.161388	-.025905
2.60	.581601	-.119903	-.382448	-.199802	.114459	.178122	-.028945
3.00	.643211	-.123674	-.412528	-.216853	.123573	.192666	-.031791
3.50	.686670	-.119447	-.425930	-.226325	.127007	.199290	-.033373
4.00	.698971	-.108588	-.418936	-.225876	.123301	.195894	-.032984
4.50	.689119	-.094744	-.399563	-.219423	.114865	.186176	-.031049
5.00	.665924	-.080831	-.374821	-.210305	.104047	.173528	-.028053
5.50	.636427	-.068695	-.349690	-.200819	.092720	.160487	-.024453
6.00	.605445	-.059179	-.327041	-.192223	.082143	.148621	-.020630
6.50	.575793	-.052395	-.308070	-.184989	.073004	.138667	-.016870
7.00	.548803	-.048022	-.292880	-.179106	.065554	.130784	-.013370
8.00	.503839	-.044491	-.271765	-.170377	.055420	.120355	-.007564
9.00	.469155	-.044833	-.258685	-.163934	.050102	.114757	-.003513
*10.	.441885	-.046620	-.249790	-.158491	.047687	.111685	-.000992

Note: θ is measured in units of λ/D .

Table 4

Antenna Gain Correlation for a Static System

$C_s(\theta)$

(D/r_o) \ θ	0.03	0.1	0.2	0.3	0.5	0.7	1.0	1.3	1.6	2.0	2.4	2.8	3.3
.01	.999	.988	.952	.893	.722	.506	.182	-.047	-.131	-.068	.038	.060	-.009
.03	.999	.988	.952	.893	.722	.506	.182	-.047	-.131	-.068	.038	.060	-.009
.10	.999	.988	.952	.893	.723	.508	.184	-.045	-.130	-.068	.037	.059	-.009
.20	.999	.988	.952	.894	.725	.510	.188	-.041	-.127	-.067	.036	.058	-.008
.30	.999	.988	.952	.895	.727	.514	.194	-.035	-.123	-.067	.034	.057	-.008
.50	.999	.988	.953	.897	.733	.524	.208	-.021	-.113	-.066	.030	.054	-.006
.70	.999	.989	.955	.900	.739	.534	.223	-.006	-.103	-.065	.026	.050	-.004
1.00	.999	.989	.956	.903	.747	.548	.242	.014	-.089	-.063	.020	.046	-.002
1.30	.999	.989	.957	.905	.752	.557	.256	.028	-.080	-.062	.015	.042	-.001
1.50	.999	.989	.957	.906	.755	.561	.261	.033	-.077	-.063	.013	.041	.000
1.70	.999	.989	.958	.907	.756	.563	.264	.035	-.076	-.064	.011	.040	.001
2.00	.999	.989	.958	.907	.756	.564	.265	.035	-.077	-.067	.008	.039	.002
2.30	.999	.989	.958	.907	.756	.563	.263	.032	-.081	-.071	.006	.039	.003
2.60	.999	.989	.958	.906	.755	.562	.260	.028	-.085	-.074	.005	.039	.004
3.00	.999	.989	.957	.906	.754	.559	.256	.023	-.090	-.077	.004	.041	.006
3.50	.999	.989	.957	.905	.752	.555	.250	.016	-.096	-.081	.004	.043	.007
4.00	.999	.989	.957	.904	.749	.552	.244	.010	-.102	-.083	.005	.045	.008
4.50	.999	.989	.956	.903	.748	.548	.239	.004	-.106	-.084	.007	.047	.009
5.00	.999	.989	.956	.903	.746	.545	.235	-.000	-.109	-.084	.008	.049	.009
5.50	.999	.989	.956	.902	.744	.543	.231	-.004	-.112	-.085	.010	.051	.009
6.00	.999	.989	.955	.902	.743	.540	.228	-.008	-.114	-.084	.012	.053	.009
6.50	.999	.989	.955	.901	.742	.538	.225	-.011	-.116	-.084	.014	.054	.008
7.00	.999	.989	.955	.901	.740	.536	.222	-.014	-.118	-.084	.015	.055	.008
8.00	.999	.989	.955	.900	.738	.533	.217	-.018	-.121	-.083	.018	.057	.007
9.00	.999	.988	.954	.899	.737	.530	.213	-.022	-.123	-.082	.020	.058	.006
*10.	.999	.988	.954	.899	.735	.528	.210	-.025	-.124	-.081	.022	.059	.004

Note: θ **is measured in units of** λ/D .

Table 5

Antenna Gain Correlation for a Tracking System

$C_T(\theta)$

(D/r_o) \ θ	0.03	0.1	0.2	0.3	0.5	0.7	1.0	1.3	1.6	2.0	2.4	2.8	3.3
.01	.999	.988	.952	.893	.722	.506	.182	-.047	-.131	-.068	.038	.060	-.009
.03	.999	.988	.952	.893	.722	.506	.182	-.047	-.131	-.068	.038	.060	-.009
.10	.999	.988	.952	.893	.722	.506	.182	-.047	-.131	-.068	.038	.060	-.009
.20	.999	.988	.952	.893	.722	.506	.182	-.047	-.131	-.068	.038	.060	-.009
.30	.999	.988	.952	.893	.722	.506	.182	-.047	-.131	-.068	.038	.060	-.009
.50	.999	.988	.952	.893	.722	.506	.182	-.047	-.131	-.068	.038	.060	-.009
.70	.999	.988	.952	.893	.722	.507	.183	-.046	-.130	-.067	.038	.060	-.009
1.00	.999	.988	.952	.893	.723	.507	.183	-.046	-.130	-.067	.038	.060	-.009
1.30	.999	.988	.952	.893	.723	.508	.184	-.045	-.129	-.067	.038	.059	-.009
1.50	.999	.988	.952	.894	.723	.508	.185	-.044	-.128	-.067	.038	.059	-.009
1.70	.999	.988	.952	.894	.723	.508	.185	-.043	-.128	-.066	.038	.059	-.009
2.00	.999	.988	.952	.894	.724	.509	.186	-.042	-.127	-.066	.038	.059	-.009
2.30	.999	.988	.952	.894	.724	.510	.188	-.041	-.126	-.065	.037	.058	-.009
2.60	.999	.988	.952	.894	.725	.511	.189	-.039	-.124	-.065	.037	.058	-.009
3.00	.999	.988	.952	.895	.726	.512	.191	-.037	-.123	-.064	.037	.057	-.009
3.50	.999	.988	.952	.895	.727	.514	.194	-.034	-.120	-.064	.036	.056	-.009
4.00	.999	.988	.953	.895	.728	.516	.197	-.031	-.118	-.064	.035	.055	-.009
4.50	.999	.988	.953	.896	.729	.519	.200	-.028	-.116	-.064	.033	.054	-.009
5.00	.999	.988	.953	.896	.730	.521	.203	-.025	-.114	-.064	.032	.053	-.009
5.50	.999	.988	.953	.897	.732	.523	.206	-.022	-.113	-.065	.030	.052	-.008
6.00	.999	.988	.953	.897	.733	.524	.208	-.020	-.112	-.066	.028	.051	-.007
6.50	.999	.988	.954	.898	.733	.525	.210	-.019	-.112	-.067	.027	.051	-.006
7.00	.999	.988	.954	.898	.734	.526	.211	-.018	-.113	-.069	.025	.050	-.005
8.00	.999	.988	.954	.898	.735	.527	.211	-.019	-.114	-.072	.023	.051	-.003
9.00	.999	.988	.954	.898	.735	.527	.211	-.020	-.116	-.074	.023	.052	-.002
*10.	.999	.988	.954	.898	.734	.526	.209	-.022	-.118	-.075	.023	.053	-.000

Note: θ is measured in units of λ/D .

APPENDIX IV

PRELIMINARY PARAMETER CONSIDERATIONS FOR A WAVEFRONT DISTORTION SENSITIVE STAR TRACKER

D. L. Fried

This Appendix is a reproduction of Optical Science Consultants Report No. TR-067 (July 1972) as provided by that organization.

Introduction

We have previously discussed the concept of reciprocity in optical propagation, and drawn upon this to demonstrate that the antenna gain of a laser transmitter will be exactly the same as that of a diffraction-limited imaging system, if both have the same aperture, the same wavelength, and a common propagation path to a distant point source. This, then, allows us to propose a measurement of expected antenna gain for a ground-based laser transmitter, linked to a receiver in space, by measuring the antenna gain of a high resolution ground-based telescope viewing a star.

In order to measure the antenna gain of the imaging system, we proposed to track a bright star with an image dissector, and while tracking it, measure the peak intensity of the image spot. By doing this as a function of optics diameter and of the tracking servo bandwidth, it will then be possible to determine antenna gain corresponding to both an ordinary and a fast-tracking laser transmitter. Not only will the measurement data allow us to determine the average antenna gain, but it will also provide data on the antenna gain statistics.

In this document, we shall consider some of the parameters that will affect the quality of the data we will be able to obtain from an experiment. First we consider the effect of various size pinholes in the focal plane (i. e., in the image dissector) upon our ability to measure antenna gain, and then turn our attention to photometric and signal-to-noise ratio considerations.

Antenna Gain Measurement

We consider an ideal optical system with aperture diameter D and effective focal length F, forming an image of a point source at infinity. If $\vec{x}$ denotes a two-dimensional vector in the aperture plane, and $\vec{y}$ denotes a two-dimensional vector in the focal plane, then it can be shown that $U(\vec{y})$ the (scalar) wave function in the focal plane can be written as

PRECEDING PAGE BLANK-NOT FIL

$$U(\vec{y}) = K(\vec{y}) \int d\vec{x}\ u(\vec{x})\ e^{-i k \vec{x} \cdot \vec{y}/F} \quad , \tag{1}$$

where the integration over $\vec{x}$ is restricted to the aperture, $u(\vec{x})$ is the (scalar) wave function in the aperture plane, $k = 2\pi/\lambda$ is the optical wave number, and $K(\vec{y})$ is a scaling factor whose magnitude, K, is independent of $\vec{y}$. Hence the intensity in the focal plane at $\vec{y}$ is

$$I(\vec{y}) = \tfrac{1}{2} U^*(\vec{y})\, U(\vec{y})$$

$$= \tfrac{1}{2} K^2 \iint d\vec{x}\ d\vec{x}'\ u^*(\vec{x})\, u(\vec{x}')\ \exp\left[i k (\vec{x}' - \vec{x}) \cdot \vec{y}/F\right] \quad . \tag{2}$$

If a pinhole of radius a is located at the origin in the focal plane (i.e., the $\vec{y}$-plane), then the total signal passed by the pinhole will be

$$S(a) = \int_{\text{Pinhole}} d\vec{y}\ I(\vec{y}) \quad . \tag{3}$$

By substituting Eq. (2) into Eq. (3), and interchanging the order of integrations, we get

$$S(a) = \tfrac{1}{2} K^2 \iint_{(\text{Aperture})^2} d\vec{x}\ d\vec{x}'\ u^*(\vec{x})\, u(\vec{x}') \left\{ \int_{\text{Pinhole}} d\vec{y}\ \exp\left[i\, \frac{k(\vec{x}' - \vec{x})}{F} \cdot \vec{y} \right] \right\} . \tag{4}$$

The evaluation of the quantity in the curly brackets is a straightforward mathematical procedure making use of the fact that

$$\int_0^{2\pi} d\varphi\ e^{i p \cos\varphi} = 2\pi\, J_0(p) \quad , \tag{5}$$

and that

$$\int p\, dp\ J_0(p) = p\, J_1(p) \quad . \tag{6}$$

Using these two equations, we can show that the quantity in the curly brackets in Eq. (4) has the value

$$\left\{ \cdots \right\} = \frac{2\pi F \alpha}{k|\vec{x}-\vec{x}'|} J_1\left(\frac{k|\vec{x}-\vec{x}'|\alpha}{F}\right)$$

$$= \pi \alpha^2 \left[\frac{2 J_1(k|\vec{x}-\vec{x}'|\alpha/F)}{k|\vec{x}-\vec{x}'|\alpha/F}\right] \quad . \tag{7}$$

We call explicit attention to the fact that when α is very small, the quantity in the square brackets is very nearly equal to unity.

The antenna gain is directly proportional to the peak intensity in the focal plane, or to the intensity at the origin. Nominally, the two are identical. In a tracking system we "move the focal plane around" so that the two are made to be identical.* For a non-tracking system, the peak intensity may not be at the focal plane origin, which simply means that wavefront distortion has moved the main lobe of the antenna pattern away from the direction defined by the focal plane origin. Nonetheless, it is the antenna gain associated with the origin that our system would work with and for which we should be performing our calculations.

With a very small pinhole, the value of $S(\alpha)$ is obviously proportional to the antenna gain. Unfortunately, for reasons associated with signal-to-noise ratio considerations, we would like to use a not-so-small pinhole. In this case, $S(\alpha)$ is only related to the antenna gain. If we make α too large, the relationship becomes very poor. We need to know how well $S(\alpha)$ is related to antenna gain as a function of α, so that we can pick the largest value of α compatible with the desired measurement accuracy. Since $S(\alpha)$ is proportional to antenna gain for very small values of α, and since $S(\alpha)$ has a factor of pinhole area, i.e., $\pi\alpha^2$, which itself is quite irrelevant to $S(\alpha)$'s relationship to antenna gain, it follows that $F(\alpha)$, which is a quantity that measures how well $S(\alpha)$ is

---

* In the case of a tracking antenna system, the wave function $u(\vec{x})$ in Eq. (4) has to be considered not simply as the distorted wave function, but rather as the distorted wave function less its linear tilt component of distortion associated with the region of the antenna aperture.

related to antenna gain, has the form

$$F(\alpha) = \left[\frac{1}{\pi\alpha^2} S(\alpha)\right] \Bigg/ \left[\lim_{\alpha\to 0} \frac{1}{\pi\alpha^2} S(\alpha)\right] . \tag{8}$$

$F(\alpha)$ equals unity denotes a perfect correlation between $S(\alpha)$ and antenna gain, while a value of zero indicates the $F(\alpha)$ is not related to antenna gain.

Now, if we substitute Eq. (7) into Eq. (4), and that into Eq. (8), taking note of the limiting form for the r.h.s. of Eq. (7) when α is very small, we get

$$F(\alpha) = \frac{\iint_{(\text{Aperture})^2} d\vec{x}\, d\vec{x}'\, u^*(\vec{x})\, u(\vec{x}') \left[\frac{2 J_1(k|\vec{x} - \vec{x}'|\alpha/F)}{k|\vec{x} - \vec{x}'|\alpha/F}\right]}{\iint_{(\text{Aperture})^2} d\vec{x}\, d\vec{x}'\, u^*(\vec{x})\, u(\vec{x}')} \tag{9}$$

At this point, we can no longer postpone taking cognizance of the fact that $u(\vec{x})$ is a random function, so that $F(\alpha)$ is also a random function. (In the case $\alpha = 0$, $F(\alpha) = 1$, which means that although $F(\alpha)$ may be considered a random variable, its probability density is a delta function at $F(\alpha) = 1$. For any non-zero value of α, $F(\alpha)$ is a more conventional type of random variable.) We shall argue that by replacing $u(\vec{x})\, u^*(\vec{x}')$ by unity in our evaluation of $F(\alpha)$, we conservatively underestimate the value of $F(\alpha)$. By conservative, we mean that our results will represent a lower limit on the true value of $F(\alpha)$. If, for example, we pick α so that $F(\alpha)$, as computed, equals 0.9, then we can be sure that the actual value of $F(\alpha)$ will be described by a probability density function which is concentrated around values of $F(\alpha) \geq 0.9$. For clarity, we shall use the notation $\tilde{F}(\alpha)$ to denote the approximation defined by replacing $u(\vec{x})\, u^*(\vec{x}')$ by unity in Eq. (9).

$$\tilde{F}(\alpha) = \frac{\iint\limits_{(\text{Aperture})^2} d\vec{x}\; d\vec{x}' \left[\frac{2\, J_1(k|\vec{x} - \vec{x}'|\,\alpha/F)}{k|\vec{x} - \vec{x}'|\,\alpha/F} \right]}{\iint\limits_{(\text{Aperture})^2} d\vec{x}\; d\vec{x}'}$$

$$= \frac{16}{\pi^2 D^4} \iint\limits_{(\text{Aperture})^2} d\vec{x}\; d\vec{x}' \left[\frac{2\, J_1(k|\vec{x} - \vec{x}'|\,\alpha/F)}{k|\vec{x} - \vec{x}'|\,\alpha/F} \right] . \qquad (10)$$

Our basis for arguing the suitability of replacing $u(\vec{x})\, u^*(\vec{x}')$ by unity in Eq. (9) to obtain Eq. (10) is that the quantity in the square brackets in the integral in the numerator of the r.h.s. of Eq. (9) causes less weight to be associated with large values of $|\vec{x} - \vec{x}'|$ than with small values, more so the larger α is. The fact that $F(\alpha)$ is less than unity is due to this. It is the fact that this quantity in the square brackets at least partially "ignores" the contribution of $u(\vec{x})\, u^*(\vec{x}')$ for large values of $|\vec{x} - \vec{x}'|$ that leads to the reduced values of $F(\alpha)$. On the other hand, the integration over all combinations of values of $\vec{x}$ and $\vec{x}'$ that have a particular value of $|\vec{x} - \vec{x}'|$ can be thought of as at least a partial average of $u(\vec{x})\, u^*(\vec{x}')$ — but we know that the ensemble average value of $u(\vec{x})\, u^*(\vec{x}')$ is a function of $|\vec{x} - \vec{x}'|$ and not otherwise of $\vec{x}$ or $\vec{x}'$, and that the value of $\langle u(\vec{x})\, u^*(\vec{x}') \rangle$ decreases as $|\vec{x} - \vec{x}'|$ increases. This means that the presence of $u(\vec{x})\, u^*(\vec{x}')$ in both the integral in the numerator and the denominator of the r.h.s. of Eq. (9) leads to a similar de-emphasis of the large values of $|\vec{x} - \vec{x}'|$ and tends to counter the effect of the quantity in the square brackets, and thereby tends to bring the value of the two integrals close together and make $F(\alpha)$ closer to unity.* By replacing $u(\vec{x})\, u^*(\vec{x}')$ by unity, we make the value of $\tilde{F}(\alpha)$

* This leads to the conclusion that for a strongly distorted wave function, for which, of course, we would expect the image spot in the focal plane to be noticeably larger than the diffraction-limited spot produced by an undistorted wave, a given required value of $F(\alpha)$ can be achieved with a larger value of α. The large spot allows a large pinhole radius (i.e., a large value of α) to be used. The most severe limitation on allowed value of α occurs for the undistorted wave, for which $u(\vec{x})\, u^*(\vec{x}') \equiv 1$.

smaller than $F(\alpha)$, thereby insuring a conservative result in that we may expect $F(\alpha)$ to be closer to unity than $\tilde{F}(\alpha)$, assuring that a sufficiently small pinhole size will be chosen. Based on this line of reasoning, we now proceed with the evaluation of $\tilde{F}(\alpha)$.

To carry out the evaluation of Eq. (10), we transform the coordinates to

$$\vec{p} = \vec{x} - \vec{x}' \quad , \tag{11a}$$

$$\vec{q} = \tfrac{1}{2}(\vec{x} + \vec{x}') \quad , \tag{11b}$$

so that

$$\tilde{F}(\alpha) = \frac{16}{\pi^2 D^4} \int\int d\vec{p}\ d\vec{q}\ W(q + \tfrac{1}{2}\vec{p})\, W(\vec{q} - \tfrac{1}{2}\vec{p}) \left[\frac{2 J_1 (k p \alpha/F)}{k p \alpha/F}\right] , \tag{12}$$

where

$$p = |\vec{p}| \quad , \tag{13}$$

W is a step function which is unity so long as its argument has a magnitude less than $D/2$, and is zero for larger magnitudes. Thus

$$W(\vec{x}) = \begin{cases} 1 & \text{if } |\vec{x}| \le \tfrac{1}{2} D \\ 0 & \text{if } |\vec{x}| > \tfrac{1}{2} D \end{cases} \tag{14}$$

Quite obviously W "defines" the interior of a circle of diameter D . The two W functions are used in Eq. (12) to replace the limits on the integrations in Eq. (10). In Eq. (12), the $\vec{p}$ and $\vec{q}$ integrations are to be understood as being over the infinite plane, with the practical limits being defined by the W functions.

In examining Eq. (12), we see that the $\vec{q}$-integration can be performed quite independent of the Bessel function term. Recognizing that in the $\vec{q}$-plane the two W functions simply define two circles, each of diameter D , whose centers are separated by a distance $\pm \tfrac{1}{2}\vec{p}$, we see from Eq. (14) that the $\vec{q}$-integration simply yields the area of overlap of the two circles. By a little plane trigonometry, it can be shown that

$$\int d\vec{q}\; W\left(\vec{q} + \tfrac{1}{2}\vec{p}\right) W\left(\vec{q} - \tfrac{1}{2}\vec{p}\right) = \begin{cases} \tfrac{1}{2} D^2 \{\text{arc cosine } (p/D) - (p/D)\sqrt{1 - (p/D)^2}\}, & \text{if } p \le D \\ 0, & \text{if } p > D \end{cases} \quad (15)$$

It is convenient at this point to make use of the approximation[1]

$$\{\text{arc cosing } x - x\sqrt{1 - x^2}\} \approx \tfrac{1}{2}\pi \left(1 - \tfrac{5}{4} x + \tfrac{1}{4} x^4\right) , \quad (16)$$

so that we get upon substitution of Eq. (16) into Eq. (15), and substitution of the result of that into Eq. (12)

$$\tilde{F}(\alpha) = \frac{4}{\pi D^2} \int_{p<D} d\vec{p} \left[1 - \tfrac{5}{4} (p/D) + \tfrac{1}{4} (p/D)^4\right] \left[\frac{2 J_1(k p \alpha/F)}{k p \alpha/F}\right] . \quad (17)$$

It is convenient at this point to perform the angular part of the $\vec{p}$-integration, (treating it as an integration over polar coordinates) and introduce the parameters and replacement variable

$$r = p/D \quad (18a)$$

$$A = k \alpha D/F = 2\pi \alpha/f\lambda , \quad \text{where} \quad f = F/D \quad (18b)$$

so that

$$\tilde{F}(\alpha) = \frac{16}{A} \int_0^1 dr \left[1 - \tfrac{5}{4} r + \tfrac{1}{4} r^4\right] J_1(A r) . \quad (19)$$

The evaluation of this integral is straightforward, if somewhat tedious. We treat it in three separate parts, i.e.,

$$\tilde{F}(\alpha) = \frac{16}{A} \left[\tilde{F}_1(\alpha) - \tfrac{5}{4} \tilde{F}_2(\alpha) + \tfrac{1}{4} \tilde{F}_3(\alpha)\right] , \quad (20)$$

where

$$\tilde{F}_1(\alpha) = \int_0^1 dr\; J_1(A r) , \quad (21a)$$

$$\tilde{F}_2(\alpha) = \int_0^1 ar\; r J_1(A r) , \quad (21b)$$

$$\tilde{F}_3(\alpha) = \int_0^1 dr\; r^4 J_1(A r) , \quad (21c)$$

From Dwight[2], Eq. (835.2), we see that

$$\tilde{F}_1(\alpha) = A^{-1} [1 - J_0(A)] \quad . \tag{22}$$

Making note of the fact that from Dwight, Eq. (801.90)

$$-d [J_0(x)] = J_1(x)\, dx \quad , \tag{23}$$

and integrating by parts, we get

$$\tilde{F}_2(\alpha) = A^{-2} \left\{ [-x J_0(x)]_0^A + \int_0^A J_0(x)\, dx \right\}$$

$$= -A^{-1} J_0(A) + A^{-2} \int_0^A J_0(x)\, dx \quad . \tag{24}$$

The integral on the r.h.s. of Eq. (24) can't be reduced further, but its value is tabulated in Table 11.1 of Handbook of Mathematical Functions[3] so we can consider it to be as much a known function as is $J_0(A)$ in Eq. (24).

The evaluation of $\tilde{F}_3(\alpha)$ requires repeated integration by parts. By making use of Dwight, Eq. (801.6), we get after some manipulation

$$\tilde{F}_3(\alpha) = -A^{-1} J_0(A) + 4 A^{-2} J_1(A) - A^{-3} J_2(A) \quad . \tag{25}$$

Substituting Eq.'s (22), (24), and (25) into Eq. (20), we get

$$\tilde{F}(\alpha) = 16 A^{-2} + 16 A^{-3} J_1(A) - 32 A^{-4} J_2(A) - 20 A^{-3} \int_0^A J_0(x)\, dx \, . \tag{26}$$

Using appropriate tables, we have carried out the evaluation of $\tilde{F}(\alpha)$ as given in Eq. (26). The results are plotted in Fig. 1. We see that $\tilde{F}(\alpha)$ takes a value of 0.9 when $A = 1.85$, i.e., when $\alpha = 0.294\, f\lambda$. This is the pinhole size which we recommend for the experiment in order to insure that we will obtain a reasonably accurate (i.e., 90% accurate) measurement of

antenna gain. The critical question is, of course, how much of the image intensity will this size pinhole transmit. To evaluate this, we assume that we are measuring near diffraction-limited performance, and therefore may assume that the image intensity distribution is the Airy diffraction pattern. The fraction of the total image energy in the Airy pattern within various size circles is shown in Fig. 2, which is taken from Born and Wolf[4] (their Fig. 8.13). For $A = 1.85$, we see that the fraction of the energy that will pass through the pinhole is about 0.175 of the total incident energy.

With this information, we are now ready to turn to the purely photometric aspects of the problem, and calculate background and signal photon flux rates, and the associated signal-to-noise ratio in our star tracker image dissector system. We treat these matters in the following sections. First, however, we specify the basic system parameters.

System Parameters

The pertinent optical parameters for our experiment are the following --

Spectral Band -- We choose the system to have a spectral band of $\lambda - \frac{1}{2}\Delta\lambda$ to $\lambda + \frac{1}{2}\Delta\lambda$, where

$$\lambda = 5000\ \text{Å} \quad , \quad \Delta\lambda = 2000\ \text{Å} \ . \tag{27}$$

It follows from Eq.'s (73a) and (73b) of reference 5 that wavefront distortion is so well correlated over this spectral band — the two most extreme wavelengths have their separate distortions so well correlated to each other — that their cross correlation is exactly equal to the autocorrelation of the distortion at wavelength λ.

Pinhole Size - We choose the pinhole size to satisfy the condition $A = 1.85$, from which it follows that the pinhole radius is

$$\alpha = 0.204\, f\lambda \tag{28}$$

We need not specify f , the optics speed, as this will only be of significance in terms of defining a practical pinhole size. (We shall, in a later appendix, choose an f-number of the order of f = 100 or 200 to make the pinhole large enough to be practical, but at this point, we have no need to specify this value.)

Optics Diameter - The optical system will be required to operate with a variety of aperture diameters. It is, however, convenient to reference all results to a 10 cm diameter, since useful diameters will never be much larger than this, although they may be several times smaller. For convenience, we introduce the parameter d , to accommodate this range, and write for the aperture diameter

$$D = 10\, d \quad \text{cm.} \tag{29}$$

With these parameters thus specified, we now proceed with the calculation of the background and stellar signal photon flux levels we expect.

Background Photon Flux

The background photon flux collected by the pinhole can be written as

$$N_B = \tfrac{1}{4}\, \pi\, D^2\, \tilde{N}_\lambda\, (\Delta\lambda/\lambda)\, \delta\Omega/E_{ph} \quad , \tag{30}$$

where E_{ph} is the energy per photon, and at 5000 $\mathring{A}$,

$$E_{ph} = 4 \times 10^{-19} \ \text{J/ph} \quad , \tag{31}$$

$\delta\Omega$ is the solid angle subtended by the pinhole defined field-of-view, and is

$$\delta\Omega = \pi\, \alpha^2 / F^2 \quad , \tag{32}$$

(with F being the focal length, so $F/D = f$), and $\tilde{N}_\lambda$ is the spectral radiance index, as discussed in reference 6, which for 5000 Å and bright daylight conditions is

$$\tilde{N}_{5000} \approx 1.7 \times 10^{-3} \text{ W/cm}^2\text{-ster} \quad . \tag{33}$$

Making all of the appropriate substitutions, and noting that the dependence on diameter, focal length, and f-number cancel each other out, we find that

$$\begin{aligned} N_s &= \tfrac{1}{4} \pi \tilde{N}_\lambda (\Delta\lambda/\lambda) \pi (1.472 \times 10^{-5})^2/4 \times 10^{-19} \\ &= 1.337 \times 10^{9} \tilde{N}_\lambda (\Delta\lambda/\lambda) \\ &= 9.09 \times 10^{5} \text{ ph/sec} \quad . \end{aligned} \tag{34}$$

Because the image dissector's quantum efficiency will be less than unity, not all of these photons will be detected, but for our purposes here, we need not concern ourselves with exactly what the quantum efficiency will be. We are now ready to turn our attention to the question of what the stellar signal photon flux will be.

Stellar Signal Photon Flux

A zero bolometric magnitude star produces an energy flux of 2.52×10^{-5} erg/cm²-sec, according to Allen[7], page 191. Treating the star as a 6000 K black body, which is typical of most stars, we find that there is $0.403 - 0.140 = 0.263$ part of the total energy in the spectral region from 6000 Å to 4000 Å. This means that a zero magnitude star provides, in our spectral band, 6.63×10^{-6} erg/cm²-sec $\equiv 6.63 \times 10^{-13}$ W/cm². Considering the photons in the spectral band as being at approximately 5000 Å, we see that there are 1.657×10^{6} ph/cm²-sec, due to a typical zero magnitude star. A star of magnitude m will produce a photon irradiance

$$H_m = 1.657 \times 10^6 \varphi_m \text{ ph/cm}^2\text{-sec} \quad , \tag{35}$$

where

$$\varphi_m = 10^{-m/2.5} \tag{36}$$

so that

$$\varphi_0 = 1 \ , \quad \varphi_1 = 0.398 \ , \quad \varphi_2 = 0.1585 \ , \quad \varphi_3 = 0.0631 \ . \tag{36'}$$

The collected signal flux is just the product of the aperture area $\frac{1}{4}\pi D^2$ times H_m, and times a factor of 0.175 to allow for the failure of the pinhole to collect most of the stellar image flux. Thus we get for the stellar signal flux rate

$$N_s = \tfrac{1}{4}\pi D^2 H_m(0.175)$$

$$= 2.28 \times 10^7 d^2 \varphi_m \text{ ph/sec} \quad . \tag{37}$$

For values of d and φ_m reasonably close to unity, it is apparent that not only will the photon flux due to the star at least equal that due to the daytime background, but equally important, it will be large enough so that the number collected in a millisecond measurement period will allow an adequate signal-to-noise ratio.

References

1. R. E. Hufnagel, "Simple Approximation to Diffraction Limited MTF," Appl. Opt. 10, 2547 (1971)
2. H. B. Dwight, "Tables of Integrals and Other Mathematical Data," 3rd Edition, MacMillan Co., New York (1957)
3. M. Abramowitz and I. A. Stegan, "Handbook of Mathematical Functions," U. S. Government Printing Office, Washington, D. C. (1964)
4. M. Born and E. Wolf, "Principles of Optics," Pergamon Press, New York (1964)
5. D. L. Fried, "Spectral and Angular Covariance of Scintillation for Propagation in a Randomly Inhomogeneous Medium," Appl. Opt. 10, 721 (1971)

References (Continued)

6. D. L. Fried and J. B. Seidman, "Heterodyne and Photon-Counting Receivers for Optical Communications," Appl. Opt. 6, 245 (1967)

7. C. W. Allen, "Astrophysical Quantities," 2nd Edition, Athlane Press, London (1964).

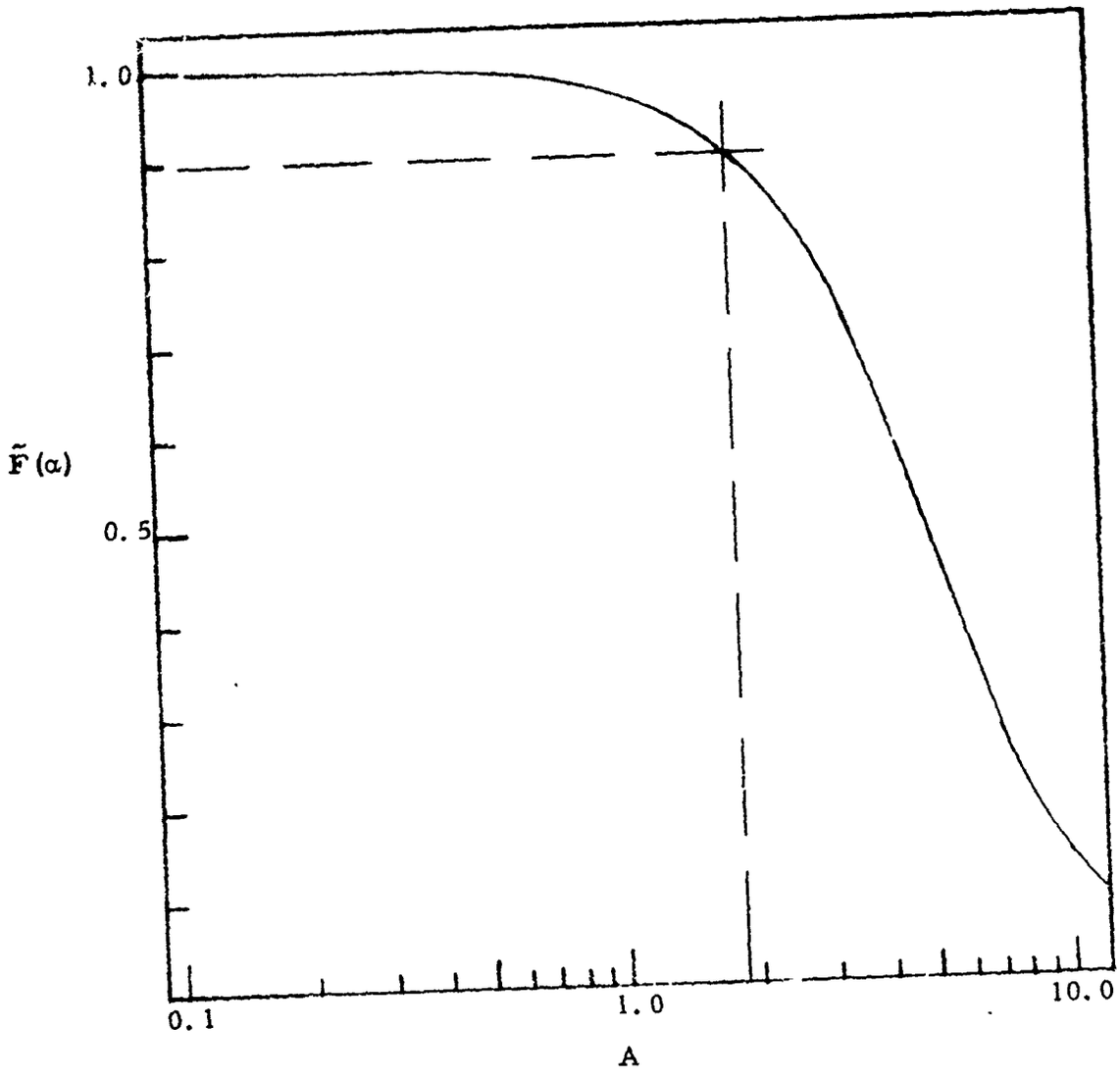


Figure 1. Dependence of $\tilde{F}(\alpha)$ Upon A. $\tilde{F}(\alpha)$ is a measure of the accuracy with which a pinhole of radius α measures the antenna gain for an aperture diameter D with optics focal length F, for operation at wavelength λ. $A = 2\pi \alpha D/F\lambda$.

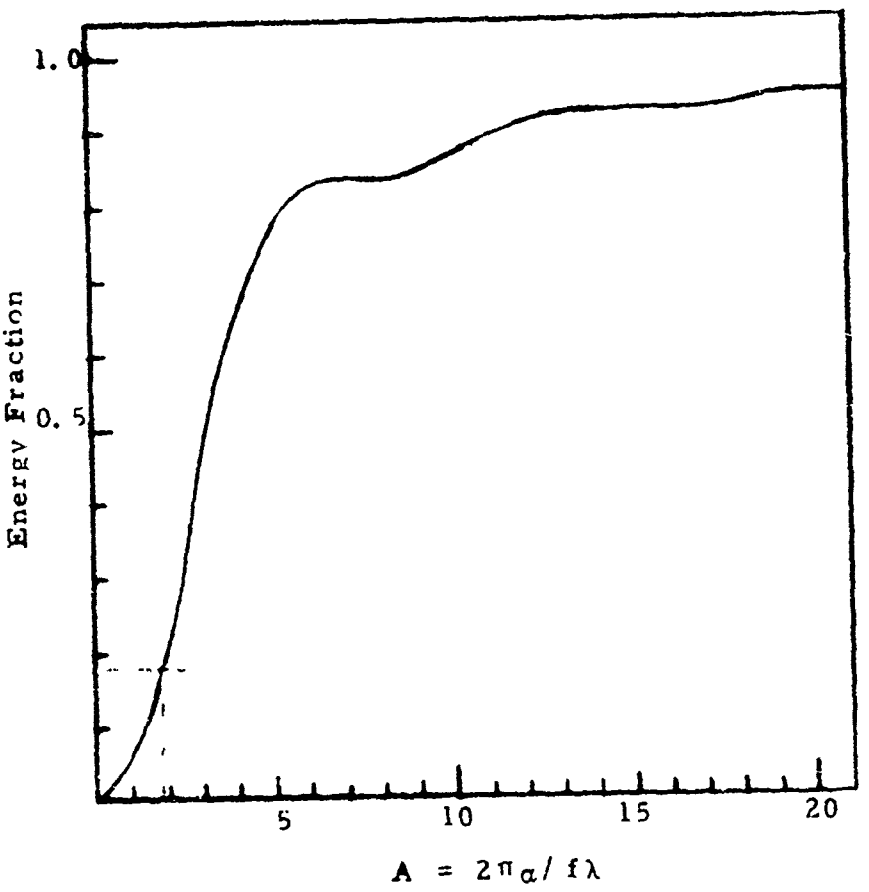


Figure 2. Fraction Of The Total Energy In The Frannhofer Diffraction Pattern Of A Circular Aperture Contained Within A Circle Of Radius α .

APPENDIX V

NOTES ON THE DESIGN OF A WAVEFRONT DISTORTION SENSITIVE STAR TRACKER TELESCOPE

D. L. Fried

This Appendix is a reproduction of Optical Science Consultants Report No. TR-071 (August 1972) as provided by that organization.

PRECEDING PAGE BLANK-NOT F

Introduction

In this appendix, we take up the problem of the design of a photoelectric telescope suitable for performance of the measurements discussed in Appendix IV. "Preliminary Parameter Considerations for a Wavefront Distortion Sensitive Star Tracker." Our primary emphasis here will be on the optical and electro-optical design aspects of the problem, with only minor treatment of signal-to-noise ratio aspects of the problem. We divide our treatment into five sections. In the order of their presentation, they are: 1) definition of the optical train; 2) analysis of aberrations; 3) considerations relative to the placement of baffles and stops; 4) electro-optic detector definition; and 5) data processing definition and analysis. We start with consideration of the optical train.

Telescope Optical Train

The optical train is designed to allow operation at near constant f-number with aperture diameter adjustable from 2 cm to 20 cm. We have selected an f/200 speed as the nominal speed for design of the pin-hole in the photodetector. Using the criteria established in Appendix IV that the pin-hole radius should be

$$\alpha = 0.294\, f\lambda$$

with $\lambda = 0.5 \times 10^{-6}$ m, and f/200 gives

$$\alpha = 29.4 \times 10^{-6} \text{ m}$$

$$\equiv 1.15 \times 10^{-3} \text{ inches} .$$

We have briefly examined the problems involved in designing a constant f-number zoom lens arrangement with a 10:1 range and have, instead, decided to utilize a set of interchangeable magnifier pairs, allowing a moderate change in f-number by varying an iris to change the aperture. Examining Appendix IV, we have concluded that with the pin-hole as large as

$$\alpha = \frac{3}{2} \times 0.294\, f\lambda$$

PRECEDING PAGE BLANK-NOT FIL

we still would get adequate quality measurement results,* and would actually have a somewhat better light gathering situation. We have therefore configured an optical train design which would allow the f-number to vary from f/200 to f/133.

The optical train is laid out in schematic form in Fig. 1. The primary is an 8-inch diameter off-axis section of a 16-inch diameter parabolic mirror. It can be seen in Fig. 1 that because the primary mirror is half the size of the source mirror, the folding mirror has to protrude into the entrance aperture. This is only of possible significance when the system is used with its full 8-inch diameter aperture, and even then is only of rather limited importance. Since it obstructs such a little portion of the full aperture, its effect on antenna gain is almost entirely negligible. (We could avoid the obscuration only if we are willing to take our off-axis mirror from a source mirror at least 18-inches in diameter, rather than from a 16-inch diameter mirror.) For overall size considerations, and taking account of both mirror fabrication and off-axis image aberration problems, we have selected the primary focal length as 80-inches.

Tracing the light through the optical chain shown in Fig. 1, we see that after the folding mirror, the light is brought to focus at the field stop. The field stop is sized to allow a circular field of view of 1 mrad diameter. This means the opening's physical size is 0.08 inches. The light passing through the field stop is collected by a 45.75 mm focal length microscope objective and thereby collimated.

---

*The change would reduce a guarantee of better than 90% accuracy in measuring instantaneous antenna gain to 80%. Measurement of average antenna gain would only be affected by a fixed ratio which could be exactly compensated.

The collimated light then passes the chromatic elements box. This box contains the band pass filter which limits the spectral range of the signal to the 0.4 μ to 0.6 μ spectral range. It also contains a pair of prisms designed to compensate for the chromatic dispersion of the atmosphere. (Details regarding the dispersion compensating prisms are presented later.)

The light leaves the chromatic element box, still collimated, and enters the variable magnification unit. The variable magnification unit contains a seven position magnifier wheel. Each of the positions (except the 1X position, which is empty) contains a pair of microscope objectives arranged nose-to-nose and adjusted so that a collimated beam entering (the rear of) one microscope objective leaves the (rear of the) other objective in a collimated condition, but having been subjected to a MX magnification. By rotating the wheel, the beam can be made to pass through different parts and receive different magnifications. The available magnifications are nominally 2X, 1.5X, 1X, $\frac{2}{3}$X, $\frac{1}{2}$X, $\frac{1}{3}$X, $\frac{1}{4}$X. The microscope-objectives combination to provide these magnifications, specified in terms of available effective focal lengths, are as listed in Table 1. It is significant to note that because the beam entering and leaving the magnification unit is collimated, there is no very tight tolerance on the insertion of magnification optics in the beam. The only serious tolerance concerns the alignment of the pair of microscope objectives with respect to each other. Placement in the beam has thousandths of an inch, as distinct from fraction of a micron, tolerance.

After leaving the magnification unit, the beam falls on a 18.3 cm focal length lens (the tube magnification lens from a modern microscope), which is the last focusing element in the optical train. In Table 2, we show the effective focal length of the system for each magnification listed in Table 1, as well as showing the diameters corresponding to f/200 and f/133 operation. After this, the converging beam passes through a 9:1

Table 1

Magnifier Microscope-Objectives Combination

Nominal Magnification	Effective Focal Length (mm)		Actual Magnification
	Front	Rear	
2x	18	9.1	1.978x
1.5x	27	18	1.5x
1x	None	None	1x
$\frac{2}{3}$x	18	27	0.6667x
$\frac{1}{2}$x	9.1	18	0.5056x
$\frac{1}{3}$x	9.1	27	0.3370x
$\frac{1}{4}$x	4.6	18	0.2555x

Table 2

System Effective Focal Length and Effective Diameter at f/200 and f/133 Operation for the Magnifications Listed in Table 1 .

Magnification	Effective Focal Length (cm)	Effective Diameter cm	
		f/200	f/133
2x	2754	13.77	20.71
1.5x	2065	10.33	15.53
1x	13x77,	6.886	10.35
$\frac{2}{3}$x	918.2	4.591	6.904
$\frac{1}{2}$x	688.6	3.443	5.177
$\frac{1}{3}$x	459.1	2.295	3.452
$\frac{1}{4}$x	344.3	1.722	2.589

pellicle beam splitter. 90% of the beam energy comes to focus on an image dissector, with the remaining 10% falling on a photocell. The image dissector has a working photocathode diameter of nominally 1-inch, with a pin-hole diameter of 2.3×10^{-3} inches. The photocell is a low frequency (i.e., quasi-d.c.) device with a circular sensitive area of about 0.1 inches diameter. (This allows the photocell to measure the total light flux from a star independent of image quality, while the image dissector is measuring a small fraction of the flux.

We started our discussion of the optical train with the primary mirror. Actually, however, the first elements in the optical train are the two irises, one just in front of the primary mirror, and one at the front of the telescope tube. Each of the irises is adjustable over the range of 2 cm to 20 cm diameter, with the two adjusted in synchronism except that the rear iris is taken as the defining aperture so that to accommodate a 1 mrad full field-of-view, it is necessary that the forward iris be open approximately an extra 0.2 cm. The forward iris is introduced with the objective of cutting down on stray radiation. Its placement is dictated by the requirement that it be forward of the folding mirror so that it will not block the converging beam coming from the primary mirror. (In fact, except for this consideration, we would utilize a number of irises along the full length of the telescope tube to help suppress stray radiation.)

This completes our description of the optical train. We now take up the subject of aberrations, the limitations they impose, and their compensation.

Aberrations

The entire purpose of the experimental equipment we are describing is to measure the quality of the image of a star which atmospheric turbulence will allow us to form. Anything else which degrades the quality if the image is extraneous and will lead to confusing results. It is therefore important that we identify and be prepared to avoid any such source of aberration.

These are the coma in the primary optics, and chromatic dispersion at large zenith angles due to the atmosphere.

The microscope-objective optics which we plan on using are well corrected over a large field-of-view, and since moreover we will not be using these elements at anywhere near their full design aperture, we can be assured that they will not introduce any noticeable aberration. The only element which can introduce significant aberration is the primary. With its full diameter, i.e., 20 cm, it appears to be approximately an f/10 optical system. However, for calculation of sagittal coma, which is the dominant aberration, we must take note of the fact that the primary mirror is a segment of an f/5 paraboloid. Since the equation for sagittal coma, β , is

$$\beta = \frac{\varphi}{16\ (f/\#)^2}$$

where φ is the field-of-view half angle, we see that for $\varphi\ (= \frac{1}{2}$ mrad$) = 5 \times 10^{-4}$ rad , the aberration is only 1.25 μrad , while for $\varphi\ (= \frac{1}{10}$ mrad$) = 1 \times 10^{-4}$ rad , the aberration is only 0.25 μrad. In view of the fact that for the 20 cm diameter, the diffraction angle is

$$\frac{\lambda}{D} = 2.5\ \mu\text{rad} , \qquad (@\ \lambda = 5000\ \text{Å})$$

it follows that during acquisition, when we are searching a field-of-view of 0.5 mrad radius, coma will be smaller than diffraction spreading, while inside the 0.1 mrad field-of-view angular radius, within which we will be making our measurements, coma will be so small compared to diffraction as to be of no consequence in terms of its effect on the data.

Because of the very high angular resolution involved in our measurements, atmospheric dispersion can be significant as an aberration mechanism. We intend to operate over the spectral band from $\lambda = 4000$ Å to $\lambda = 6000$ Å , over which range the atmospere's refractive index varies from $n = 1 + 298.1 \times 10^{-6}$ @ $\lambda = 4000$ Å to $n = 1 + 291.9 \times 10^{-6}$ @ $\lambda = 6000$ Å , a difference in refractive index of $dn = 6.2 \times 10^{-6}$. It

can be shown that for a star at zenith angle θ , its apparent position will be spread over the angular range $d\theta$ due to this spread in refractive index.

$$d\theta = -\frac{dn}{n} \tan\theta \approx -\, dn \tan\theta \quad .$$

If we could allow a spread of 2.5×10^{-6} rad, which is obviously excessive for the 20 cm diameter aperture (and is possibly too much even when we are working with a 5 cm diameter aperture), we would be restricted to zenith angles of 23° or less. If we could allow as much as 5×10^{-6} rad dispersion, we would still be restricted to zenith angles of less than 40°. This is obviously an excessive limitation and we have, therefore, incorporated into the chromatic element box, in the optical train, the chromatic dispersion compensating prism pair alluded to previously. This consists of two pair of very small angle prisms, one pair of crown and the other of flint glass. for example. (The important point is not the type of glass, but the fact that the two types of glass have different dispersion.) By rotating the two wedges (i.e., the small angle prisms) of one type of glass in a plane perpendicular to the beam direction, it is possible to adjust the effective wedge angle and thereby the chromatic dispersion introduced by the pair. With a proper setting of the two pairs of wedges with respect to each other and in terms of each of their effective angles, it is then possible to introduce a negatively oriented chromatic dispersion, exactly able to cancel the effect of the atmospheric dispersion. These angles can be adjusted so as to allow cancellation at any zenith angle. We have incorporated the two pairs of prisms so as to allow the beam to pass undeviated. However, it may be possible to work with a single pair if the total deviation is small enough. A decision on this matter will depend on the details of the total design, and is postponed until a later time.

At this point, having completed our consideration of abberrations, we now turn our attention to the subject of baffle requirements. This we take up in the next section.

Baffle Requirements

All of our calculations of signal-to-noise ratio and system performance have been based on the assumption that any background would be due to the projection of the sky on the focal plane by the optical system. Since the optical system at f/200 only illuminates a solid angle of 2.5×10^{-5} steradians in front of the focal plane, it is obvious that stray light coming in from the rest of the hemisphere, even if strongly attenuated, can easily exceed the amount included in our calculations.* To avoid this, careful attention has to be paid to the baffle design.

It would be desirable to restrict the cone angle incident on the photodetectors directly to f/200. However, because of the field-of-view of the system, the beam may enter the final lens anywhere over a wide range, and as a consequence, the cone angle can not be restricted as much as f/200. Probably f/10 to f/20 is all the restriction we can obtain at that point. We introduce further restriction to the passage of stray light at the first microscope objective where we can achieve an f/10 baffle rejection of stray light. The primary optics are baffled by the telescope tube and the pair of irises at the front and rear of the tube. These two irises provide a further f/10 attenuation. This, in conjunction with the very small size of the field stop aperture relative to the tube dimensions, is expected to provide adequate baffling against daytime stray radiation.

We call attention to the requirement that the telescope tube project forward sufficiently far that it prevents direct illumination of the small cavity just forward of the field stop. We also require, of course, that all surfaces be painted flat black, probably with a paint like the 3-M velvet.

It would be desirable to be able to give an exact statement for the baffle attenuation -- but unfortunately, the theory of baffle performance is not well enough advanced to allow this. However, on the basis of the number of restrictions we have been able to put in the way of stray radiation, each representing a fairly small angle restriction. we feel fairly confident that

* Obviously, this problem is only serious for daytime operation. For night operation, modest baffle performance should suffice.

stray radiation rejection performance will be adequate.

At this point, we are now ready to turn our attention to definition of the electro-optic detectors per se and their mode of operation. We take this up in the next section.

Electro-Optic Detectors

There are two electro-optic detectors in the instrument, viewing the collected signal. As stated previously, they are an image dissector and a quasi-d. c. photosensor. They share the collected flux in a ratio of 9:1, with the larger share going to the image dissector. The sensitive area of the quasi-d. c. sensor is large enough that when a star is in the center of the system's field-of-view, the entire image of the star will fall within the sensitive area. The sensor itself can be either a small lowgain photomultiplier, or possibly a vacuum or solid state photodiode. It is intended to be used only to measure the change in system transmission when the magnification optics are changed, and therefore can work with a very low, quasi-d. c. noise bandwidth. As a consequence, its sensitivity will be quite high, almost no matter what type of detector is used. Moreover, since its basic function is simply to measure changes in sensitivity as the magnification is changed, it does not require absolute calibration or long term stability. If its sensitivity is constant over a 10-minute period to within a few percent, and measurements are repeatable to that precision, that should be sufficient.

The image dissector is the basic detector in the system. It is used to acquire and track the star being observed, and is used to measure the intensity of the stellar image at the center of the image pattern. The tracking information is generated by causing the effective aperture of the image dissector to move and trace out a cruciform pattern over the photocathode. The pattern is shown in Fig. 2. Using standard techniques, if the extent of the pattern is large enough to pass beyond the range of the image, the necessary tracking information can be obtained to allow the center of the cruciform scan to be positioned over the center of the image. (The displacement

of the center of the scan pattern from the nominal center of the photocathode can then be used to control the pointing drive for the telescope, so that the optics are never required to work very far off of boresight.) In order to be sure to track all stellar jitter associated with the atmosphere, we plan to complete a cruciform scan pattern once per millisecond. This will permit high frequency tracking information to be generated. (However, in order to also allow generation of antenna gain information when atmospheric tilt is not tracked out, we will require ability to adjust the tracking servo loop bandwidth so that we can slow it down to the point where such rapidly varying tilt will not be tracked.

In Fig. 3a, we show the horizontal and vertical deflection fields that might be used to generate the cruciform pattern. However, this pattern spends very little time with the aperture at the center of the scan pattern, which is where we wish to make image intensity measurements, so as to determine the effective antenna gain. In order to improve our data collection capability, we therefore plan on use of the horizontal and vertical deflection fields shown in Fig. 3b. This pattern allows us to make two, $\frac{1}{6}$ msec long measurements of intensity at the center of the image, each millisecond, or 2000 sample measurements per second. As we shall develop in the next section, it is important that the sample measurements be independent. We therefore recommend that a very wide bandwidth preamplifier, say 50 to 100 kHz, follow the image dissector anode. This output would be filtered by a boxcar integrator, with an integration period of $\frac{1}{6}$ msec, activated each time the scan pattern stopped at the center. The outputs of the boxcar integrator would be recorded for antenna gain determination. In the next section, we take up the problem of data processing, signal-to-noise ratio and its effect on the measurements.

Data Processing

If the signal-to-noise ratio were no concern to us, data processing for antenna gain statistics would be very easy. We would simply plot the probability density of the antenna gain as measured during each $\frac{1}{6}$ msec

period, and from this we could easily derive all pertinent statistics. In fact, however, the signal-to-noise ratio is generally a problem and our data processing has to be specially tailored to accommodate this problem. In what follows, we shall assume that the data processing is to be performed by a digital computer, using the individual samples, so that complexity of the processing is not a particular problem. We shall first formulate some estimates of the signal and noise in various situations. We shall then consider the kind of data processing that would be appropriate and shall estimate how good we might expect the performance to be.

To calculate the expected signal strength, we make use of Eq. (37) from Appendix IV. For an aperture of diameter D (cm) and viewing a star of magnitude m, the available signal flux rate that could fall on the sensitive area (i.e., the aperture region) of the image dissector photocathode is

$$N_s = 2.28 \times 10^6 D^2 \varphi_m \quad \text{photons/sec.}$$

where

$$\varphi_0 = 1 \quad , \quad \varphi_1 = 0.398 \quad , \quad \varphi_2 = 0.1585 \quad , \quad \varphi_3 = 0.0631 \quad .$$

Allowing for an optics transmission of $\tau = 0.3$, a photocathode quantum efficiency of $\eta = 0.1$, and an integration time $\Delta t = \frac{1}{6} \times 10^{-3}$ sec, we see that the detected flux will be

$$I_s = N_s \tau \eta \Delta t = 1.14 D^2 \varphi_m \quad \text{photoelectrons.}$$

The background photon flux during the daytime, according to Eq. (34) from Appendix IV, will be

$$N_B = 9.09 \times 10^6 \quad \text{photons/sec,}$$

resulting in a detected flux of

$$I_B = 4.55 \quad \text{photoelectrons.}$$

(During the night time, this number will be nearly zero.) For an aperture as large as 5 cm diameter, I_s , even with a first magnitude star, the stellar signal will be enough larger than the background that the background contribution to the noise will be negligible. For a larger aperture, this is clearly the case and we need not distinguish between day and night performance -- except as it may affect acquisition. However, when we wish to work with a 2 cm aperture diameter, the two flux rates are comparable for a first magnitude star, and performance will be somewhat poorer than for night time operation.

We note that in general the available signal-to-noise voltage ratio, SNR_v , where

$$SNR_v = \frac{I_s}{\sqrt{I_s + I_B}}$$

will be of the order of 2 to 10. These are marginal to only fair signal-to-noise ratios, and for the purpose of measuring antenna gain statistics, they are apparently inadequate. However, if we think in terms of calculation of the moments of the antenna gain distribution, we can circumvent this limitation, and because many data points are used in calculating the moments, can expect an improvement of the order of $\sqrt{N}$ in the precision of our results. Thus, if we start with individual sample measurements with a fractional precision of 0.5, corresponding to a signal-to-noise voltage ratio of 2:1, and if we used 1 minute's data, so that we had N = 120,000 individual measurements, a calculation of antenna gain variance would have a precision of $0.5\sqrt{120,000} = 0.0014$, which is certainly more than adequate. By calculating the first several moments, we can determine most of the important characteristics of the antenna gain distribution, all with this sort of precision, although we start with a raw data signal-to-noise voltage ratio that is rather poor.

It should be noted that there is nothing particularly spectacular or unusual in our developing very precise signal statistics from a noisy signal. In the case of a first moment determination, this is just a matter of

averaging over a long enough time -- and is a routine process. As far as second moment determination is concerned, the practice of measuring the correlation function (or the power spectrum) for a signal contaminated with a great deal of noise is a well known procedure and is regularly accomplished. All that is needed is the ability to process a large enough set of data. The correlation function (and power spectrum) can be very precisely determined even though there is a great deal of noise present. The only problem is to separate the contribution of the noise from that due to the signal of interest. We note that the contribution due to the noise is deterministic with only a relatively small random component -- otherwise it would not be possible to make meaningful measurements of a noise power spectrum. The problem is to make a measurement of the variance which is not only precise (i.e., not random), but also is not contaminated by an unknown contribution due to the noise. In our case, we do this by measuring the correlation function only for time differences for which the noise correlation is zero.

The key to the process is in the way we manipulate the raw data so as to prevent the photon shot noise distribution from biasing the results. For example, if we simply calculated the variance of the raw data, its precision would be as good as indicated above. However, the accuracy would be very far off since the variance we determined would be due to a combination of antenna gain variance and shot noise variance. The shot noise variance would bias the results so badly that they would be essentially useless. To avoid this, we simply would calculate not the variance of the data, but rather the covariance for a time delay of 0.5 msec, i.e., the time between one sample and the next. So long as the antenna gain variations are well correlated over this time interval (which seems highly likely since the time is shorter than the expected rate over which turbulence will move one aperture diameter), the effect is the same as if we were calculating the zero time delay covariance. However, because of the way the electronics were specified, i.e., very wide bandwidth followed by a boxcar

integrator, there should be no correlation in the shot noise between samples. As a consequence, the shot noise contribution will be absent, i.e., tend to zero, for the time delay covariance. In the next section, we indicate mathematically why this proves to be so. Also, we indicate mathematically how this sort of enhancement would arise, but for a slightly different case. The appendix treats a case which does not quite correspond to Poisson statistics but for which, like Poisson statistics and unlike the simple additive noise case, the contaminating noise magnitude is dependent on the magnitude of the signal whose statistics we wish to study. For this case, we show exactly how the mathematics of the processing results in the suppression of the effect of the contaminating noise.

Covariance of a Product of Statistically Independent Random Variables.

In this section, we wish to consider the problem of calculating the covariance of a data set $\{d_i\}$, where each data point d_i is the product of two random variables, u_i and v_i, i.e.,

$$d_i = u_i v_i \quad .$$

This corresponds in an approximate sense to the situation of antenna gain data, where u_i can be considered the antenna gain variation, and v_i is a factor accounting for the shot noise variation. We treat them multiplicatively to allow for the fact that when u_i is large, the shot noise variation is larger. Strictly speaking, if we want our analogy with Poisson shot noise statistics to be accurate, we should allow the statistics of v_i to vary with the magnitude of u_i, though the actual random value of v_i would be independently chosen from the v_i statistics. However, to attempt to incorporate this feature into our model would excessively complicate our analysis. We have therefore chosen to approximately represent the statistics of a randomly fluctuating signal amplitude with shot noise by the product $u_i v_i$. The atmospheric turbulence induced antenna gain variation corresponds to the u_i fluctuation. If the signal

were very strong, there would be no significant shot noise and u_i itself would accurately represent the fluctuating signal that would be received. But when the signal is weak, though u_i is the signal level that ought to be received, shot noise will randomly modulate the nominal value of u_i. Multiplication by v_i represents this random modulation. When u_i takes a large value, the fluctuation induced by v_i is large -- when u_i has a small value, the fluctuation induced by v_i is smaller. This is similar to the shot noise case for which we expect larger shot noise variations when the nominal signal level is larger and smaller fluctuations when the nominal signal level is smaller. It is important to note that in this formulation v_i is a random variable whose value is chosen independent of the value of u_i, i.e., v_i and u_i are independent random variables.

In accordance with the discussion in the main text, we would calculate

$$\sigma_{d'^2} = \frac{1}{N} \sum_{i=1}^{N} (d_i - \bar{d})(d_{i+1} - \bar{d})$$

where

$$\bar{d} = \frac{1}{N} \sum_{i=1}^{N} d_i = \langle d_i \rangle = \langle u_i v_i \rangle \quad .$$

Since u_i and v_i are independent, it follows th-

$$\langle u_i v_i \rangle = \langle u_i \rangle \langle v_i \rangle$$

so that

$$\bar{d} = \bar{u}\,\bar{v}$$

where

$$\bar{u} = \frac{1}{N} \sum_{i=1}^{N} u_i = \langle u_i \rangle$$

$$\bar{v} = \frac{1}{N} \sum_{i=1}^{N} v_i = \langle v_i \rangle$$

Since

$$(u_i v_i - \bar{u}\,\bar{v}) = (u_i - \bar{u})(v_i - \bar{v}) + \bar{u}\,(v_i - \bar{v}) + \bar{v}\,(u_i - \bar{u})$$

and

$$(u_{i+1} v_{i+1} - \bar{u}\,\bar{v}) = (u_{i+1} - \bar{u})(v_{i+1} - \bar{v}) + \bar{u}(v_{i+1} - \bar{v}) + \bar{v}\,(u_{i+1} - \bar{u})$$

as can be verified by simply carrying out all the multiplications on the right hand side of each equation, then we can write

$$\begin{aligned}(d_i - \bar{d})\,(d_{i+1} - \bar{d}) &= (u_i v_i - \bar{u}\,\bar{v})(u_{i+1} v_{i+1} - \bar{u}\,\bar{v}) \\ &= [(u_i - \bar{u})(v_i - \bar{v}) + \bar{u}\,(v_i - \bar{v}) + \bar{v}\,(u_i - \bar{u})] \\ &\quad \times [(u_{i+1} - \bar{u})(v_{i+1} - \bar{v}) + \bar{u}\,(v_{i+1} - \bar{v}) + \bar{v}\,(u_{i+1} - \bar{u})] \quad .\end{aligned}$$

If we substitute this into the expression for $\sigma_{d'}^2$, we see that we have nine product terms in the summation. Thus,

$$\begin{aligned}\sigma_{d'}^2 = \frac{1}{N} \sum_{i=1}^{N} \{ &(u_i - \bar{u})\,(u_{i+1} - \bar{u})\,(v_i - \bar{v})\,(v_{i+1} - \bar{v}) \\ &+ \bar{u}\,(u_i - \bar{u})\,(v_i - \bar{v})\,(v_{i+1} - \bar{v}) + (u_i - \bar{u})\,(u_{i+1} - \bar{u})\,\bar{v}\,(v_i - \bar{v}) \\ &+ \bar{u}\,(u_{i+1} - \bar{u})\,(v_i - \bar{v})\,(v_{i+1} - \bar{v}) + \bar{u}^2 (v_i - \bar{v})\,(v_{i+1} - \bar{v}) \\ &+ \bar{u}\,(u_{i+1} - \bar{u})\,\bar{v}\,(v_i - \bar{v}) + (u_i - \bar{u})\,(u_{i+1} - \bar{u})\,\bar{v}\,(v_{i+1} - \bar{v}) \\ &+ \bar{u}\,(u_i - \bar{u})\,\bar{v}\,(v_{i+1} - \bar{v}) + \bar{v}^2 (u_i - \bar{u})\,(u_{i+1} - \bar{u}) \} \quad .\end{aligned}$$

The important point to recognize here is that since

$$\langle u_i - \bar{u} \rangle = 0$$

$$\langle v_i - \bar{v} \rangle = 0$$

$$\langle (v_i - \bar{v})(v_{i+1} - \bar{v}) \rangle = \langle v_i - \bar{v} \rangle \langle v_{i+1} - \bar{v} \rangle = 0$$

$$\langle (u_i - \bar{u})(u_{i+1} - \bar{u}) \rangle = \langle (u_i - \bar{u})^2 \rangle = \sigma_u^2 \quad ,$$

then the only term in the summation expression for $\sigma_{d'}^2$ which does not go to zero as N increases is the last term. Thus

$$\sigma_{d'}^2 \approx \bar{v}^2 \frac{1}{N} \sum_{i=1}^{N} (u_i - \bar{u})^2$$

$$= \bar{v}^2 \sigma_u^2 \quad .$$

As we indicated, the result is that $\sigma_{d'}^2$ is an unbiased estimate of the variance of u (scaled by a factor $\bar{v}^2$.) The noise variance in v does not bias the result. It is expected to produce noise in the result for $\sigma_{d'}^2$ since the other terms, while they tend to zero, approach it in a random walk with their contribution to $\sigma_{d'}^2$ decreasing as $N^{-\frac{1}{2}}$.

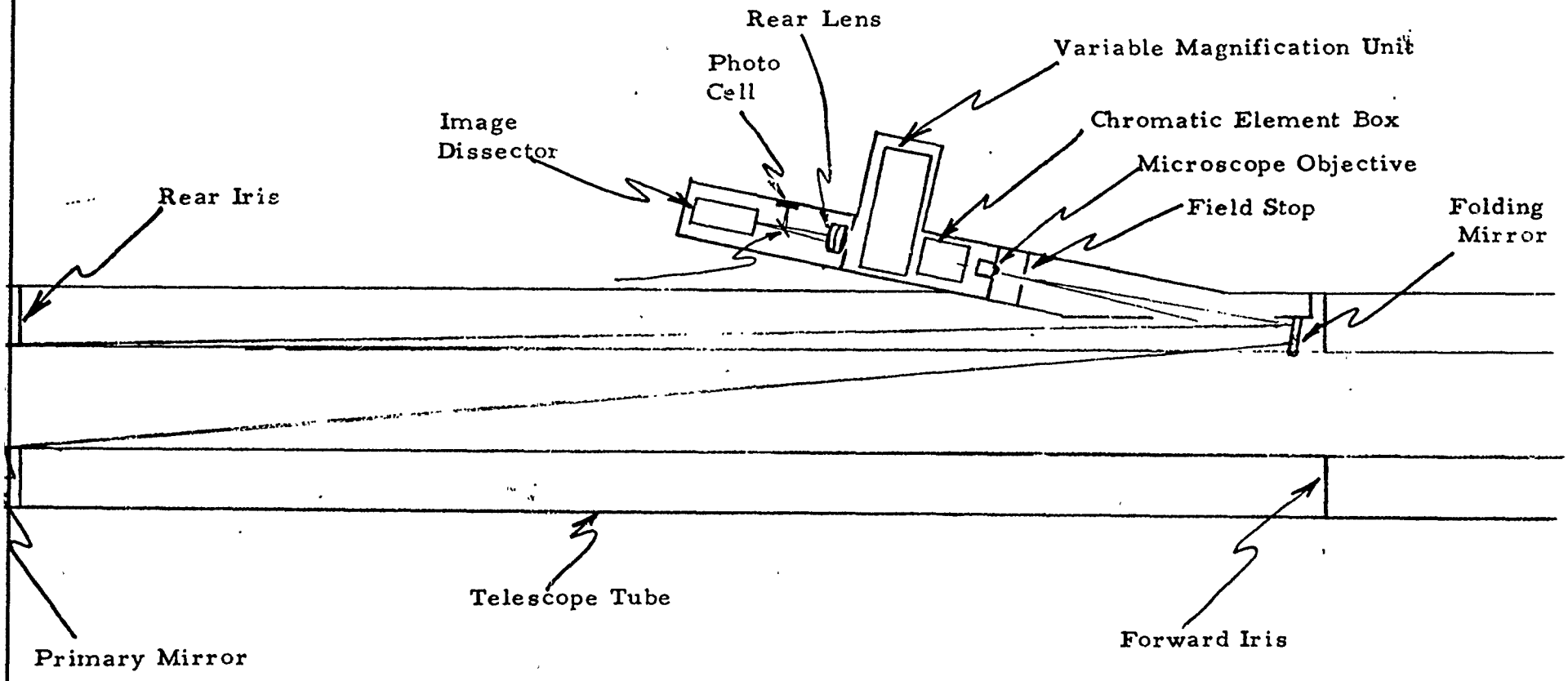


Figure 1. Schematic of Telescope Optics Layout

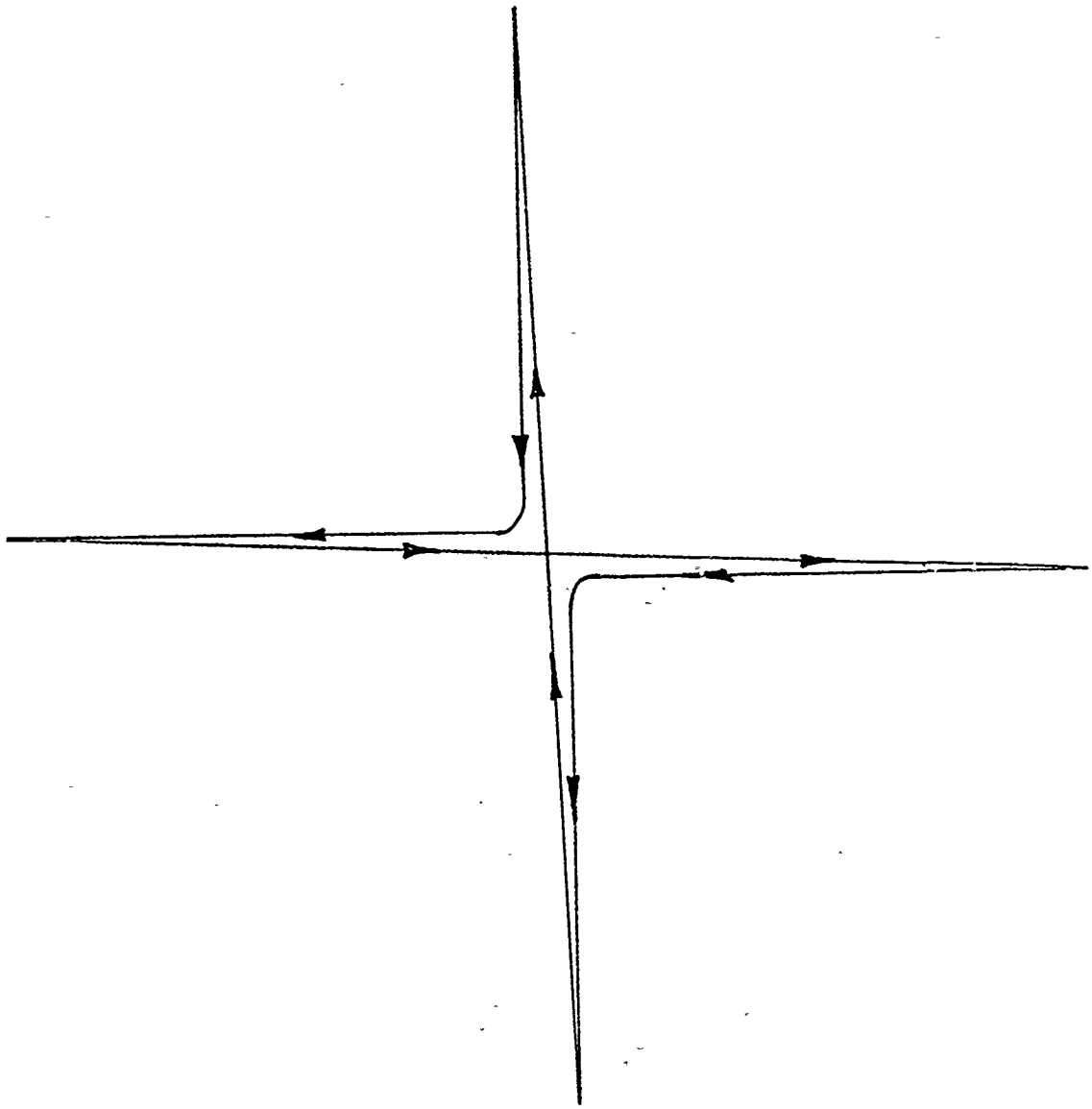


Figure 2. Cruciform Scan Pattern

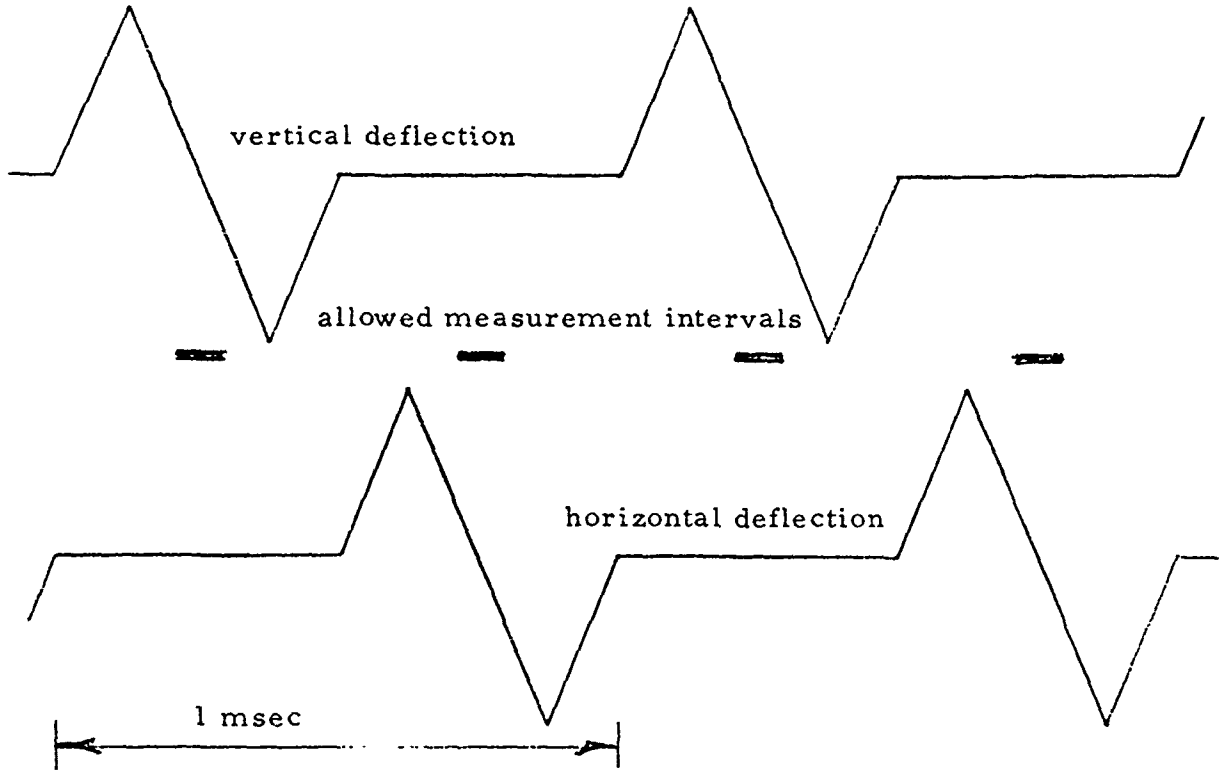


Figure 3a. Deflection Fields for Cruciform Scan -- No Pause at Center. The heavy bars, "allowed measurement interval" indicate the period when the scan is near the center.

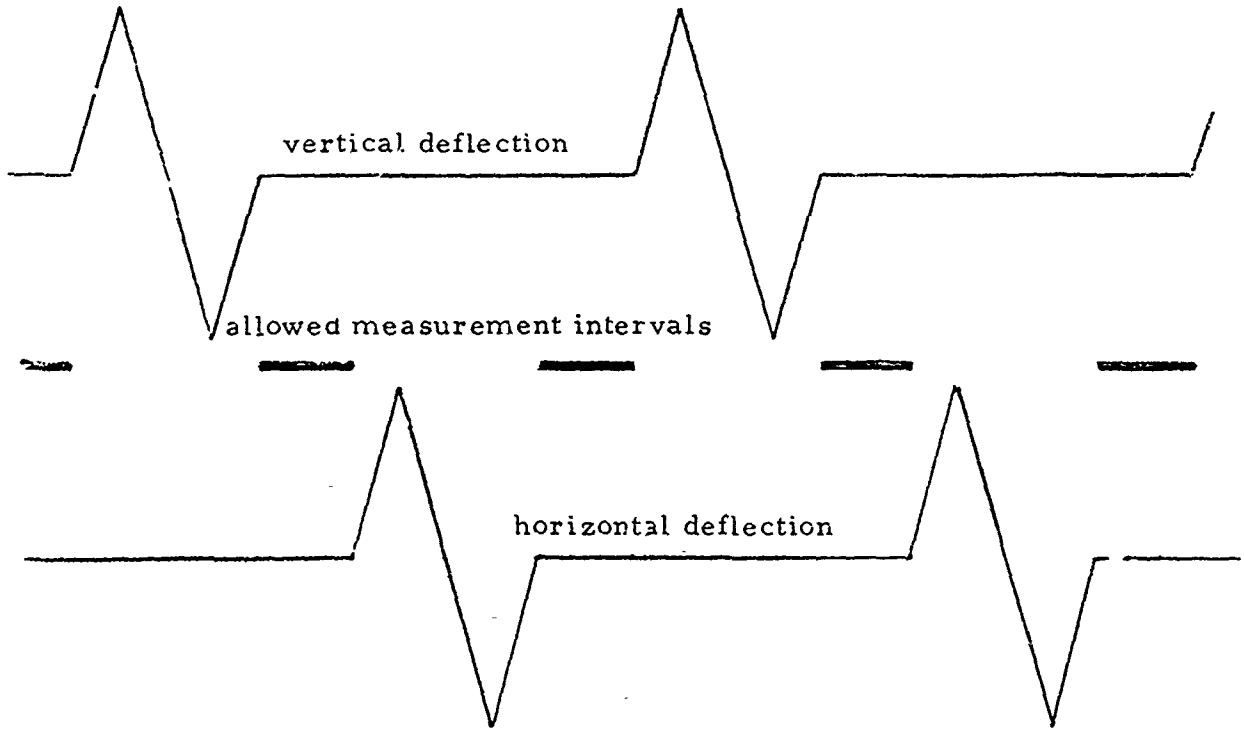


Figure 3b. Deflection Fields for Cruciform Scan -- With Pause at Center. The heavy bars, "allowed measurement interval" indicate the period when the scan is at the center.

APPENDIX VI

METHOD OF COMPUTING STAR DESIGNATION DATA AS USED AT VANDENBERG AIR FORCE BASE

Following is a description of the method used to compute the azimuth and elevation where:

RA	=	apparent right ascension of the star in hours
DC	=	apparent declination of the star in degrees
SMRA1	=	mean right ascension for year after the current year in seconds of a degree
SMDC1	=	mean declination for year after the current year in seconds of a degree

A, B, C, and D are the Besselian day numbers for the correction for the aberration, precession, and nutation units (seconds of arc) where:

M	=	precession in right ascension in seconds of arc
N	=	precession in declination in seconds of arc
e	=	Mean obliquity of the ecliptic in degrees and fraction of a degree
SMRA	=	mean right ascension of the star for the current year in degrees
SMDC	=	mean declination of the star for the current year in degrees

The following equations are used to compute the star constants, a, a', b, b', c, c', d, and d', where:

a	=	$m/n + \sin(SMRA) \cdot \tan(SMDC)$
b	=	$\cos(SMRS) \cdot \tan(SMDC)$
c	=	$\cos(SMRA) \cdot \sec(SMDC)$
d	=	$\sin(SMRA) \cdot \sec(SMDC)$
a'	=	$\cos(SMRA)$
b'	=	$\sin(SMRA)$
c'	=	$\tan(e) \cdot \cos(SMDC) - \sin(SMRA) \cdot \sin(SMDC)$
d'	=	$\cos(SMRA) \cdot \sin(SMDC)$

The corrected right ascension will then be

$$RA = SMRA + Aa + Bb + Cc + Dd \quad (1)$$

and the corrected declination will be

$$DC = SMDC + Aa' + Bb' + Cc' + Dd' \quad (2)$$

However, if the month of the year for which the azimuth and elevation of a star is desired should fall after June, then SMRA and SMDC in the above equations are replaced by SMRA1 and SMDC1 in Eqs. (1) and (2), respectively, where

$$SMRA1 = SMRA + M + N[\sin(SMRA)] \cdot \sin(SMDC)/\cos(SMDC)$$
$$SMDC1 = SMDC + N[\cos(SMRA)]$$

The local hour angle is then computed from the equation

$$LHA^\circ = 360^\circ - 15(RA^h) + 15(ST^h) - LO^\circ + (15.04106864)^* Z$$

Where LO is the longitude of the observer and Z is Zulu Time (Greenwich Mean Time or Universal Time) and the superscript h stands for hours and fraction of an hour.

LHA is reduced by 360° until $0° < LHA° < 360°$

Next, the elevation is computed as shown below:

$$EL = \sin^{-1} [\sin(DC) \cdot \sin(LA) + \cos(LA) \cdot \cos(LHA) \cdot \cos(DC)]$$

where

LA = the latitude of the observer
E = EL + refraction correction

The azimuth is then computed as follows:

$$A = \sin^{-1} [-\sin(LHA) \cdot \cos(DC) / \cos(EL)]$$

The elevation and azimuth are then converted into degrees, mils, or radar octal as requested.

The mils values for azimuth or elevation are obtained from the relationship:

$$mils = degrees \times 17.777777$$

The octal values for azimuth or elevation are obtained from the relationship:

Conversion to octal of bit count where the bit count = mils * 40.96 (there are exactly 40.96 bits per mil on the basis of an 18-bit angle encoder system).

APPENDIX VII

DERIVATION OF COORDINATE TRANSFORMATION OF SIDEREAL MOUNT

PRECEDING PAGE BLANK-NOT FILM

1. COORDINATE TRANSFORMATION

Let X''', Y''', Z''' be the sidereal mount axes, and X, Y, Z be the local site axes. The X-Y plane is horizontal, and Z is the local vertical. β is the site latitude base tilt angle or 'mount angle;" α is the declination angle; and γ is the right ascension angle.

a. Coordinate Conversion From (X''', Y''', Z''') to (X'', Y'', Z'')

$$\begin{bmatrix} X'' \\ Y'' \\ Z'' \end{bmatrix} = \begin{bmatrix} \cos\gamma & -\sin\gamma & 0 \\ \sin\gamma & \cos\gamma & 0 \\ 0 & 0 & 1 \end{bmatrix} \begin{bmatrix} X''' \\ Y''' \\ Z''' \end{bmatrix}$$ (See Figure VII-1)

b. Coordinate Conversion From (X'', Y'', Z'') to (X', Y', Z')

$$\begin{bmatrix} X' \\ Y' \\ Z' \end{bmatrix} = \begin{bmatrix} \cos\alpha & 0 & -\sin\alpha \\ 0 & 1 & 0 \\ \sin\alpha & 0 & \cos\alpha \end{bmatrix} \begin{bmatrix} X'' \\ Y'' \\ Z'' \end{bmatrix}$$ (See Figure VII-2)

c. Coordinate Conversion From (X', Y', Z') to (X, Y, Z)

$$\begin{bmatrix} X \\ Y \\ Z \end{bmatrix} = \begin{bmatrix} 1 & 0 & 0 \\ 0 & \cos\beta & -\sin\beta \\ 0 & \sin\beta & \cos\beta \end{bmatrix} \begin{bmatrix} X' \\ Y' \\ Z' \end{bmatrix}$$ (See Figure VII-3)

d. Coordinate Conversion From (X''', Y''', Z''') to (X, Y, Z)

$$\begin{bmatrix} X \\ Y \\ Z \end{bmatrix} = \begin{bmatrix} \cos\alpha & 0 & -\sin\alpha \\ 0 & 1 & 0 \\ \sin\alpha & 0 & \cos\alpha \end{bmatrix} \begin{bmatrix} X' \\ Y' \\ Z' \end{bmatrix}$$ (See Figure VII-4)

$$= \begin{bmatrix} 1 & 0 & 0 \\ 0 & \cos\beta & -\sin\beta \\ 0 & \sin\beta & \cos\beta \end{bmatrix} \begin{bmatrix} \cos\alpha & 0 & -\sin\alpha \\ 0 & 1 & 0 \\ \sin\alpha & 0 & \cos\alpha \end{bmatrix} \begin{bmatrix} X'' \\ Y'' \\ Z'' \end{bmatrix}$$

$$= \begin{bmatrix} 1 & 0 & 0 \\ 0 & \cos\beta & -\sin\beta \\ 0 & \sin\beta & \cos\beta \end{bmatrix} \begin{bmatrix} \cos\alpha & 0 & -\sin\alpha \\ 0 & 1 & 0 \\ \sin\alpha & 0 & \cos\alpha \end{bmatrix} \begin{bmatrix} \cos\gamma & -\sin\gamma & 0 \\ \sin\gamma & \cos\gamma & 0 \\ 0 & 0 & 1 \end{bmatrix} \begin{bmatrix} Y''' \\ Y''' \\ Z''' \end{bmatrix}$$

PRECEDING PAGE BLANK-NOT

$$= \begin{bmatrix} \cos\alpha\ \cos\gamma & -\cos\alpha\ \sin\gamma \\ \sin\alpha\ \sin\beta\ \cos\gamma + \cos\beta\ \sin\gamma & \sin\alpha\ \sin\beta\ \sin\gamma + \cos\beta\ \cos\gamma \\ \sin\alpha\ \cos\beta\ \cos\gamma + \sin\beta\ \sin\gamma & -\sin\alpha\ \cos\beta\ \sin\gamma + \sin\beta\ \cos\gamma \end{bmatrix}$$

$$\begin{bmatrix} -\sin\alpha \\ -\cos\alpha\ \sin\beta \\ \cos\alpha\ \cos\beta \end{bmatrix} \begin{bmatrix} X''' \\ Y''' \\ Z''' \end{bmatrix}$$

2. PROJECTION OF THE OPTICAL AXIS ONTO THE X, Y, Z COORDINATE SYSTEM

Let the X''' axis of the X''', Y''', Z''' coordinate system be the optical axis. The unit vector along the optical axis is $(X''' = 1,\ Y''' = 0,\ Z''' = 0) = U_{X'''}$. After coordinate conversion from (X''', Y''', Z''') to (X, Y, Z), $U_{X'''}$ becomes

$$\begin{bmatrix} x_{X'''} \\ y_{X'''} \\ z_{X'''} \end{bmatrix} = \begin{bmatrix} \cos\alpha\ \cos\gamma \\ -\sin\alpha\ \sin\beta\ \cos\gamma + \cos\beta\ \sin\gamma \\ \sin\alpha\ \cos\beta\ \cos\gamma + \sin\beta\ \sin\gamma \end{bmatrix}_{X,Y,Z}$$

Define the angle E as the elevation angle between the optical axis $U_{X'''}$ and the X, Y plane, and the angle A as the azimuth angle between the projection of $U_{X'''}$ on to the X, Y plane and the X axis. Then

$$x_{X'''} = \cos E \cdot \cos A$$

$$y_{X'''} = \cos E \cdot \sin A$$

$$z_{X'''} = \sin E$$

3. ELEVATION AND AZIMUTH ANGLES OF THE OPTICAL AXIS WITH RESPECT TO THE X, Y, Z COORDINATE SYSTEM

Therefore:

$$\tan E = \frac{z_{X'''}}{\sqrt{x^2_{X'''} + y^2_{X'''}}}$$

$$\tan A = \frac{y_{X'''}}{x_{X'''}}$$

or

$$\tan E = \frac{\sin\alpha\cos\beta\cos\gamma + \sin\beta\sin\gamma}{(\cos^2\alpha\cos^2\gamma + \sin^2\alpha\sin^2\beta\cos^2\gamma + \cos^2\beta\sin^2\gamma - 2\sin\alpha\sin\beta\cos\beta\sin\gamma\cos\gamma)^{1/2}}$$

$$\tan A = \frac{-\sin\alpha\ \sin\beta\ \sin\gamma + \cos\beta\ \sin\gamma}{\sin\alpha\ \cos\beta\ \cos\gamma + \sin\beta\ \sin\gamma}$$

4. FIELD ROTATION ANGLE R

Define the field rotation angle R as the angle between the Y''' axis and the vector W formed by the intersection of the X, Y plane and the Y''', Z''' plane.

The intersecting vector W is given by the determinant of

$$\begin{vmatrix} i & j & k \\ 0 & 0 & 1 \\ \cos\alpha\ \cos\gamma & -\sin\alpha\ \sin\beta\ \cos\gamma + \cos\beta\ \sin\gamma & \sin\alpha\ \cos\beta\ \cos\gamma + \sin\beta\ \sin\gamma \end{vmatrix}$$

or

$$W = i\,x_W + j\,y_W + k\,z_W$$

where

$$x_W = \sin\alpha\ \sin\beta\ \cos\gamma - \cos\beta\ \sin\gamma$$

$$y_W = \cos\alpha\ \cos\gamma$$

$$z_W = 0$$

The unit vector U_W is

$$U_W = \frac{1}{\left[\left(\sin\alpha\ \cos\beta\ \cos\gamma - \cos\beta\ \sin\gamma\right)^2 + \cos^2\alpha\ \cos^2\gamma\right]^{1/2}} \begin{bmatrix} \sin\alpha\ \sin\beta\ \cos\gamma - \cos\beta\ \sin\gamma \\ \cos\alpha\ \cos\gamma \\ 0 \end{bmatrix}_{X,Y,Z}$$

The unit vector $U_{Y'''}$ on the X, Y, Z coordinate system is

$$U_{Y'''} = \begin{bmatrix} -\cos\alpha \sin\gamma \\ \sin\alpha \sin\beta \sin\gamma + \cos\beta \cos\gamma \\ -\sin\alpha \cos\beta \sin\gamma + \sin\beta \cos\gamma \end{bmatrix}_{X,Y,Z}$$

Then the cosine of the field rotation angle R is given by the interproduct of U_W and $U_{Y'''}$; hence,

$$\cos R = U_W , U_{Y'''}$$

$$= \frac{\cos\alpha \cos\beta}{\left[\left(\sin\alpha \cos\beta \cos\gamma - \cos\beta \sin\gamma\right)^2 + \cos^2\alpha \cos^2\gamma\right]^{1/2}}$$

5. SUMMARY

Given angles α, β, and γ,

$$\tan E = \frac{\sin\alpha \cos\beta \cos\gamma + \sin\beta \sin\gamma}{\left(\cos^2\alpha \cos^2\gamma + \sin^2\alpha \sin^2\beta \cos^2\gamma + \cos^2\beta \sin^2\gamma - 2 \sin\alpha \sin\beta \cos\beta \sin\gamma \cos\gamma\right)^{1/2}}$$

$$\tan A = \frac{-\sin\alpha \sin\beta \cos\gamma + \cos\beta \sin\gamma}{\sin\alpha \cos\beta \cos\gamma + \sin\beta \sin\gamma}$$

$$\cos R = \frac{\cos\alpha \cos\beta}{\left[\left(\sin\alpha \cos\beta \cos\gamma - \cos\beta \sin\gamma\right)^2 + \cos^2\alpha \cos^2\gamma\right]^{1/2}}$$

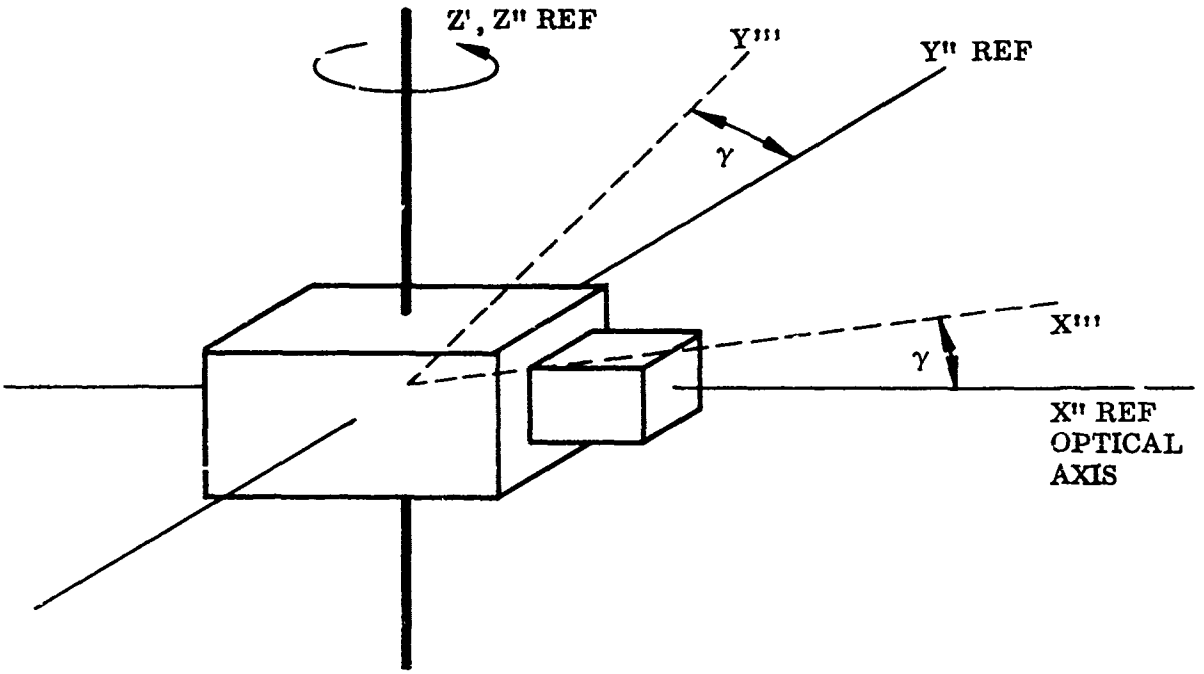


Figure VII-1

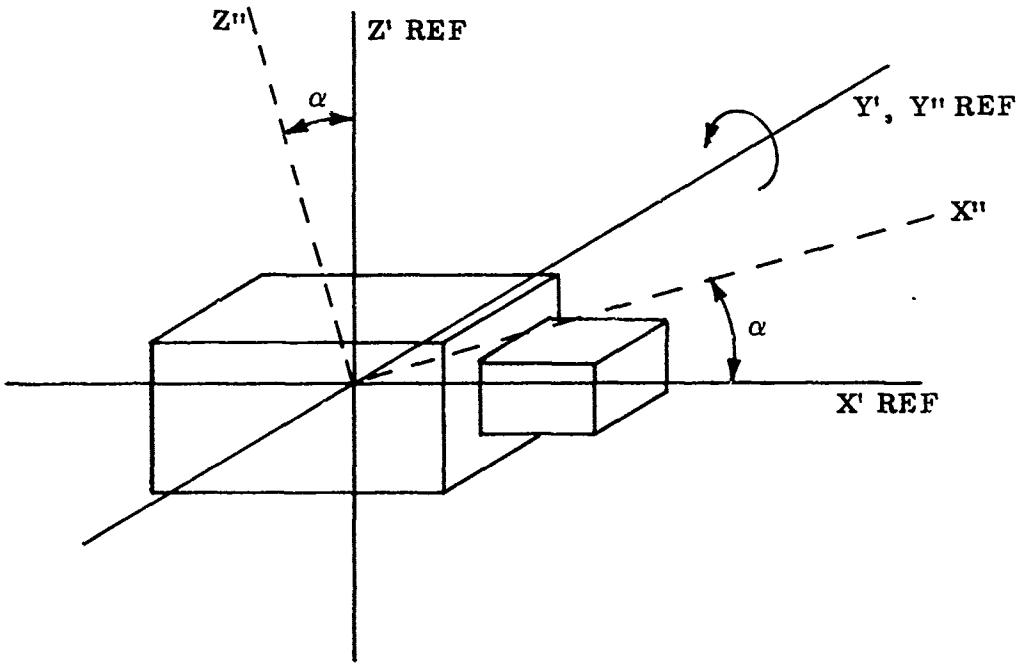


Figure VII-2

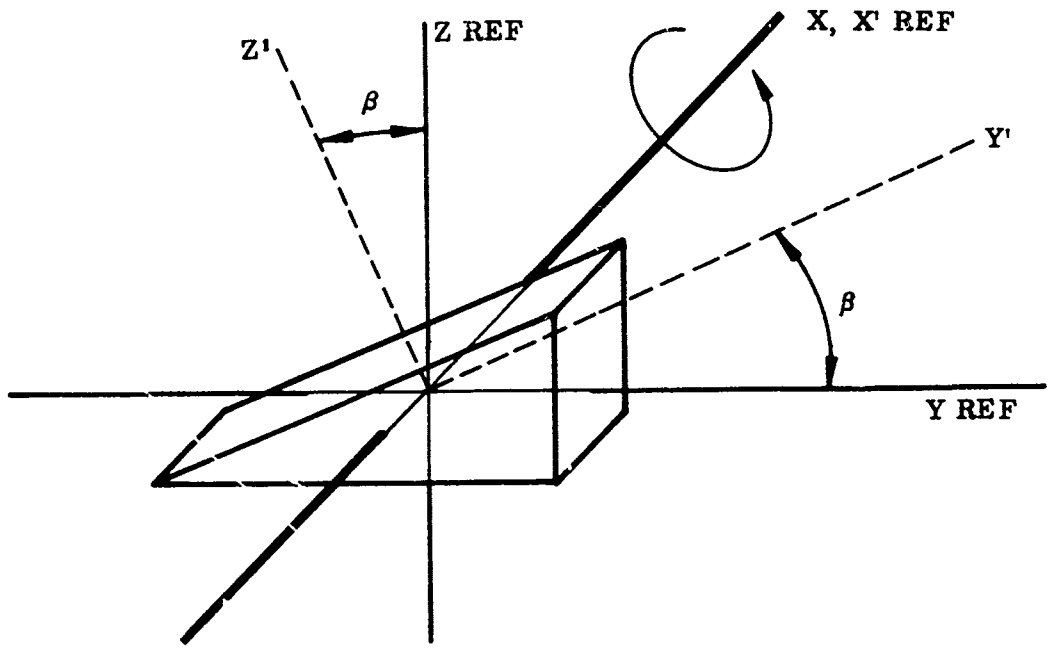


Figure VII-3

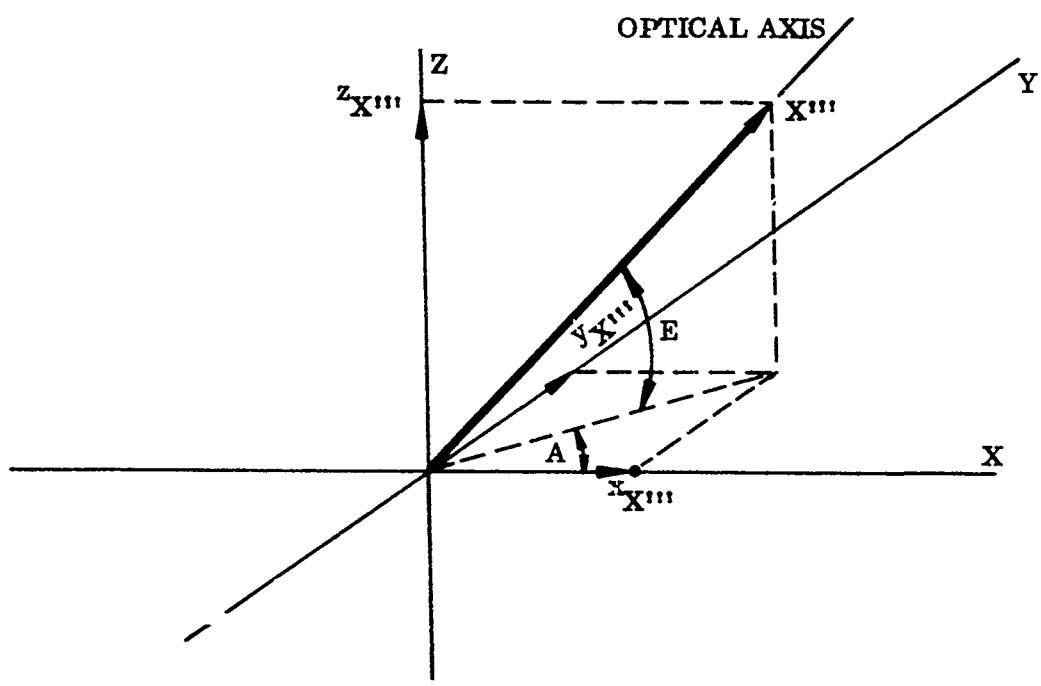


Figure VII-4

APPENDIX VIII

NOVA TIMING FOR CONVERSION, PROCESSING, AND RECORDING

1. GENERAL

This appendix considers two configurations – the SUPER NOVA with semiconductor memory and core memory, and the NOVA 800 with core memory. Time budgets are given for 100, 75 and 50 percent of the nominal 80-kHz sampling rate.

Over a 1-msec interval, the summations ΣA_i, ΣE_i, and ΣI_i can be performed with single precision integer addition on a 16-bit NOVA machine. Specifically, since

$$0 \leq A_i , E_i < 2^8 \quad \text{and} \quad 0 \leq I_i \leq 2^{10}$$

then

$$0 \leq \sum_{i=1}^{20} A_i , \sum_{i=1}^{20} E_i , \sum_{i=1}^{40} I_i \leq 2^{16}$$

Therefore, each of these summations can be computed, employing the following control statements:

Statements			SN[a] (μsec)	SN, SC[a] (μsec)
LOOP	LDA	ϕ , + ϕ , 2	1.6	1.2
	ADD	ϕ , 1	0.8	0.3
	INC	3 , 3 , SZR	0.8	0.3
	JMP	LOOP	0.8	0.3
			4.0	2.1

(a) Timing for SUPER NOVA employing core memory, and SUPER NOVA employing 300-msec semiconductor (SC) memory, respectively.

PRECEDING PAGE BLANK-NO

Hence,for 1 msec, the time budget is

Sample Rate (%)	SUPER NOVA (NOVA 800)[a] (μsec)	SUPER NOVA, SC (μsec)
100	320	168
75	240 (330)	126
50	160 (220)	84

(a) NOVA 800 takes approximately 1.36 times longer than the SUPER NOVA in this application.

2. COMPUTING SUMS OF PRODUCTS

Over a 1-msec interval, the sums of products

$$\sum_{i=1}^{20} A_i * A_{i+1} \quad \text{and} \quad \sum_{i=1}^{20} E_i * E_{i+1}$$

will require double precision integer addition and single precision integer multiplication on a 16-bit NOVA machine. Therefore, each of these summations can be carried out employing the following generic control statements:

Statements			SN (μsec)	SN, SC (μsec)
LOOP	LDA		1.6	1.2
	LDA		1.6	1.2
	MUL		3.8	3.7
	ADDZ		0.8	0.3
	INC		0.8	0.3
	ADD		0.8	0.3
	MOV		0.8	0.3
	ING		0.8	0.3
	JMP	LOOP	0.8	0.3
			11.4	7.9

The time budget for 1 msec is:

Sample Rate (%)	SUPER NOVA (NOVA 800)[a] (μsec)	SUPER NOVA, SC (μsec)
100	456	316
75	342 (610)	237
50	228 (410)	158

(a) NOVA 800 takes approximately 1.7 times longer than the SUPER NOVA plus a 20 μsec setup time for the two summation loops.

3. ADC AND TAPE OUTPUT BLOCK TRANSFERS

The number of words in each input buffer determines the number of ADC output samples which will be transferred from the ADC to main memory via the DMA in a block transfer mode. In this mode, the problem program sets up the block transfer, then turns the transfer function over to the ADC controller. The time taken to set up the transfer is independent of block length; that is, the longer the block the less effect this time has on the time budget. Even though the block transfer is accomplished automatically, the control processor is used on a "cycle stealing" basis to handle each sample. Using the high-speed data channel,this requires 0.8 μsec of processor time per sample. Thus over a 1-msec period:

Sample Rate (%)	SUPER NOVA (NOVA 800)[a] (μsec)
100	66.4
75	50.4
50	34.4

(a) Times include 3 voice samples per 1-msec interval plus a 12.5-μsec setup time for each block transfer.

Tape writing will also be accomplished in a block transfer mode at an average 8k words/sec; 1 μsec of processor time is taken for each word. This is compatible with the 16k byte/sec transfer rate possible with the NOVA specified tape drive. Thus the processor times are 8, 6, and 4 μsec for 100, 75, and 50 percent of the nominal sampling rate plus the voice samples.

4. SUMMARY

The time budget for a 1-msec interval is as follows:

Sampling Rate (%)	NOVA 800 (μsec)	SUPER NOVA (μsec)	SN, SC (μsec)
100	–	902	610
75	1048	690	471
50	721	479	333

This budget includes the conversion and recording times for A_i, E_i, I_i, and V_i. Setup times for conversion and recording block transfers were amortized over 12.5-msec intervals.

APPENDIX IX

MEASUREMENT RESULTS – FADE CORRELATION EXPERIMENT

This appendix presents the data tabulations produced by the Fourier Analyzer during the Fade Correlation Experiment. For each measurement (designated by a "measurement number") there are four tabulations, each preceded by a line labeled SF (for "scale factors"), as follows:

(1) Square of normalized cross-correlation function (first 32 values)

(2) Autocorrelation function of the A-signal (first 32 values). The zeroth value (first entry in this tabulation) is the variance of the A-signal.

(3) Zero-frequency or d-c value of the A-signal. One pair of entries appears, the first being the real part of the zero frequency term of the A-signal Fourier spectrum, i.e., the d-c value, and the second being the imaginary part which is automatically zero for the zero-frequency term.

(4) Power spectral density of A-signal expressed in units of 0.01 dB. The columns of zeros can be disregarded because these values represent the imaginary parts of each of the power spectrum components, and they are all automatically zero.

The SF headings for the first three tabulations on each page have three parts, as follows:

(1) A numerical scale factor applicable to all entries and equal to ten to that exponent.

(2) A code distinguishing time domain variables (0) from Fourier domain variables (4).

(3) A code designating the input sampling conditions. The number 59 denotes a sample size per data block of 256, extending over a 200-msec interval. For this condition, the frequency interval Δf of the power spectrum tabulation is 5 Hz. Code 60 denotes a 256-point sample extending over 100 msec. The corresponding Δf is 10 Hz.

For the fourth (power spectrum) tabulation, the three SF elements have the following meaning:

(1) Number of dB to be added to the values indicated by the table to obtain values referenced to a level of $(1 \text{ volt})^2$. For example, the second entry in the power spectrum tabulation for Measurement No. 1 is $-11.95 \text{ dB} - 30.00 \text{ dB} = -41.95 \text{ dB}$.

(2) Variable code (6) indicating power spectral density in dB units.

(3) Input sampling condition – same meaning as for other tabulations.

PRECEDING PAGE BLANK-NOT FILME

The experimental conditions applicable to each measurement are those indicated by Table IX-1 for the corresponding Measurement No., and more generally, by the discussion in Section II, 5, c.

In the power spectrum calculation, the zero frequency component was set equal to zero. In the following tabulations, this component is reproduced as -50.00 S.F., rather than $-\infty$, as this is the largest negative dB value that can be represented.

Table XI-1 Fade Correlation Measurement Conditions — 450-ft Outdoor Path

Measurement No.	$d_A = d_B$ = Primary Aperture Diameter (cm)
1	1.25
2	1 25
3	2.50
4	2.50
5	2.50
6	2.50
7	5.0
8	5.0
9	5.0

MEASUREMENT NO. 1

```
SF      -4       0      59
(   0)     9707    9800    9069    8354    7507    6666    5827    5101
(   8)     4436    3887    3380    2942    2629    2312    2024    1770
(  16)     1550    1339    1152     985     866     737     617     517
(  24)      435     360     296     238     195     153     117      86
/

SF      -7       0      59
(   0)     3515    3466    3374    3229    3067    2882    2703    2520
/

SF      -5       4      59
(   0)    -7158       0
/

SF     -40       6      59
(   0)    -5000       0     -232       0     -418       0     -752       0
(   4)     -798       0     -996       0    -1158       0    -1251       0
(   8)    -1447       0    -1489       0    -1645       0    -1597       0
(  12)    -1745       0    -1675       0    -1972       0    -1984       0
(  16)    -2099       0    -2209       0    -2160       0    -2231       0
(  20)    -2510       0    -2475       0    -2560       0    -2705       0
(  24)    -2786       0    -2911       0    -3032       0    -2838       0
(  28)    -2982       0    -3199       0    -3225       0    -3350       0
/
```

MEASUREMENT NO. 2

```
SF      -4       3      59
(   0)    9627    9669    8804    8001    7032    6152    5307    4581
(   8)    3941    3416    2935    2526    2211    1929    1657    1432
(  16)    1242    1062     914     788     692     591     510     427
(  24)     363     298     244     193     159     125      95      73
/

SF      -7       0      59
(   0)    4199    4128    3989    3774    3548    3302    3075    2846
/

SF      -5       4      59
(   0)   -7565       0
/
```

```
SF     -30       6      59
(   0)   -5000       0   -1195       0   -1338       0   -1655       0
(   4)   -1821       0   -1900       0   -1978       0   -2156       0
(   8)   -2212       0   -2496       0   -2425       0   -2532       0
(  12)   -2483       0   -2682       0   -2758       0   -2791       0
(  16)   -2932       0   -3107       0   -3160       0   -3091       0
(  20)   -3109       0   -3155       0   -3368       0   -3199       0
(  24)   -3689       0   -3722       0   -3681       0   -3630       0
(  28)   -3673       0   -3816       0   -3911       0   -4067       0
/
```

MEASUREMENT NO. 3

```
SF      -4       0      60
(   0)     9378    9570    9357    9121    9082    8812    8597    8275
(   8)     8020    7799    7456    7144    6832    6496    6166    5827
(  16)     5519    5182    4842    4515    4254    3948    3630    3333
(  24)     3105    2824    2555    2321    2128    1916    1705    1505
/

SF      -6       0      60
(   0)     8601    8518    8507    8400    8386    8265    8182    8033
/

SF      -5       4      60
(   0)   -15198
/

SF     -20       6      60
(   0)    -5000       0     -528       0    -1154       0    -1453       0
(   4)    -1952       0    -2106       0    -2628       0    -2831       0
(   8)    -2970       0    -3032       0    -3192       0    -3243       0
(  12)    -3368       0    -3393       0    -3477       0    -3623       0
/
```

MEASUREMENT NO. 4

```
SF      -4       0      60
(   0)     9155   9163   8789   8550   8264   7997   7599   7321
(   8)     6925   6660   6236   5947   5631   5338   5003   4697
(  16)     4437   4147   3857   3590   3368   3132   2899   2669
(  24)     2502   2280   2099   1917   1783   1620   1475   1314
/

SF      -6       0      60
(   0)    16545  16354  16269  15986  15842  15544  15266  14931
/

SF      -4       4      60
(   0)    -2949       0
/
```

POWER SPECTRUM PRINTOUT NOT OBTAINED

MEASUREMENT NO. 5

```
SF      -4       0      60
(   0)     9601    9523    9240    8929    8633    8297    7897    7491
(   8)     7061    6665    6235    5820    5446    5041    4646    4263
(  16)     3944    3599    3294    2988    2738    2478    2227    2014
(  24)     1832    1625    1459    1290    1171    1036     909     792
/

SF      -6       0      60
(   0)     5104    5052    5023    4936    4875    4772    4664    4535
/

SF      -5       4      60
(   0)   -10438       0
/

SF     -20       6      60
(   0)    -5000       0     -851       0    -1314       0    -1573
(   4)    -1775       0    -2162       0    -2292       0    -2519
(   8)    -2686       0    -2883       0    -3225       0    -3146
(  12)    -3356       0    -3406       0    -3433       0    -3544
(  16)    -3602       0    -3720       0    -3669       0    -3778
(  20)    -3883       0    -3924       0    -3924       0    -4079
(  24)    -4079       0    -4079       0    -4079       0    -4322
(  28)    -4225       0    -4225       0    -4322       0    -4225
/
```

MEASUREMENT NO. 6

```
SF      -4       0      60
(   0)     9420    9595    9268    9112    8943    8722    8393    8104
(   8)     7790    7534    7114    6798    6441    6060    5711    5346
(  16)     5029    4658    4332    3995    3738    3436    3135    2855
(  24)     2627    2377    2137    1913    1736    1540    1346    1180
/

SF      -6       0      60
(   0)     7155    7099    7075    6989    6943    6838    6736    6604
/

SF      -4       4      60
(   0)    -2548       0
/
```

```
SF     -20       6      60
(   0)    -5000       0     -660       0    -1078       0    -1617       0
(   4)    -1862       0    -2241       0    -2542       0    -2681       0
(   8)    -2766       0    -2961       0    -3161       0    -3271       0
(  12)    -3419       0    -3477       0    -3509       0    -3669       0
(  16)    -3694       0    -3748       0    -3720       0    -3845       0
(  20)    -3845       0    -4021       0    -4021       0    -4021       0
(  24)    -4021       0    -4226       0    -4146       0    -4226       0
(  28)    -4447       0    -4447       0    -4447       0    -4623       0
/
```

MEASUREMENT NO. 7

```
SF      -4       0      59
(   0)    9131    8981    8517    7969    7295    6577    5836    5086
(   8)    4382    3742    3138    2615    2181    1779    1451    1165
(  16)     947     742     591     452     359     273     208     152
(  24)     111      79      54      34      22      11       5       2
/

SF      -6       0      59
(   0)    6615    6536    6396    6172    5906    5589    5265    4892
/

SF      -5       4      59
(   0)   -7786       0
/

SF     -30       6      59
(   0)   -5000       0     -51       0     -75       0    -519       0
(   4)    -463       0    -566       0    -756       0    -858       0
(   8)   -1109       0   -1214       0   -1260       0   -1430       0
(  12)   -1675       0   -1817       0   -1802       0   -1951       0
(  16)   -2108       0   -2307       0   -2356       0   -2374       0
(  20)   -2433       0   -2613       0   -2707       0   -2749       0
(  24)   -2864       0   -2903       0   -2864       0   -2947       0
(  28)   -2995       0   -2995       0   -3022       0   -3060       0
/
```

MEASUREMENT NO. 8

```
SF       -4       0      59
(   0)     8801    8749    8304    7822    7255    6571    5830    5124
(   8)     4437    3837    3267    2782    2389    2025    1727    1470
(  16)     1278    1094     948     816     714     616     527     438
(  24)      370     297     236     179     136      94      60      36
/

SF       -6       0      59
(   0)     3651    3614    3553    3438    3313    3144    2967    2771
/

SF       -5       4      59
(   0)    -4474       0
/
```

POWER SPECTRUM PRINTOUT NOT OBTAINED

MEASUREMENT NO. 9

```
SF      -4       0      59
(   0)     8406    8281    7645    7057    6339    5584    4783    4051
(   8)     3352    2745    2203    1749    1387    1072     828     628
(  16)      482     361     269     198     148     106      72      49
(  24)       34      20      11       4       1       0       0       0
/

SF      -6       0      59
(   0)     4870    4822    4738    4581    4409    4172    3919    3632
/

SF      -5       4      59
(   0)    -3680       0
/
```

NOTE: POWER SPECTRUM VALUES IN FOLLOWING TABLE READ FROM CRT DISPLAY PHOTOGRAPH - ACCURACY APPROX. 0.25 DB

```
SF     -30       6      59
(   0)    -5000       0   -0100       0   -0400       0   -0400       0
(   4)    -0600       0   -0700       0   -0950       0   -0950       0
(   8)    -0950       0   -1300       0   -1700       0   -1500       0
(  12)    -1900       0   -1650       0   -2100       0   -240..      0
(  16)    -2600       0   -2550       0   -2650       0   -3200       0
(  20)    -3100       0   -3250       0   -3350       0   -3350       0
(  24)    -3500       0   -3500       0   -3700       0   -3700       0
(  28)    -3700       0   -3900       0   -3900       0   -3900       0
```

REFERENCES

1. U.S. Air Force Systems Command, Space and Missile Systems Organization, Laser Communication Preliminary Subsystem Design for the Space Data Relay Subsystem, Final Report, SAMSO TR-71-252 (LMSC-B290200, 2 vol.) 19 Nov 1971 (S)

2. R. F. Lutomirski and H. T. Yura, "Propagation of a Finite Optical Beam in an Inhomogeneous Medium," Appl. Opt., 10, 1971, p. 1652

3. A. Papoulis, Probability, Random Variables, and Stochastic Processes, McGraw-Hill, New York, 1965

4. V. W. Cooley and J. W. Tukey, "An Algorithm for the Machine Calculation of Complex Fourier Series," Math. Comp., 19, 1965, pp. 297–301

5. W. J. Smith, Modern Optical Engineering – The Design of Optical Systems, McGraw-Hill, New York, 1966, pp. 84, 298

6. D. L. Fried, "Statistics of a Geometric Representation of Wave-Front Distortion," J. Opt. Soc. Am., Vol. 55, Nov 1965, pp. 1427–1935

7. Air Force Systems Command, Air Force Avionics Laboratory, Acquisition and Tracking Performance Evaluation, Technical Report AFAL-TR-72-21 Wright-Patterson Air Force Base, Ohio (Contract F33615-72-C-1941), Mar 1973

8. J. R. Kerr, Propagation of Multiwavelength Laser Radiation Through Atmospheric Turbulence (Technical Report under RADC Contract F30602-72-C-0470), Jan 1973

9. B. Stromgren, "Vierteljahrsschr," Astronomical Society, 70, 65 (1965)

10. Caratheodory, C., "Hamburger Math.," Einzelschriften, 28 (1940)

11. Bouwers, A., Achievements in Optics, Elsevier, New York (1946)

12. Linfoot, E. H., "Monthly Notices of the Royal Astronomical Society," 109, 279 (1949); 111, 75 (1951)

13. I. S. Bowen, Stars and Stellar Systems, I – Telescopes, G. P. Kuiper and B. M. Middlehurst, eds. University of Chicago Press, Chicago, 1960, p. 43

14. ITT-Gilfillan, Inc., Final Design/Report for ODC Daylight Tracking Study, (ITT-FEC P.O. WC-1331, Air Force Contract F-04697-67-C-001), Dec 1971

15. R. I. Mitchell and F. F. Forbes, "Stellar Photometric Data for Six Different Photocathode Materials and the Silicon Detector," Communications of the Lunar and Planetary Laboratory, University of Arizona, 5 Dec 1968

16. W. L. Wolfe, ed., Handbook of Military Infrared Technology, U.S. Government Printing Office, Washington, D.C.

17. Dietze, Gerhard, Einführung in die Optik der Atmosphäre (Introduction to Atmospheric Optics), Geest & Partig, Leipsig, Germany, 1957

UNCLASSIFIED
Security Classification

DOCUMENT CONTROL DATA - R & D

(Security classification of title, body of abstract and indexing annotation must be entered when the overall report is classified)

1. ORIGINATING ACTIVITY (Corporate author)	2a. REPORT SECURITY CLASSIFICATION
Lockheed Palo Alto Research Laboratory Lockheed Missiles & Space Company, Inc. Palo Alto, California 94304	Unclassified 2b. GROUP

3 REPORT TITLE

ATMOSPHERIC TRANSMISSION MEASUREMENT 1

4 DESCRIPTIVE NOTES (Type of report and inclusive dates)

Final Report – 22 May 1972 to 8 March 1973

5. AUTHOR(S) (First name, middle initial, last name)

H. V. Hance
B. D. Grabois

6. REPORT DATE	7a. TOTAL NO. OF PAGES	7b. NO. OF REFS
August 1973	292	21

8a. CONTRACT OR GRANT NO.	9a. ORIGINATOR'S REPORT NUMBER(S)
F33615-72-C-1938 b. PROJECT NO. 405B c. d.	LMSC-D315126 9b. OTHER REPORT NO(S) (Any other numbers that may be assigned this report) AFAL-TR-73-154

10 DISTRIBUTION STATEMENT

Distribution is limited to U.S. Government agencies only; test and evaluation data, March 1973. Other requests for this document must be referred to AFAL/TEL/405B, Wright-Patterson AFB, Ohio 45433.

11 SUPPLEMENTARY NOTES	12. SPONSORING MILITARY ACTIVITY
	Air Force Avionics Laboratory Wright-Patterson Air Force Base, Ohio

13 ABSTRACT

A novel method for improving the performance of laser communication links through a turbulent atmosphere, called "fast tracking," has been demonstrated experimentally in the laboratory to be both theoretically sound and practicable. Also, a design has been prepared for an atmospheric transmission measurement (ATM) system suitable for use at field sites for evaluation of atmospheric turbulence effects on ground-to-space laser communication links. The ATM system makes use of a fast-response (1 msec) star tracker and image intensity sensor; it is relatively simple and economical to use because neither flight hardware nor flight operations is involved, and it is capable of day or night operation. A field measurement plan is presented that is designed to aid in the selection of laser transmitter sites and to indicate the performance of ground-to-space links using those sites.

Because the concept of optical antenna gain reciprocity is central to both the fast-tracking technique and to the ATM system, an initial experimental objective of the program was to test this theory. The key test was conducted over a 450-ft outdoor path using two laser-transmitter/pinhole-receiver units directed toward one another. In each unit, the transmitter and receiver were in a conjugate relationship to one another and shared a common aperture, as required by the theory. For a series of measurements with beam diameters from 1.25 to 5 cm, the normalized cross correlation of the two received signals was found to be 0.964 ± 0.023 (σ), a value in satisfactory agreement with the theoretical value of unity. As beam breakup ranged from negligible to severe for the range of aperture sizes used, the validity of reciprocity theory is considered to be well substantiated for all beam-perturbation conditions of practical interest.

(Continued)

DD FORM 1 NOV 65 1473

UNCLASSIFIED
Security Classification

DD1473, Section 13 (Cont.)

To provide quantitative criteria for the design of the experiments, the reciprocity theory was reviewed in detail and was extended to cover the quasicoherent pinhole-detector receiver using a pinhole of finite size. Boresight requirements also were derived for a fast-tracking transmitter.

In the fast-tracking experiment, an optical tracker associated with the transmitting laser sensed angle deflections of the beam from a beacon laser co-located with the receiver and applied an equal correction to the transmitter by means of beam steering optics. When using artificial turbulence that produced tracking errors similar to those expected with real atmospheric turbulence, it was found that activation of the beam steerers reduced signal strength fluctuations at the receiver by 18 dB or more. The magnitude of this improvement is regarded as adequate to demonstrate the soundness of the fast-tracking concept.

14 KEY WORDS	LINK A		LINK B		LINK C	
	ROLE	WT	ROLE	WT	ROLE	WT
Atmospheric Transmission Measurement						
Optical Communication						
Optical Atmospheric Fading						
Atmospheric Fading Reduction						
Optical Reciprocity Theory						

END 11-73